Western University

Scholarship@Western

10-18-2012 12:00 AM

Subsynchronous Resonance in Wind Farms

Akshaya Kumar Moharana
The University of Western Ontario

Supervisor
Rajiv K. Varma
The University of Western Ontario

Follow this and additional works at: https://ir.lib.uwo.ca/etd

Part of the Power and Energy Commons

Recommended Citation

Moharana, Akshaya Kumar, "Subsynchronous Resonance in Wind Farms" (2012). *Electronic Thesis and Dissertation Repository*. 912.
https://ir.lib.uwo.ca/etd/912

SUBSYNCHRONOUS RESONANCE IN WIND FARMS

(Spine title: Resonance in Wind Farms)

(Thesis format: Monograph)

by

Akshaya Kumar <u>Moharana</u>

Graduate Program
in
Engineering Science

Department of Electrical and Computer Engineering

A thesis submitted in partial fulfillment
of the requirements for the degree of
Doctor of Philosophy

The School of Graduate and Postdoctoral Studies
The University of Western Ontario
London, Ontario, Canada

THE UNIVERSITY OF WESTERN ONTARIO
School of Graduate and Postdoctoral Studies

CERTIFICATE OF EXAMINATION

Supervisor   Examiners

_____   _____
Dr. Rajiv K. Varma   Dr. Udaya D. Annakkage

Supervisory Committee
                                                    _____
                                                    Dr. Horia Hangan
_____

                                                    _____
                                                    Dr. Mohammad Dadash Zadeh
_____

                                                    _____
                                                    Dr. Lyndon J. Brown

The thesis by

Akshaya Kumar <u>Moharana</u>

entitled:

Subsynchronous Resonance in Wind Farms

is accepted in partial fulfillment of the
requirements for the degree of
Doctor of Philosophy

_____   _____
            Date   Chair of the Thesis Examination Board

ii

ABSTRACT

Large-scale integration of wind farms in transmission networks has led to several challenges; one of which is the need for increased transmission capacity to transport a bulk amount of wind power. Series compensation is an established means of enhancing the power transfer capability of existing transmission lines and is being increasingly considered for integrating large wind power plants. However, series compensated transmission lines may cause subsynchronous resonance (SSR) in turbine-generators, which can lead to electrical instability at subsynchronous frequencies and potential turbine-generator shaft failures.

This thesis deals primarily with the potential of subsynchronous resonance in induction generator based wind farms connected to series compensated lines. Two types of induction generators - single cage and double cage, are considered to develop a state space model of the overall wind farm system. Eigenvalue analyses followed by participation factor analysis and sensitivity studies are performed over a wide range of operating conditions. These analyses include variations in the size of wind farm, wind power output, and series compensation levels. The potential for SSR in a wind farm is examined through a comprehensive small signal analysis. A novel equivalent circuit analysis is also presented in this thesis for investigating the impact of fault at wind farm terminals based on the resonant speeds of wind turbine generators. Both eigenvalue analysis and equivalent circuit studies are reasonably validated through electromagnetic transient simulations carried out using PSCAD/EMTDC software. These studies are conducted for both modified IEEE First SSR Benchmark systems and Second SSR Benchmark systems, and with three different commercially available wind turbine generators. It is found that induction generator effect based SSR may be experienced with large wind farms even at realistic levels of series compensation.

This thesis proposes a STATCOM to alleviate SSR in such series compensated wind farms. Two STATCOM controllers are proposed and their performances compared. A detailed SSR study is also conducted to examine the impact of HVDC lines on induction

generator based wind farms. However, it is concluded that HVDC converter controller may not have the potential for torsional interaction with IG based wind farms.

This thesis also presents a study of turbine trippings in a large commercially operated wind farm in Ontario. Detailed analysis has led to the conclusion that the trippings were caused due to harmonic resonances resulting from large transmission capacitor and wind park capacitors. Several recommendations are made in this thesis to avoid the future wind turbine trippings.

Keywords

Dedicated to my

Parents

ACKNOWLEDGMENTS

First of all, I would like to express my deep and sincere gratitude to my supervisor Prof. Rajiv K. Varma for his excellent supervision, invaluable guidance and immense support during this work. I consider myself fortunate for having had the opportunity and work with him. His advice in all respects is of tremendous value. No words are adequate to express my gratefulness to him.

I am also very grateful to Dr. Michael Dang and Ravi Seethapathy, Hydro One Inc. for providing me with a rare opportunity to work with real industrial problems.

I am extremely fortunate to have learned from Dr. Jin Jiang, Dr. L. J. Brown, Dr. A. Yazdani, Dr. J. Samarabandu, and Dr. M. E. Saadany during various courses offered by them.

I sincerely thank Prof. L. Mansinha and his family for their help and support during my stay in London. I have learned a lot from Prof. Mansinha. It has been a great pleasure to be in the company of his family.

I am highly grateful to Prof. P. K. Dash, Director Research SOA University, Bhubaneswar, India, for his active guidance during the research project on VSC HVDC. I sincerely acknowledge the cooperation I got from Prof. Dash and his research group.

I am extremely grateful to my friends Byomakesh, Jon, Mahendra, Gagan, Arif and Ehsan for their constant encouragement, support, companionship, and availability. Words are really not enough to express my sincere gratitude for their unbounded help and care.

I would like to express my affectionate appreciation to my family for their unwavering faith and continuous support during my long academic education. I sincerely extend my

TABLE OF CONTENTS

LIST OF TABLES

LIST OF FIGURES

LIST OF ABBREVIATIONS

IG	:	Induction Generator
DFIG	:	Doubly Fed Induction Generator
FBM	:	First Benchmark Model
SBM	:	Second Benchmark Model
SSR	:	Subsynchronous Resonance
IGE	:	Induction Generator Effect
TI	:	Torsional Interaction
FACTS	:	Flexible AC Transmission Systems
SVC	:	Static Var Compensator
STATCOM	:	Static Synchronous Compensator
TCSC	:	Thyristor Controlled Series Capacitor
WTG	:	Wind Turbine Generator
FFT	:	Fast Fourier Transform
LCC	:	Line Commutated Converter
HVDC	:	High Voltage Direct Current
MOV	:	Metal Oxide Varistor
PSCAD	:	Power System Computer Aided Design
EMTDC	:	Electro-Magnetic Transient for DC
URS	:	Upper Resonant Speed
LRS	:	Lower Resonant Speed
WF	:	Wind Farm
PCC	:	Point of Common Coupling
SS	:	Substation
THD	:	Total Harmonic Distortion

LIST OF SYMBOLS

δ_{tg}	:	Torsional angle between wind turbine and induction geenartor
ω_t	:	Angular speed of wind turbine
ω_g	:	Angular speed of generator
H_t	:	Inertia constant of wind turbine
H_g	:	Inertia constant of generator
K_{tg}	:	Shaft stiffness between wind turbine and generator
D_{tg}	:	Damping coefficient between wind turbine and generator
R_s	:	Stator resistance per phase
$X_{s\sigma}$	:	Unsaturated stator leakage reactance per phase
R_r	:	Rotor resistance per phase
$X_{r\sigma}$	:	Unsaturated rotor leakage reactance per phase
X_m	:	Unsaturated mutual reactance between the stator and rotor windings
R_{r1}	:	First-cage rotor resistance per phase
$X_{r1\sigma}$	:	Unsaturated first-cage rotor leakage reactance per phase
R_{r2}	:	Second-cage rotor resistance per phase
$X_{r2\sigma}$	:	Unsaturated second-cage rotor leakage reactance per phase
C_g	:	Capacitance of wind turbine generator terminal capacitor
R	:	Transmission line resistance
L	:	Transmission line inductance
C	:	Series capacitance
K	:	Series compensation level
L_{dc}	:	DC transmission line inductance
R_{dc}	:	DC transmission line resistance
C_{dc}	:	DC link capacitance
T_w	:	Mechanical torque input to the wind turbine

T_g	:	Electromagnetic torque output of the generator
ω_s	:	Synchronous frequency (376.99 rad/s)
s	:	Slip of induction generator.
I_{ds}, I_{qs}	:	d-q axis stator current of single-cage induction generator
I_{dr}, I_{qr}	:	d-q axis rotor current of single-cage induction generator
I_{dr1}, I_{qr1}	:	d-q axis first-cage rotor current double-cage induction generator
I_{dr2}, I_{qr2}	:	d-q axis second-cage rotor current double-cage induction generator
E_d, E_q	:	d-q axis induced rotor voltage of single-cage induction generator
E_{d1}, E_{q1}	:	d-q axis induced rotor voltages across first-cage of double-cage induction generator
E_{d2}, E_{q2}	:	d-q axis induced rotor voltages across second-cage of double-cage induction generator
V_{ds}, V_{qs}	:	d-q axis voltage at the generator terminal
V_s	:	Wind turbine generator terminal bus voltage
I_d, I_q	:	d-q axis current of series compensated transmission line
V_{cd}, V_{cq}	:	d-q axis voltage across series capacitor
V_{bd}, V_{bq}	:	d-q axis voltage at infinite bus
V_b	:	Infinite bus voltage
V_{dr}	:	Rectifier station DC bus voltage
V_{di}	:	Inverter station DC bus voltage
V_{dc}	:	DC link capacitor voltage
I_{dr}	:	DC current injected from rectifier
I_{di}	:	DC current absorbed by inverter
α	:	Rectifier station firing angle
γ	:	Inverter station firing angle

Chapter 1

INTRODUCTION

1.1 GENERAL

In the last thirty years the wind energy industry has seen a rapid growth in comparison to other renewable energy industries. Enhanced technology and design improvements have played a significant role in increasing their penetration levels. The size of the wind turbines has increased, the cost has been reduced, and controllability of the wind power plants much improved, in recent years. The advancements in power electronics have placed wind energy as a serious and competitive alternative to other renewable sources [1]-[18]. Particularly North Europe, Germany, Spain, USA, Canada, China, and India have shown a strong achievement in expanding the wind energy systems. By the end of 2011, worldwide installed capacity reached 238 GW [1], [8], [11]. China, with 63 GW installed capacity, has become the leader of the international wind industry. Many countries have now set the target of generating 20% of their energy from renewable energy sources by 2020, of which wind energy is recognized as the prime contributor [5], [11]-[14].

In a commercially operated wind turbine, the mechanical drive train system transmits the rotor torque and feeds it to the electrical generator. Then the electrical generator converts the mechanical energy into electrical energy. In modern horizontal axis wind turbines, the mechanical system is one of the most complex systems. Based on the speed control of the wind turbine, it is operated in two modes: a) fixed speed, and b) variable speed [19]-[24]. In the case of a fixed speed wind turbine, the generator rotates at or near constant speed regardless of the wind speed. The speed is determined by the supply frequency of the network connected to the generator. These types of wind turbines produce maximum power at a particular wind speed and are equipped with squirrel cage induction generators, which are cheap, robust, and simple to operate. However, large reactive

power consumption and poor power quality are the major disadvantages of this wind turbine generator system [19], [22], [23].

In the case of a variable speed wind turbine maximum aerodynamic efficiency is gained by adapting different speeds of the turbine. This is achieved by keeping the tip speed ratio fairly constant [19], [20]. The input mechanical torque to the generator remains constant. Of the squirrel cage induction generator and synchronous generator, both could be used in this type of wind turbine. With the recent developments in power electronics, this topology is becoming popular very fast. Most wind farms in Europe and North America use Doubly Fed Induction Generators (DFIG) and the most recent trend is to use full converter based wind turbine generators [19], [23], [25].

However, there are large number of wind farms across USA, India, and Australia, etc., which utilize fixed speed Induction Generator based wind turbines. Currently many of these larger scale wind farms are either in operation or under construction. Brahmanvel wind farm in India has a total rating of 549.1 MW. The largest IG based wind farm in USA is the Twin Groves wind farm in Illinois with an installed capacity of 396 MW. A few of the other large scale IG based wind farms are Maple Ridge wind farm (321.75 MW) in New York, Fowler Ridge wind farm (300.30 MW) in Indiana, Pioneer Prairie wind farm (301.95 MW) in Iowa, and Stateline wind farm (300.96 MW) on the border of Washington and Oregon, USA [8], [9], [10], [14]-[18].

In the last 20 years, transmission technologies have benefited from a new stage of innovation. Today over two thirds of new large-scale transmission systems planned or under construction are high-voltage direct current (HVDC) systems. HVDC systems are an essential component of power systems to meet the growth in demand for electricity. Around the world, HVDC is being relied upon to integrate large amounts of intermittent renewable energy capacity, as well as the rapid capacity expansion of bulk power transmission to meet vibrant economic growth in the developing world [26]-[33].

Device dependent subsynchronous oscillations have been defined as the interaction between the turbine-generator torsional system and the power system components. Such interaction with turbine-generators has been found with DC converter controls, variable

speed motor controllers and power system stabilizers. There is a potential for such interaction for any wide bandwidth controller located near the turbine-generator. From the field test carried out in 1977 in North Dakota, it was found that the basic HVDC controls created growing torsional oscillations of the turbine-generator. Careful analysis of the test results shows that any HVDC converter has the potential for creating subsynchronous torsional oscillations in turbine generators that are connected to the same bus as the HVDC converter [34]-[41].

As the application of HVDC for the wind farm interconnection grows, a threat of SSR interaction also increases. However, no study has yet been undertaken in detail to address the concern of SSR interaction of the wind farm with HVDC current controllers.

1.2 SUBSYNCHRONOUS RESONANCE

Subsynchronous resonance is an electrical power system condition where the electric network exchanges energy with a turbine generator at one or more of the natural frequencies of the combined system below the synchronous frequency of the system [42]-[45]. Series compensation in the line results in excitation of subsynchronous currents at an electrical frequency f_{er} given by

$$f_{er} = f_0 \sqrt{\frac{X_c}{X_N}} \tag{1.1}$$

where, X_c is the reactance of the series capacitor, X_N is the reactance of the line including that of the generator and transformer, and f_0 is the nominal frequency of the power system. Typically X_c can be up-to 60-70% of X_N. Hence, $f_{er} < f_0$. The subsynchronous currents result in rotor torques and currents at the complementary frequency as f_r.

$$f_r = f_o - f_{er} \tag{1.2}$$

These rotor currents result in subsynchronous armature voltage components that may enhance subsynchronous armature currents to produce SSR. There are two aspects of the SSR: i) Self-excitation involving both an induction generator effect and torsional interaction, and ii) Transient torque (also called transient SSR).

1.2.1   Induction Generator Effect

Induction generator effect involves only electric system dynamics. Generator armature currents at subsynchronous frequency $\left(f_{er}\right)$ produce a component of rotating mmf in the armature air gap of angular velocity $2\pi f_{er}$. This mmf interacts with the main field air gap mmf to produce torques at subsynchronous frequency $\left(f_0 - f_{er}\right)$ and at super-synchronous frequency $\left(f_0 + f_{er}\right)$. If the generator rotor torsional mode frequency $\left(f_n\right)$ is different from the subsynchronous torque frequency $\left(f_0 - f_{er}\right)$ then relatively little torsional interaction takes place. However, because the rotor circuits are turning more rapidly than the rotating mmf, the resistance to the subsynchronous current viewed from the armature terminal is negative due to the commonly understood induction machine theory. When this negative resistance exceeds the sum of the armature and network resistance at the resonant frequency $\left(f_{er}\right)$, the armature currents can be sustained or grow. This phenomenon is called induction generator effect [42]-[45].

Wind farm comprising squirrel cage induction generators are also susceptible to the induction generator effect. As the rotating MMF produced by the subsynchronous frequency armature currents moves at speed ω_s, which is slower than the speed of the rotor ω_r, the resistance of the rotor (at the subsynchronous frequency viewed from the armature terminals) is negative as the slip 's' of the induction generator is negative. The slip is defined as:

$$s = \frac{\omega_s - \omega_r}{\omega_s} \qquad (1.3)$$

When self-excitation starts in a network, subsynchronous electrical currents will tend to increase rapidly.

1.2.2   Torsional Interaction

Torsional interaction involves both the electrical and mechanical system dynamics. When the frequency of the subsynchronous component of the armature voltage is close to or aligns with the electrical system natural frequency, the resultant subsynchronous current

will produce a rotor torque that is phased to sustain rotor oscillation. The torques at rotor torsional frequencies may then be amplified and potentially lead to shaft failure. This interplay between the electrical and mechanical system is known as torsional interaction [42]-[45].

1.2.3   Torque Amplification

System disturbance such as fault and switching of lines in the network may excite the oscillatory torque in the shaft of the generator. The shaft torque response is not sinusoidal with a single frequency, but contains contributions from many components including unidirectional, exponentially decaying, and oscillatory torques from subsynchronous to multiples of network frequency. Due to SSR, the subsynchronous frequency component may have large amplitude immediately following the disturbance that may be damped out subsequently. Each occurrence of the high amplitude transient torques may lead to cyclic fatigue in the shaft system [42]-[45].

1.3   TECHNIQUES FOR STUDY OF SUBSYNCHRONOUS RESONANCE

There are several techniques available for the study of subsynchronous resonance in power systems. The most common techniques are:

   (a)   Frequency scanning
   (b)   Eigenvalue analysis
   (c)   Electromagnetic transient simulation

1.3.1   Frequency Scanning

The frequency scanning technique is a fundamental technique for preliminary analysis of subsynchronous resonance. It involves the determination of the driving point impedance over the frequency range of interest as viewed from the neutral bus of the generator under study. In this technique, the equivalent resistance and reactance are computed by looking into the network from a point behind the stator winding of a particular generator, as a function of the frequency. Should there be a frequency at which the reactance is zero and resistance is negative, self-sustaining oscillations at that frequency would be expected

due to the induction generator effect. Frequency scanning can sometimes provide information regarding the possible problems with torsional interaction and transient torques. This method is easy to use and is fast [34], [42]-[49].

1.3.2   Eigenvalue Analysis

Eigenvalue analysis is extensively utilized for the study of torsional interaction and induction generator effect. This analysis is studied through the linearized model of the power system. The basic procedure of the eigenvalue analysis encompasses:

  (a)   Development of a positive sequence model of the power system

  (b)   Modeling of generator electrical circuits

  (c)   Modeling of turbine-generator spring mass system

  (d)   Calculation of eigenvalues of the interconnected systems

  (e)   Real component of eigenvalues corresponding to the subsynchronous modes of the turbine-generator spring mass system indicates the severity of torsional interaction

  (f)   Real component of eigenvalues corresponding only to electrical system resonant frequencies reveals the severity of the induction generator effects problem

The real part of the eigenvalue is a direct measure of the positive or negative damping for each mode [34]-[46], [50], [51].

1.3.3   Transient Torque Analysis

In order to determine the potential for SSR torque amplification, electromagnetic transient analysis is performed to find the peak transient shaft torque that is to be expected when a fault or equipment switch takes place in a series compensated line [34], [42], [43], [46].

In this thesis, SSR analysis is carried out through a comprehensive eigenvalue analysis that is then reasonably validated through the electromagnetic transient simulation in PSCAD/EMTDC software.

1.4 SUBSYNCHRONOUS RESONANCE IN SYNCHRONOUS GENERATORS

After the first series capacitor in the world was installed at Ballston, New York in 1928, the applications of series capacitors have increased significantly. A detailed study conducted in 1937 found the foundation of the subsynchronous resonance issues to be in power systems, as caused by series capacitors [52]. Three case studies are presented in this paper. Case-1 shows the response of a lightly loaded transformer connected through a series capacitor. It resulted in a large and steady exciting current in the transformer. Similarly, the impact of a series capacitor on the hunting of the synchronous generator is shown in Case-II. In this case, an interconnected system is considered. In Case-III, self-excitation of an induction motor operating in series with a series capacitor is discussed. Analytical methods are proposed in this paper for the analysis of each case. Details of self-excitation of an induction motor operating in series with a fixed capacitor are presented in [53]. Until 1970 not much work had been reported on SSR when the shaft damage occurred at Mohave generating station due to the subsynchronous interaction between the turbine-generator and the series capacitor. Because of the repeated occurrence of the incident at the Mohave station, this issue was taken up seriously and the very first paper on SSR of synchronous generator connected to series compensated transmission line was presented in 1973 [54]. Since then, a multitude of papers have been published in various journals and conference proceedings. Many mitigation techniques such as bypass switch, passive filter, and FACTS devices have been proposed to mitigate the SSR oscillation in the network.

1.5 SUBSYNCHRONOUS RESONANCE IN WIND FARMS

Large-scale integration of wind farms in the transmission and distribution networks has led to several challenges [55], [56]. One of these challenges is the need for substantial upgrading of grid transmission infrastructures including the construction of new transmission lines to accommodate the increased power flow from the wind plants [26]-[28]. It is well known that series compensation is an effective means of enhancing the power transfer capability of existing transmission lines. Hence, it is being increasingly considered for integrating large wind generation plants [28], [57]. Series capacitors have

been known to cause subsynchronous resonance (SSR) as described above. Furthermore, the presence of series capacitors in the line may also potentially cause subsynchronous resonance (SSR) in induction generator based wind turbine generators [26], [53].

Two papers [58], [59] presented a detailed analytical and experimental result of subsynchronous resonance of a squirrel cage induction motor and a deep bar induction motor, respectively, fed by a series compensated feeder.

In 2003, the impact of a large-scale integration of wind farms into a utility grid was studied [26], which focused on major interconnection issues. In this paper, both conventional IG based wind farms and DFIG wind farms are considered. Wind farm interaction with series compensated transmission line was discussed for the first time in this paper. Based on the simulation studies with squirrel cage induction generator based wind farms, induction generator effect was detected in the presence of the series capacitor.

In December 2005, Xcel energy released a report on the study of a series capacitor in the Wilmarth-Lakefield transmission system [60]. This report specifically discussed the impact of the series capacitor on the interconnected network and turbine generators connected at various points in the network. Series compensation of 65% was considered for the analysis according to this report. A 107 MVA wind farm based on 100 DFIGs was proposed at the Lakefield system. Induction generator effect and torsional interaction were studied thoroughly using the frequency scanning method. Induction generator effect was found to be dependent on the rotor circuit parameter and operating slip of the DFIG. For the analysis, the slip was varied between -30% to +30%. From the frequency scanning, unstable SSR induction generation effect was detected at 10Hz. Stator impedance and rotor impedance were found to be responsible for the resonant frequency and equivalent negative resistance, respectively. This study suggested that when a large number of wind turbines are aggregated, the SSR issue might become more prominent. Different sizes of wind farms and their impact on the SSR were a major contribution of the work. However, no small signal analysis or electromagnetic transient studies were performed.

Five papers published between 2006 and 2008 discussed SSR issues in wind farms and its mitigation using Flexible AC Transmission (FACTS) Controllers [61]-[65]. In [61] the authors studied the potential of SSR through a frequency domain model of the induction generator based wind farm. It was found that torsional modes may be excited by an electrical fault in the network but any unstable torsional interaction was not indicated. In [62] a double-cage induction generator based 500 MW wind farm was connected to a series compensated transmission line. Several electromagnetic transient simulation results shown in this paper indicated the potential of induction generator effect in the wind farm following a fault in the network. However, it only happened with a high level of series compensation. A FACTS device-static var compensator (SVC) was proposed to mitigate the SSR oscillation in the wind farm [63]. The authors proposed a damping controller in which speed deviation was considered as the input signal. However, no eigenvalue analysis was provided to illustrate the improved stability in a closed loop system. Since wind farms are spread over a large geographical area, the specific generator speed that was used for the damping of SSR oscillation was not discussed. Another paper [64] showed the mitigation of SSR using Thyristor Controlled Series Capacitor (TCSC). A damping controller was also proposed in this paper to mitigate the SSR oscillation in the wind farm. A further paper [65] presented a comparative study of mitigation of SSR oscillation using two FACTS devices: a) SVC and b) TCSC. Several electromagnetic transient simulations carried out in PSCAD/EMTDC were shown in this paper for SSR in wind farms of size between 100 MW to 500 MW. TCSC with and auxiliary damping controller was found to be superior over the SVC with a similar damping controller for mitigation of the SSR oscillation in the wind farm following a symmetrical fault in the network.

Two papers were published on the mitigation of SSR in wind farms using static synchronous compensators (STATCOM) and static synchronous series compensators (SSSC) [66], [67]. In these papers a 100 MW squirrel cage induction generator based wind farm was connected to a series compensated transmission line. A shaft monitoring system was proposed to monitor the shaft oscillation following the disturbance in the network. Several low pass and band pass filters were proposed to achieve the objective of monitoring the torsional oscillations. Auxiliary damping controllers were proposed to

mitigate the oscillation in the wind turbines. A generator speed feedback signal is used for the damping of the torsional interactions. Another damping signal was also derived from the active power generated by the wind farm in a fixed time interval. However, in a large wind farm, selection of an appropriate speed signal for the damping would be a challenging task for the control engineer. In these two papers, no induction generator effect was found, rather a torsional interaction was reported following a fault in the network.

Modeling of DFIG based wind farm connected to a series compensated transmission line was presented in [68]. Small signal analysis and time domain simulations were carried out in this paper. Impact of a series capacitor and control parameters on the SSR oscillation were reported. Further studies of SSR with DFIG based wind farms were reported in [69]-[72]. A detailed modeling of the DFIG based wind farm connected to a series compensated transmission line was reported in these papers. Small signal analysis followed by a time-domain simulation was performed to examine the SSR conditions. DFIG converter controller design and its interactions with series capacitor were studied. Through participation factor analysis, authors established a criterion to detect and mitigate the SSR by choosing suitable controller parameters.

There are two events related to SSR that have already occurred in the wind farms connected to a series compensated transmission line. In October 2009 a single line to ground fault occurred on a 345 kV series compensated line connected to two large wind farms in Texas, of capacity ≈485 MW. After the fault, once the faulted line was cleared, the wind farm continued to operate radially with a single 345 kV line with 50% series compensation. Then, the SSR interaction between the wind turbine generator control and series capacitor initiated and grew sufficiently large to damage the wind turbines as voltage exceeded 2 pu before the series capacitor was bypassed. From the priliminary analysis it was found that the control interaction of the DFIG based wind turbine controller and series capacitor caused the undamped voltage oscillations [73].

Another incident was witnessed in the Buffalo Ridge area of Minnesota. Many wind farms are planned and connected to the 345 kV series compensated transmission line in

southwestern Minnesota. In one case, the series compensation level was chosen to be 60% in a 54 mile line. One end of the line was connected to a 150 MW wind farm. During the commissioning process of the series capacitor, one line was taken out before the series capacitor was bypassed. During this operation the wind farm output was 15 MW and only one of the six synchronous generators (46 MW) was connected to line. The switching operation resulted in the radial operation of the wind farm with the series compensated transmission line. The system tripped due to the flashover in the generator bus duct resulting in the bypass of the series capacitor. Generator current recorded during the event was analyzed and the presence of DC component along with a low frequency component (9-13 Hz) was confirmed. This was later confirmed as the subsynchronous resonance that was caused due to the interaction of the DFIG controller and the series compensated transmission line [60], [74].

A report on the impact of wind farms in SSR in a power system was released in 2011[75]. This report was prepared based on the incident witnessed in the Gulf wind farm in Texas. Through the frequency scanning method only, an analysis of the SSR was performed. The major focus was given to the converter and its control on the basis of practical experience. The impact of rotor current controller bandwidth and DC link voltage controller bandwidth was tested by performing a time domain simulation in PSCAD/EMTDC. The study was later extended to see the impact of the grid side converter's reactive power controller bandwidth and PLL bandwidth. From these simulations it was found that rotor side converter current controller and PLL exhibit a greater impact on the SSR oscillation. The impact of the DC link controller bandwidth was found to be the least. At the same time, the magnitude of power flow was also found to impact the SSR oscillations.

To protect wind farms from SSR oscillations, a relayhas recently been developed by ERL phase power technologies [74]. This relay is useful to detect the oscillation of frequency band between 5-25 Hz. This development was the result of collaborative research between the Xcel energy and ERL phase power technology. A real issue of SSR oscillation in a DFIG based wind farm connected to a series compensated transmission line was the motivation of this development.

1.6   SSR IN WIND FARMS CONNECTED TO HVDC LINES

As the application of HVDC for the wind farm interconnection grows, the threat of SSR interaction between the wind turbines and HVDC controllers also increases. From previous research it has been found that the torsional interaction of HVDC controller is less dangerous than the series compensated transmission line [34], when connected to a large synchronous generator [37], [38], [40],[77], [78]. However, impact study on the IG based wind farm has not been done thoroughly. The potential of SSR in wind farms connected to HVDC line was first indicated in [26]. In [82], a study of torsional interaction of wind turbine and HVDC controller is presented. This is demonstrated only through the transient simulations. In addition, the impact of various parameters was not studied. In this thesis, a systematic study of the potential SSR in an induction generator based wind farm connected to series compensated line and HVDC system is presented. A parallel AC-DC system configuration used for the analysis of SSR with synchronous generator is utilized in this paper [78].

1.7   HARMONIC RESONANCE IN WIND FARMS

Network resonance issues appear in wind farms due to the presence of power factor correction capacitors, bus capacitors, and underground cables. The interaction between the network reactances and the above capacitances may result in series and parallel resonance. When the harmonic level exceeds the allowable limit it may cause damage to the substation equipment and consumer equipment as well [79], [80]. Amplification of harmonic over voltage may also result in tripping of the wind turbines.

Broadly, the harmonic resonance can be of two types: a) series resonance, and b) parallel resonance. In the case of series resonance the impedance becomes low at resonant frequency that causes the flow of large current in the network. Sometimes this also causes high distortion in the voltage at the distant buses. However, parallel resonance is associated with high impedance at resonant frequencies. It causes large distortion in the voltage and produces large harmonics current [81]-[84].

If the harmonic current from the wind farm aligns with the resonant mode, significant voltage amplification may occur. Since modern wind farms use power electronics

converters for grid interfacing, a significant amount of the characteristic harmonics current emission from these converters may cause parallel resonance problem in the network at certain resonant frequencies [85], [86].

There are many papers published on the harmonic resonance issue. In [87] the authors considered a DFIG based wind farm and calculated the harmonic emission. Exact estimation of harmonic emission is essential as harmonic current injection from a wind farm may cause the parallel resonance at the PCC. This paper [87] presented several simulated results and real time measurements of an actual commercial wind farm. Impact of harmonic emission on the wind farm operation has also been discussed in this paper. In [88] a study was carried out for the detection of harmonic current in an 18 MW induction generator based wind farm. It is found that lower order harmonics are the most dominant. Harmonic distortion in fixed speed wind farms are least influenced by the operating condition such as change in wind speed [79]. Recently a 101.2 MW full converter based wind farm in Canada suffered from a harmonic resonance issue that caused the tripping of several wind turbines. From the preliminary study it was found that the turbine tripping was due to the temporary over voltage which was caused by the parallel resonance at the PCC. This phenomenon needs further investigation.

1.8   OBJECTIVES AND SCOPE OF THE THESIS

The objectives and the scope of the thesis are:

 (a)   To develop a comprehensive system model for the study of subsynchronous resonance in induction generator based wind farms connected to series compensated transmission lines and to validate small signal eigenanalysis study results through electromagnetic transient simulation studies.

 (b)   To investigate the effect of various factors, such as the level of series compensation, power output and rating of wind farms, locations of faults in a wind farm radially connected to series compensated network.

 (c)   To investigate the mutual interaction between induction generator based wind farms connected to series compensated lines.

 (d)   To design a STATCOM controller for mitigating subsynchronous resonance in the wind farm connected to series compensated line.

(e) To examine the potential of subsynchronous resonance in induction generator based wind farms connected to HVDC lines together with parallel series compensated line.

(f) To investigate the issue of harmonic resonance and its impact on a commercially operated wind farm.

1.9 OUTLINE OF THESIS

The chapter wise summary of the work done in this thesis is given below.

Chapter 2 reports the development of an overall system model for an induction generator based wind farm connected to a series compensated transmission line. Models of various subsystems including induction generator mechanical drive train, series compensated line, STATCOM, lien commutated converter (LCC) based HVDC lines, and full converter based commercial wind farms have been developed. The per unit model of single-cage and double-cage induction generators were developed by synchronously rotating d-q reference frame. To predict the behavior of the induction generators during terminal fault, an equivalent circuit modeling is introduced and that predicts the unstable resonant speed bands. Dynamic aggregation of wind turbines is also presented in this chapter. Finally, the mechanical drive train and induction generator model are reasonably validated through an electromagnetic transient simulation carried out using PSCAD/EMTDC software.

Chapter 3 presents the analysis of subsynchronous resonance in a single-cage induction generator based wind farm connected to a series compensated transmission line. The analysis is carried out over a wide range of operating conditions such as: variation in size of the wind farm, variation in power output and series compensation level. The study is carried out in two steps. First, a small signal analysis is carried out to determine the eigenvalues at different equilibrium points. Then, participation factor and sensitivity analysis are done in support of the eigenvalue analysis. Further, to validate the small signal analysis, a time domain simulation of the study system is performed in PSCAD/EMTDC.

Chapter 4 presents a comprehensive analysis of subsynchronous resonance in a double-cage induction generator wind farm connected to a series compensated transmission line. Eigenvalue analysis is carried out for a wide range of variation in wind farm size, power output, and series compensation levels. Participation factor analysis followed by the sensitivity analysis is performed to examine the SSR phenomenon in the wind farm. Validation of the small signal models is performed through the time domain simulations in PSCAD/EMTDC. Fault studies are performed at different locations to evaluate the potential for the rise in the shaft torque. An equivalent circuit theory analysis technique is presented to estimate the resonant speed bands of the wind turbine generators. This chapter also shows studies with various other commercially available double-cage induction generators to exemplify subsynchronous resonance issues in the induction generator based wind farms.

Chapter 5 is concerned with an analysis of subsynchronous resonance in wind farms connected to non-radial series compensated transmission lines. The IEEE second benchmark system-I is adapted for the study. A detailed *d-q* model of the network is developed in this chapter that is then utilized for eigenvalue analysis. Small signal analysis is then reasonably validated through detail time domain simulation in PSCAD/EMTDC. Impact of fault on the wind farm is examined. Potential for SSR during normal and contingency operating period are also investigated.

Chapter 6 deals with mitigation of subsynchronous resonance in double-cage induction generator based wind farms connected to a series compensated transmission line using STATCOM. Two STATCOM controllers are proposed in this chapter for the mitigation of subsynchronous resonance. A comprehensive eigenvalue analysis is carried out to prove the effectiveness of the controllers. Eigenvalue analysis is first carried out with the controllers and then a time domain simulation is performed in PSCAD/EMTDC. The Singular Value Decomposition (SVD) technique is used for the optimal choice of the control inputs to damp out the concerned oscillatory mode. Through various fault studies, the effectiveness of the STATCOM controllers is reasonably validated. The impact of a wind farm collector cable system is also examined. A case study with a single-cage

induction generator is also reported where the proposed STATCOM is utilized for damping of subsynchronous oscillations.

Chapter 7 presents the analysis of subsynchronous resonance in a wind farm connected to a HVDC line in parallel with AC transmission line. Two types of AC transmission lines are considered. In one case, the line is uncompensated; and in another case the line is series compensated. The motivation behind the use of a series compensated line is to evaluate the contribution of both systems (series capacitor and HVDC controller) on the potential for SSR oscillation in the wind farm. The studies include eigenvalue analysis, participation factor analysis, and sensitivity analysis. Electromagnetic transient simulations are then carried out to confirm the small signal analysis.

Chapter 8 deals with the harmonic resonance analysis in an actual commercially operated wind farm. A 101.2 MW full converter based wind farm is connected to a 230 kV network through overhead lines and underground cables. Due to switching of large grid capacitors, several wind turbines were tripped on at least five occasions. This chapter presents an in-depth analysis of the harmonic resonance that may be the possible reason behind the harmonic over voltage that caused the wind turbines to trip. First, the entire wind farm and the network are modeled in PSCAD/EMTDC software. To examine the harmonic resonance, impedance scan is performed and compared with the frequency spectrum of the recorded voltage and current signals. The capacitor switching event is performed in accordance to the field operation. The simulated results are compared with the field-recorded data. Since another wind farm is coming up with identical configuration in close vicinity, the potential for harmonic resonance is also examined for both wind farms. Recommendations are made for the wind farms to operate with specific combinations of park capacitors to avoid harmonic resonance issues.

A brief overview of the major contributions of this thesis and suggestions for the future work constitute the ninth and concluding chapter.

Chapter 2

MODELING OF WIND TURBINE GENERATOR SYSTEMS

2.1   INTRODUCTION

This chapter presents a detailed modeling of various subsystems in an induction generator based wind farm connected to a series compensated transmission line. The objective of this chapter is to create an overall system model for examining the potential of subsynchronous resonance in such a system.

The wind farm is modeled as two sub-systems. One represents the mechanical drive train, whereas the other sub-system accounts for the electrical circuit of the generator. Two types of induction generator models are introduced in this chapter, both of which are used extensively in this thesis. The wind turbine generator system model is reasonably validated in one case by considering a symmetrical fault in the electrical network and also a step change in mechanical torque input. Small signal analysis is carried out utilizing the user written programs in MATLAB, while all electromagnetic transient simulations are carried out with PSCAD/EMTDC software [89], [90].

2.2   SYSTEM DESCRIPTION

The study system is depicted in Figure 2.1, in which an induction generator based wind farm is connected to a series compensated transmission line. This system is a modified IEEE First SSR Benchmark system [44]. The original benchmark system was proposed to facilitate the computer simulation of subsynchronous resonance in a power system that was based on the Navajo project 892.4 MVA synchronous generator connected to a 500 kV transmission system. In this thesis, the conventional synchronous generator is replaced with a large induction generator based wind farm. The configuration of a typical wind farm is shown in Figure 2.2 [19]. It is assumed that there are 'n' numbers of identical wind turbines and all are connected to PCC through the collector cables of adequate rating. For the modeling purpose, the study system is divided into two sub-

systems: i) wind farm, and ii) transmission line. The wind farm is subdivided further into two sub-systems: i) mechanical drive train, and ii) electrical generator. A detail modeling technique of each sub-system is presented in this chapter. While modeling the wind farm, no collector cables are considered between the wind turbine generators and interfacing transformer shown in Figure 2.1.
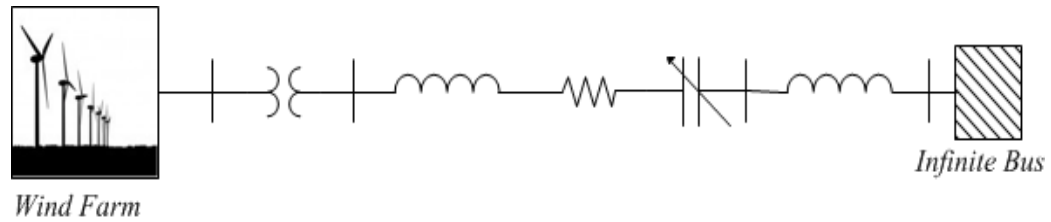
Figure 2.1 Series compensated line connected to induction generator based wind farm
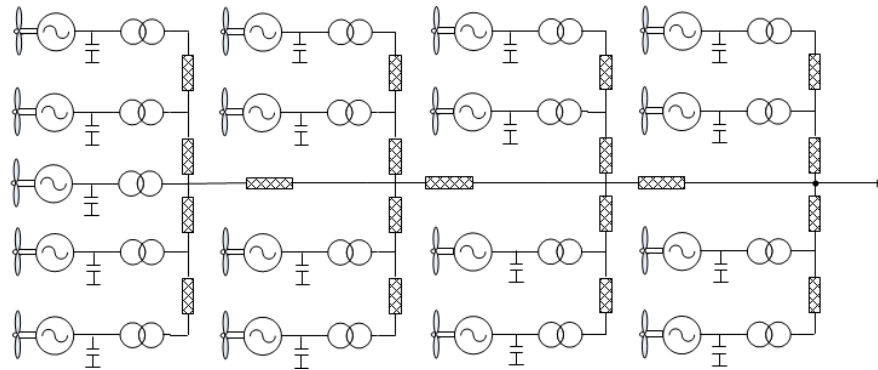
Figure 2.2 Typical wind farm connection

2.3   DRIVE TRAIN SYSTEM

The drive train system is treated as a sub-system along with a rotating mass and several torsionally elastic components. The vibrational modes of a wind turbine can be excited by external influences such as stochastic fluctuations of the rotor torque caused by wind turbulence and output torque of the electrical generator.

The vibrational response of a torsional system is determined by three elasto-mechanical parameters such as i) the moment of inertia of the rotating masses, ii) the torsional stiffness of the elastic shafts and connecting elements, and iii) the torsional damper

constants. These three parameters are usually determined from the design and material properties of the drive train components involved [20].

The drive train of a wind turbine generator system typically consists of a blade pitching mechanism with a spinner, a hub with three/two blades, a rotor shaft, and a gear box with a breaker and electrical generator. Considering it as a three mass drive train system, the proportion of the inertial moments of these sub-systems contributing to the overall inertial moment of the drive train of wind turbines with widely differing sizes and technical concepts can be distributed as follows [21]. The hub with blades comprises 85-92% of the total polar moment of inertia, whereas the generator rotor constitutes 5-10%, and the rest of the drive train system contributes 1-2%. Unlike the moment of inertia, the generator represents the largest torsional stiffness, which is approximately 100 times the rotor shaft stiffness and approximately 50 times the stiffness of the hub with blades [21]. In general, for modal analysis of a multi-mass drive train system the rotor is treated as a contribution of discrete masses connected together by springs represented by their damping and stiffness coefficient.
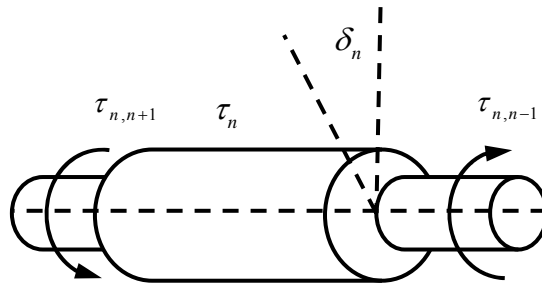
Figure 2.3 Torque acting on n-th mass

For the generic drive train system shown in Figure 2.3, a dynamic equation of the n-th mass can be written by a second order differential equation where all the torques are calculated at one side of a gear exits.

$$2H_n \frac{d^2}{dt^2}(\delta_n) = \tau_n + \left(\tau_{n,n+1} - \tau_{n,n-1}\right) - D_n \frac{d}{dt}(\delta_n) \tag{2.1}$$

The torque of the shafts can be written as:

$$\tau_{n,n+1} = K_{n,n+1}\left(\delta_{n+1} - \delta_n\right) + D_{n,n+1}\left(\frac{d}{dt}\left(\delta_{n+1}\right) - \frac{d}{dt}\left(\delta_n\right)\right) \tag{2.2}$$

$$\tau_{n,n-1} = K_{n,n-1}\left(\delta_n - \delta_{n-1}\right) + D_{n,n-1}\left(\frac{d}{dt}\left(\delta_n\right) - \frac{d}{dt}\left(\delta_{n-1}\right)\right) \tag{2.3}$$

Substituting (2.2) and (2.3) in (2.1), the motion equation of the n-th mass can be expanded as

$$2H_n\frac{d^2}{dt^2}\left(\delta_n\right) = \tau_n + K_{n,n+1}\left(\delta_{n+1} - \delta_n\right) + D_{n,n+1}\left(\frac{d}{dt}\left(\delta_{n+1}\right) - \frac{d}{dt}\left(\delta_n\right)\right)$$
$$-K_{n,n-1}\left(\delta_n - \delta_{n-1}\right) - D_{n,n-1}\left(\frac{d}{dt}\left(\delta_n\right) - \frac{d}{dt}\left(\delta_{n-1}\right)\right) - D_n\frac{d}{dt}\left(\delta_n\right) \tag{2.4}$$

Rearranging (2.4)

$$2H_n\frac{d^2}{dt^2}\left(\delta_n\right) = \tau_n + K_{n,n+1}\left(\delta_{n+1} - \delta_n\right) - K_{n,n-1}\left(\delta_n - \delta_{n-1}\right)$$
$$+ D_{n,n+1}\left(\frac{d}{dt}\left(\delta_{n+1}\right) - \frac{d}{dt}\left(\delta_n\right)\right) - D_{n,n-1}\left(\frac{d}{dt}\left(\delta_n\right) - \frac{d}{dt}\left(\delta_{n-1}\right)\right) - D_n\frac{d}{dt}\left(\delta_n\right) \tag{2.5}$$

The above equations can be rewritten as a set of two first order equations:

$$\frac{d}{dt}\left(\delta_n\right) = \omega_n - \omega_{ns} \tag{2.6}$$

$$2H_n\frac{d}{dt}\left(\omega_n\right) = \tau_n + K_{n,n+1}\left(\delta_{n+1} - \delta_n\right) - K_{n,n-1}\left(\delta_n - \delta_{n-1}\right)$$
$$+ D_{n,n+1}\left(\omega_{n+1} - \omega_n\right) - D_{n,n-1}\left(\omega_n - \omega_{n-1}\right) - D_n\omega_n \tag{2.7}$$

where,

δ_n : Torsional angle of n th mass (rad)

ω_n : Angular speed of n th mass (rad/s)

H_n : Inertia constant of n th mass (s)

τ_n : External torque applied to n-th mass (pu)

$\tau_{n+1,n}$: Torque between $(n+1)$ th and n th mass (pu)

$\tau_{n,n-1}$: Torque between n th and $(n-1)$ th mass (pu)

$K_{n+1,n}$: Shaft stiffness between $(n+1)$ th and n th mass (pu)

$K_{n,n-1}$: Shaft stiffness between n th and $(n-1)$ th mass (pu)

D_n : Damping coefficient of n th mass (pu)

$D_{n+1,n}$: Damping coefficient between $(n+1)$ th and n th mass (pu)

$D_{n,n-1}$: Damping coefficient between n th and $(n-1)$ th mass (pu)

Assuming there are N number of discrete masses present in the drive train system, the above equations of the drive train are written in the linear state space form as:

$$\dot{x} = Ax + Bu \tag{2.8}$$

where,

$x = \begin{bmatrix} \Delta\delta_1 & \Delta\delta_2 & \ldots\ldots & \Delta\delta_N & | & \Delta\omega_1 & \Delta\omega_2 & \ldots\ldots & \Delta\omega_N \end{bmatrix}^T$ and

$u = \begin{bmatrix} \Delta\tau_1 & \Delta\tau_2 & \ldots\ldots & \Delta\tau_N \end{bmatrix}^T$.

$A = \begin{bmatrix} 0 & I \\ K & D \end{bmatrix}$ and $B = \begin{bmatrix} 0 \\ I \end{bmatrix}$.

The state matrix A is used for the computation of eigenvalues for the modal analysis of the drive train system. From the power system analysis point of view, the drive train system model of a specific order is therefore developed and presented in the following sections.

2.3.1 Three-mass Drive Train

Considering the significant impact of bending flexibility of the rotor blades on the transient stability of a wind turbine, the blades can be split into two parts. The rigid parts of the blades are merged into the hub whose inertia constant can be assumed as H_h. The flexible part of the blades can be aggregated and the corresponding inertia constant can be assumed as H_b. The shaft stiffness and damping coefficient between the hub and the blade are assumed as K_{bh} and D_{bh}, respectively. Similarly, the shaft stiffness and damping coefficient between the hub and the generator rotor can be expressed as K_{hg} and D_{hg}, respectively, whereas the inertia constant of the generator rotor mass is taken as H_g. The equivalent three mass drive train system is shown in Figure 2.4 [20]-[22], [91], [92].
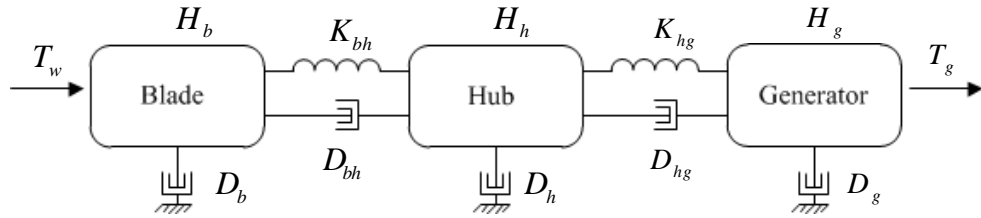
Figure 2.4 Three-mass drive train system

The three-mass torsional system can be represented as follows:

$$\frac{d}{dt}(\delta_b) = \omega_b \tag{2.9}$$

$$\frac{d}{dt}(\delta_h) = \omega_h \tag{2.10}$$

$$\frac{d}{dt}(\delta_g) = \omega_g \tag{2.11}$$

$$2H_b \frac{d}{dt}(\omega_b) = T_w - K_{bh}(\delta_b - \delta_h) - D_{bh}(\omega_b - \omega_h) - D_b \omega_b \tag{2.12}$$

$$2H_h \frac{d}{dt}(\omega_h) = K_{bh}(\delta_b - \delta_h) + D_{bh}(\omega_b - \omega_h) - K_{hg}(\delta_h - \delta_g)$$
$$- D_{hg}(\omega_h - \omega_g) - D_h \omega_h \tag{2.13}$$

$$2H_g \frac{d}{dt}(\omega_g) = K_{hg}(\delta_h - \delta_g) + D_{hg}(\omega_h - \omega_g) - D_g \omega_g - T_g \tag{2.14}$$

where,

δ_b :   Torsional angle of blades (rad)

δ_h :   Torsional angle of hub (rad)

δ_g :   Torsional angle of generator (rad)

ω_b :   Angular speed of blades (rad/s)

ω_h :   Angular speed of hub (rad/s)

ω_g :   Angular speed of generator (rad/s)

H_b :   Inertia constant of blades (s)

H_h : Inertia constant of hub (s)

H_g : Inertia constant of generator (s)

K_{bh} : Shaft stifness between blades and hub (pu)

K_{hg} : Shaft stifness between hub and generator (pu)

D_b : Damping coefficient of blades (pu)

D_h : Damping coefficient of hub (pu)

D_g : Damping coefficient of generator (pu)

D_{bh} : Damping coefficient between blades and hub (pu)

D_{hg} : Damping coefficient between hub and generator (pu)

T_w : Mechanical torque input to wind turbine (pu)

T_g : Electromagnetic torque output of generator (pu)

The above equations are expressed in the linear state space form as:

$$\dot{x}_{bhg} = \left[A_{bhg}\right]x_{bhg} + \left[B_{bhg}\right]u_{bhg} \tag{2.15}$$

$$y_{bhg} = \left[C_{bhg}\right]x_{bhg} \tag{2.16}$$

where,

$$x_{bhg} = \begin{bmatrix} \Delta\delta_b & \Delta\delta_h & \Delta\delta_g & \Delta\omega_b & \Delta\omega_h & \Delta\omega_g \end{bmatrix}^T$$

$$x_{bhg} = \begin{bmatrix} \Delta T_m & -\Delta T_g \end{bmatrix}^T, \quad \left[A_{bhg}\right] = \begin{bmatrix} 0_{3\times3} & I_{3\times3} \\ K_{bhg} & D_{bhg} \end{bmatrix},$$

$$K_{bhg} = \begin{bmatrix} -\dfrac{K_{bh}}{2H_b} & \dfrac{K_{bh}}{2H_b} & 0 \\[3ex] \dfrac{K_{bh}}{2H_h} & -\dfrac{\left(K_{bh}+K_{hg}\right)}{2H_h} & \dfrac{K_{hg}}{2H_h} \\[3ex] 0 & \dfrac{K_{hg}}{2H_g} & -\dfrac{K_{hg}}{2H_g} \end{bmatrix},$$

$$D_{bhg} = \begin{bmatrix} -\dfrac{(D_{bh}+D_b)}{2H_b} & \dfrac{D_{bh}}{2H_b} & 0 \\[2ex] \dfrac{D_{bh}}{2H_h} & -\dfrac{(D_{bh}+D_h+D_{hg})}{2H_h} & \dfrac{D_{hg}}{2H_h} \\[2ex] 0 & \dfrac{D_{hg}}{2H_g} & -\dfrac{(D_{hg}+D_g)}{2H_g} \end{bmatrix},$$

$$\begin{bmatrix} B_{bhg} \end{bmatrix} = \begin{bmatrix} 0_{4\times2} \\ I_{2\times2} \end{bmatrix} \text{ and } \begin{bmatrix} C_{bhg} \end{bmatrix} = \begin{bmatrix} 0 & 0 & 1 & 0 & 0 & 0 \\ 0 & 0 & 0 & 0 & 0 & 1 \end{bmatrix}.$$

2.3.2 Two-mass Drive Train System

The three-mass drive train system discussed above can be converted into a two-mass drive train system. The two-mass drive train system is widely used for studying the power system stability including the wind turbine generators [20]-[22], [91]-[94]. A typical two-mass drive train system is shown in Figure 2.5.
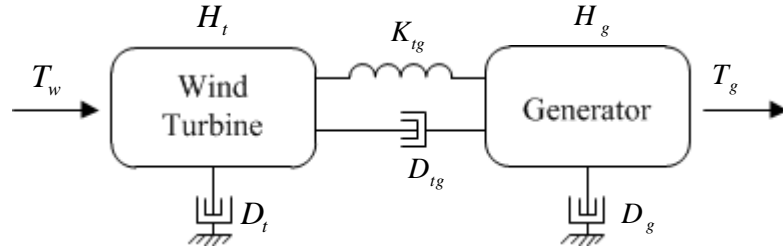
Figure 2.5 Two-mass drive train system

The equivalent shaft stiffness can be obtained from the parallel equivalent shaft stiffness given below. The equivalent inertia constant can be expressed as the summation of the inertia constant of the blade and the hub.

$$\frac{1}{K_{tg}} = \frac{1}{K_{bh}} + \frac{1}{K_{hg}} \tag{2.17}$$

$$H_t = H_b + H_h \tag{2.18}$$

The differential equations of a two-mass system are written as:

$$\frac{d}{dt}\left(\delta_t\right) = \omega_t \tag{2.19}$$

$$\frac{d}{dt}\left(\delta_g\right) = \omega_g \tag{2.20}$$

$$2H_b\frac{d}{dt}\left(\omega_t\right) = T_w - K_{tg}\left(\delta_t - \delta_g\right) - D_{tg}\left(\omega_t - \omega_g\right) - D_t\omega_t \tag{2.21}$$

$$2H_g\frac{d}{dt}\left(\omega_g\right) = K_{tg}\left(\delta_t - \delta_g\right) + D_{tg}\left(\omega_t - \omega_g\right) - D_g\omega_g - T_g \tag{2.22}$$

Equations (2.19)-(2.22) can be reduced to a third order system as written below. The self-damping is neglected here.

$$\frac{d}{dt}\left(\delta_{tg}\right) = \frac{d}{dt}\left(\delta_t\right) - \frac{d}{dt}\left(\delta_g\right) = \omega_t - \omega_g \tag{2.23}$$

$$2H_t\frac{d}{dt}\left(\omega_t\right) = T_w - K_{tg}\delta_{tg} - D_{tg}\left(\omega_t - \omega_g\right) \tag{2.24}$$

$$2H_g\frac{d}{dt}\left(\omega_g\right) = K_{tg}\delta_{tg} + D_{tg}\left(\omega_t - \omega_g\right) - T_g \tag{2.25}$$

where,

δ_{tg} : Torsional angle between wind turbine and generator (rad)

ω_t : Angular speed of wind turbine (rad/s)

ω_g : Angular speed of generator (rad/s)

H_t : Inertia constant of wind turbine (s)

H_g : Inertia constant of generator (s)

D_t : Damping coefficient of wind turbine (pu)

D_g : Damping coefficient of generator (pu)

D_{tg} : Damping coefficient between wind turbine and generator (pu)

K_{tg} : Shaft stifness between wind turbine and generator (pu)

T_w : Mechanical torque input to wind turbine (pu)

T_g : Electromagnetic torque output of generator (pu)

In practice, the large difference between the speed of the wind turbine and the generator makes the gear box an essential part of the system. The gearbox separates the two shaft systems. However, the impact of the generator rotor shaft can be neglected being of very small size. In the presence of the gearbox, all of the parameters must be transformed to either high-speed shaft side or low speed shaft side. In this work since the electrical network is present in the high-speed shaft side, all of the turbine parameters are referred to the generator rotor side. The low-speed shaft stiffness and inertia constants when referred to the high-speed side are:

$$H_t^G = \frac{H_t}{N^2} \tag{2.26}$$

$$K_{tg}^G = \frac{K_{tg}}{N^2} \tag{2.27}$$

where, $N = \dfrac{\omega_g}{\omega_t}$ is the gearbox ratio.

The motion equations of a two-mass torsional system are now presented in the state space form.

$$\dot{x}_{tg} = \left[A_{tg} \right] x_{tg} + \left[B_{tg} \right] u_{tg} \tag{2.28}$$

$$y_{bhg} = \left[C_{tg} \right] x_{tg} \tag{2.29}$$

where, $x_{tg}^t = \begin{bmatrix} \Delta\omega_t & \Delta\delta_{tg} & \Delta\omega_g \end{bmatrix}$,

$$\left[A_{tg} \right] = \begin{bmatrix} \dfrac{-D_{tg}}{2H_t} & \dfrac{-K_{tg}}{2H_t} & \dfrac{-D_{tg}}{2H_t} \\ 1 & 0 & -1 \\ \dfrac{D_{tg}}{2H_g} & \dfrac{K_{tg}}{2H_g} & \dfrac{D_{tg}}{2H_g} \end{bmatrix}, \left[B_{tg} \right] = \begin{bmatrix} 1 & 0 \\ 0 & -1 \end{bmatrix}, \left[C_{tg} \right] = \begin{bmatrix} 0 & 1 & 0 \\ 0 & 0 & 1 \end{bmatrix} \text{ and } u_{tg} = \Delta u_{bhg}$$

2.3.3 Single-mass Drive Train System

In this model all of the components of the torsional system are lumped together to result in a single-mass system as shown in Figure 2.6 [20]-[22]. The equivalent inertia constant of the single mass-system can be written as:

$$H_{wt} = H_t + H_g \tag{2.30}$$
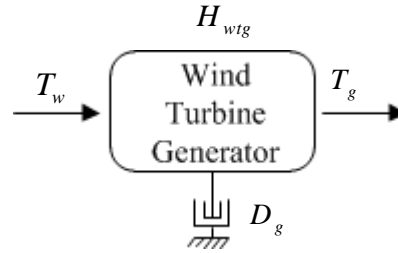
Figure 2.6 Single-mass drive train

The differential equation of the single-mass drive train system is written as:

$$2H_{wtg}\frac{d}{dt}\left(\omega_g\right) = T_w - D_g\omega_g - T_g \tag{2.31}$$

where,

ω_g : Angular speed of generator (rad/s)

H_{wtg} : Inertia constant of wind turbine generator system (s)

T_w : Mechanical torque input to wind turbine generator system (pu)

T_g : Electromagnetic torque output of generator (pu)

2.3.4 Aggregation of Drive Train System

Since a large number of wind turbines are connected to a common bus, it is assumed that the disturbance originating in the bus affects the performance of all of the individual machines identically, and the individual rotor oscillations lie in phase with each other. All of the wind turbines are therefore connected in parallel, mechanically [19], [91], [95]. The equivalent model variables of a wind farm considering N number of turbines are expressed as:

$$H_t = \sum_{k=1}^{N} H_{tk} \tag{2.32}$$

$$H_g = \sum_{k=1}^{N} H_{gk} \tag{2.33}$$

$$K_{tg} = \sum_{k=1}^{N} K_{tgk} \qquad (2.34)$$

$$D_{tg} = \sum_{k=1}^{N} D_{tgk} \qquad (2.35)$$

2.4 WIND TURBINE GENERATOR

A wind turbine generator system converts the mechanical energy from the wind into electrical energy. Based on the rotational speed, the wind turbine generators are classified into two categories: i) fixed speed generator, and ii) variable speed generator. There are four types of wind turbine generators that are used in commercial wind farms. These include squirrel cage induction generator (SCIG), wound field synchronous generator (WFSG), doubly-fed induction generator (DFIG), and permanent magnetic synchronous generator (PMSG) [19]-[25].

A fixed-speed wind turbine generator consists of a conventional squirrel cage induction generator that is directly connected to the grid. The slip of the induction generator varies with the power generated. However, the variations are within 1%-2% of the rated generator speed. In this type of generator, since the rotor speed cannot be controlled, variation in the wind speed causes fluctuation in the input torque that is directly translated into variable power output. The fluctuation in the mechanical torque input also puts stress on the drive train system of a wind turbine. Since there is large speed difference between the wind turbine hub and the generator, a gearbox is used to connect the low-speed shaft of the wind turbine with the high-speed wind turbine generator.

2.4.1 Operating Principle of Fixed Speed Induction Generator

When the speed of a squirrel cage induction motor exceeds the rated speed, the slip becomes negative and the induced torque is reversed. The power produced by the induction generator increases with the increase in the torque applied to its shaft by the prime mover. However, due to the absence of external excitation, the induction generator does not produce reactive power, rather draws it from the grid. In this scenario, to maintain the stator magnetic field, an external source of reactive power, capacitor bank, is

always connected at the terminal. For a fixed-speed wind turbine generator, properly chosen capacitor provides reactive power to maintain unity power factor.

In an induction machine the stator windings are identical, sinusoidally distributed and displaced by 120 degrees. Similarly, the rotor circuit also has three identical sinusoidally distributed windings. However, the majority of induction machines are not equipped with coiled wound rotor windings. Instead, the current flows in the copper or aluminum bars, which are uniformly distributed and all bars are terminated on a common ring at each end of the rotor. In practical machines the conductors are not placed in the plane of the axis of rotation of the rotor; instead they are skewed slightly with the axis of rotation. This reduces the harmonic torques produced due to the harmonic MMF waves. For the modeling and analysis purpose, it is assumed that the induction machine is a linear and MMF-harmonic free device [96]-[99]. Two types of induction generators are considered here. The detailed modeling technique of both type of generators are presented in this chapter. Since the mechanical power is directly converted to electrical power by means of an induction generator, no controller is involved in the electrical part of a fixed-speed wind turbine generator.

2.4.2 Single-cage Induction Generator

The rotor of a squirrel cage induction generator is composed of a laminated core and rotor slots. The rotor circuit consists of only one winding housed in the rotor slots. The equivalent circuit of a single-cage induction generator is shown in Figure 2.7.
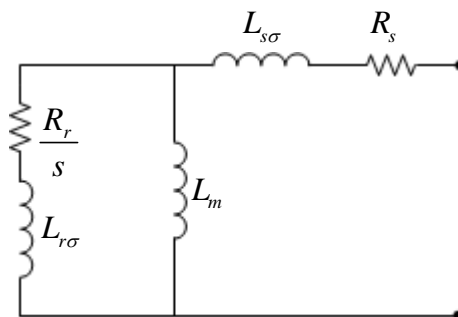
Figure 2.7 Equivalent circuit of a single-cage induction generator.

The mathematical model of a single-cage induction generator is developed in the synchronously rotating *d-q* reference frame [19], [97], [99]-[101]. The general assumptions considered during the modeling are as follows:

(a) Stator pole does not make any variation in the induction of the rotor circuit

(b) Rotor slots do not affect the stator inductance

(c) Magnetic saturation and hysteresis are neglected

(d) Stator and rotor parameters are symmetrical

(e) Capacitance of the windings is neglected

2.4.2.1 *Model-I*

This model is based on the generalized flux linkage equation, which is widely used in the literature for the stability study of the wind turbine generator system. The Model-I expressed by a set of differential equations written in *d-q* frame of reference is given below.

$$\frac{1}{\omega_s}\frac{d}{dt}\lambda_{ds} = -R_s I_{ds} + \lambda_{qs} - V_{ds} \tag{2.36}$$

$$\frac{1}{\omega_s}\frac{d}{dt}\lambda_{qs} = -R_s I_{qs} - \lambda_{ds} - V_{qs} \tag{2.37}$$

$$\frac{1}{\omega_s}\frac{d}{dt}\lambda_{dr} = -R_r I_{dr} + s\lambda_{qr} \tag{2.38}$$

$$\frac{1}{\omega_s}\frac{d}{dt}\lambda_{qr} = -R_r I_{qr} - s\lambda_{dr} \tag{2.39}$$

where,

$$\lambda_{ds} = X_s I_{ds} + X_m I_{dr} \tag{2.40}$$

$$\lambda_{qs} = X_s I_{qs} + X_m I_{qr} \tag{2.41}$$

$$\lambda_{dr} = X_r I_{dr} + X_m I_{ds} \tag{2.42}$$

$$\lambda_{qr} = X_r I_{qr} + X_m I_{qs} \tag{2.43}$$

$$X_s = X_{s\sigma} + X_m \tag{2.44}$$

$$X_r = X_{r\sigma} + X_m \tag{2.45}$$

Using (2.40)-(2.43) in (2.36)-(2.39), the dynamic equations can be re-arranged as:

$$\frac{X_s}{\omega_s}\frac{d}{dt}I_{ds} + \frac{X_m}{\omega_s}\frac{d}{dt}I_{dr} = -R_s I_{ds} + \left(X_s I_{qs} + X_m I_{qr}\right) - V_{ds} \tag{2.46}$$

$$\frac{X_s}{\omega_s}\frac{d}{dt}I_{qs} + \frac{X_m}{\omega_s}\frac{d}{dt}I_{qr} = -R_s I_{qs} - \left(X_s I_{ds} + X_m I_{dr}\right) - V_{qs} \tag{2.47}$$

$$\frac{X_r}{\omega_s}\frac{d}{dt}I_{dr} + \frac{X_m}{\omega_s}\frac{d}{dt}I_{ds} = -R_r I_{dr} + s\left(X_r I_{qr} + X_m I_{qs}\right) \tag{2.48}$$

$$\frac{X_r}{\omega_s}\frac{d}{dt}I_{qr} + \frac{X_m}{\omega_s}\frac{d}{dt}I_{qs} = -R_r I_{qr} - s\left(X_r I_{dr} + X_m I_{ds}\right) \tag{2.49}$$

where,

ω_s	:	Synchronous frequency (376.99 rad/s)
R_s	:	Stator resistance per phase (pu)
$X_{s\sigma}$	:	Stator leakage reactance per phase (pu)
R_r	:	Rotor resistance per phase (pu)
$X_{r\sigma}$	:	Rotor leakage reactance per phase (pu)
X_m	:	Mutual reactance between the stator and rotor windings (pu)
V_{ds}, V_{qs}	:	d-q axis voltage at generator terminal (pu)
I_{ds}, I_{qs}	:	d-q axis stator current (pu)
I_{dr}, I_{qr}	:	d-q axis rotor current (pu)

Linearizing the differential equations (2.46)-(2.49), the induction generator model in linear state space form can be written as:

$$\dot{x}_G = [A_G]x_G + [B_G]u_G \tag{2.50}$$

where,

$$x_G^t = \begin{bmatrix} \Delta I_{ds} & \Delta I_{qs} & \Delta I_{dr} & \Delta I_{qr} \end{bmatrix} \tag{2.51}$$

$$u_G^t = \begin{bmatrix} \Delta \omega_g & \Delta V_{ds} & \Delta V_{qs} \end{bmatrix} \tag{2.52}$$

2.4.2.2 *Model-II*

In this model, the induction generator is represented as a voltage behind the transient reactance [22], [99]. The model is essentially derived from the basic flux linkage model shown in (2.36)-(2.39).

From (2.42)and (2.43) the rotor currents can be expressed as:

$$I_{dr} = \frac{\lambda_{dr} - X_m I_{ds}}{X_r} \tag{2.53}$$

$$I_{qr} = \frac{\lambda_{qr} - X_m I_{qs}}{X_r} \tag{2.54}$$

Now substituting I_{dr} and I_{qr} in (2.36) and (2.37)

$$\lambda_{ds} = X_s I_{ds} + X_m \frac{\lambda_{dr} - X_m I_{ds}}{X_r} \tag{2.55}$$

$$\lambda_{qs} = X_s I_{qs} + X_m \frac{\lambda_{qr} - X_m I_{qs}}{X_r} \tag{2.56}$$

Rearranging (2.55) and (2.56),

$$\lambda_{ds} = \left(X_s - \frac{X_m^2}{X_r} \right) I_{ds} + \frac{X_m}{X_r} \lambda_{dr} \tag{2.57}$$

$$\lambda_{qs} = \left(X_s - \frac{X_m^2}{X_r} \right) I_{qs} + \frac{X_m}{X_r} \lambda_{qr} \tag{2.58}$$

Now, introducing two induced voltage E_d and E_q in (2.57)and (2.58)

$$\lambda_{ds} = X_0 I_{ds} + E_q \tag{2.59}$$

$$\lambda_{qs} = X_0 I_{qs} - E_d \tag{2.60}$$

where,

$$X_0 = \left(X_s - \frac{X_m^2}{X_r} \right) \tag{2.61}$$

$$E_q = \frac{X_m}{X_r} \lambda_{dr} \tag{2.62}$$

$$E_d = -\frac{X_m}{X_r}\lambda_{qr} \tag{2.63}$$

From (2.62) and (2.63), the rotor fluxes are defined as:

$$\lambda_{dr} = \frac{X_r}{X_m}E_q \tag{2.64}$$

$$\lambda_{qr} = -\frac{X_r}{X_m}E_d \tag{2.65}$$

Using E_d and E_q in (2.53) and (2.54),

$$I_{dr} = \frac{1}{X_m}E_q - \frac{X_m}{X_r}I_{ds} \tag{2.66}$$

$$I_{qr} = -\frac{1}{X_m}E_d - \frac{X_m}{X_r}I_{qs} \tag{2.67}$$

$$\frac{1}{\omega_s}\frac{d}{dt}\left(X_0 I_{ds} + E_q\right) = -R_s I_{ds} + \left(X_0 I_{qs} - E_d\right) - V_{ds} \tag{2.68}$$

$$\frac{1}{\omega_s}\frac{d}{dt}\left(X_0 I_{qs} - E_d\right) = -R_s I_{qs} - \left(X_0 I_{ds} + E_q\right) - V_{qs} \tag{2.69}$$

$$\frac{1}{\omega_s}\frac{X_r}{X_m}\frac{d}{dt}E_q = -R_r\left(\frac{1}{X_m}E_q - \frac{X_m}{X_r}I_{ds}\right) - s\frac{X_r}{X_m}E_d \tag{2.70}$$

$$-\frac{1}{\omega_s}\frac{X_r}{X_m}\frac{d}{dt}E_d = -R_r\left(-\frac{1}{X_m}E_d - \frac{X_m}{X_r}I_{qs}\right) - s\frac{X_r}{X_m}E_q \tag{2.71}$$

Rearranging (2.68) and (2.71),

$$\frac{X_0}{\omega_s}\frac{d}{dt}I_{ds} + \frac{1}{\omega_s}\frac{d}{dt}E_q = -R_s I_{ds} + \left(X_0 I_{qs} - E_d\right) - V_{ds} \tag{2.72}$$

$$\frac{X_0}{\omega_s}\frac{d}{dt}I_{qs} - \frac{1}{\omega_s}\frac{d}{dt}E_d = -R_s I_{qs} - \left(X_0 I_{ds} + E_q\right) - V_{qs} \tag{2.73}$$

$$\frac{d}{dt}E_q = -\frac{1}{T_0}\left(E_q - \frac{X_m^2}{X_r}I_{ds}\right) - s\omega_s E_d \tag{2.74}$$

$$\frac{d}{dt}E_d = -\frac{1}{T_0}\left(E_d + \frac{X_m^2}{X_r}I_{qs}\right) + s\omega_s E_q \tag{2.75}$$

where, X_0 is the open circuit reactance and T_0 is the open circuit time constant.

$$T_0 = \frac{X_r}{\omega_s R_r} \qquad (2.76)$$

The dynamic equations of the induction generator are now linearized. Arranging in the linear state space form, the complete model of the induction generator is represented as:

$$\dot{x}_G = [A_G] x_G + [B_G] u_G \qquad (2.77)$$

where
$$x_G^t = \begin{bmatrix} \Delta I_{ds} & \Delta I_{qs} & \Delta E_d & \Delta E_q \end{bmatrix} \qquad (2.78)$$

$$u_G^t = \begin{bmatrix} \Delta \omega_g & \Delta V_{ds} & \Delta V_{qs} \end{bmatrix} \qquad (2.79)$$

2.4.3 Double-Cage Induction Generator

Most of the time the induction generators are modeled as a simple squirrel cage induction machine as in previous section. However, most of the induction generators above 5 kW have a double squirrel cage rotor. In comparison to single-cage machines, these generators are widely used in the wind farms where slip varies over a wide range. There are four types of double-cage induction machines as per NEMA standards: i) class-A, ii) class-B, iii) class-C and, iv) class-D. Class-C design is the most widely used type for its superior torque-slip characteristic [98]. In the double-cage rotor there are two electrical circuits. One circuit is placed at the outer surface of the rotor, very close to the stator winding. The other circuit is located in the deeper part of the cage. When the current flows in the outer conductor, it is tightly coupled with the stator, thus exhibiting a smaller leakage reactance but higher resistance due to a smaller cross section of the copper bar. Similarly when the current flows in the deeper bar, being very lightly coupled, it exhibits a larger leakage reactance but smaller resistance due to a large cross section of the copper bar. The rotor circuit acts as if two separate circuits are connected in parallel to each other.

During rated power output of the wind farm, the rotor reactance remains low due to the smaller slip (0-1%). This results in a uniform current flow in the rotor bars. Further, due to the large cross section of inner rotor bars the efficiency remains high because of less power loss in the rotor. During any transient events in the network, when the speed deviates from the rated value, the slip increases significantly. During those high slip

conditions the reactance of the inner rotor circuit increases and forces the current to flow in the circuit on the surface of the rotor that offers low reactance. Due to a smaller cross section of these outer circuit conductors, a high resistance is experienced which offers a higher torque in comparison to a single-cage induction generator operating with same slip [96], [99], [102]-[105].

In literature two types of double-cage induction generator models are available. Figure 2.8 (a) and (b) represent two models that are equivalent. References [104] and [105] have shown the conversion of parameters from the name plate data of a double-cage machine to an electromagnetic transient model. Since manufacturers' data are not readily available to the researchers, the constant parameter model of the double-cage is adopted for various studies related to the grid integration of fixed-speed wind farms. A new method has been proposed to derive different parameters of a double-cage induction generator from the manufacturer provided data: nominal mechanical power, nominal power factor, maximum torque, starting torque, and current [106]. In [104] and [105] a detailed study of the equivalence between different double-cage induction machine models with six, seven and eight parameters have been presented. For a fair comparison between the small signal model and nonlinear model available in PSCAD/EMTDC software, the model shown in Figure 2.8 (b) is adopted in this work. The conversion of parameters from one model to another model is presented in Appendix A.
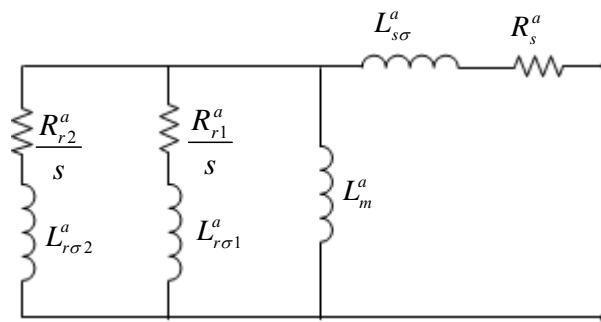
(a) Model-I
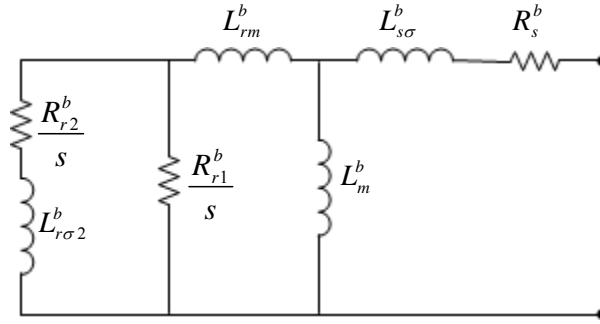
(b) Model-II

Figure 2.8 Equivalent circuit of double-cage induction generator

The mathematical model of a double-cage induction generator is developed in a manner that closely resembles the derivation of the per unit d-q model of a single-cage induction generator. Several assumptions are considered which are as follows:

(a) The core and mechanical losses are neglected.

(b) The machine is symmetric.

(c) Both rotor windings are magnetically coupled and the effects of space harmonics are neglected.

(d) Each of the two cages is short circuited by independent end rings.

(e) No inter-bars current can flow as rotor bars are insulated from the iron.

(f) Saturation effect and other nonlinearities are neglected.

2.4.3.1 *Model-I*

The basic differential equations of the double-cage induction generators are written in d-q reference frame as [105], [106]:

$$\frac{1}{\omega_s}\frac{d}{dt}\lambda_{ds} = -R_s I_{ds} + \lambda_{qs} - V_{ds} \tag{2.80}$$

$$\frac{1}{\omega_s}\frac{d}{dt}\lambda_{qs} = -R_s I_{qs} - \lambda_{ds} - V_{qs} \tag{2.81}$$

$$\frac{1}{\omega_s}\frac{d}{dt}\lambda_{dr1} = -R_{r1} I_{dr1} + s\lambda_{qr1} \tag{2.82}$$

$$\frac{1}{\omega_s}\frac{d}{dt}\lambda_{qr1} = -R_{r1} I_{qr1} - s\lambda_{dr1} \tag{2.83}$$

$$\frac{1}{\omega_s}\frac{d}{dt}\lambda_{dr2} = -R_{r2}I_{dr2} + s\lambda_{qr2} \tag{2.84}$$

$$\frac{1}{\omega_s}\frac{d}{dt}\lambda_{qr2} = -R_{r2}I_{qr2} - s\lambda_{dr2} \tag{2.85}$$

The flux linkage equations are:

$$\lambda_{ds} = X_s I_{ds} + X_m I_{dr1} + X_m I_{dr2} \tag{2.86}$$

$$\lambda_{qs} = X_s I_{qs} + X_m I_{qr1} + X_m I_{qr2} \tag{2.87}$$

$$\lambda_{dr1} = X_m I_{ds} + X_{r1} I_{dr1} + X_{12} I_{dr2} \tag{2.88}$$

$$\lambda_{qr1} = X_m I_{qs} + X_{r1} I_{qr1} + X_{12} I_{qr2} \tag{2.89}$$

$$\lambda_{dr2} = X_m I_{ds} + X_{12} I_{dr1} + X_{r2} I_{dr2} \tag{2.90}$$

$$\lambda_{qr2} = X_m I_{qs} + X_{12} I_{qr1} + X_{r2} I_{qr2} \tag{2.91}$$

where,

$$X_{12} = X_m + X_{rm} \tag{2.92}$$

$$X_s = X_{s\sigma} + X_m \tag{2.93}$$

$$X_{r1} = X_{r1\sigma} + X_{12} \tag{2.94}$$

$$X_{r2} = X_{r2\sigma} + X_{12} \tag{2.95}$$

The electromagnetic torque can be expressed as,

$$T_g = X_m\left(\left(I_{qr1} + I_{qr2}\right)I_{ds} - \left(I_{dr1} + I_{dr2}\right)I_{qs}\right) \tag{2.96}$$

where,

R_s :   Stator resistance per phase (pu)

$X_{s\sigma}$:   Stator leakage reactance per phase (pu)

R_{r1} :   First-cage rotor resistance per phase (pu)

$X_{r1\sigma}$:   First-cage rotor leakage reactance per phase (pu)

R_{r2} :   Second-cage rotor resistance per phase (pu)

$X_{r2\sigma}$: Second-cage rotor leakage reactance per phase (pu)

X_m : Mutual reactance between the stator and rotor windings (pu)

V_{ds}, V_{qs} : d-q axis voltage at generator terminal (pu)

I_{ds}, I_{qs} : d-q axis stator current (pu)

I_{dr1}, I_{qr1} : d-q axis first-cage rotor current (pu)

I_{dr2}, I_{qr2} : d-q axis second-cage rotor current(pu)

To develop the state space model of the induction generator differential equations presented in (2.80)-(2.85) are linearized. The system now can be written in the form of

$$\dot{x}_G = [A_G] x_G + [B_G] u_G \tag{2.97}$$

where,

$$x_G^t = \begin{bmatrix} \Delta I_{ds} & \Delta I_{qs} & \Delta I_{dr1} & \Delta I_{qr1} & \Delta I_{dr2} & \Delta I_{qr2} \end{bmatrix} \tag{2.98}$$

$$u_G^t = \begin{bmatrix} \Delta \omega_g & \Delta V_{ds} & \Delta V_{qs} \end{bmatrix} \tag{2.99}$$

2.4.3.2 Model-II

This model is implemented as a voltage source behind the transient reactance, which is derived in a similar manner the derivation of the single-cage induction generator Model-II [22], [99]. The detailed derivations are given below. This model is based on the basic flux linkage equations shown in (2.80)-(2.85).

From (2.88)-(2.91), the rotor currents can be written as:

$$I_{dr1} = \frac{X_{r2}}{X_{r1}X_{r2} - X_{12}^2} \lambda_{dr1} - \frac{X_{12}}{X_{r1}X_{r2} - X_{12}^2} \lambda_{dr2} + \frac{X_m(X_{12} - X_{r2})}{X_{r1}X_{r2} - X_{12}^2} I_{ds} \tag{2.100}$$

$$I_{qr1} = \frac{X_{r2}}{X_{r1}X_{r2} - X_{12}^2} \lambda_{qr1} - \frac{X_{12}}{X_{r1}X_{r2} - X_{12}^2} \lambda_{qr2} + \frac{X_m(X_{12} - X_{r2})}{X_{r1}X_{r2} - X_{12}^2} I_{qs} \tag{2.101}$$

$$I_{dr2} = \frac{X_{r1}}{X_{r1}X_{r2} - X_{12}^2} \lambda_{dr2} - \frac{X_{12}}{X_{r1}X_{r2} - X_{12}^2} \lambda_{dr1} + \frac{X_m(X_{12} - X_{r1})}{X_{r1}X_{r2} - X_{12}^2} I_{ds} \tag{2.102}$$

$$I_{qr2} = \frac{X_{r1}}{X_{r1}X_{r2} - X_{12}^2}\lambda_{qr2} - \frac{X_{12}}{X_{r1}X_{r2} - X_{12}^2}\lambda_{qr1} + \frac{X_m(X_{12} - X_{r1})}{X_{r1}X_{r2} - X_{12}^2}I_{qs} \qquad (2.103)$$

Simplifying (2.100)-(2.103),

$$I_{dr1} = \frac{X_{r2}}{X_{r1}X_{r2} - X_{12}^2}\lambda_{dr1} - \frac{X_{12}}{X_{r1}X_{r2} - X_{12}^2}\lambda_{dr2} - \frac{X_m X_{r2\sigma}}{X_{r1}X_{r2} - X_{12}^2}I_{ds} \qquad (2.104)$$

$$I_{qr1} = \frac{X_{r2}}{X_{r1}X_{r2} - X_{12}^2}\lambda_{qr1} - \frac{X_{12}}{X_{r1}X_{r2} - X_{12}^2}\lambda_{qr2} - \frac{X_m X_{r2\sigma}}{X_{r1}X_{r2} - X_{12}^2}I_{qs} \qquad (2.105)$$

$$I_{dr2} = \frac{X_{r1}}{X_{r1}X_{r2} - X_{12}^2}\lambda_{dr2} - \frac{X_{12}}{X_{r1}X_{r2} - X_{12}^2}\lambda_{dr1} \qquad (2.106)$$

$$I_{qr2} = \frac{X_{r1}}{X_{r1}X_{r2} - X_{12}^2}\lambda_{qr2} - \frac{X_{12}}{X_{r1}X_{r2} - X_{12}^2}\lambda_{qr1} \qquad (2.107)$$

Rewriting (2.104)-(2.107), the rotor currents can be simplified as,

$$I_{dr1} = \frac{X_{r2}}{X_r}\lambda_{dr1} - \frac{X_{12}}{X_r}\lambda_{dr2} - \frac{X_m X_{r2\sigma}}{X_r}I_{ds} \qquad (2.108)$$

$$I_{qr1} = \frac{X_{r2}}{X_r}\lambda_{qr1} - \frac{X_{12}}{X_r}\lambda_{qr2} - \frac{X_m X_{r2\sigma}}{X_r}I_{qs} \qquad (2.109)$$

$$I_{dr2} = -\frac{X_{12}}{X_r}\lambda_{dr1} + \frac{X_{r1}}{X_r}\lambda_{dr2} \qquad (2.110)$$

$$I_{qr2} = -\frac{X_{12}}{X_r}\lambda_{qr1} + \frac{X_{r1}}{X_r}\lambda_{qr2} \qquad (2.111)$$

where,

$$X_r = X_{r1}X_{r2} - X_{12}^2 \qquad (2.112)$$

Replacing (2.108)-(2.111) in (2.86)-(2.87), the stator fluxes are:

$$\lambda_{ds} = \left(X_s - \frac{X_m^2 X_{r2\sigma}}{X_r}\right)I_{ds} + \left(\frac{X_m X_{r2}}{X_r} - \frac{X_m X_{12}}{X_r}\right)\lambda_{dr1} + \left(\frac{X_m X_{r1}}{X_r} - \frac{X_m X_{12}}{X_r}\right)\lambda_{dr2} \, (2.113)$$

$$\lambda_{qs} = \left(X_s - \frac{X_m^2 X_{r2\sigma}}{X_r}\right)I_{qs} + \left(\frac{X_m X_{r2}}{X_r} - \frac{X_m X_{12}}{X_r}\right)\lambda_{qr1} + \left(\frac{X_m X_{r1}}{X_r} - \frac{X_m X_{12}}{X_r}\right)\lambda_{qr2} \, (2.114)$$

Rewriting (2.113) and (2.114)

$$\lambda_{ds} = X_0 I_{ds} + \frac{X_m X_{r2\sigma}}{X_r} \lambda_{dr1} \tag{2.115}$$

$$\lambda_{qs} = X_0 I_{qs} + \frac{X_m X_{r\sigma2}}{X_r} \lambda_{qr1} \tag{2.116}$$

where,

$$X_0 = \left(X_s - \frac{X_m^2 X_{r2\sigma}}{X_r} \right) \tag{2.117}$$

Now, introducing new *d-q* axis voltage components

$$E_{q1} = \left(\frac{X_m X_{r2\sigma}}{X_r} \right) \lambda_{dr1} \tag{2.118}$$

$$E_{d1} = -\left(\frac{X_m X_{r2\sigma}}{X_r} \right) \lambda_{qr1} \tag{2.119}$$

$$E_{q2} = \frac{X_{12}}{X_r} \lambda_{dr2} \tag{2.120}$$

$$E_{d2} = -\frac{X_{12}}{X_r} \lambda_{qr2} \tag{2.121}$$

From (2.118)-(2.121), the flux linkages can be expressed as,

$$\lambda_{ds} = X_0 I_{ds} + E_{q1} \tag{2.122}$$

$$\lambda_{qs} = X_0 I_{qs} - E_{d1} \tag{2.123}$$

$$\lambda_{dr1} = \left(\frac{X_r}{X_m X_{r2\sigma}} \right) E_{q1} \tag{2.124}$$

$$\lambda_{qr1} = -\left(\frac{X_r}{X_m X_{r2\sigma}} \right) E_{d1} \tag{2.125}$$

$$\lambda_{dr2} = \frac{X_r}{X_{12}} E_{q2} \tag{2.126}$$

$$\lambda_{qr2} = -\frac{X_r}{X_{12}} E_{d2} \tag{2.127}$$

Using (2.122)-(2.127) rotor currents can be re arranged as follows:

$$I_{dr1} = \left(\frac{X_{r2}}{X_m X_{r2\sigma}}\right) E_{q1} - E_{q2} - \left(\frac{X_m X_{r2\sigma}}{X_r}\right) I_{ds} \tag{2.128}$$

$$I_{qr1} = -\left(\frac{X_{r2}}{X_m X_{r2\sigma}}\right) E_{d1} + E_{d2} - \left(\frac{X_m X_{r2\sigma}}{X_r}\right) I_{qs} \tag{2.129}$$

$$I_{dr2} = -\left(\frac{X_{12}}{X_m X_{r2\sigma}}\right) E_{q1} + E_{q2} \tag{2.130}$$

$$I_{qr2} = \left(\frac{X_{12}}{X_m X_{r2\sigma}}\right) E_{d1} - E_{d2} \tag{2.131}$$

Finally, using the rotor currents and stator flux equations in (2.80)-(2.85),

$$\frac{1}{\omega_s} X_0 \frac{d}{dt} I_{ds} + \frac{1}{\omega_s} \frac{d}{dt} E_{q1} = -R_s I_{ds} + X_0 I_{qs} - E_{d1} - V_{ds} \tag{2.132}$$

$$\frac{1}{\omega_s} X_0 \frac{d}{dt} I_{qs} - \frac{1}{\omega_s} \frac{d}{dt} E_{d1} = -R_s I_{qs} - X_0 I_{ds} - E_{q1} - V_{qs} \tag{2.133}$$

$$\frac{d}{dt} E_{d1} = -\frac{\omega_s R_{r1}}{X_r} \left(X_{r2} E_{d1} - \left(X_m X_{r2\sigma}\right) E_{d2} + \frac{\left(X_m X_{r2\sigma}\right)^2}{X_r} I_{qs} \right) + s\omega_s E_{q1} \tag{2.134}$$

$$\frac{d}{dt} E_{q1} = -\frac{\omega_s R_{r1}}{X_r} \left(X_{r2} E_{q1} - \left(X_m X_{r2\sigma}\right) E_{q2} - \frac{\left(X_m X_{r2\sigma}\right)^2}{X_r} I_{ds} \right) - s\omega_s E_{d1} \tag{2.135}$$

$$\frac{d}{dt} E_{d2} = -\frac{\omega_s R_{r2}}{X_r} \left(-\frac{X_{12}^2}{X_m X_{r2\sigma}} E_{d1} + X_{12} E_{d2} \right) + s\omega_s E_{q2} \tag{2.136}$$

$$\frac{d}{dt} E_{q2} = -\frac{\omega_s R_{r2}}{X_r} \left(-\frac{X_{12}^2}{X_m X_{r2\sigma}} E_{q1} + X_{12} E_{q2} \right) - s\omega_s E_{d2} \tag{2.137}$$

The electromagnetic torque can now be expressed in terms of rotor-induced voltages, as

$$T_g = \lambda_{qs} I_{ds} - \lambda_{ds} I_{qs} \tag{2.138}$$

$$T_g = -\left(E_{d1} I_{ds} + E_{q1} I_{qs} \right) \tag{2.139}$$

In order to perform eigenvalue analysis, the differential equations of the double-cage induction generator are linearized and arranged in a liner state space form.

$$\dot{x}_G = \left[A_G \right] x_G + \left[B_G \right] u_G \tag{2.140}$$

where,

$$x_G^t = \left[\Delta I_{ds} \quad \Delta I_{qs} \quad \Delta E_{d1} \quad \Delta E_{q1} \quad \Delta E_{d2} \quad \Delta E_{q2} \right] \tag{2.141}$$

$$u_G^t = \left[\Delta \omega_g \quad \Delta V_{ds} \quad \Delta V_{qs} \right] \tag{2.142}$$

2.4.4 Aggregation of Induction Generators

Aggregation of wind turbines is an important issue during the planning of grid integration of large-scale wind farms and its stability studies. One of the important considerations for the aggregation is to understand the potential for mutual interaction between the various wind turbines in a wind farm. Reactive power compensation and stability of power systems are done typically based upon the aggregated modeling of wind turbine [107]-[111]. However, aggregation of wind turbine generators is somewhat different from the aggregation of simple induction machines for motor application [95]. The oscillation in the power output of the induction generator is dominated by the dynamics of the mechanical drive train due to the fact that the inertia constant of the wind turbine is much higher than that of induction generator.

In this thesis, the aggregation of the wind turbines has been performed for the investigation of subsynchronous resonance. The rating of an aggregated wind farm can be expressed as the summation of the rating of each machine:

$$S_{eq} = \sum_{k=1}^{N} S_k \tag{2.143}$$

where S_k is the kVA rating of single machine and S_{eq} is the rating of the equivalent machine. This is known as the kVA weighted averaging, one of the most commonly used methods of aggregating induction machines for power system stability study. In a wind farm, if all the induction machines are not identical then aggregated parameters are calculated as the weighted average of the respective parameter of individual machines [107], [108]. The generalized method for the calculation of the aggregated parameters $\left(x_{agg} \right)$ of the generator is as follows:

$$x_{agg} = \sum_{k=1}^{N} \alpha_k x_k \tag{2.144}$$

where, x_k is the parameter of k-th generator and α_k is a factor, which is calculated as

$$\alpha_k = \frac{S_k}{\sum_{k=1}^{N} S_k} \tag{2.145}$$

The aggregation of shunt capacitors $\left(C_g\right)$ at the terminal of an induction generator can be done as,

$$C_g = \sum_{k=1}^{N} C_{gk} \tag{2.146}$$

where, C_{gk} is the shunt capacitance at the k-th generator terminal.

The aggregated model of a wind farm can thus be represented as shown in Figure 2.9.
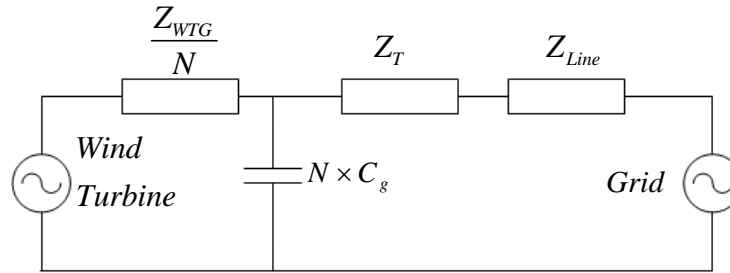
Figure 2.9 Circuit representation of aggregated wind farm model

2.5 SHUNT CAPACITOR AT GENERATOR TERMINAL

The reactive power demand of the induction generator that is catered by a local capacitor bank depends on its terminal voltage and the power output. For a constant voltage at the terminal, the reactive power demand of the wind turbine generator increases with increase in the power output. However, the reactive power demand is not linearly dependent on the active power output of the wind turbine. For wind power application, shunt capacitor banks are split into multiple stages. Each stage of the capacitor bank is connected based on the active power output. A simple shunt capacitor is shown in Figure 2.10. For the analysis, the voltage across the capacitor can be written in *d-q* reference frame as given below [34].

$$C_g \frac{d}{dt}V_{ds} = I_{ds} - I_d + \omega_s C_g V_{qs} \tag{2.147}$$

$$C_g \frac{d}{dt}V_{qs} = I_{qs} - I_q - \omega_s C_g V_{ds} \tag{2.148}$$

where,

C_g : Shunt capacitor at the terminal of induction generator (pu)

I_{ds}, I_{qs} : d-q axis current of induction generator (pu)

I_d, I_q : d-q axis current of series compensated transmission line (pu)

V_{ds}, V_{qs} : d-q axis voltage at the wind turbine generator terminal (pu)
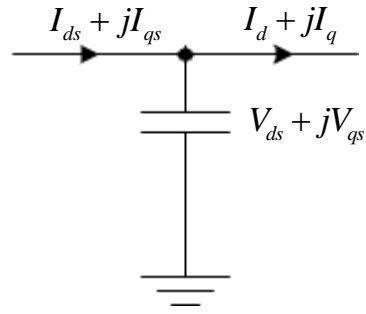
Figure 2.10 Shunt capacitor at the terminal of the wind turbine generator

2.6 SERIES COMPENSATED TRANSMISSION LINE

The series compensated line is depicted in Figure 2.11. The dynamic equations expressed in the synchronously rotating d-q reference frame [34], [42] are:

$$L\frac{d}{dt}I_d = V_{ds} - RI_d + \omega_s LI_q - V_{cd} - V_{bd} \tag{2.149}$$

$$L\frac{d}{dt}I_q = V_{qs} - RI_q - \omega_s LI_d - V_{cq} - V_{bq} \tag{2.150}$$

$$C\frac{d}{dt}V_{cd} = I_d + \omega_s C V_{cq} \tag{2.151}$$

$$C\frac{d}{dt}V_{cq} = I_q - \omega_s C V_{cd} \tag{2.152}$$

where,

R :   Transmission line resistance (pu)

L :   Transmisison line inductance including transformer and infinite grid inductance (pu)

C :   Series capacitance (pu)

V_{ds}, V_{qs} : d-q axis voltage at the wind turbine generator terminal (pu)

I_d, I_q : d-q axis current of series compensated transmission line (pu)

V_{cd}, V_{cq} : d-q axis voltage across series capacitor (pu)

V_{bd}, V_{bq} : d-q axis voltage at the infinite bus (pu)
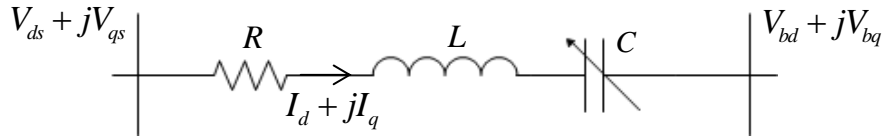
Figure 2.11 Series compensated transmission line

Linearizing the differential equations, the state space model of the network including the shunt capacitor is now written as:

$$\dot{x}_N = [A_N] x_N + [B_N] u_N \tag{2.153}$$

where,

$$x_N^t = \begin{bmatrix} \Delta V_{ds} & \Delta V_{qs} & \Delta I_d & \Delta I_q & \Delta V_{cd} & \Delta V_{cq} \end{bmatrix} \tag{2.154}$$

$$u_N^t = \begin{bmatrix} \Delta I_{ds} & \Delta I_{qs} & \Delta V_{bd} & \Delta V_{bq} \end{bmatrix} \tag{2.155}$$

2.7   EQUIVALENT CIRCUIT MODEL

In an induction generator, when the slip changes, the effective rotor resistance also gets changed. At subsynchronous frequencies the negative slip causes the effective rotor resistance to be more negative. When this negative resistance exceeds the net positive sequence resistance of the circuit, the subsynchronous oscillations may start to grow. The above concept is further investigated for a wind farm that is connected to a series-compensated transmission line. The study system shown in Figure 2.1 is now modeled as

a positive sequence equivalent circuit. Figure 2.12 and Figure 2.13 show the equivalent circuit of the study system with single-cage and double-cage induction generators, respectively. To identify the impact of a series capacitor (C) on the performance of an induction machine, this analysis was first proposed in [53] and then applied to induction motors in [58] and [59].
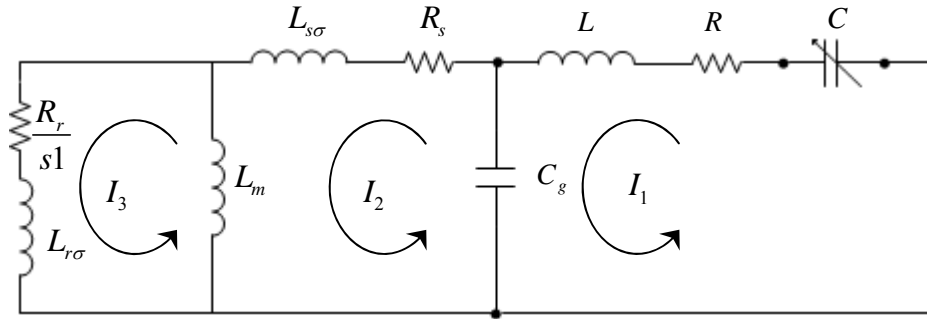
Figure 2.12 Equivalent circuit of study system with single-cage induction generator
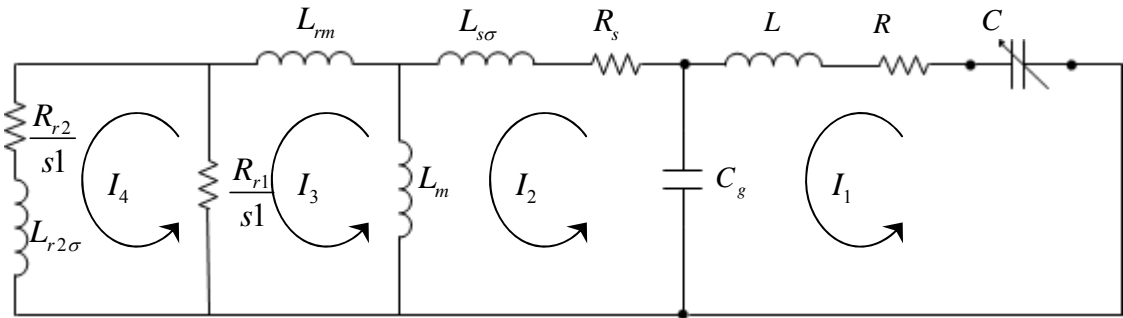
Figure 2.13 Equivalent circuit of study system with double-cage induction generator

Applying Kirchhoff's Voltage Law (KVL) to the equivalent system shown in Figure 2.12 and Figure 2.13 the loop equation can be written as:

$$V = I \times Z \tag{2.156}$$

Since the main focus is to evaluate the impact of natural frequency oscillations, the external voltage source is neglected here. Hence, with the single-cage induction generator:

$$V^t = \begin{bmatrix} 0 & 0 & 0 \end{bmatrix} \tag{2.157}$$

$$I^t = \begin{bmatrix} I_1 & I_2 & I_3 \end{bmatrix} \tag{2.158}$$

The characteristic polynomial of the impedance matrix is obtained by calculating the determinant as below.

$$\det|Z(s)| = a_5 s^5 + a_4 s^4 + a_3 s^3 + a_2 s^2 + a_1 s + a_0 \tag{2.159}$$

where,

$$Z = \begin{bmatrix} N\left(R + \rho L + \dfrac{1}{\rho C}\right) + \dfrac{1}{\rho C_g} & -\dfrac{1}{\rho C_g} & 0 \\[3mm] -\dfrac{1}{\rho C_g} & R_s + \rho\left(L_{s\sigma} + L_m\right) + \dfrac{1}{\rho C_g} & -\rho L_m \\[3mm] 0 & -\rho L_m & \dfrac{R_r}{s1} + \rho\left(L_{r\sigma} + L_m\right) \end{bmatrix} \tag{2.160}$$

Similarly, with a double-cage induction generator:

$$Z = \begin{bmatrix} N\left(R + sL - \dfrac{1}{sC}\right) - \dfrac{1}{sC_g} & \dfrac{1}{sC_g} & 0 & 0 \\[3mm] \dfrac{1}{sC_g} & R_s + sL_s - \dfrac{1}{sC_g} & -sL_m & 0 \\[3mm] 0 & -sL_m & \dfrac{R_{r1}}{s1} + sL_{12} & -\dfrac{R_{r1}}{s1} \\[3mm] 0 & 0 & -\dfrac{R_{r1}}{s1} & \dfrac{R_{r1} + R_{r2}}{s1} + sL_{r\sigma 2} \end{bmatrix} \tag{2.161}$$

$$V^t = \begin{bmatrix} 0 & 0 & 0 & 0 \end{bmatrix} \tag{2.162}$$

$$I^t = \begin{bmatrix} I_1 & I_2 & I_3 & I_4 \end{bmatrix} \tag{2.163}$$

In (2.160) and (2.161) the slip of the induction generator is expressed as '$s1$' to avoid confusion with the Laplace term 's'. The characteristic polynomial of the impedance matrix is obtained by calculating the determinant as below.

$$\det|Z(s)| = a_6 s^6 + a_5 s^5 + a_4 s^4 + a_3 s^3 + a_2 s^2 + a_1 s + a_0 \tag{2.164}$$

In Chapter 3 and Chapter 4, the equivalent circuit theory is utilized to estimate the resonant speed band of the induction generators.

2.8 VALIDATION OF INDUCTION GENERATOR MODEL

In Sec. 2.4, the mathematical models of two types of induction generators are developed. For the validation of these dynamic models a simple study system is considered as shown in Figure 2.14. In this system an induction generator based wind turbine is connected to the grid through a transformer and collector cable.
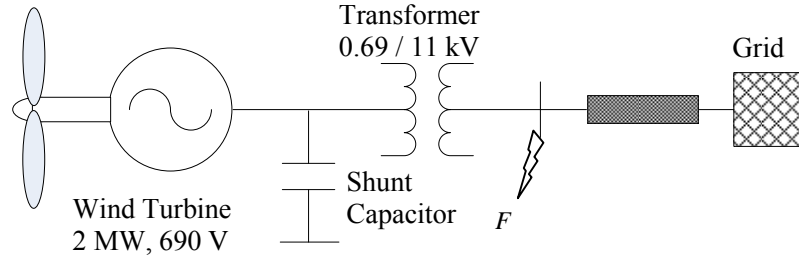
Figure 2.14 Study system for the validation of induction generator model

The system shown in Figure 2.14 is divided into three sub-systems: a) mechanical drive train, b) induction generator and, c) electrical network including transformer and shunt capacitor. Two types of induction generators, single-cage and double-cage, are considered. The differential equations of each sub-system are written in the state space form.

$$\dot{x}_{WT} = [A_{TT}]x_{WT} + [A_{TG}]x_G + [A_{TN}]x_N + [B_T]u_{WT} \tag{2.165}$$

$$\dot{x}_G = [A_{GT}]x_{WT} + [A_{GG}]x_G + [A_{GN}]x_N \tag{2.166}$$

$$\dot{x}_N = [A_{NT}]x_{WT} + [A_{NG}]x_G + [A_{NN}]x_N + [B_N]u_N \tag{2.167}$$

Combining (2.165)-(2.167), the complete study system is defined as

$$
\begin{bmatrix} \dot{x}_{WT} \\ \dot{x}_G \\ \dot{x}_N \end{bmatrix} = \underbrace{\begin{bmatrix} A_{TT} & A_{TG} & A_{TN} \\ A_{GT} & A_{GG} & A_{GN} \\ A_{NT} & A_{NG} & A_{NN} \end{bmatrix}}_{A} \begin{bmatrix} x_{WT} \\ x_G \\ x_N \end{bmatrix} + \begin{bmatrix} B_T & 0_{3\times2} \\ 0_{n\times1} & 0_{n\times2} \\ 0_{4\times1} & B_N \end{bmatrix} \begin{bmatrix} u_{WT} \\ u_N \end{bmatrix} \tag{2.168}
$$

where, $n=4$ and 6 for single-cage and double-cage IG, respectively.

$x_{WT}^t = \begin{bmatrix} \Delta\omega_t & \Delta\delta_{tg} & \Delta\omega_g \end{bmatrix}, x_N^t = \begin{bmatrix} \Delta V_{ds} & \Delta V_{qs} & \Delta I_d & \Delta I_q \end{bmatrix}, u_{WT} = \begin{bmatrix} \Delta T_w \end{bmatrix}$ and

$$u_N^t = \begin{bmatrix} \Delta V_{bd} & \Delta V_{bq} \end{bmatrix}.$$

For a single-cage induction generator:

$$x_G^t = \begin{bmatrix} \Delta I_{ds} & \Delta I_{qs} & \Delta E_d & \Delta E_q \end{bmatrix}.$$

For a double-cage induction generator:

$$x_G^t = \begin{bmatrix} \Delta I_{ds} & \Delta I_{qs} & \Delta E_{d1} & \Delta E_{q1} & \Delta E_{d2} & \Delta E_{q2} \end{bmatrix}.$$

2.8.1 Eigenvalue Analysis

The system eigenvalues are calculated at two different power output conditions. The state matrix A used for the eigenvalue calculations is defined in (2.168). The *eig* function in MATLAB is used to calculate the eigenvalues that are shown in Table 2.1. In the case of a single-cage induction generator, there are eleven states defined in (2.168) which results in five complex conjugate eigenvalues and one real eigenvalue. Similarly, a double-cage induction generator results in thirteen states: six complex conjugate eigenvalues and one real eigenvalue. The various oscillatory modes are network mode-1 and 2, synchronous mode, electromechanical mode, torsional mode, and non-oscillatory mode. In the case of a double-cage rotor, one additional oscillatory mode is introduced by the rotor circuit; labeled as rotor mode throughout this thesis. The real part of a complex eigenvalue indicates the stability of the corresponding mode and the imaginary part shows the oscillatory frequency.

Table 2.1 Eigenvalue of a grid connected induction generator

Modes	Single-cage IG		Double-cage IG	
	P=0.5 pu	P=1 pu	P=0.5 pu	P=1 pu
Network mode-1	-5.993 ± 3514.3i	-5.963 ± 2916.8i	-7.639 ± 3418.5i	-7.567 ± 2751.4i
Network mode-2	-6.317 ± 2760.4i	-6.368 ± 2162.8i	-8.299 ± 2664.6i	-8.425 ± 1997.5i
Synchronous mode	-9.723 ± 376.79i	-9.722 ± 376.79i	-9.817 ± 376.57i	-9.816 ± 376.57i
Rotor mode	X	X	-62.43 ± 0.70012i	-62.36 ± 2.8335i
Electromechanical mode	-3.815 ± 38.944i	-4.023 ± 38.405i	-5.507 ± 36.016i	-5.909 ± 35.238i
Torsional mode	-0.317 ± 3.6109i	-0.361 ± 3.6127i	-0.442 ± 3.5795i	-0.543 ± 3.584i
Non-oscillatory mode	-8.057	-7.514	-9.0754	-8.101

From the eigenvalues shown in Table 2.1 it is observed that a double-cage induction generator results in a more stable system as compared to a single-cage induction generator. Oscillatory frequencies of all of the low frequency modes are lower than the corresponding frequencies of modes with a single-cage induction generator. For example, at P=1 pu power output the electromechanical mode eigenvalues are -4.023 ± 38.405i and -5.909 ± 35.238i for a single-cage and double-cage induction generator, respectively. This demonstrates that the electromechanical mode of the double-cage induction generator is more stable than the single-cage induction generator. The oscillatory frequency is also found to be less.

2.8.2 Participation Factor Analysis

In power systems, participation factor analysis is very much used to determine the impact of one or more states on the damping of a particular system mode (eigenvalue) [50], [99]. The participation factors provide a measure of the influence of each dynamic state on a given mode. Consider a linear system

$$\dot{x} = Ax \qquad (2.169)$$

The participation factor p_{ki} is a sensitivity measure of the ith eigenvalue to the (k,k) diagonal entry of the system A matrix. This is expressed as

$$p_{ki} = \frac{\partial \lambda_i}{\partial a_{kk}} \qquad (2.170)$$

where λ_i is the ith eigenvalue and a_{kk} is the kth diagonal entry of A. The more common expression for the participation factor can be defined as

$$p_{ki} = \frac{\omega_{ki} v_{ik}}{\omega_i^T v_i} \qquad (2.171)$$

where ω_{ki} and v_{ik} are the kth entries of the left and right eigenvectors associated with λ_i. Participation factors are commonly normalized for the ease of comparison and interpretation.

Participation factor analysis is now carried out to examine the influence of various states on a specific mode in the study system. Figure 2.15 presents the normalized participation

factor of selected modes shown in Table 2.1. In the case of a particular mode, the largest participation factor indicates the maximum contribution of the concerned state. Table 2.2 and Table 2.3 show the states of the system with two types of induction generators. The state-id numbers are shown while presenting the participation factor of different modes in Figure 2.15.

Table 2.2 Participation factor analysis of a single-cage induction generator

Sub-system	Wind Turbine			Induction Generator				Network			
State-Id	1	2	3	4	5	6	7	8	9	10	11
State	$\Delta\omega_t$	$\Delta\delta_{tg}$	$\Delta\omega_g$	ΔI_{ds}	ΔI_{qs}	ΔE_d	ΔE_q	ΔV_{ds}	ΔV_{qs}	ΔI_d	ΔI_q

Table 2.3 Participation factor analysis of a double-cage induction generator

Sub-system	Wind Turbine			Induction Generator						Network			
State-Id	1	2	3	4	5	6	7	8	9	10	11	12	13
State	$\Delta\omega_t$	$\Delta\delta_{tg}$	$\Delta\omega_g$	ΔI_{ds}	ΔI_{qs}	ΔE_{d1}	ΔE_{q1}	ΔE_{d2}	ΔE_{q2}	ΔV_{ds}	ΔV_{qs}	ΔI_d	ΔI_q

Figure 2.15 (a) shows the participation factor of the synchronous mode that is contributed by the *d-q* axis stator current and the line current. However, the stator currents are found to be dominant in case of both types of generators. The participation factors associated with the electromechanical mode are shown in Figure 2.15 (b). The generator speed and q axis voltage of the rotor circuit both contribute to this mode. Similarly, the participation factor associated with the torsional mode and non-oscillatory modes are shown in Figure 2.15 (c) and (d). It is found that the torsional mode is largely influenced by the drive train system and the electrical network does not have any influence on it. This characteristic is seen in both types of induction generators. The non-oscillatory mode is mainly contributed to by the rotor circuit dynamics, particularly the *q* axis voltage. The electrical network does not have any influence on this mode.

(a) Synchronous mode

(b) Electromechanical mode

(c) Torsional mode
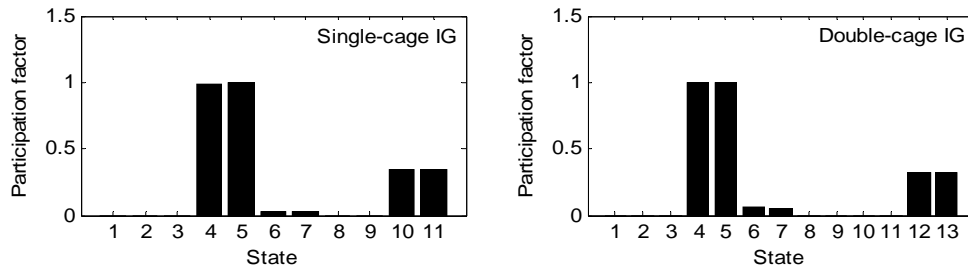
(d) Non-oscillatory mode
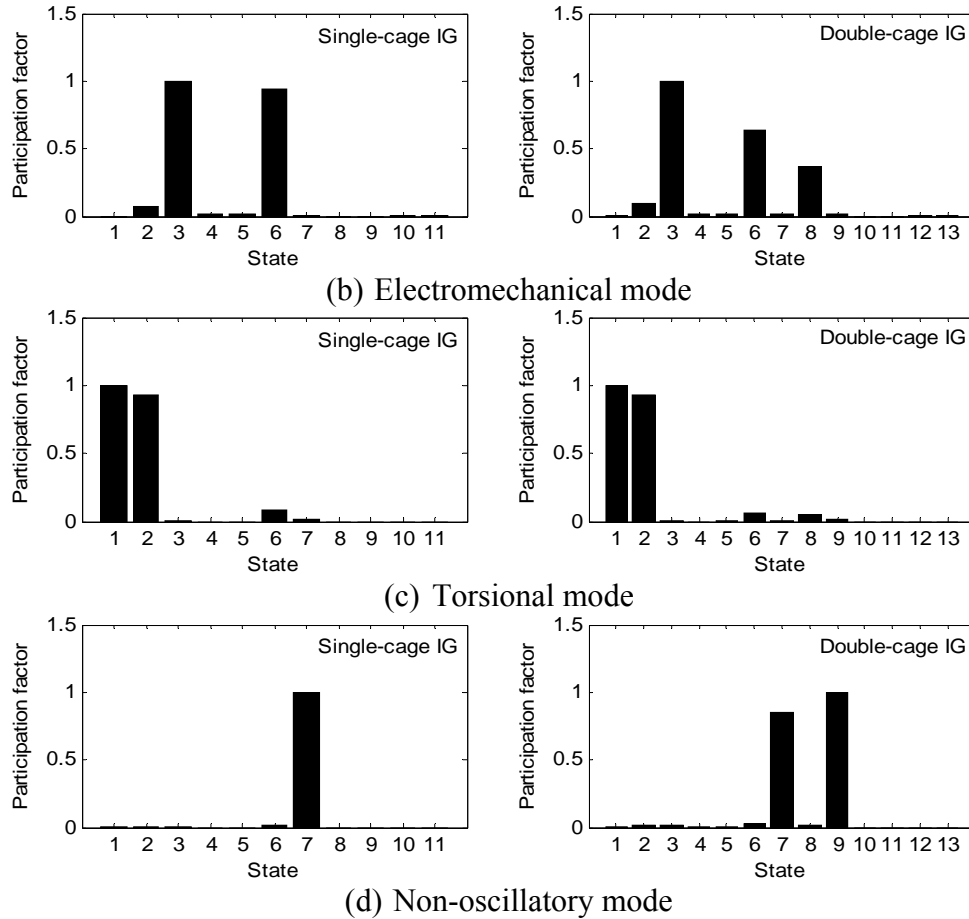
Figure 2.15 Participation factors of selected modes

2.8.3   Electromagnetic Transient Simulation

The validation of the small signal model is carried out through a time domain simulation of the study system using the electromagnetic transient program PSCAD/EMTDC. The validation is done for two cases: i) steady state behaviors and, ii) transient behaviors.

2.8.3.1 *Steady State Simulation*

Two operating points are chosen as portrayed in Table 2.1. Four variables (active and reactive power output, voltage at the terminal, and speed of the generator) are calculated and depicted in Table 2.4. The steady state solution of the system model is compared with the results obtained from the electromagnetic transient simulation. In all cases both the results match very closely, which validates the small signal model in a steady state condition.

Table 2.4 Steady validation of small signal model

Measured Parameters	Single-cage IG				Double-cage IG			
	Pm=0.5 pu		Pm=1 pu		Pm=0.5 pu		Pm=1 pu	
	Small signal	PSCAD	Small signal	PSCAD	Small signal	PSCAD	Small signal	PSCAD
$P_g(pu)$	0.498	0.498	0.994	0.996	0.498	0.497	0.993	0.992
$Q_g(pu)$	-0.298	-0.293	-0.454	-0.447	-0.312	-0.310	-0.512	-0.503
$V_s(pu)$	1.000	1.000	0.999	0.999	1.000	1.000	0.999	0.999
$\omega_g(pu)$	1.003	1.003	1.006	1.006	1.004	1.004	1.008	1.008

2.8.3.2 *Transients Simulation*

In the transient simulation, electrical and mechanical disturbances are considered. A six cycle three phase fault is simulated at location *F* at t=4 sec. When the fault occurs, the electromagnetic torque starts oscillating and then it stabilizes gradually. The electromagnetic torque of both generators following the fault is depicted in Figure 2.16 (a). This shows the presence of the multiple frequency components. The oscillations in both generators seem to be similar. Similarly the impacts of the fault on the shaft torque and generator speed are shown in Figure 2.16 (b) and (c), respectively. However, in this case, a low frequency oscillation is seen. In order to estimate the different frequency components, an FFT analysis of the electromagnetic and the shaft torque is carried out and the results are shown in Figure 2.16 (d). The PSCAD/EMTDC simulation results are recorded at a rate of 64 samples per cycle and FFT analysis is carried out by multiplying a gaussian window with the corresponding signals. The estimated frequencies from the FFT match very well with the calculated damped frequencies shown in Table 2.1. For instance, in the case of a single-cage induction generator, the estimated electromechanical mode oscillatory frequency is 38.29 rad/s (6.09 Hz) which matches very closely with the calculated damped frequency of 38.405 rad/s. Similarly, in the case of a double-cage induction generator, the estimated oscillatory frequency of 35.34 rad/s (5.62 Hz) matches with the predicted damped frequency of 35.238 rad/s. The FFT of the shaft torque is also carried out and estimated frequencies are shown in Figure 2.16 (d), matching with the calculated damped frequencies depicted in Table 2.1.

(a) Electromagnetic torque

(b) Shaft torque

(c) Generator speed

(d) FFT of electromagnetic torque and shaft torque
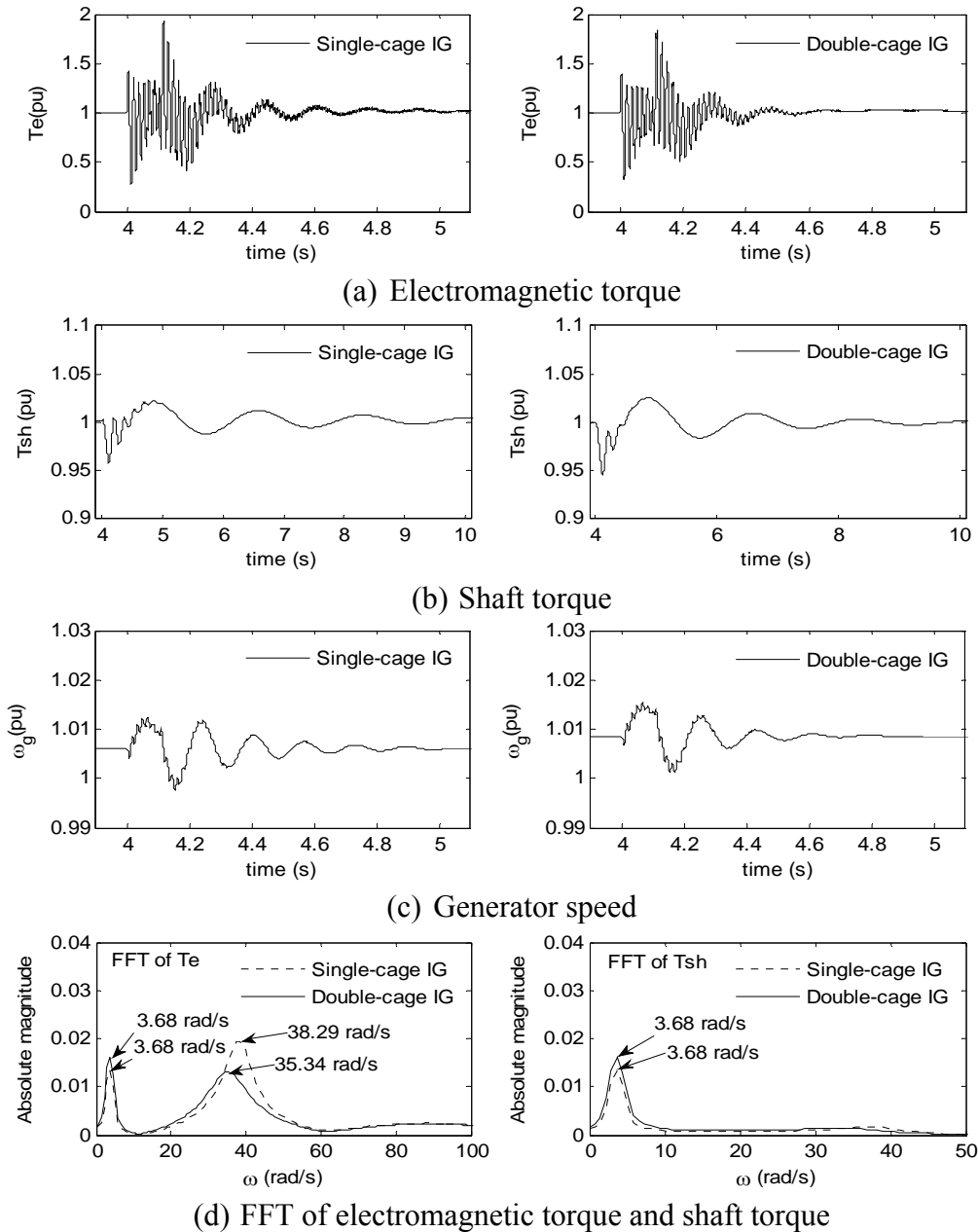
Figure 2.16 Performance of IG for a three phase fault

The validation of the small signal model for a mechanical disturbance is performed through a reduction in input mechanical torque from 1 pu to 0.85 pu at t=4 sec. The impact of the step change results in a step change in electromagnetic torque and shaft torque of the induction generator, both of which are shown in Figure 2.17 (a). It is observed that, the electromagnetic and shaft torque oscillations of a double-cage induction generator are damped out faster than the single-cage induction generator. This corroborates the eigenvalue analysis that shows a comparatively more stable system with

a double-cage induction generator. The FFT of electromagnetic torque and shaft torque are shown in Figure 2.17 (b). The estimated frequency of 3.68 rad/s matches very closely with the calculated damped frequency of 3.56-3.57 rad/s. From this study it is found that the change in the wind speed may excite the torsional mode of the wind turbine. The mathematical model developed in this chapter predicts the torsional mode frequency very accurately.

(a) Electromagnetic torque and shaft torque

(b) FFT of electromagnetic and shaft torque
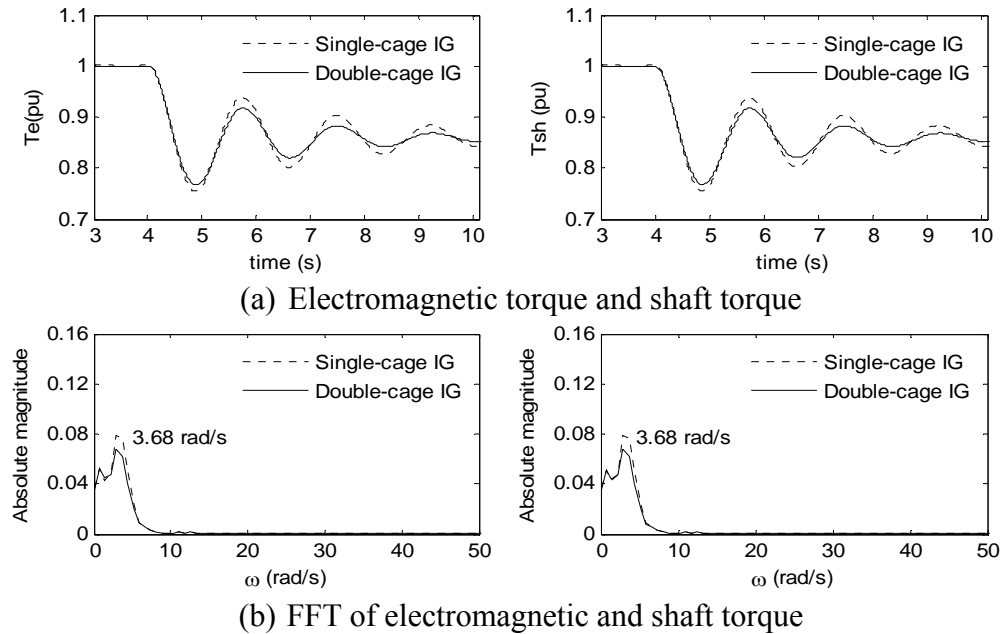
Figure 2.17 Impact of step change in wind speed

2.9 CONCLUSIONS

A comprehensive modeling of each component of an induction generator based wind farm connected to a series compensated transmission line is presented in this chapter. The study system is divided into multiple sub-systems. The dynamic model of the multi-mass wind turbine, induction generator, and series compensated transmission line are developed and linearized to develop the linear state space model of each system. The aggregation technique used for the modeling of large wind farms is also discussed. The detailed eigenvalue analysis followed by the normalized participation factor analysis is carried out to study the system stability. The dynamic model of the wind turbine generator system is reasonably validated with the electromagnetic transient simulations done with PSCAD/EMTDC software.

In commercially operated induction generator based wind farms, double-cage induction generators are widely used because of their superior performance and better reliability in comparison to the single-cage induction generators. However, detailed data for the generator electric circuit is not always available for the power system analysis. In many cases also, the data available for the study are in ill condition. In literature there are two models of double-cage induction generator, but the electromagnetic transient software PSCAD/EMTDC uses only one model which is more accurate, but complex. Hence, a data conversion technique is applied which is presented in Appendix-A to convert the traditional double-cage induction generator circuit to a circuit that is available in electromagnetic transient software PSCAD/EMTDC.

Chapter 3

SUBSYNCHRONOUS RESONANCE ANALYSIS OF SINGLE-CAGE INDUCTION GENERATOR BASED WIND FARMS

3.1   INTRODUCTION

In this chapter, a detailed analysis of subsynchronous resonance is carried out for a single-cage induction generator based wind farm connected to series compensated transmission line. Wind turbine generators with a single-cage rotor circuit are commonly utilized in wind power systems. Hence, a subsynchronous resonance study is done considering a single-cage induction generator. The dynamic models of a single-cage induction generator are presented in [19], [22]. In this analysis, the impact of the size of the wind farm, wind farm power output, and level of series compensation are studied.

A detailed state space model of the study system is developed for small signal analysis which includes eigenvalue analysis, participation factor analysis, and sensitivity studies. Electromagnetic transient simulations are then done to validate the eigenvalue analysis results. This is done during both steady state and transients.

This chapter further examines the impact of location of the fault and position of the series capacitor bank. An equivalent circuit theory analysis is also presented to investigate wind farm response to fault at the generator terminal.

3.2   SYSTEM DESCRIPTION

The study system considered in this chapter is shown in Figure 3.1. A large induction generator based wind farm is connected to a series compensated transmission line. The wind farm is represented by an equivalent induction generator model, which is achieved through the aggregation of large numbers of identical induction generators. The aggregation technique is already described in Chapter 2. The size of the wind farm is

varied between 100 MW and 500 MW and each wind turbine is rated with 2 MW. The level of series compensation is also varied from 10% to 100%.
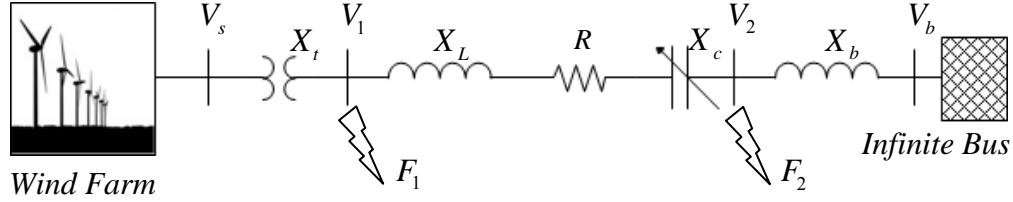
Figure 3.1 Study system

3.3 MODELING OF STUDY SYSTEM

The study system is modeled in the state space form for small signal analysis. For simplicity, the study system is divided into three sub-systems: i) mechanical drive train, ii) single-cage induction generator, and iii) network. The dynamic equations of each sub-system are briefly described below. The detailed modeling of each sub-system is given in Chapter 2.

3.3.1   Drive Train System

The differential equations of the two-mass drive train system are written as:

$$2H_t \frac{d}{dt}\omega_t = T_w - K_{tg}\delta_{tg} - D_{tg}\left(\omega_t - \omega_g\right) \tag{3.1}$$

$$\frac{d}{dt}\delta_{tg} = \omega_t - \omega_g \tag{3.2}$$

$$2H_g \frac{d}{dt}\omega_g = K_{tg}\delta_{tg} + D_{tg}\left(\omega_t - \omega_g\right) - T_g \tag{3.3}$$

3.3.2   Induction Generator

The single-cage induction generator is modeled as a voltage source behind the transient reactance. The detailed model is presented in Sec. 2.4.2. The *d-q* axis differential equations of the induction generator model are:

$$\frac{X_0}{\omega_s}\frac{d}{dt}I_{ds} + \frac{1}{\omega_s}\frac{d}{dt}E_q = -R_sI_{ds} + \left(X_0I_{qs} - E_d\right) - V_{ds} \tag{3.4}$$

$$\frac{X_0}{\omega_s}\frac{d}{dt}I_{qs} - \frac{1}{\omega_s}\frac{d}{dt}E_d = -R_sI_{qs} - \left(X_0I_{ds} + E_q\right) - V_{qs} \tag{3.5}$$

$$\frac{d}{dt}E_q = -\frac{1}{T_0}\left(E_q - \frac{X_m^2}{X_r}I_{ds}\right) - s\omega_sE_d \tag{3.6}$$

$$\frac{d}{dt}E_d = -\frac{1}{T_0}\left(E_d + \frac{X_m^2}{X_r}I_{qs}\right) + s\omega_sE_q \tag{3.7}$$

3.3.3 Network

The network includes the shunt capacitor at the wind turbine generator, interfacing transformer, and the series compensated transmission line. The equivalent transformer leakage reactance is merged with the line inductive reactance. The saturation effect of the transformer and effect of line charging capacitances are also neglected. The dynamic equations of the network in *d-q* frame of reference are:

$$C_g\frac{d}{dt}V_{ds} = I_{ds} - I_d + \omega_sC_gV_{qs} \tag{3.8}$$

$$C_g\frac{d}{dt}V_{qs} = I_{qs} - I_q - \omega_sC_gV_{ds} \tag{3.9}$$

$$L\frac{d}{dt}I_d = V_{ds} - RI_d + \omega_sLI_q - V_{cd} - V_{bd} \tag{3.10}$$

$$L\frac{d}{dt}I_q = V_{qs} - RI_q - \omega_sLI_d - V_{cq} - V_{bq} \tag{3.11}$$

$$C\frac{d}{dt}V_{cd} = I_d + \omega_sCV_{cq} \tag{3.12}$$

$$C\frac{d}{dt}V_{cq} = I_q - \omega_sCV_{cd} \tag{3.13}$$

All the state variables are defined in Chapter 2

3.3.4　Complete System Model

The dynamic equations of all the sub-systems are linearized and the complete system state space model is developed by interfacing all of the sub-systems as shown Figure 3.2. Each sub-system in state space form is written as:

$$\dot{x}_{WT} = [A_{TT}]x_{WT} + [A_{TG}]x_G + [B_T]u_{WT} \tag{3.14}$$

$$\dot{x}_G = [A_{GT}]x_{WT} + [A_{GG}]x_G + [A_{GN}]x_N \tag{3.15}$$

$$\dot{x}_N = [A_{NG}]x_G + [A_{NN}]x_N + [B_N]u_N \tag{3.16}$$

Combining (3.14)-(3.16), the state space model of the overall study system is written as:

$$\dot{x}_{sys} = [A_{sys}]x_{sys} + [B_1]u_1 + [B_2]u_2 \tag{3.17}$$

$$y_{sys} = [C_{sys}]x_{sys} \tag{3.18}$$

where,

$$x^t_{sys} = \begin{bmatrix} x^t_{WT} & x^t_G & x^t_N \end{bmatrix} \tag{3.19}$$

$$y^t_{sys} = \begin{bmatrix} \Delta P_{WF} & \Delta Q_{WF} \end{bmatrix} \tag{3.20}$$

$$x^t_{WT} = \begin{bmatrix} \Delta\omega_t & \Delta\delta_{tg} & \Delta\omega_g \end{bmatrix} \tag{3.21}$$

$$x^t_G = \begin{bmatrix} \Delta I_{ds} & \Delta I_{qs} & \Delta E_d & \Delta E_q \end{bmatrix} \tag{3.22}$$

$$x^t_N = \begin{bmatrix} \Delta V_{ds} & \Delta V_{ds} & \Delta I_d & \Delta I_q & \Delta V_{cd} & \Delta V_{cq} \end{bmatrix} \tag{3.23}$$

$$u_1 = \begin{bmatrix} \Delta T_w \end{bmatrix} \tag{3.24}$$

$$u_2 = \begin{bmatrix} \Delta V_{bd} \\ \Delta V_{bq} \end{bmatrix} \tag{3.25}$$

The state and input matrices are defined as follows:

$$[A_{sys}] = \begin{bmatrix} A_{TT} & A_{TG} & 0_{3\times6} \\ A_{GT} & A_{GG} & A_{GN} \\ 0_{6\times3} & A_{NG} & A_{NN} \end{bmatrix} \tag{3.26}$$

$$[B_1] = \begin{bmatrix} B_T \\ 0_{4\times1} \\ 0_{6\times1} \end{bmatrix}, [B_2] = \begin{bmatrix} 0_{3\times2} \\ 0_{4\times2} \\ B_N \end{bmatrix} \tag{3.27}$$
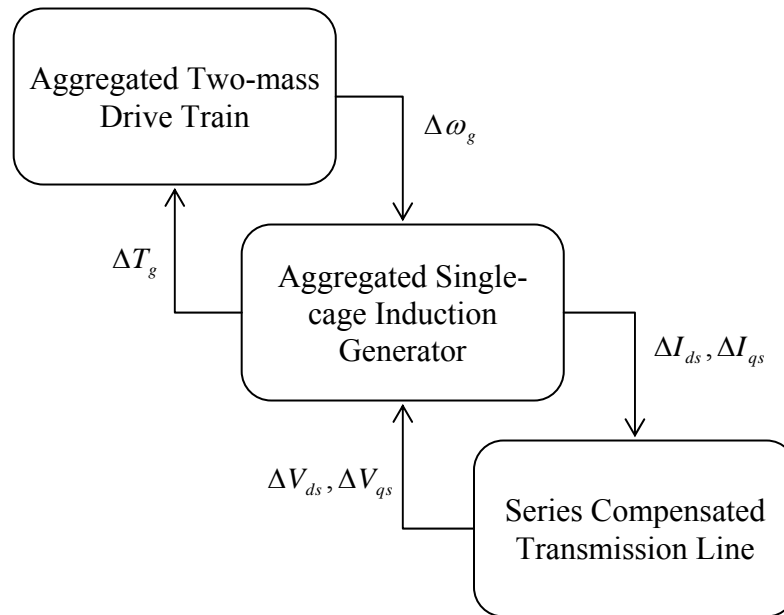
Figure 3.2 Sub-system interconnections

3.4 SMALL SIGNAL ANALYSIS

3.4.1 Eigenvalue Analysis

The system eigenvalues are calculated at several equilibrium points and depicted in Table 3.1. Six complex conjugate eigenvalues and one real eigenvalue are obtained from the state space model of the complete system. The different modes are: i) network mode 1 and network mode 2, ii) super synchronous mode, iii) electrical mode, iv) electromechanical mode, v) torsional mode, and vi) non-oscillatory mode. When series compensation is not considered, the electrical mode gets eliminated, as shown in Table 3.1. In Table 3.1, the system eigenvalues are calculated for the variation in the wind farm size and level of series compensation. Although a wide range of series compensation level is considered during the study, system eigenvalues for some selected compensation levels only are shown in Table 3.1.

With an uncompensated transmission line, all the modes shown in Table 3.1 are found stable. The electromechanical mode stability gets reduced with the increasing size of the wind farm. However, it remains substantially stable with low oscillatory frequency. This

shows a decrease in the oscillatory frequency as well. Further, the torsional mode stability increases with the increase in the size of the wind farm. The increase in the absolute real part of eigenvalues indicates improved stability of the torsional mode with respect to increase in the wind farm size. The oscillatory frequency, though, remains almost constant. Under such a scenario the non-oscillatory mode stability is reduced as well.

The system eigenvalues considering series compensation are also depicted in Table 3.1. The inclusion of the series capacitor increases the number of dynamic equations to thirteen, which results in seven modes. The three modes: electrical, electromechanical, and torsional are important from the SSR point of view and are discussed in detail. From Table 3.1 it is found that the electrical mode stability and the damped frequency both decrease with an increase in the series compensation level. Further, when size of the wind farm is increased, keeping the series compensation level constant, the electrical mode stability gets improved. However, the electrical mode resonant frequency f_{er} drops significantly with increase in size of the wind farm. It is noticed that at certain level of series compensation the real part of the electrtical mode eigenvalues becomes positive, which signifies the potential for the induction generator effect SSR. A similar trend is seen for different sizes of the wind farms listed in Table 3.1.

The impact of series compensation on the electromechanical mode and torsional mode are also illustrated in Table 3.1. At a constant series compensation level, any increase in the size of the wind farm results in a declining stability of the electromechanical mode. The oscillatory frequency associated with the electromechanical mode also gets reduced simultaneously. It is seen that the stability of the mode increases with the increase the level of series compensation, yet the damped frequency increases only marginally. The torsional mode stability increases with the increased wind farm size, but an increase in the series compensation level reduces the stability. The oscillatory frequency of the torsional mode remains almost constant in both cases. From the analysis over a wide range of series compensation level and wind farm size, it is found that the torsional mode never becomes unstable. Hence, no potential for the torsional interaction is anticipated in wind farms connected to series compensated transmission lines.

Table 3.1 System eigenvalues for different size of wind farm

Modes	100 MW	200 MW	300 MW	400 MW	500 MW
No Series Compensation					
Network Mode-1	-6.540 ± 2747.8i	-7.104 ± 2270.1i	-7.439 ± 2064.8i	-7.655 ± 1929i	-7.793 ± 1806i
Network Mode-2	-7.040 ± 1993.9i	-8.086 ± 1516.2i	-8.802 ± 1310.9i	-9.339 ± 1175.2i	-9.795 ± 1052.2i
Sup. Sync. Mode	-10.06 ± 376.8i	-10.22 ± 376.84i	-10.32 ± 376.8i	-10.39 ± 376.88i	-10.44 ± 376.9i
Electrical Mode	X	X	X	X	X
Elect-mech. Mode	-3.834 ±37.504i	-3.045 ±33.146i	-2.581 ± 29.769i	-2.312 ± 26.895i	-2.207 ± 24.185i
Torsional Mode	-0.364 ±3.6066i	-0.399 ±3.5752i	-0.454 ± 3.5552i	-0.539 ± 3.5659i	-0.644 ± 3.6587i
Non-osc. Mode	-7.065	-5.0301	-3.544	-2.267	-0.981
50% Series Compensation					
Network Mode-1	-6.521 ± 2763.5i	-7.072 ± 2297.4i	-7.407 ± 2110.9i	-7.633 ± 2006.1i	-7.795 ± 1935.8i
Network Mode-2	-7.008 ± 2009.6i	-8.018 ± 1543.5i	-8.701 ± 1357i	-9.194 ± 1252.3i	-9.571 ± 1182i
Sup. Sync. Mode	-6.031 ± 520.6i	-6.020 ± 555.46i	-5.96 ± 574.34i	-5.901 ± 586.4i	-5.85 ± 594.81i
Electrical Mode	-2.779 ± 232.5i	-2.543 ± 197.35i	-2.59 ± 178.32i	-2.720 ± 166.22i	-2.872 ± 157.81i
Elect-mech. Mode	-4.437 ± 40.502i	-3.822 ± 37.808i	-3.362 ± 35.536i	-3.009 ± 33.567i	-2.734 ± 31.821i
Torsional Mode	-0.351 ± 3.625i	-0.360 ± 3.6076i	-0.373 ± 3.5913i	-0.389 ± 3.5765i	-0.410 ± 3.5639i
Non-osc. Mode	-8.489	-7.071	-5.961	-5.052	-4.279
70% Series Compensation					
Network Mode-1	-6.513 ± 2768.8i	-7.059 ± 2304.9i	-7.392 ± 2121.7i	-7.619 ± 2021.5i	-7.784 ± 1957.4i
Network Mode-2	-6.996 ± 2014.9i	-7.993 ± 1551i	-8.666 ± 1367.9i	-9.152 ± 1267.7i	-9.52 ± 1203.6i
Sup. Sync. Mode	-6.159 ± 546.63i	-6.132 ± 587.73i	-6.057 ± 610.03i	-5.986 ± 624.3i	-5.926 ± 634.27i
Electrical Mode	-2.008 ± 206.04i	-1.414 ± 164.24i	-1.253 ± 141.45i	-1.271 ± 126.84i	-1.372 ± 116.64i
Elect-mech. Mode	-4.758 ± 41.938i	-4.336 ± 40.321i	-3.984 ± 38.882i	-3.681 ± 37.575i	-3.416 ± 36.372i
Torsional Mode	-0.347 ± 3.6326i	-0.350 ± 3.6222i	-.3540 ± 3.6122i	-0.358 ± 3.6024i	-0.365 ± 3.593i
Non-osc. Mode	-9.18	-8.175	-7.330	-6.607	-5.977
85% Series Compensation					
Network Mode-1	-6.507 ± 2772.5i	-7.049 ± 2309.5i	-7.380 ± 2127.5i	-7.608 ± 2028.9i	-7.774 ± 1967i
Network Mode-2	-6.987 ± 2018.5i	-7.975 ± 1555.6i	-8.642 ± 1373.6i	-9.123 ± 1275.1i	-9.487 ± 1213.2i
Sup. Sync. Mode	-6.238 ± 563.69i	-6.200 ± 608.85i	-6.117 ± 633.39i	-6.039 ± 649.1i	-5.974 ± 660.11i
Electrical Mode	-1.371 ± 188.59i	-0.322 ± 142.16i	0.249 ± 116.45i	0.6167 ± 99.635i	0.8924 ± 87.567i
Elect-mech. Mode	-5.045 ± 43.139i	-4.894 ± 42.653i	-4.812 ± 42.314i	-4.786 ± 42.099i	-4.815 ± 41.997i
Torsional Mode	-0.344 ± 3.6383i	-0.343 ± 3.6336i	-0.343 ± 3.629i	-0.342 ± 3.6243i	-0.342 ± 3.6197i
Non-osc. Mode	-9.757	-9.178	-8.655	-8.179	-7.743

To summarize the impact of series compensation and the size of a wind farm, the variation of electrical mode eigenvalues are depicted in Figure 3.3. The loci of the electrical mode crosses the y-axis at a certain level of series compensation, known as the critical series compensation level which is unique for different size of the wind farms. The damping ratio of the electrical mode is calculated and shown in Figure 3.4. The damping ratio is calculated from the eigenvalues as given below [50], [99].

$$\zeta = -\frac{\sigma}{\sqrt{\sigma^2 + \omega^2}} \tag{3.28}$$

where,

$$\lambda = \sigma + j\omega \tag{3.29}$$

σ is the real part of the complex eigenvalue and ω is the imaginary part in rad/s.

The damping ratio indeed becomes negative beyond the critical series compensation level. This indicates the potential for the undamped SSR oscillation in the wind farm. It is noted that the unstable electrical mode represents the induction generator effect SSR.
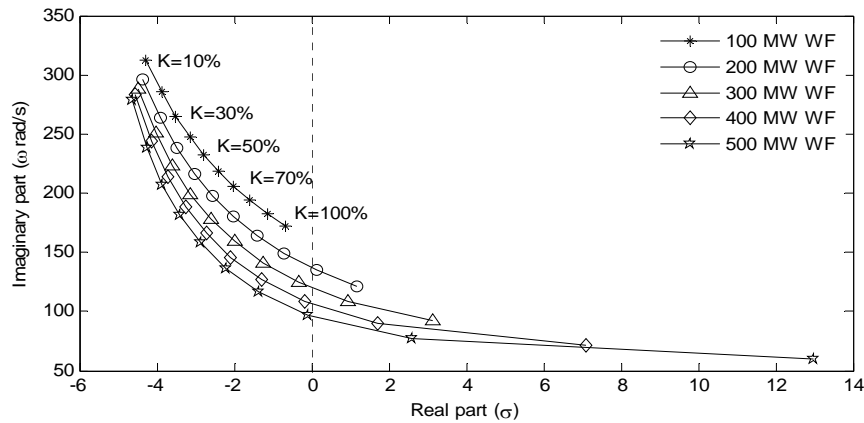
Figure 3.3 Electrical mode eigenvalues
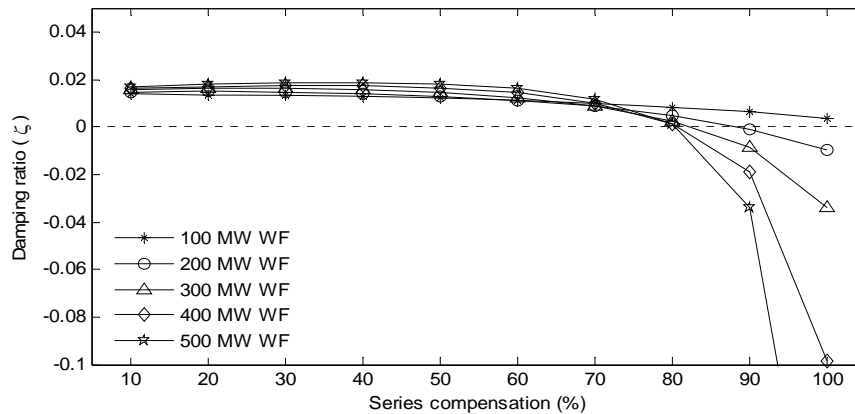
Figure 3.4 Electrical mode damping ratio

There are several commercially available induction generators used for power system stability study [105], [112]. The system eigenvalues are now calculated for five different commercially available induction generators of different makes. The eigenvalues shown in Table 3.1 are based upon IG-1 whose parameters are given in Appendix-B, whereas Table 3.2 shows the eigenvalues for other induction generators IG2-IG5. It is found that the impact of a series capacitor on the wind farm is similar to the results shown in Table

3.1. However, the critical compensation levels are different for the different induction generators based wind farms. The critical series compensation levels are depicted in Table 3.3. It is observed that except IG-2, in all cases the critical compensation levels are found beyond the 70% series compensation.

Table 3.2 System eigenvalues with different induction generator data

Modes	IG-1	IG-2	IG-3	IG-4	IG-5
100 MW					
Network Mode-1	-6.5079±2772.5i	-7.0322±2625i	-6.68±2563.5i	-6.538±2616.5i	-6.1573±2531.4i
Network Mode-2	-6.9872±2018.5i	-7.6948±1871.1i	-7.2594±1809.6i	-7.1036±1862.5i	-6.5896±1777.4i
Sup. Sync. Mode	-6.2385±563.69i	-7.057±562.02i	-6.6145±557.15i	-6.3333±539.58i	-5.8256±541.34i
Electrical Mode	-1.3716±188.59i	-0.6858±190.34i	-1.0454±195.43i	-0.1617±213.52i	-1.3186±211.73i
Elect-mech. Mode	-5.0456±43.139i	-6.7705±42.185i	-6.127±40.636i	-7.6558±35.22i	-5.529±36.122i
Torsional Mode	-0.3447±3.6383i	-0.4789±3.6271i	-0.4758±3.6191i	-0.8345±3.5555i	-0.5773±3.5856i
Non-osc. Mode	-9.7573	-12.919	-11.569	-13.068	-9.7635
200 MW					
Network Mode-1	-7.0491±2309.5i	-7.8382±2187.7i	-7.3238±2129i	-7.1613±2139i	-6.5626±2075.1i
Network Mode-2	-7.9753±1555.6i	-9.1262±1433.8i	-8.4687±1375.1i	-8.3433±1385.1i	-7.4611±1321.2i
Sup. Sync. Mode	-6.2003±608.85i	-6.9007±607.13i	-6.5514±602.26i	-6.434±584.28i	-5.9357±586.03i
Electrical Mode	-0.32206±142.16i	0.83397±144.15i	0.23908±149.37i	1.2427±168.35i	-0.33932±166.45i
Elect-mech. Mode	-4.8941±42.653i	-6.5902±41.697i	-5.9443±40.169i	-7.4246±34.88i	-5.3593±35.749i
Torsional Mode	-0.34386±3.6336i	-0.47825±3.6228i	-0.47541±3.615i	-0.83743±3.5534i	-0.57828±3.5827i
Non-osc. Mode	-9.1786	-12.159	-10.924	-12.406	-9.2874
300 MW					
Network Mode-1	-7.3809±2127.5i	-8.3372±2015.3i	-7.7272±1956.8i	-7.5715±1947.1i	-6.8309±1888.8i
Network Mode-2	-8.642±1373.6i	-10.099±1261.4i	-9.3107±1203i	-9.2689±1193.1i	-8.1252±1134.9i
Sup. Sync. Mode	-6.1171±633.39i	-6.7221±631.76i	-6.4372±627.23i	-6.4024±610.24i	-5.9391±612.35i
Electrical Mode	0.24906±116.45i	1.6957±118.52i	0.95934±123.53i	2.0552±141.93i	0.2292±139.58i
Elect-mech. Mode	-4.8121±42.314i	-6.5032±41.317i	-5.8279±39.79i	-7.2375±34.565i	-5.218±35.409i
Torsional Mode	-0.34329±3.629i	-0.47795±3.6186i	-0.47539±3.611i	-0.84117±3.5515i	-0.57976±3.5799i
Non-osc. Mode	-8.6553	-11.47	-10.335	-11.789	-8.8324
400 MW					
Network Mode-1	-7.608±2028.9i	-8.6812±1921.6i	-8.0079±1863i	-7.8672±1841.5i	-7.0179±1789i
Network Mode-2	-9.1234±1275.1i	-10.806±1167.8i	-9.9329±1109.2i	-9.9881±1087.6i	-8.6283±1035.2i
Sup. Sync. Mode	-6.0399±649.1i	-6.571±647.59i	-6.3316±643.45i	-6.343±627.67i	-5.9161±629.5i
Electrical Mode	0.61679±99.635i	2.2711±101.76i	1.4222±106.51i	2.5744±124.07i	0.57673±121.92i
Elect-mech. Mode	-4.7869±42.099i	-6.4924±41.026i	-5.7634±39.486i	-7.0855±34.273i	-5.1048±35.112i
Torsional Mode	-0.34295±3.6243i	-0.47802±3.6145i	-0.47573±3.607i	-0.84577±3.5498i	-0.58168±3.5772i
Non-osc. Mode	-8.1792	-10.843	-9.794	-11.211	-8.4156
500 MW					
Network Mode-1	-7.7742±1967i	-8.9343±1862.6i	-8.2161±1803.7i	-8.0926±1774.3i	-7.1628±1724.2i
Network Mode-2	-9.4877±1213.2i	-11.343±1108.8i	-10.412±1049.9i	-10.564±1020.4i	-9.0399±970.37i
Sup. Sync. Mode	-5.9744±660.11i	-6.4473±658.71i	-6.2414±654.91i	-6.2802±640.31i	-5.8861±642.18i
Electrical Mode	0.89246±87.567i	2.7089±89.769i	1.7498±94.287i	2.9227±111.04i	0.80924±108.77i
Elect-mech. Mode	-4.8155±41.997i	-6.5497±40.809i	-5.7422±39.243i	-6.9617±33.999i	-5.0091±34.837i
Torsional Mode	-0.34285±3.6197i	-0.47845±3.6104i	-0.47643±3.6031i	-0.85124±3.5482i	-0.58412±3.5746i
Non-osc. Mode	-7.7437	-10.27	-9.2952	-10.668	-8.0146

Table 3.3 Critical series compensation level

Wind farm size (MW)	IG-1	IG-2	IG-3	IG-4	IG-5
100	X	88.47	96.40	X	X
200	88.70	68.50	76.62	82.20	90.43
300	82.95	64.10	72.47	76.77	82.28
400	81.14	63.25	71.55	75.25	79.45
500	80.64	63.62	71.86	75.10	78.45

3.4.2   Participation Factor Analysis

Participation factor analysis is utilized to evaluate the influence of various states on the different subsynchronous modes. A 100 MW wind farm connected to 50% series compensated line is considered to conduct the analysis. Figure 3.5 (a) shows the participation factors associated with the electrical mode, which is mainly contributed by the *d-q* axis voltage across the series capacitor, *d-q* axis stator current and transmission line current. Figure 3.5 (b) shows the participation factors associated with electromechanical mode. This mode is equally contributed by the generator speed and *d* axis induced voltage in the rotor circuit that indicates the influence of generator inertia and rotor circuit parameters on the electromechanical mode. These parameters contribute to the damping and oscillatory frequency of the electromechanical mode. Figure 3.5 (c) shows the contribution of wind turbine speed and twisting angle towards the torsional mode. Being a mechanical mode it is characterized by the wind turbine inertia and shaft stiffness. Since the wind turbine inertia is very high in comparison to the generator inertia, it is unlikely to see any torsional interaction. The participation factors associated with the non-oscillatory mode shown in Figure 3.5 (d) shows that this mode is solely contributed by the *q* axis induced voltage in the rotor circuit. This is a monotonic mode and has no impact on the SSR phenomenon in a wind farm. A similar study using the other three high frequency modes reveals that these modes are mainly contributed by the PCC voltage and line current, however they are not shown here.

(a) Electrical mode   (b) Electromechanical mode

(c) Torsional mode   (d) Non-oscillatory mode
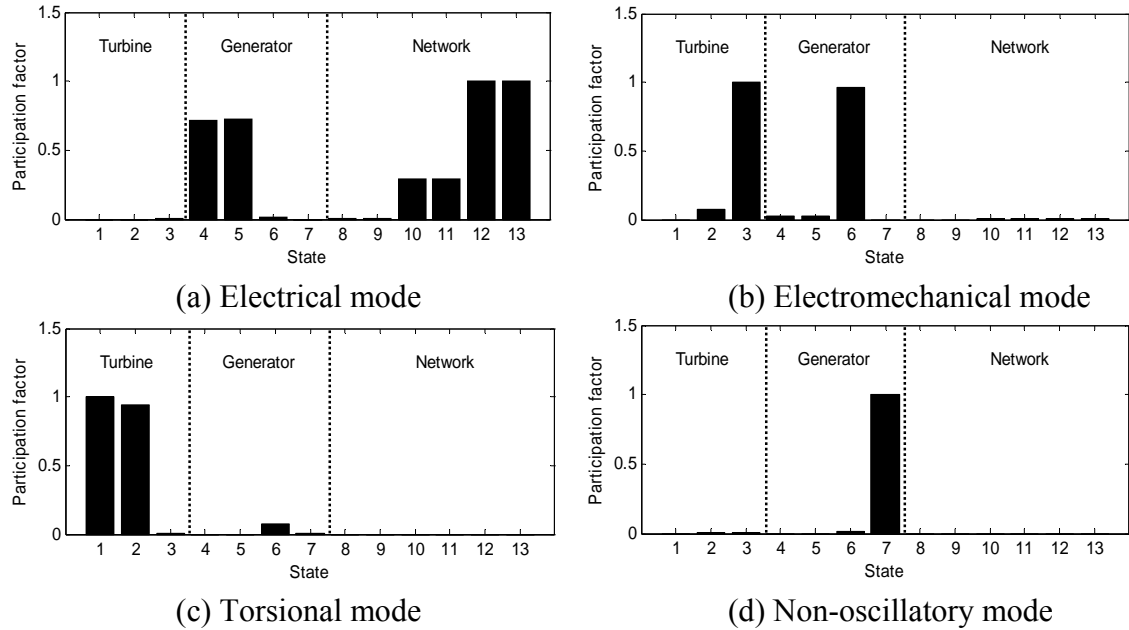
Figure 3.5 Participation factors of various modes

3.4.3   Sensitivity Analysis

This section presents the sensitivity analysis with respect to change in the electrical and mechanical parameters of the wind turbine generators [93]. The three oscillatory modes considered for the sensitivity study are: i) electrical mode, ii) electromechanical mode, and iii) torsional mode. Two different operating scenarios are chosen: i) 100 MW wind farm and ii) 500 MW wind farm producing only 100 MW output. Both wind farms are connected to a 50% series compensated line.

3.4.3.1   *Sensitivity with Respect to Electrical System Parameters*

Under the electrical parameters sensitivity study, stator resistance, stator unsaturated leakage reactance, rotor resistance, and rotor unsaturated leakage reactance are varied while all other parameters are kept constant. The aforementioned parameters are changed with respect to their nominal value, presented with a zero in the subscript. The ratios of these parameters' values to their nominal values are taken as 0.25, 0.5, 1, 1.5 and 2. Figure 3.6 shows the impact of the change in the stator resistance on the damping ratio of the electrical mode, electromechanical mode and torsional mode. It is found that the electrical mode damping ratio shown in Figure 3.6 (a) decreases with smaller stator resistance and when the stator resistance increases, the damping ratio increases gradually.

The electrical mode-damping ratio of the 100 MW wind farm is lower than the 500 MW wind farm operating with 100 MW power output condition, irrespective of the value of the stator resistance. Figure 3.6 (b) and (c) shows the impact of change in stator resistance on the electromechanical and torsional mode-damping ratios, respectively. In both cases it is found that the damping ratios are less sensitive to any variation in the stator resistance.

Figure 3.7 shows the impact of the change in the stator reactance on the three oscillatory modes. From the Figure 3.7 (a) and (b), the impact of the stator reactance on the electrical and electromechanical mode damping ratio is found to be small. The torsional mode-damping ratio only improves with stator reactance. The improvement in the damping ratio is quite large in case of a 100 MW wind farm in comparison to the 500 MW wind farm producing 100 MW output, as shown in Figure 3.7 (c).

(a) Electrical mode   (b) Electromechanical mode

(c) Torsional mode
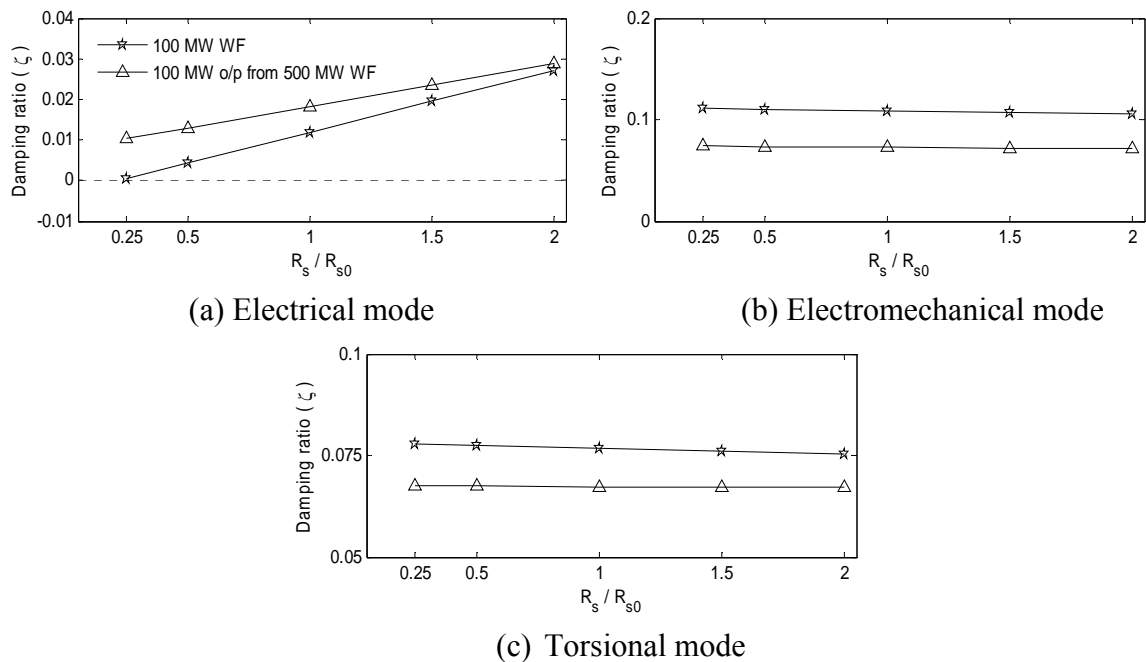
Figure 3.6 Impact of change in stator resistance

(a) Electrical mode

(b) Electromechanical mode

(c) Torsional mode
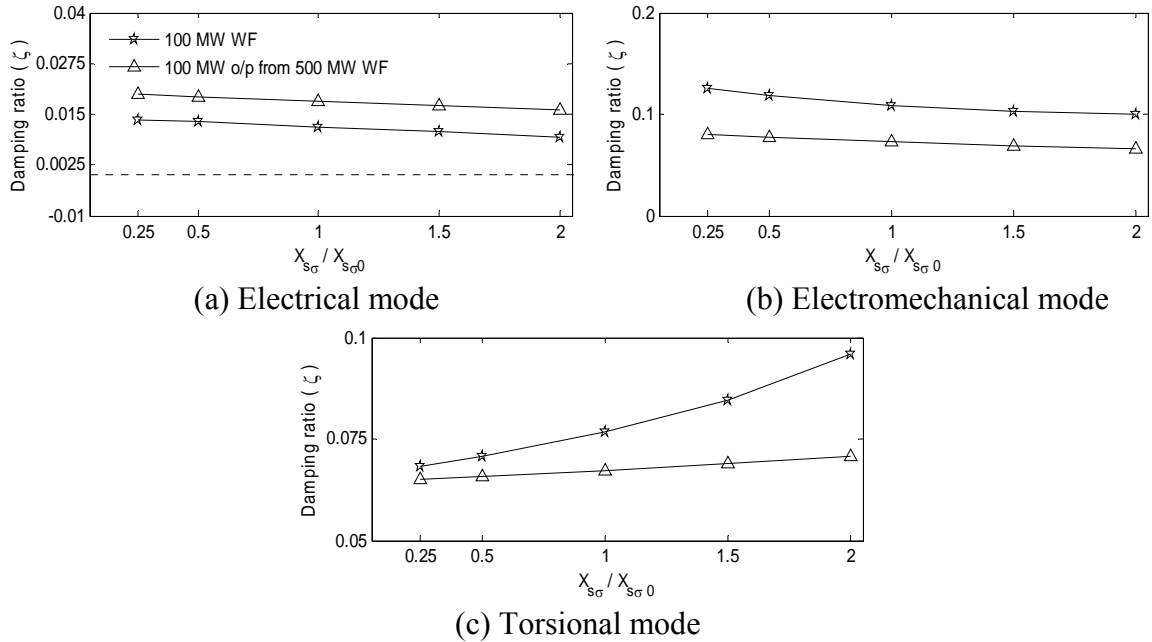
Figure 3.7 Impact of change in stator reactance

Figure 3.8 shows the influence of the rotor resistance on the damping ratio of the three aforementioned subsynchronous modes. In Figure 3.8 (a) the electrical mode-damping ratio is found to be decreasing with respect to the increase in the rotor resistance. This is quite expected, as with larger rotor resistance the net negative resistance at sub-synchronous frequency becomes higher than the net positive resistance. On the other hand, an opposite impact of the rotor resistance is seen on the electromechanical and torsional mode-damping ratios that are depicted in Figure 3.8 (b) and Figure 3.8 (c), respectively. In this case the influence of the rotor resistance is also seen to be larger for a 100 MW wind farm in comparison to a 500 MW wind farm producing 100 MW output.

Figure 3.9 shows the impact of the rotor leakage reactance. In this case the electrical mode and electromechanical mode damping ratios exhibit minimal change with respect to the variation in the rotor reactance as shown in Figure 3.9 (a) and Figure 3.9 (b), respectively. However, the torsional mode-damping ratio of the 100 MW wind farm increases with rotor leakage reactance. This is shown in Figure 3.9 (c). The torsional mode-damping ratio of the 500 MW wind farm producing 100 MW output is almost unaffected by the change in rotor reactance.

From the electrical parameter sensitivity study, it is concluded that amongst all parameters stator resistance and large rotor resistance significantly affect the electrical mode stability. The electrical mode of large wind farms is found to be more stable in comparison to small wind farms. However, smaller wind farms provide more damping to electromechanical and torsional mode.

(a) Electrical mode

(b) Electromechanical mode

(c) Torsional mode
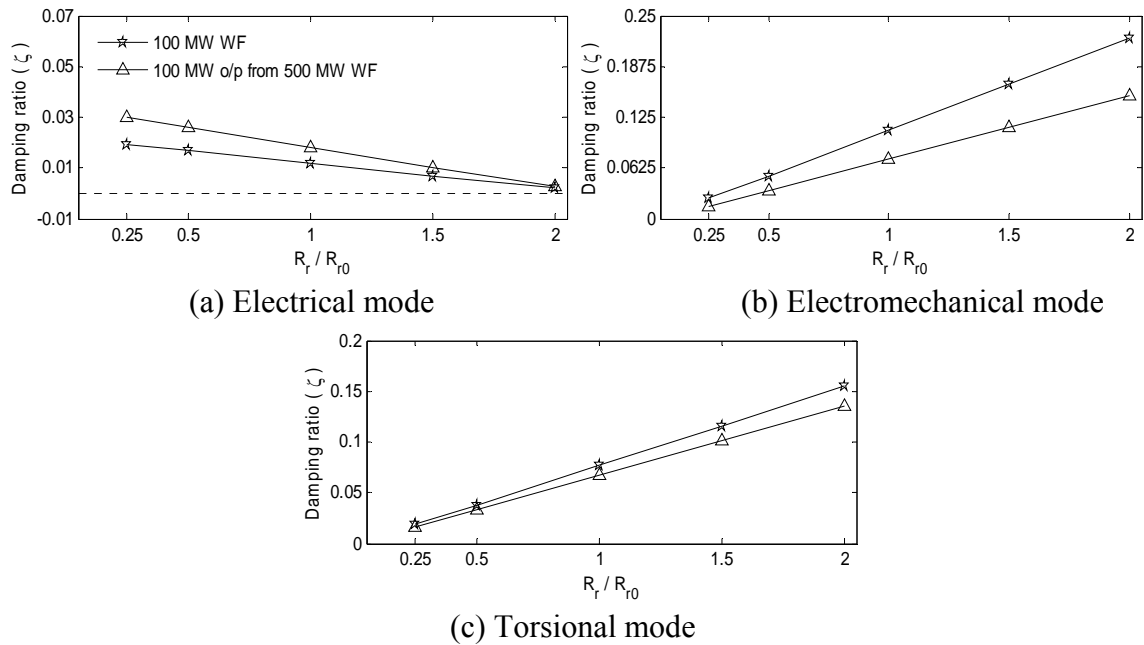
Figure 3.8 Impact of change in rotor resistance

(a) Electrical mode

(b) Electromechanical mode

(c) Torsional mode
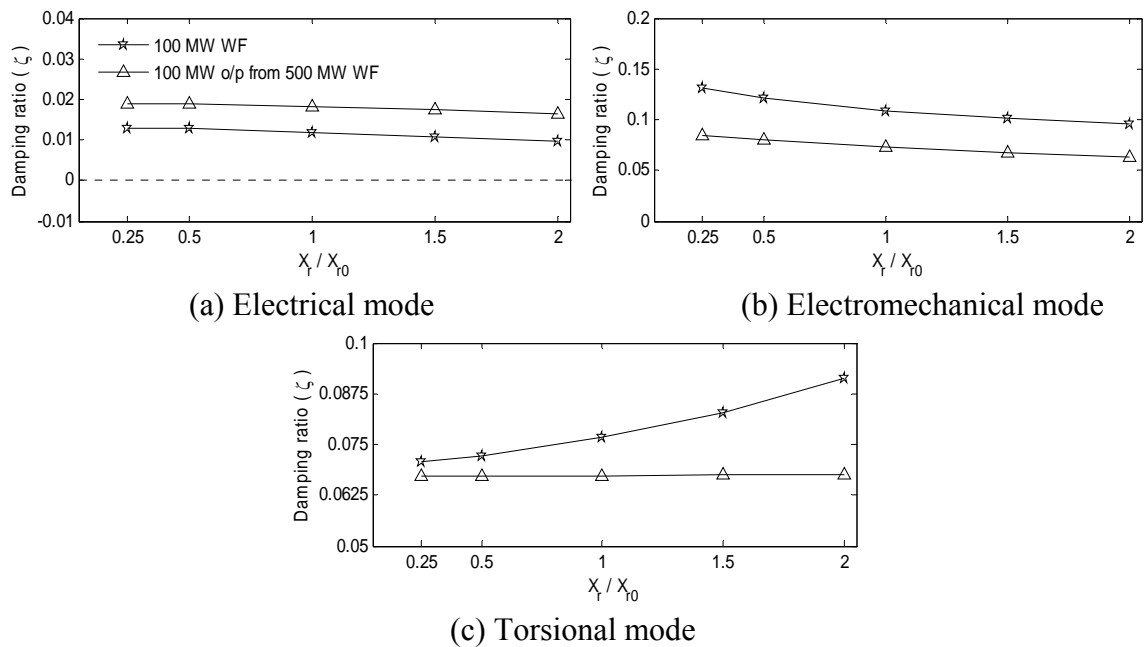
Figure 3.9 Impact of change in rotor reactance

3.4.3.2 *Sensitivity with Respect to Mechanical System Parameters*

The turbine inertia, shaft stiffness, and generator inertia are considered for the study of the mechanical parameter sensitivity. Figure 3.10 shows the variation in the damping ratios of the modes with respect to change in the turbine inertia. The electrical mode and electromechanical mode-damping ratios are found to be unresponsive to the variation as shown in Figure 3.10 (a) and (b), respectively, which is as expected. This has also been stated in the participation factor analysis of the corresponding modes. However, the torsional mode-damping ratio depicted in Figure 3.10 (c) increases linearly with the wind turbine inertia constant. Figure 3.11 shows the shaft stiffness of the wind turbine. The torsional mode-damping ratio is enhanced with an increase in the shaft stiffness. Figure 3.12 shows the influence of the generator inertia constant on these three oscillatory modes. The variation in the electrical mode is seen to be very small as shown in Figure 3.12 (a), but the increase in the generator rotor inertia improves the electromechanical mode-damping ratio as shown in Figure 3.12 (b). The change in the torsional mode-damping ratio shown in Figure 3.12 (c) is also very small.

Based on the mechanical sensitivity study, it is determined that the mechanical parameters associated with the wind turbine generator system have no influence over the electrical resonance caused by the series capacitor. The electromechanical mode and torsional mode are highly influenced by the wind turbine inertia and shaft stiffness as they have a strong coupling with the mechanical properties of the wind turbine generator. The generator inertia constant has an effect on the electromechanical mode only.

(a) Electrical mode   (b) Electromechanical mode
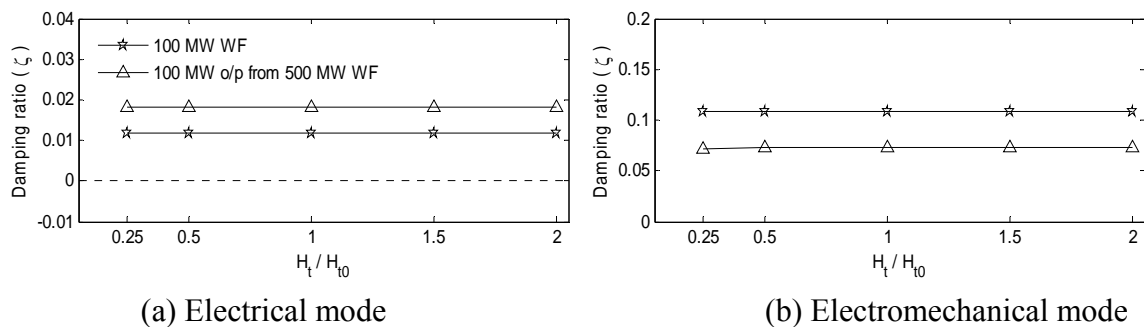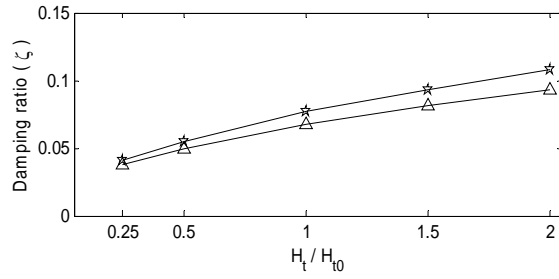
(c) Torsional mode

Figure 3.10 Impact of change in turbine inertia constant
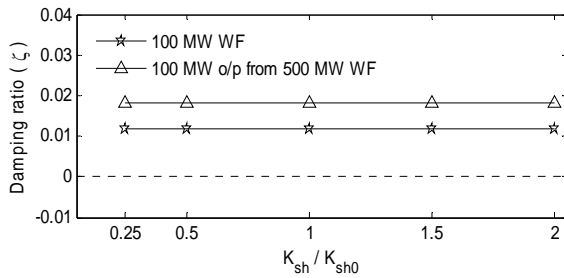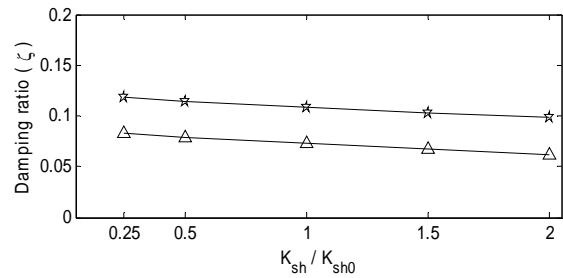
(a) Electrical mode

(b) Electromechanical mode
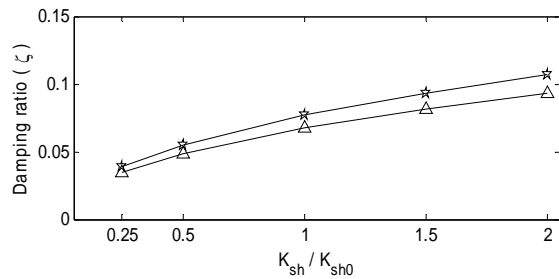
(c) Torsional mode

Figure 3.11 Impact of change in shaft stiffness
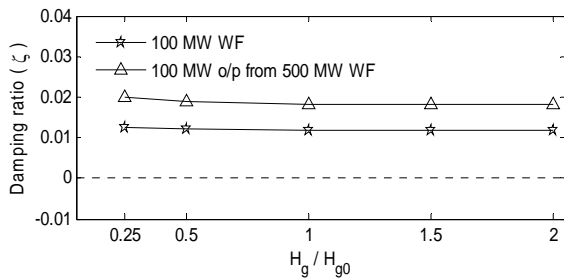
(a) Electrical mode
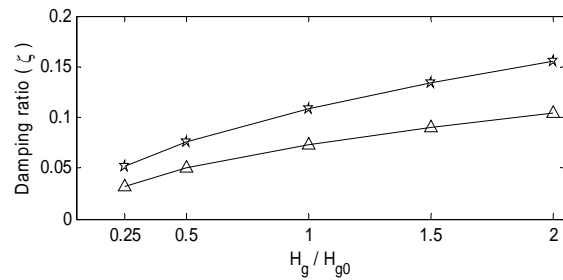
(b) Electromechanical mode
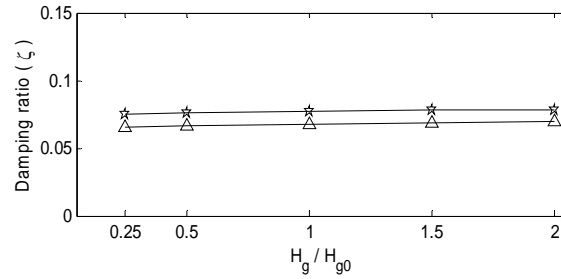
(c) Torsional mode

Figure 3.12 Impact of change in generator inertia constant

3.5 ELECTROMAGNETIC TRANSIENT SIMULATIONS

In this section, the time domain simulation results are presented. The considered study system is modeled using the inbuilt blocksets given in the PSCAD/EMTDC software package. The small signal analysis of the potential for the subsynchronous resonance in a wind farm is correlated with time domain simulations. The IG-1 data are used in all the time domain studies reported in this section. The electromagnetic transient simulations are carried out in two parts: i) steady state and ii) transient state.

3.5.1 Steady State Subsynchronous Resonance

Steady state subsynchronous resonance is primarily related to induction generator effect and torsional interaction. The potential for the SSR in steady state is predicted from the eigenvalue analysis in Table 3.1. The eigenvalue analysis is now reasonably validated with the time domain simulation results. Although no potential for the torsional interaction is observed from the eigenvalue analysis, the possibilities of the induction generator effect are seen to be high at higher level of series compensation. The time domain simulations are thus carried out for the 100 MW, 300 MW and 500 MW at different series compensation levels (K) and compared with the eigenvalue analysis results. Each case study presents simulation results with two distinct series compensation levels.

Figure 3.13 shows steady state electromagnetic torque and PCC voltage of a 100 MW wind farm with 70% and 85% series compensation. As observed from the eigenvalues shown in Table 3.1, the 100 MW wind farm may not experience the SSR due to series

compensation. The time domain simulation depicted in Figure 3.13 (a) shows that the electromagnetic torque is stable in steady state, with both the levels of series compensation. Similarly the PCC voltage also remains stable as shown in Figure 3.13 (b). Thus the time domain simulations validate the small signal analysis.

Figure 3.14 shows the steady state electromagnetic torque and PCC voltage of the 300 MW wind farm operated with 70% and 85% series compensation. With 70% series compensation no SSR oscillation is observed. However, since the critical compensation level is 82.95%, with 85% series compensation induction generator effect SSR oscillation is observed in electromagnetic torque and PCC voltage shown in Figure 3.14 (a) and Figure 3.14 (b), respectively. The SSR oscillation is self-excited and grows gradually. The FFT of the electromagnetic torque shown in Figure 3.14 (c) shows the estimated frequency of 116.3 rad/s, which matches very well the calculated electrical mode damped frequency of 116.45 rad/s. This correlation validates the eigenvalue analysis results in steady state. Similarly the induction generator effect SSR is also observed in the 500 MW wind farm, when connected to 81% series compensation. Since the critical compensation level is 80.64%, 81% series compensation leads to self-excitation in the wind farm, whereas with 70% series compensation no such oscillation is witnessed. The electromagnetic torque and PCC voltage for the two described operating conditions are shown in Figure 3.15 (a) and (b), respectively. The FFT of the electromagnetic torque is shown in Figure 3.15 (c). The estimated frequency, though not shown in Table 3.1, matches with the calculated value.

The successful correlation of the electromagnetic transient simulation results with those of eigenvalue analysis validates the small signal model. However, a detailed validation during transients is presented in the next section.
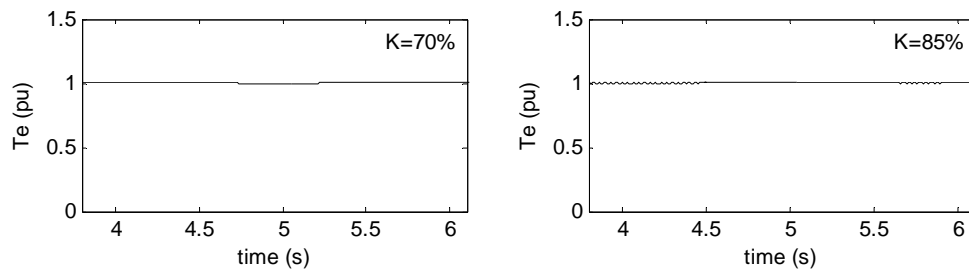
(a) Electromagnetic torque
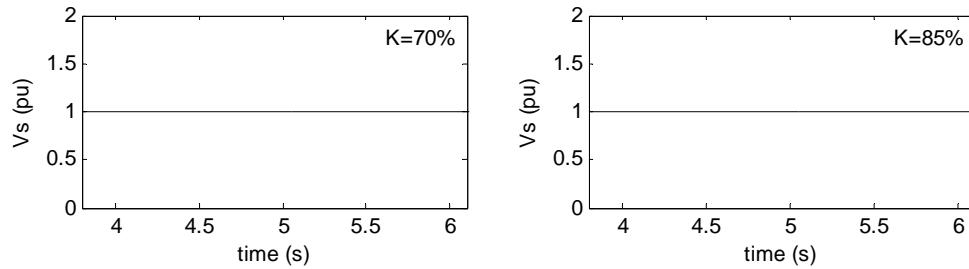
(b) PCC Voltage

Figure 3.13 Steady state performance of a 100 MW wind farm
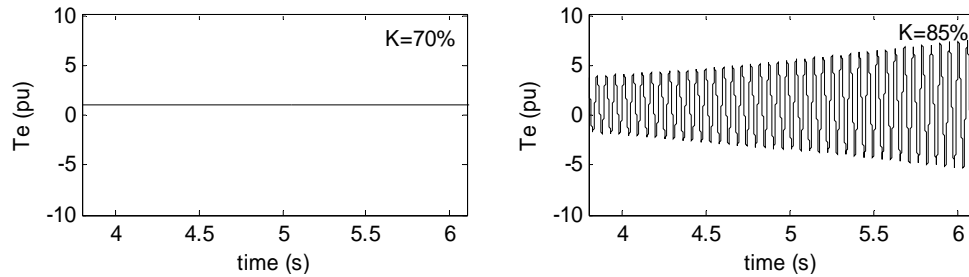
(a) Electromagnetic torque
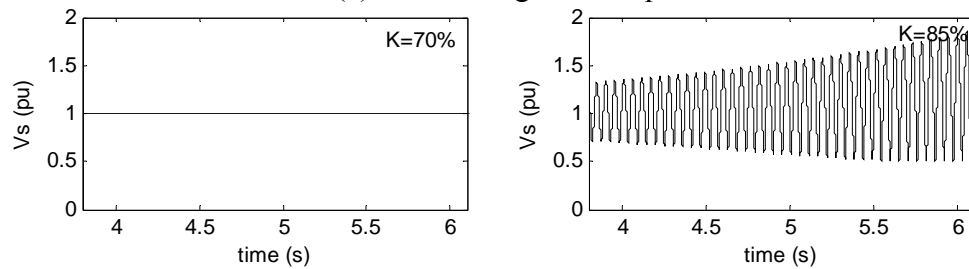
(b) PCC voltage
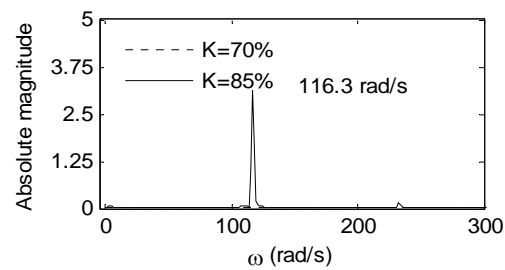
(c) FFT of electromagnetic torque

Figure 3.14 Steady state performance of a 300 MW wind farm

(a) Electromagnetic torque

(b) PCC voltage
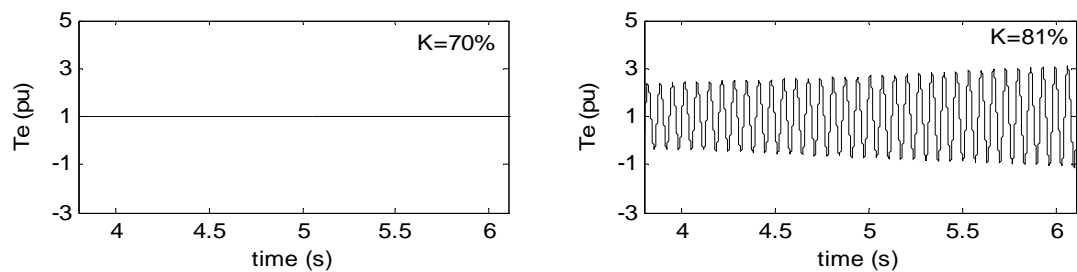
(c) FFT of electromagnetic torque
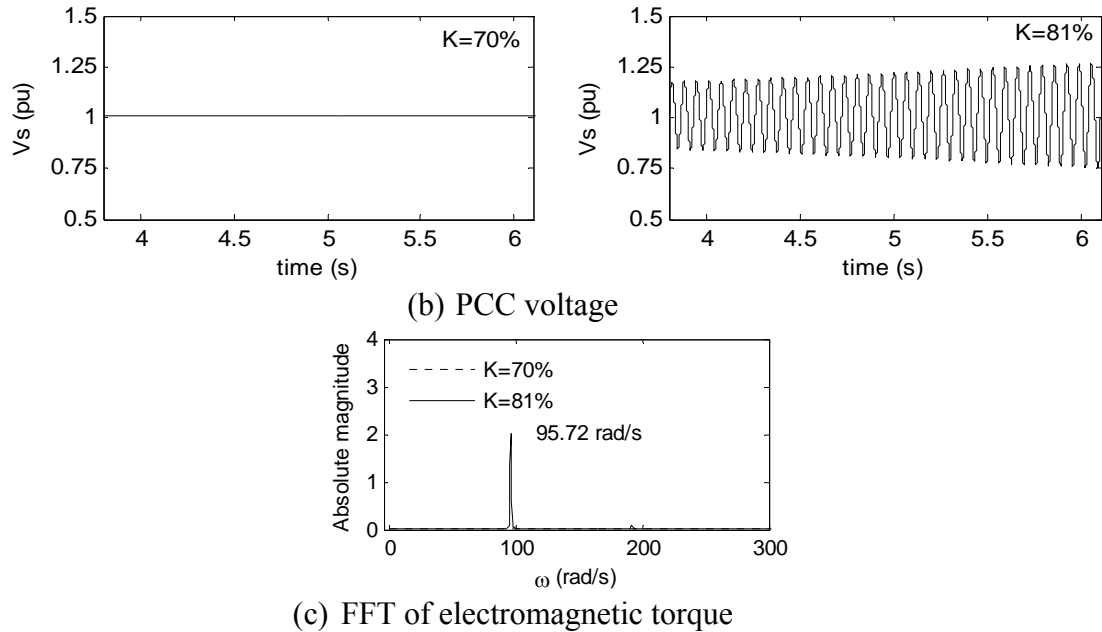
Figure 3.15 Steady state performance of a 500 MW wind farm

3.5.2 Transient Subsynchronous Resonance

A three phase fault of six cycles duration is simulated at Bus-2 (location F_2) of the study system. Figure 3.16 shows the impacts of the fault on a 100 MW wind farm connected to 70% and 85% series compensation levels. Figure 3.16 (a) shows the output power of the wind farm following the fault. As series compensation increases from 70% to 85%, the oscillations in the output power also increase. A similar response is also seen in the electromagnetic torque of the induction generator depicted in Figure 3.16 (b). The oscillation in the electromagnetic torque consists of multiple frequency components. However, the electromagnetic torque is stabilized subsequently.

The response of the shaft torque is shown in Figure 3.16 (c). It shows the low frequency oscillations that are also damped out gradually. Similarly, the generator speed and the PCC voltage following the fault are depicted in Figure 3.16 (d) and Figure 3.16 (e), respectively. It is found that in all cases the oscillations increase with the increase in the level of series compensation. Figure 3.16 (f) shows the voltage across (phase-a) the series capacitor.

To identify the multiple frequency components involved in the electromagnetic torque and shaft torque oscillations, FFT analyses of those waveforms are performed which are illustrated in Figure 3.17. The FFT of the electromagnetic torque shows the frequencies of 205.4 rad/s and 188.5 rad/s, which match with the calculated electrical mode damped frequencies of 206.04 rad/s and 188.59 rad/s, respectively shown in Table 3.1. The electromechanical mode damped frequency is also detected to be 41.25 rad/s, which closely matches with the calculated value of 41.93 rad/s and 41.193 rad/s, respectively for both series compensation levels. The FFT of the shaft torque is shown in Figure 3.17 (b), which shows the torsional mode damped frequency of 3.68 rad/s. It matches very well with the calculated value of 3.57 rad/s shown in Table 3.1.

a) Power output of wind farm

b) Electromagnetic torque

c) Shaft torque

d) Generator speed

e) PCC voltage

f) Capacitor voltage
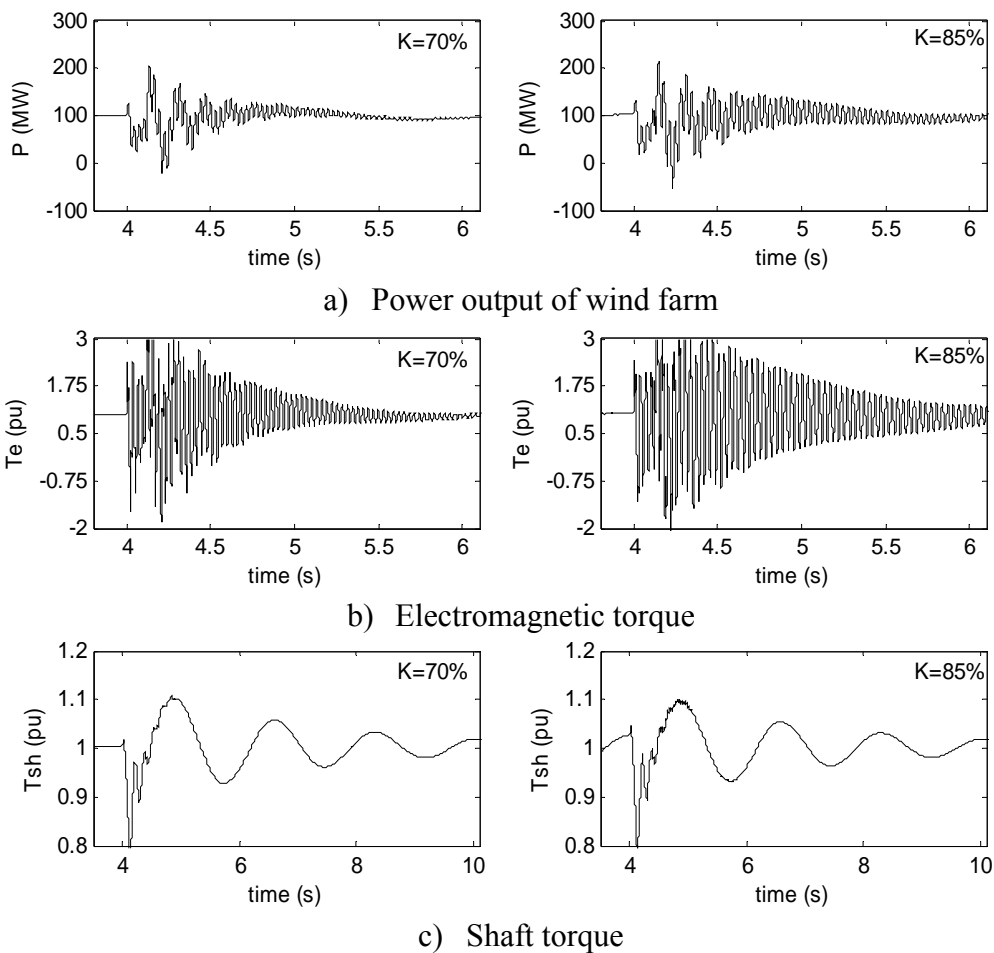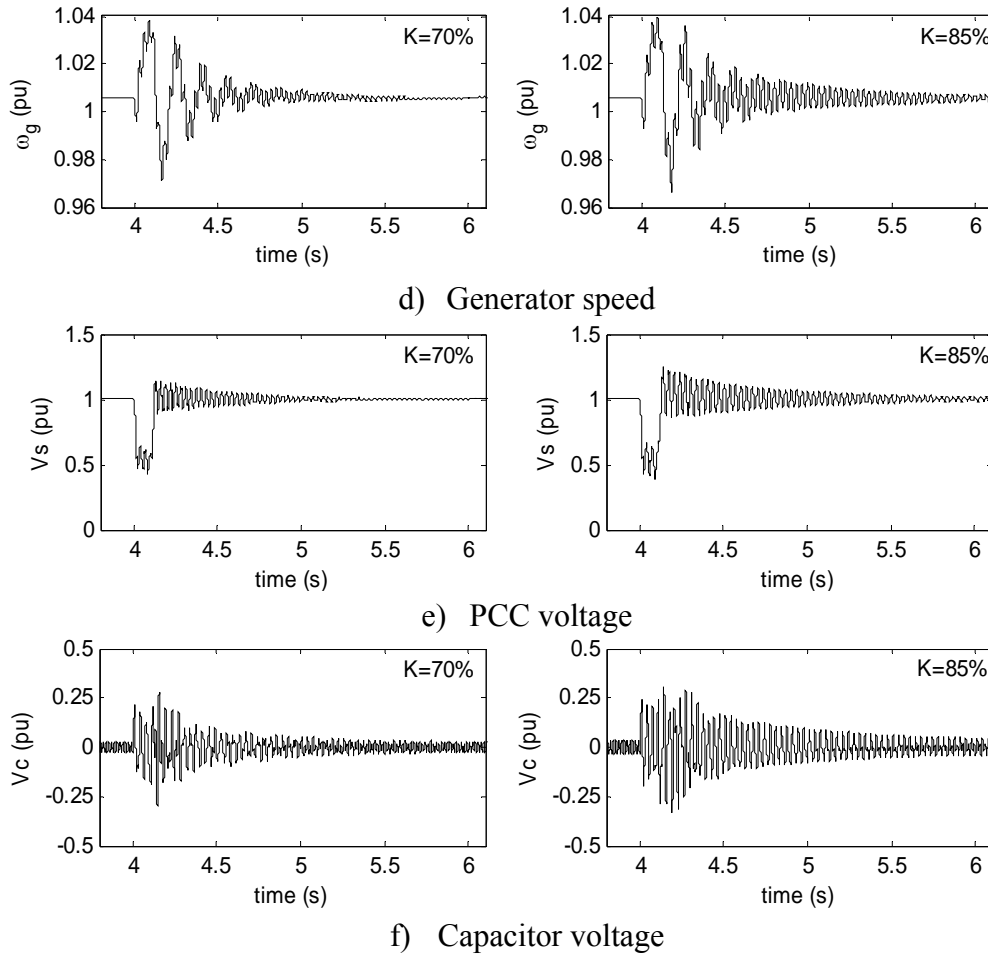
Figure 3.16 Transient SSR in a 100 MW wind farm

(a) FFT of electromagnetic torque   (b) FFT of shaft torque
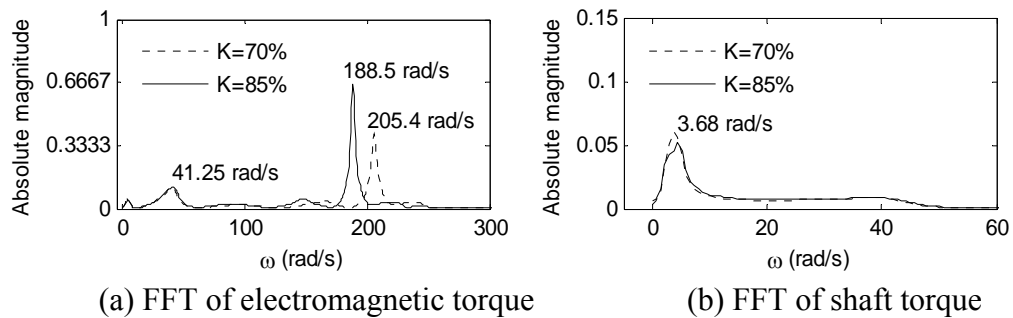
Figure 3.17 FFT of electromagnetic torque and shaft torque of a 100 MW wind farm

A similar fault study is carried out with a 300 MW wind farm connected to 70% and 85% series compensated lines. The performance of the wind farm following the fault is shown in Figure 3.18. Figure 3.18 (a) and (b) show the electromagnetic torque and shaft torque, respectively, following the fault clearance. Since the critical series compensation level is around 82.95% for a 300 MW wind farm, with 85% series compensation the oscillations

in the electromagnetic torque grow after the fault is cleared. The shaft torque also grows and attains very high amplitude due to the electrical mode instability. This is due to the fact that when the electromagnetic torque becomes zero, the accelerating torque grows which causes the high (up-to 18 pu) shaft torque. Figure 3.18 (c), (d), and (e) show the generator speed, PCC voltage, and voltage across the series capacitor. The fault results in a substantial amplification of the voltage across series capacitor. Figure 3.19 (a) and (b) show the FFT analysis of the electromagnetic torque and shaft torque, respectively. The estimated frequencies depicted in Figure 3.19 (a) and (b) match very well with the calculated damped frequencies shown in Table 3.1.

a) Electromagnetic torque

b) Shaft torque

c) Generator speed

d) PCC voltage

e) Capacitor voltage
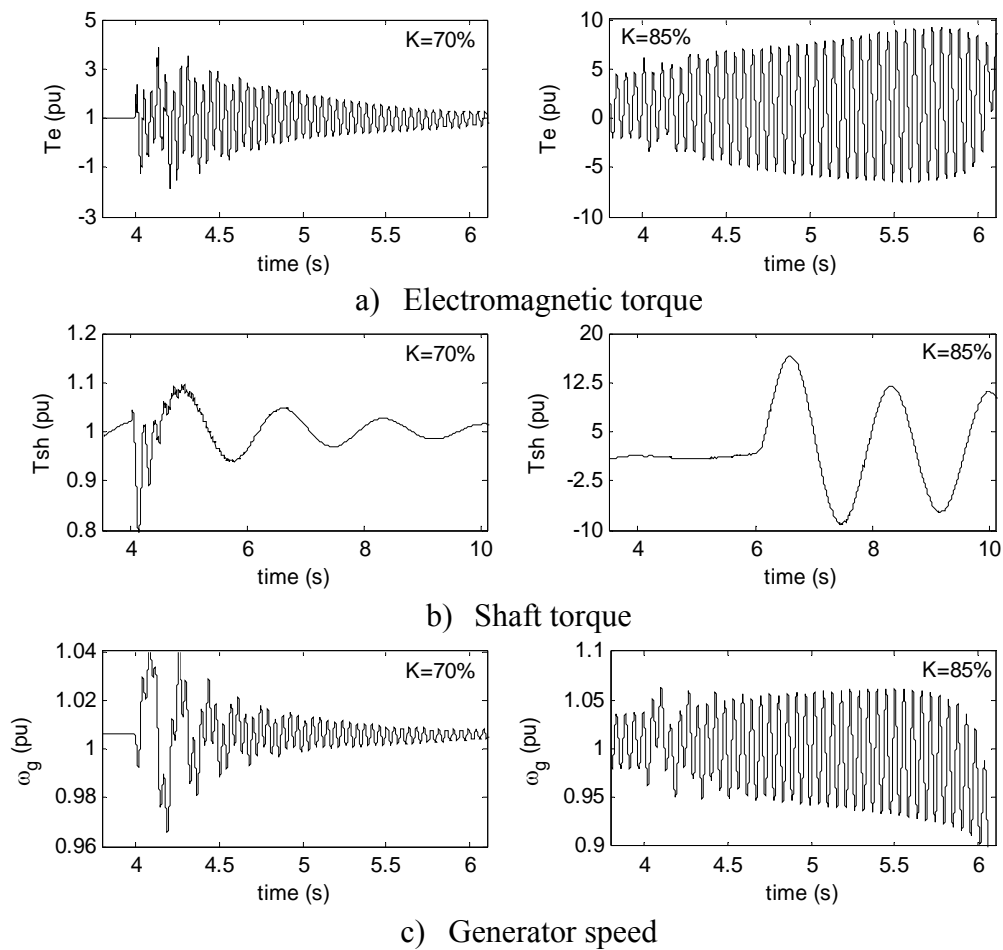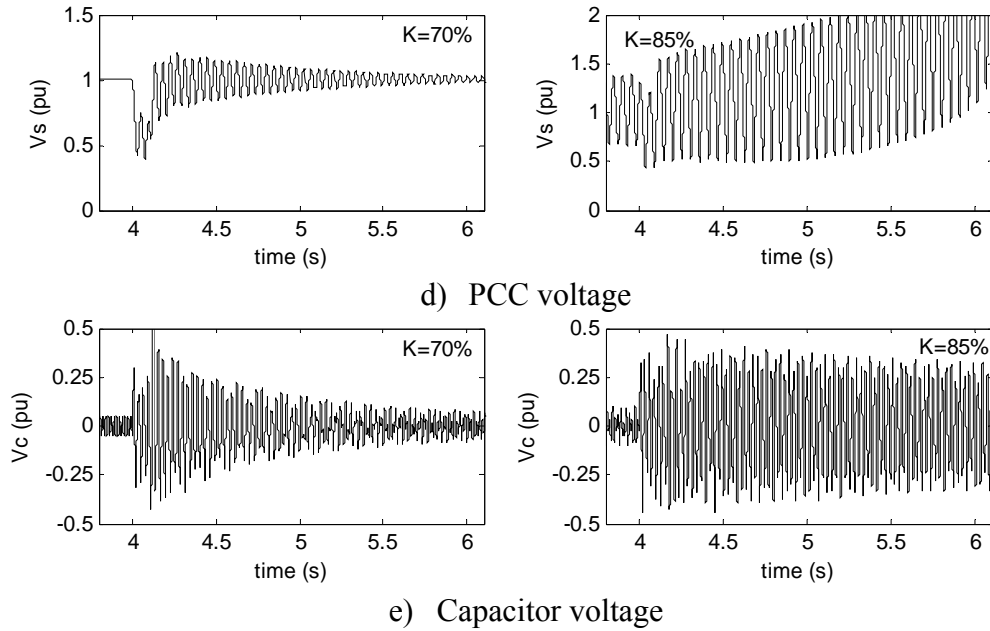
Figure 3.18 Transient SSR in a 300 MW wind farm

(a) FFT of electromagnetic torque (b) FFT of shaft torque
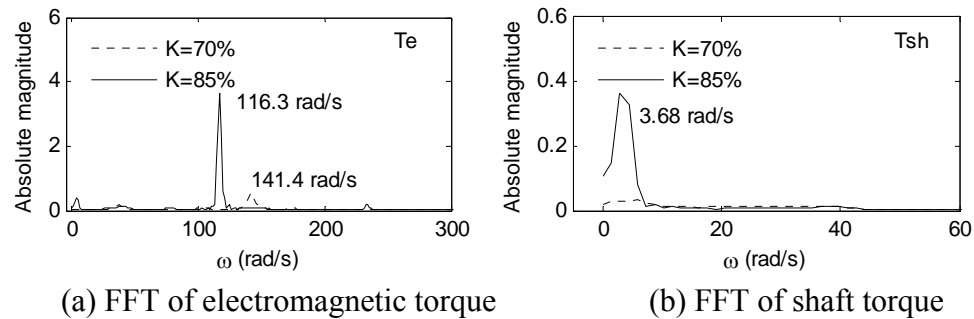
Figure 3.19 : FFT of electromagnetic torque and shaft torque of a 300 MW wind farm

Figure 3.20 shows the response of a 500MW wind farm to a three phase fault at the remote end (location F_2) of the series compensated line. Two series compensation levels considered in this case are 70% and 81%. The electromagnetic torque, shaft torque, generator speed, and PCC voltage are shown in Figure 3.20 (a), (b), (c) and (d), respectively. Since the critical series compensation level is around 80.64%, 81% series compensation causes induction generator effect SSR in the wind farm. The electromagnetic torque grows after the fault is cleared with 81% series compensation. The shaft torque also gets amplified with 81% series compensation level. The large shaft torque may cause cyclic fatigue in the shaft. A detailed analysis of shaft torque rise is discussed later.

The responses of the generator speed and PCC voltage show the oscillations in these parameters grow with 81% series compensation. Figure 3.21 shows the FFT of the electromagnetic torque and shaft torque. It is found that the electromagnetic torque is largely dominated by the electrical mode oscillation, whereas the FFT of the shaft torque shows the dominance of the torsional mode. The estimated frequencies of the oscillations match very well with the calculated value of damped frequencies given in Table 3.1. The successful correlation of the eigenvalue results and transient simulation results validate the small signal analysis to predict the SSR in wind farms.

(a) Electromagnetic torque

(b) Shaft torque

(c) Generator speed

(d) PCC voltage
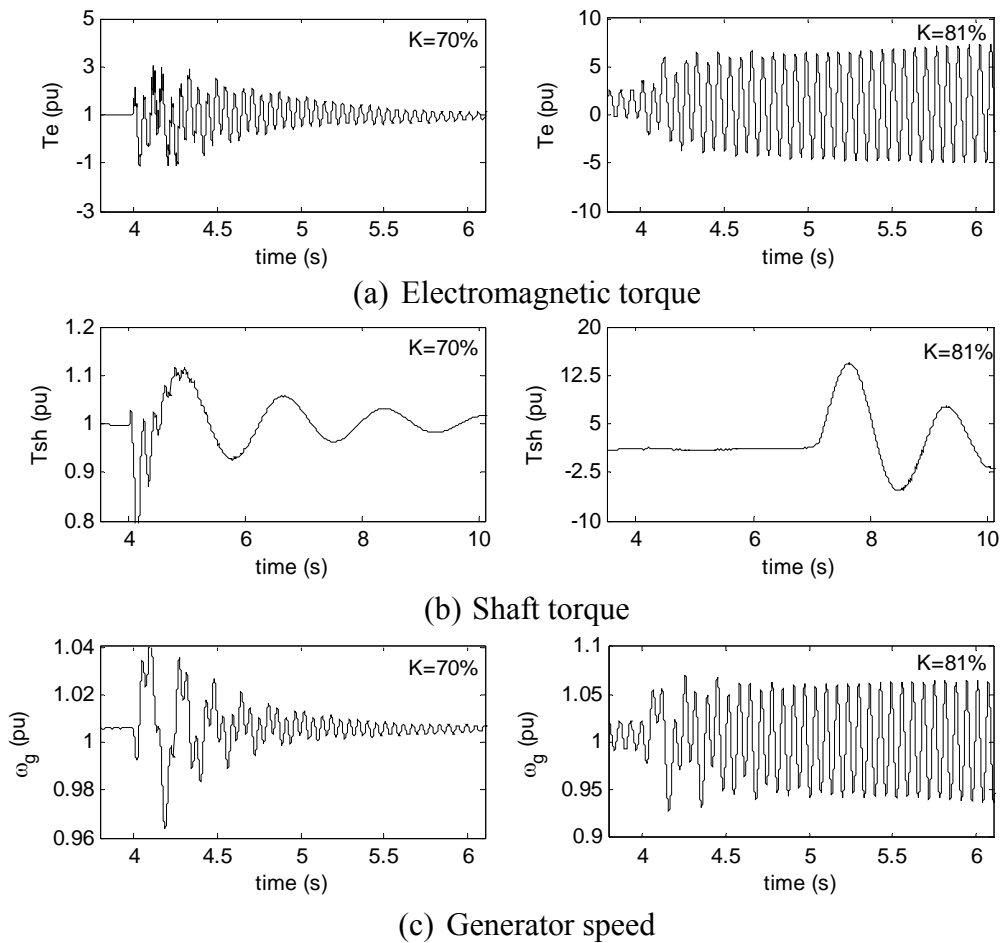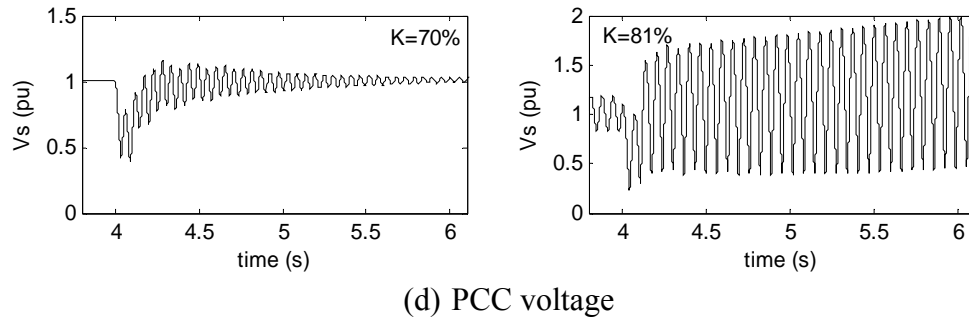
Figure 3.20 Transient SSR in a 400 MW wind farm

(a) FFT of Electromagnetic torque   (b) FFT of shaft torque
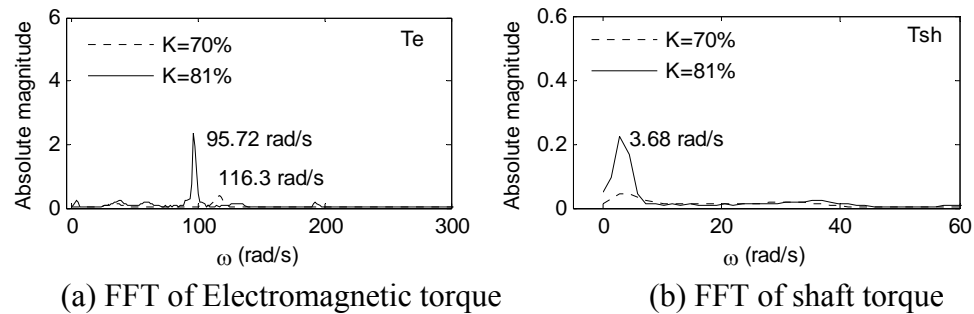
Figure 3.21 FFT of electromagnetic torque and shaft torque of a 500 MW wind farm

3.6 IMPACT OF FAULT LOCATION

The optimum location of a single capacitor bank, in terms of effectiveness of the compensation is at the center of the transmission line [42]. Most of the series capacitor applications in the USA have two capacitors placed at the both ends of a transmission line. Therefore, a study on the impact of fault location is chosen for a configuration where the series capacitor is split into two banks and each one is placed at either end of the transmission line. The modified configuration of the study system is shown in Figure 3.22, where an additional bus (Bus-3) is introduced. Three phase faults at three locations (F_1, F_2 and F_3) are simulated with PSCAD/EMTDC and the results are discussed here. The fault starts at t=4s and is cleared after 100ms.
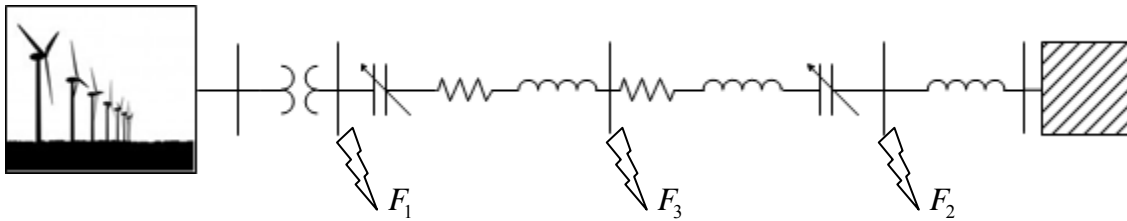
Figure 3.22 Modified study system

The time domain simulation of the modified system is carried with 50% series compensation, which is a realistic value of series compensation. The impact of the fault at different locations on the electromagnetic torque, shaft torque, and PCC voltage are discussed. Figure 3.23 shows the electromagnetic torque following the fault for 100 MW, 300 MW and 500 MW wind farms. The electromagnetic torque of a 100 MW wind farm shown in Figure 3.23 (a) illustrates the severity of the fault at the terminal (location F_1) in comparison to the fault at mid line (location F_3) and remote end (location F_2) of the line. The large electromagnetic torque is seen for a fault at the location F_1, which reaches up-to 14 pu. Although the fault at location F_3 does not cause similar increase, the peak overshoot of the electromagnetic torque attains a value of 4.5 pu. Fault at location F_2 results in much lower peak electromagnetic torque of around 3 pu. Similar observation is also found with 300 MW and 500 MW wind farm as shown in Figure 3.23 (b) and (c), respectively. It is seen that as the size of the wind farm increases, the impacts of faults at different locations get reduced. However, the terminal faults in all cases are found to cause significantly large electromagnetic torque. Hence, it is concluded that the terminal fault has a very severe impact on the electromagnetic torque of the induction generator.

(a) 100 MW wind farm

(b) 300 MW wind farm
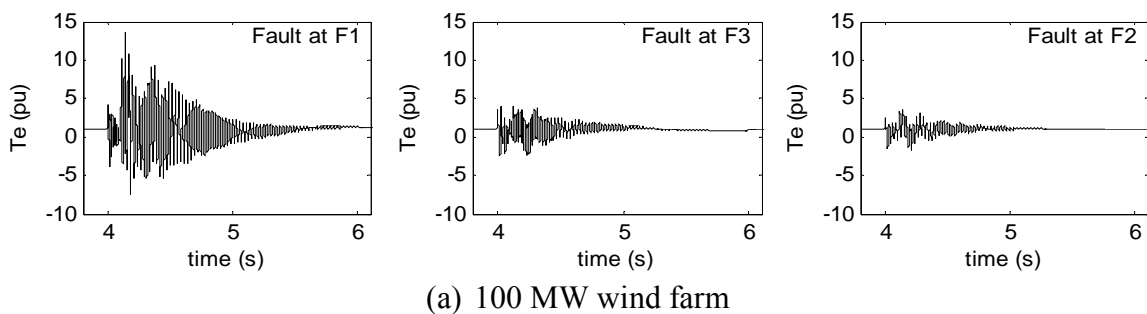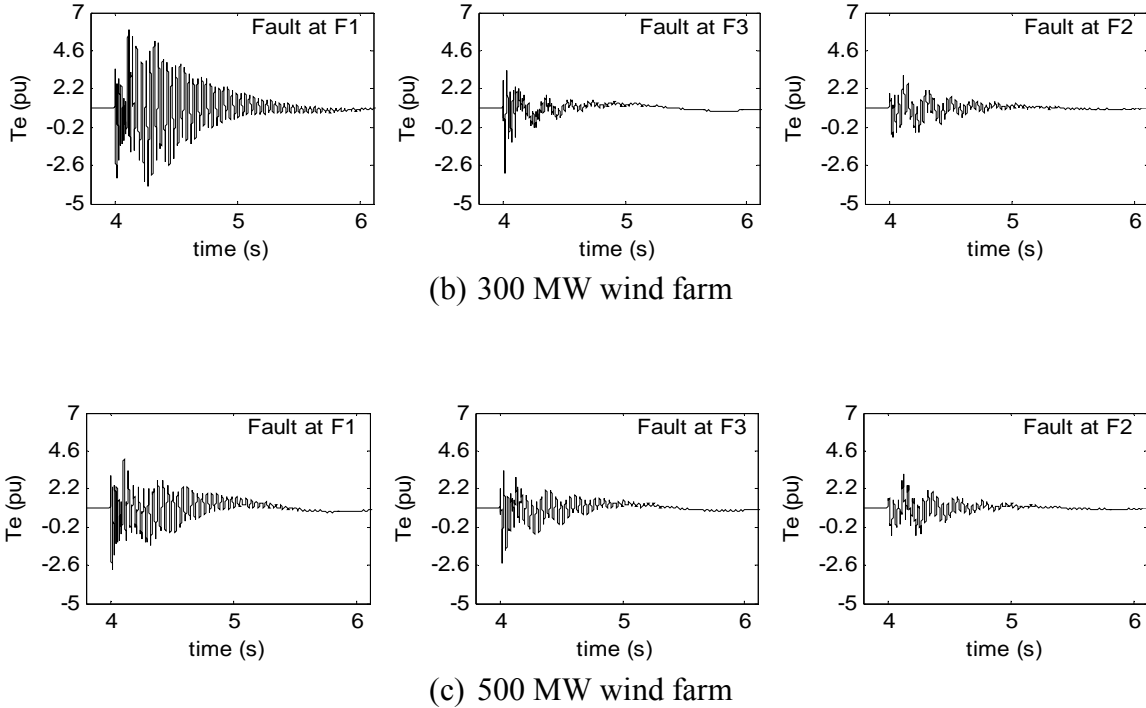
(c) 500 MW wind farm

Figure 3.23 Impact of fault location on electromagnetic torque

Figure 3.24 shows the impacts of fault locations on the shaft torque of the wind turbine generator. In the case of a 100 MW wind farm, the fault at location F_1 causes a large overshoot in the shaft torque following the clearance of the fault. This is shown in Figure 3.24 (a). The peak shaft torque reaches upto 1.8 pu which is not favorable for a rotating machine. When the fault location moves away from the wind farm, the impact is reduced. This can be seen from the reduced overshoot in the shaft torque. The fault at location F_2 shows the least overshoot. Figure 3.24 (b) shows the shaft torque disturbance of a 300 MW wind farm following the fault at three locations. In this case, faults at F_1 and F_3 exhibit similar shaft torque increase where the peak shaft torque increases upto 1.25 pu. It is understood that this much rise may not cause any damage to the shaft [54]. The impact of the fault at F_2 is quite similar to that of a 100 MW case study. The impacts of the fault location on the shaft torque of a 500 MW wind farm are shown in Figure 3.24 (c). The fault at F_1 shows a peak overshoot in the shaft torque that reaches upto 1.35 pu. However, as the fault location moves away from the wind farm, the peak overshoot is reduced subsequently.

(a) 100 MW wind farm

(b) 300 MW wind farm

(c) 500 MW wind farm
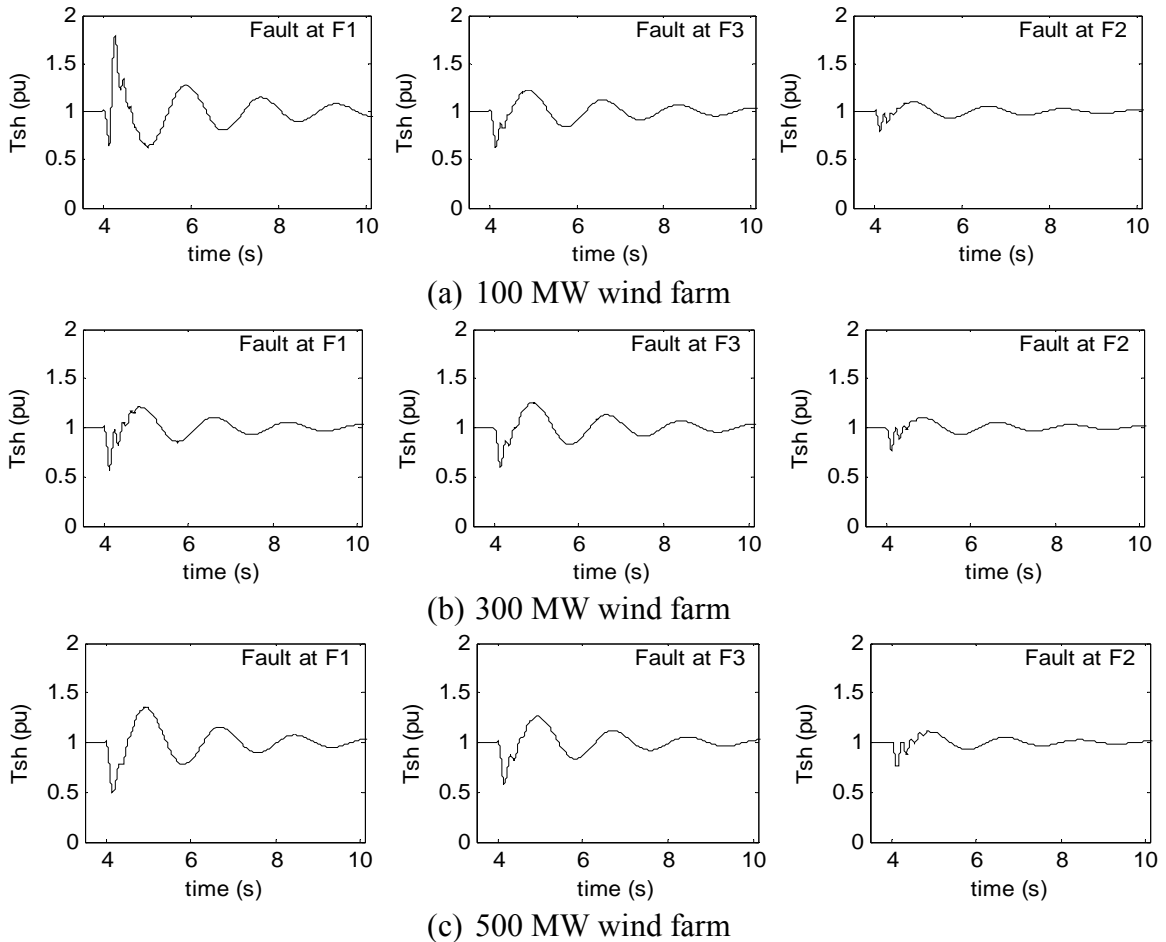
Figure 3.24 Impact of fault location on shaft torque

The behavior of PCC voltage of an induction generator based wind farm is very important during the system disturbances. In the absence of external excitation the induction generators draw the reactive power based on the voltage at the terminal. Hence, disturbance in the voltage causes fluctuation in the reactive power demand of the wind turbine generator, which affects its performance. Figure 3.25 shows the PCC voltage for faults at the three different locations. In the case of a 100 MW wind farm, the fault nearest to the wind farm (i.e. location F_1) causes the voltage rise upto 2.5 pu after the fault clearance which is shown in Figure 3.25 (a). This may force the wind turbine to trip. However, the fault at location F_2 and F_3 does not cause such rise in the PCC voltage. Figure 3.25 (b) and Figure 3.25 (c) show the PCC voltage for 300 MW and 500 MW wind farm, respectively. As the wind farm size increases, the influence of the terminal fault is reduced. It can be seen that in the case of a 300 MW wind farm, the fault

at F_1 causes a peak overshoot of 1.35pu, but for a 500 MW wind farm, it is reduced to 1.1pu. From this analysis it is seen that the series capacitor has an adverse impact on the voltage at PCC even at a realistic level of series compensation.

To get more insight of the impact of fault nearby the wind farm, a detailed analysis is carried out with an equivalent circuit model of the study system, which is reported in the next section.

(a) 100 MW wind farm

(b) 300 MW wind farm

(c) 500 MW wind farm
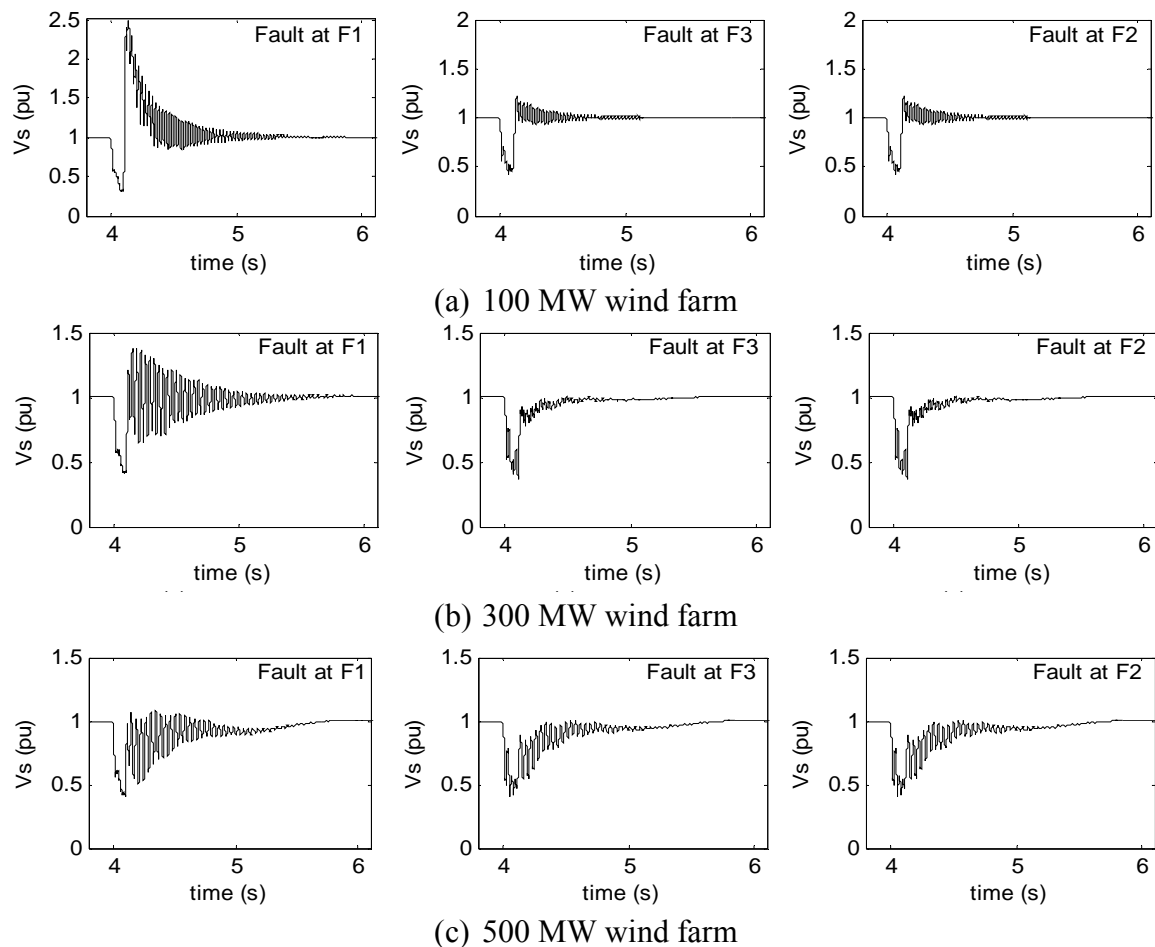
Figure 3.25 Impact of fault location on PCC voltage

3.7 HIGH SHAFT TORQUE

High shaft torque occurs during or after the clearance of the fault in a series compensated transmission line. During the fault a large amount of energy is stored in the series capacitor, which is discharged through the electrical generator after the fault is cleared. This energy is discharged in the form of current having a frequency that is a compliment

to the electrical mode damped frequency that causes induction generator effect SSR. Under such circumstances the shaft torque is quite large and the oscillatory shaft torque may reach a damaging level within 100ms. Each occurrence of this high amplitude transient torques can result in reduction of the shaft life due to the cyclic fatigue. Fatigue is defined as the process of progressive localized permanent structural change occurring in a material subjected to conditions which produce fluctuating stresses and strains at some points which may culminate in cracks or complete fracture after a sufficient number of oscillations. Once initiated, the cracks may propagate to sizes that may result in irreversible shaft damage or eventual breakage.

3.7.1   Equivalent Circuit Analysis

To study the impact of terminal fault on the wind farm, the equivalent circuit theory is applied and is described in detail in Chapter 2. A realistic level of series compensation (50%) is chosen for this case study. The equivalent circuit of the study system is shown in Figure 3.26
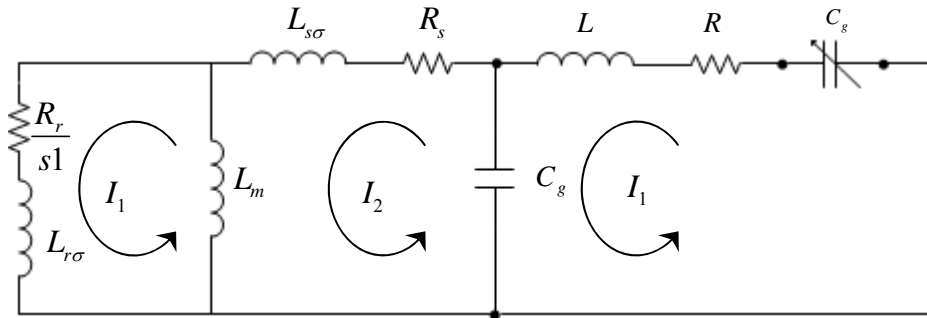
Figure 3.26 Equivalent circuit of study system with single-cage induction generator

The characteristic polynomial of the impedance matrix of the closed loop system is obtained by calculating the determinant as given below.

$$\det|Z(\rho)| = P_0 s^5 + P_1 s^4 + P_2 s^3 + P_3 s^2 + P_4 s + P_5 \tag{3.30}$$

Out of the five roots of the above polynomial, one complex conjugate pair is very sensitive to the operating slip of the induction generator. Thus, keeping all other system parameters constant, the slip of the generator is varied over a wide range and the root loci are plotted in Figure 3.27. As the slip increases, the roots move to the right, crossing the

imaginary axis and subsequently splitting into two real roots. Further increase in the slip causes them to rejoin into a complex pair, which starts traversing to the left crossing the imaginary axis and becoming stable. The points where the roots cross the imaginary axis are called the resonant points. The lower slip crossover point relates to the lower resonant speed (LRS) whereas the upper slip crossover point corresponds to the upper resonance speed (URS). From Figure 3.27 it is seen that the system is stable both above the upper resonant speed and below the lower resonant speed. However, if the speed of the generator falls between these two speeds anytime during its operation the induction generator becomes unstable and the speed continues to decrease until it is stabilized at the lower resonant speed. For the aggregated wind farm study system, the loci of the slip-sensitive roots are plotted in Figure 3.27 for different size of wind farms. The slip values are varied from +0.01 to -0.5.
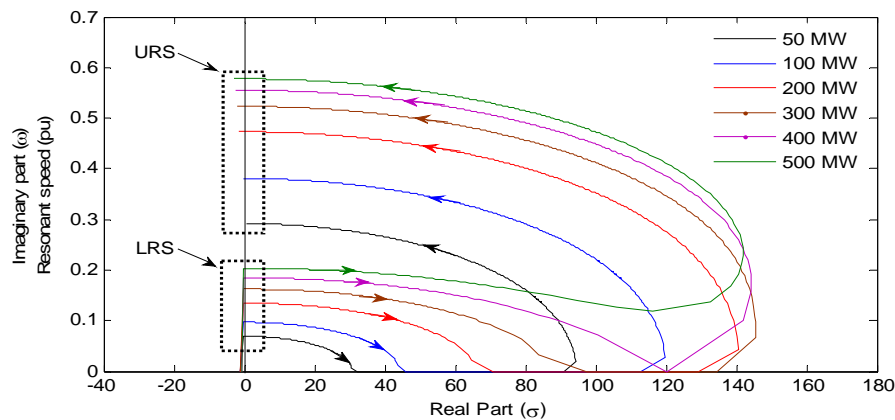
Figure 3.27 Loci of critical root with varying slip of induction generator

Table 3.4 depicts the upper resonant and the lower resonant speeds of the wind farms for varying levels of series compensation and sizes of wind farm. It is observed that as the size of the wind farm and series compensation increase, the upper and lower resonant speeds also increase. It is noted that the increase in the upper resonant speed reduces the stability margin. Hence, if the speed drops below the upper resonant speed due to any transient disturbance, it cannot recover after the clearance of the fault.

Table 3.4 Resonant speed in per unit

WF Size (MW)	Lower resonant speed (LRS)			Upper resonant speed (URS)		
	K=30%	K=50%	K=70%	K=30%	K=50%	K=70%
50	0.053	0.069	0.081	0.226	0.291	0.344
100	0.075	0.096	0.114	0.295	0.380	0.450
200	0.104	0.134	0.158	0.367	0.473	0.558
300	0.126	0.162	0.190	0.406	0.523	0.618
400	0.144	0.184	0.215	0.431	0.559	0.656
500	0.159	0.202	0.236	0.450	0.577	0.682

3.7.2   Electromagnetic Transient Simulation

Electromagnetic transient simulations are carried out at different operating conditions to validate the equivalent circuit theory analysis. The main purpose of this study is to evaluate the impact of the fault at the terminal of a wind farm. Figure 3.28 illustrates the effect of the terminal fault (location F_1) on a 50 MW wind farm with 50% series compensation, compared with the response to a similar fault at location F_2. The speed following the fault clearance is shown in Figure 3.28 (a). When the fault occurs in the network (either location), the speed of the wind turbine generator undergoes an oscillatory behavior. For a fault at location F_2, the post fault stabilization does not appear to be a concern. However, for a fault at location F_1 the speed of the wind turbine generator falls rapidly following the fault clearance. The fall in the speed continues and it enters into the unstable band of speeds defined by the lower and upper resonant speeds. In this case the upper resonant speed is 0.226pu, which is obtained from the equivalent circuit theory. Thus, when the speed falls below this value, it fails to return to normal operating condition and results in the instability of the wind turbines. The instability in the electromagnetic torque is shown in Figure 3.28 (b), which shows that the peak electromagnetic torque may reache upto 250 pu. At the same time, the fault at the remote end only causes a peak electromagnetic torque of 4 pu which is stabilized gradually within 1.5s of the fault clearance. Severe rise in shaft torque (up to 26 pu) in the shaft torque is now shown in Figure 3.28 (c) for a fault at F_1, whereas the fault at F_2 only causes 1.15 pu overshoot which is not a concern. The high shaft torque witnessed shows

the potential for the cyclic fatigue in the shaft. Recurring occurrence of such large shaft torque would cause serious damage to the shaft and gearbox of the wind turbine.

(a) Generator speed

(b) Electromagnetic torque

(c) Shaft torque
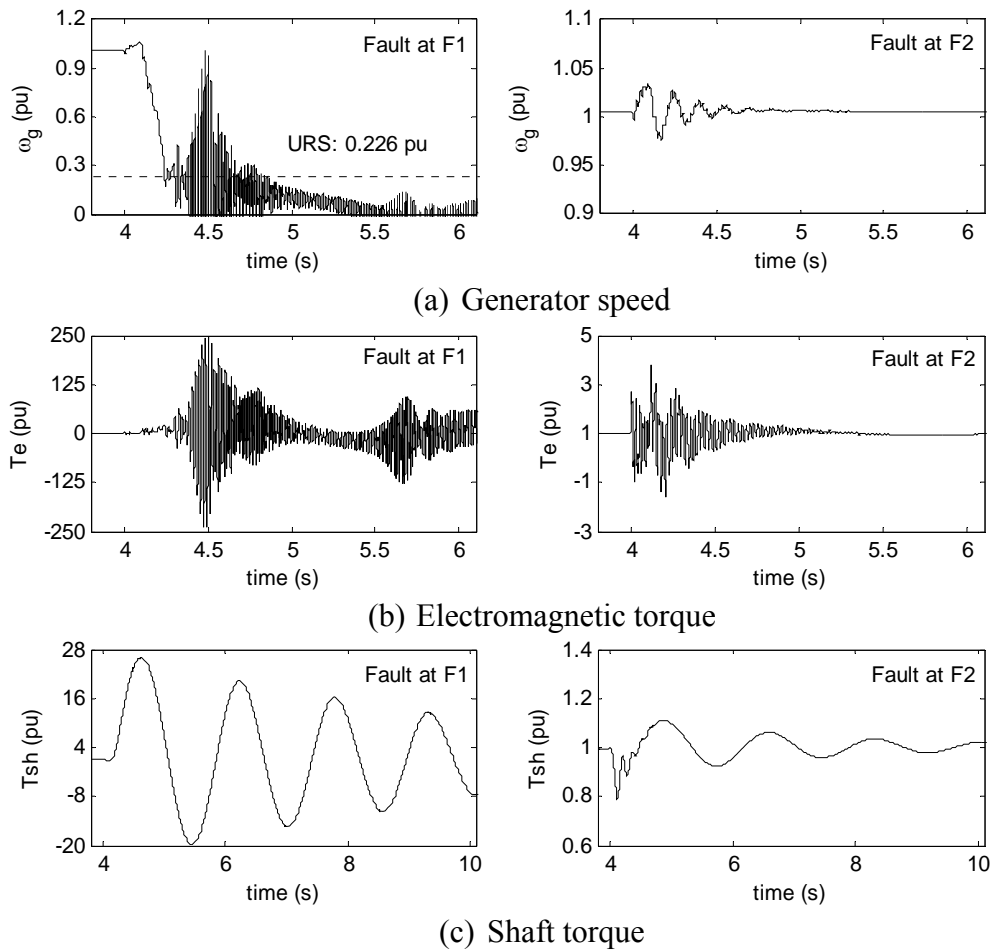
Figure 3.28 Impact of terminal fault on 50 MW wind farm

Similar study is now extended to a 300MW wind farm connected to a 50% series compensated line. In this case no such instability is found. This is due to the fact that the speed following the fault clearance does not fall below the upper resonant speed limit of 0.523 pu which is shown in Figure 3.29 (a). The electromagnetic torque following the faults at two locations is shown in Figure 3.29 (b). In case of fault at location F_1, the peak electromagnetic torque reaches up-to 5 pu, which is restricted to 3 pu when the fault occurs at location F_2. The corresponding shaft torques are shown in Figure 3.29 (c). The peak shaft torque due to fault at F_1 reaches up-to 1.25pu, whereas it reaches only upto 1.12pu for the remote end fault.

(a) Generator speed

(b) Electromagnetic torque

(c) Shaft torque
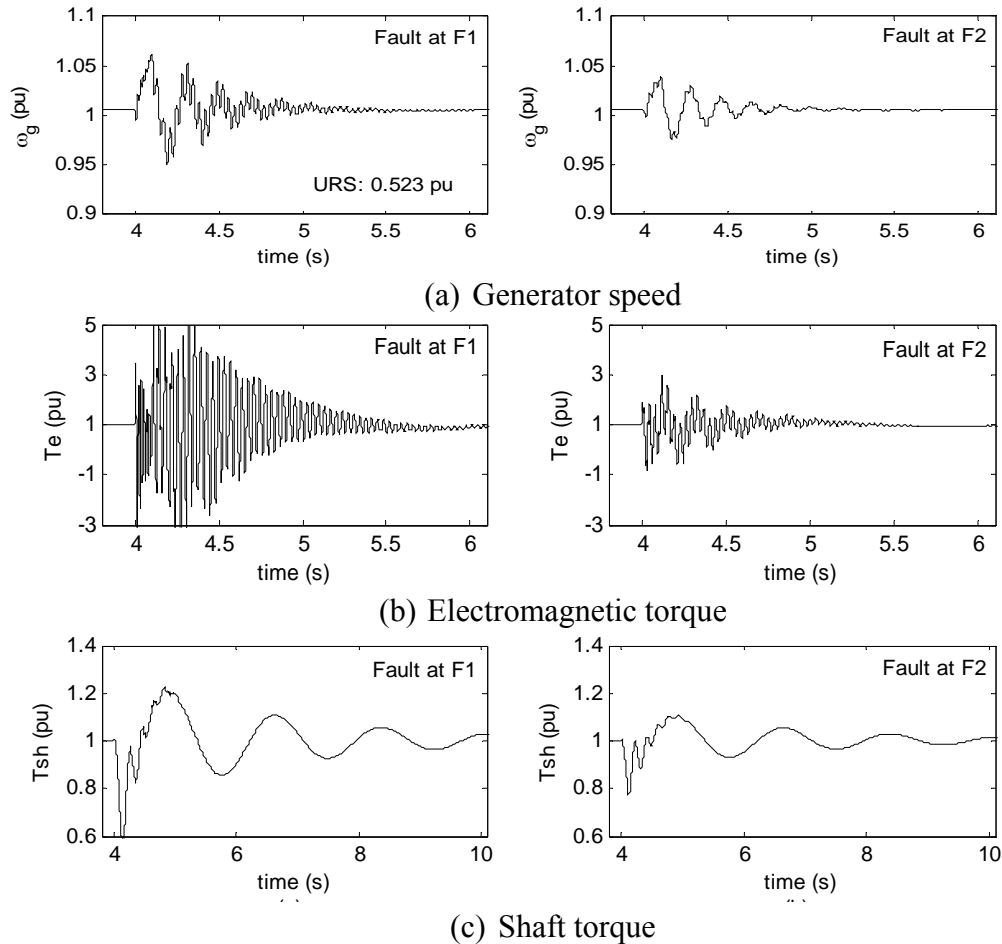
Figure 3.29 Impact of terminal fault on 300 MW wind farm

Most of the series capacitors are protected by metral oxide varistor (MOV) conducting during fault conditions to limit over voltage produced across series capacitor. The current that MOV conducts depends upon voltage drop across the capacitor which varies with fault level, location and fault resistance. A similar MOV is now connected across the series capacitor and a terminal fault is created. It is found that large voltage across the series capacitor is successfully limited to threshold value of 2 pu. It is noted that MOV works during the fault duration only and is unable to protect the wind farm from SSR oscillation due to induction generator effect.

3.8 CONCLUSIONS

A detailed analysis of the potential for the subsynchronous resonance in single-cage induction generator based wind farms connected to series compensated lines is presented

in this chapter. A comprehensive system state space model is developed for the above study system, which is the modified IEEE First Benchmark System. The eigenvalue analysis is utilized to predict the potential of SSR for a wide range of wind farm sizes, wind farm power outputs and series compensation levels. The validation is achieved through the correlation of the calculated damped frequencies with the modal frequencies obtained from the time domain simulation with PSCAD/EMTDC software. The critical levels of series compensation that could cause steady state and transient state SSR are identified. Studies with several commercially available induction generator data are also presented. An equivalent circuit theory analysis is performed to calculate the upper and lower resonant speeds of the aggregated induction generator model, which is again reasonably validated with the PSCAD/EMTDC simulations. A part of this chapter is published in [131]. The conclusions drawn from this chapter are as follows:

(a) SSR due to induction generator effect is more likely for a wind farm connected to a radial series compensated line, although this may only occur at rather high levels of series compensation.

(b) No torsional interaction between the wind turbine generators and the series compensated line is anticipated.

(c) A three-phase fault at the terminal of the wind farm may cause unacceptable large shaft torque even at a realistic level of series compensation (50%). This depends on the variation in the speed of the induction machines during the fault recovery process. If the speed falls below the upper resonant speed, the induction generator speed cannot be restored even after the clearance of the fault, and the shaft torque attains very high values that could be potentially dangerous.

The above studies indicate that single-cage induction generator based wind farms connected to series compensated lines may be subject to shaft damage for faults at wind farm terminals even at realistic levels of series compensation. Therefore, when such wind farms are contemplated to be connected to a series compensated transmission line, a thorough investigation should be performed during the planning period to detect any potential of SSR. If SSR problems are identified, suitable preventive measures may be undertaken.

Chapter 4

SUBSYNCHRONOUS RESONANCE ANALYSIS OF DOUBLE-CAGE INDUCTION GENERATOR BASED WIND FARMS

4.1 INTRODUCTION

This chapter presents the analysis of subsynchronous resonance in a double-cage induction generator based wind farm connected to a series compensated transmission line. The subsynchronous resonance study in this chapter is carried out through small signal analysis followed by a detailed time domain simulation with PSCAD/EMTDC. Under the small signal analysis, linearized state space model of each sub-system is developed and system eigenvalues are calculated at several quiescent points. The eigenvalue analysis is carried out primarily to predict the potential for SSR in wind farms which is reasonably validated through the time domain simulations. The investigation of SSR includes the impact of variation in the size of wind farm, power output and percent series compensation. Participation factor analysis followed by sensitivity study is also done to quantify the influence of various system parameters on the subsynchronous modes. The location of the fault in a series compensated network plays a critical role in large increase in the wind turbine shaft torque. The transient torque analysis is similar to the study conducted with the single-cage induction generator based wind farm, reported in Chapter 3. Further, to examine the influence of series capacitor location on shaft torque, the series capacitor bank is split into two banks and each bank is inserted at both end of the transmission line. Then, symmetrical faults at different locations are then simulated. An equivalent circuit analysis described in Chapter 2 is used that predicts the conditions for large shaft torque in wind turbines following balanced fault at the terminal of the wind farm. The equivalent circuit analysis results are reasonably validated with the time domain simulations carried out with PSCAD/EMTDC.

Different commercially available double-cage induction generators are used in this chapter to make the SSR analysis more realistic.

4.2   STUDY SYSTEM DESCRIPTION

The study system shown in Figure 4.1 is the modified IEEE First Benchmark System proposed for the study of subsynchronous resonance [44]. The synchronous generator is replaced with an aggregated wind farm employing large number of double-cage induction generators, each of 2.3 MW. It is assumed that all wind turbines and generators have identical characteristics over all range of operating conditions. The size of wind farm varies between 100 MW and 500 MW, whereas the series compensation varies from 10% to 90%. In order to simplify system modeling, wind farm collector cable impacts are neglected.
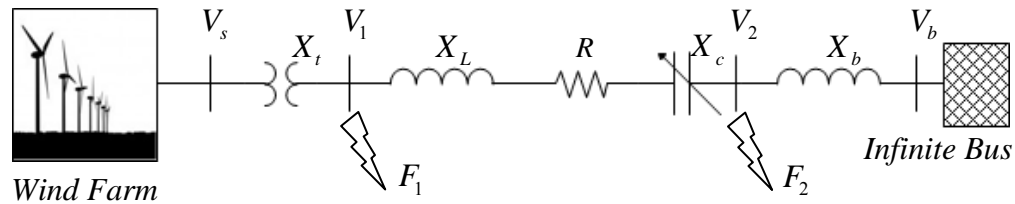
Figure 4.1 Study system

4.3   STUDY SYSTEM MODELING

For the modeling purpose, the study system shown in Figure 4.1 is split into three sub-systems: i) drive train, ii) induction generator, and iii) series compensated transmission line. The detailed modeling of each sub-system is already presented in Chapter 2. The differential equations of each sub-system are reproduced here briefly.

4.3.1   Drive Train System

A two-mass drive train system is considered to represent the drive train of the wind turbine. In a two-mass drive train system, one mass represents the aggregated dynamics of the rotor blades and the hub. The second mass characterizes the dynamics of the induction generator rotor. During the analytical modeling, all parameters in the low-speed

shaft side are transformed into the high-speed shaft side of the wind turbine. The dynamic equations of the drive train system are written as:

$$\frac{d}{dt}\omega_t = T_w - K_{tg}\delta_{tg} - D_{tg}\left(\omega_t - \omega_g\right) \tag{4.1}$$

$$\frac{d}{dt}\delta_{tg} = \omega_t - \omega_g \tag{4.2}$$

$$\frac{d}{dt}\omega_g = K_{tg}\delta_{tg} + D_{tg}\left(\omega_t - \omega_g\right) - T_g \tag{4.3}$$

4.3.2   Induction Generator

In this study the double-cage induction generator is modeled as a voltage source behind the transient reactance. The detailed derivation of the proposed model is already discussed in Chapter 2. The differential equations of the double-cage induction generator are:

$$\frac{1}{\omega_s}X_0\frac{d}{dt}I_{ds} + \frac{1}{\omega_s}\frac{d}{dt}E_{q1} = -R_sI_{ds} + X_0I_{qs} - E_{d1} - V_{ds} \tag{4.4}$$

$$\frac{1}{\omega_s}X_0\frac{d}{dt}I_{qs} - \frac{1}{\omega_s}\frac{d}{dt}E_{d1} = -R_sI_{qs} - X_0I_{ds} - E_{q1} - V_{qs} \tag{4.5}$$

$$\frac{d}{dt}E_{d1} = -\frac{1}{T_{01}}\left(X_{r2}E_{d1} - \left(X_mX_{r2\sigma}\right)E_{d2} + \frac{\left(X_mX_{r2\sigma}\right)^2}{X_r}I_{qs}\right) + s\omega_sE_{q1} \tag{4.6}$$

$$\frac{d}{dt}E_{q1} = -\frac{1}{T_{01}}\left(X_{r2}E_{q1} - \left(X_mX_{r2\sigma}\right)E_{q2} - \frac{\left(X_mX_{r2\sigma}\right)^2}{X_r}I_{ds}\right) - s\omega_sE_{d1} \tag{4.7}$$

$$\frac{d}{dt}E_{d2} = -\frac{1}{T_{02}}\left(-\frac{X_{12}^2}{X_mX_{r2\sigma}}E_{d1} + X_{12}E_{d2}\right) + s\omega_sE_{q2} \tag{4.8}$$

$$\frac{d}{dt}E_{q2} = -\frac{1}{T_{02}}\left(-\frac{X_{12}^2}{X_mX_{r2\sigma}}E_{q1} + X_{12}E_{q2}\right) - s\omega_sE_{d2} \tag{4.9}$$

4.3.3 Network

The differential equations of the network are presented below, which include the dynamics of the shunt capacitor and series compensated transmission line, including the series capacitor.

$$C_g \frac{d}{dt} V_{ds} = I_{ds} - I_d + \omega_s C_g V_{qs} \tag{4.10}$$

$$C_g \frac{d}{dt} V_{qs} = I_{qs} - I_q - \omega_s C_g V_{ds} \tag{4.11}$$

$$L \frac{d}{dt} I_d = V_{ds} - R I_d + \omega_s L I_q - V_{cd} - V_{bd} \tag{4.12}$$

$$L \frac{d}{dt} I_q = V_{qs} - R I_q - \omega_s L I_d - V_{cq} - V_{bq} \tag{4.13}$$

$$C \frac{d}{dt} V_{cd} = I_d + \omega_s C V_{cq} \tag{4.14}$$

$$C \frac{d}{dt} V_{cq} = I_q - \omega_s C V_{cd} \tag{4.15}$$

All state variables are defined in Chapter 2.

4.3.4 Complete System

The differential equations presented in (4.1)-(4.15) are non-linear. Thus, to develop a linear state space model of the complete system, all equations are linearized and then interconnected. The state space model of each sub-system is arranged below.

$$\dot{x}_{WT} = [A_{TT}] x_{WT} + [A_{TG}] x_G + [B_T] u_{WT} \tag{4.16}$$

$$\dot{x}_G = [A_{GT}] x_{WT} + [A_{GG}] x_G + [A_{GN}] x_N \tag{4.17}$$

$$\dot{x}_N = [A_{NG}] x_G + [A_{NN}] x_N + [B_N] u_N \tag{4.18}$$

Combining (4.16)-(4.18), the state space model of the study system is written as:

$$\dot{x}_{sys} = [A_{sys}] x_{sys} + [B_1] u_1 + [B_2] u_2 \tag{4.19}$$

$$y_{sys} = [C_{sys}] x_{sys} \tag{4.20}$$

where,

$$x_{sys}^t = \begin{bmatrix} x_{WT}^t & x_G^t & x_N^t \end{bmatrix} \tag{4.21}$$

$$x_{WT}^t = \begin{bmatrix} \Delta \omega_t & \Delta \delta_{tg} & \Delta \omega_g \end{bmatrix} \tag{4.22}$$

$$x_G^t = \begin{bmatrix} \Delta I_{ds} & \Delta I_{qs} & \Delta E_{d1} & \Delta E_{q1} & \Delta E_{d2} & \Delta E_{q2} \end{bmatrix} \tag{4.23}$$

$$x_N^t = \begin{bmatrix} \Delta V_{ds} & \Delta V_{ds} & \Delta I_d & \Delta I_q & \Delta V_{cd} & \Delta V_{cq} \end{bmatrix} \tag{4.24}$$

$$y_{sys}^t = \begin{bmatrix} \Delta P_{WF} & \Delta Q_{WF} \end{bmatrix} \tag{4.25}$$

$$u_1 = \begin{bmatrix} \Delta T_W \end{bmatrix} \tag{4.26}$$

$$u_2 = \begin{bmatrix} \Delta V_{bd} \\ \Delta V_{bq} \end{bmatrix} \tag{4.27}$$

The state matrix and input matrix are defined as follows:

$$\begin{bmatrix} A_{sys} \end{bmatrix} = \begin{bmatrix} A_{TT} & A_{TG} & 0_{3\times 6} \\ A_{GT} & A_{GG} & A_{GN} \\ 0_{6\times 3} & A_{NG} & A_{NN} \end{bmatrix} \tag{4.28}$$

$$\begin{bmatrix} B_1 \end{bmatrix} = \begin{bmatrix} B_T \\ 0_{6\times 1} \\ 0_{6\times 1} \end{bmatrix}, \begin{bmatrix} B_2 \end{bmatrix} = \begin{bmatrix} 0_{3\times 2} \\ 0_{6\times 2} \\ B_N \end{bmatrix} \tag{4.29}$$

The state matrix $\begin{bmatrix} A_{sys} \end{bmatrix}$ in (4.28) is used for the eigenvalue analysis discussed in the next section where, $\begin{bmatrix} A_{sys} \end{bmatrix}$ is a 15×15 sized matrix, $[B_1]$ is a 15×1 matrix and $[B_2]$ is a 15×2 matrix.

4.4 SMALL SIGNAL ANALYSIS

4.4.1 Eigenvalue Analysis

The complete system state space model presented in (4.19) is utilized for the calculation of system eigenvalues. Considering various initial conditions, the steady state solutions are obtained and eigenvalues are calculated for the corresponding operating conditions. The initialization technique used in this chapter is presented in Appendix A. The wind farm size is varied between 100 MW and 500 MW and the series compensation level is

varied between 10% and 90%. The eigenvalues are also calculated for a 500 MW wind farm producing variable output. This is performed from the viewpoint of evaluating the impact of series compensation during the wind speed variation.

4.4.1.1 *Variation in Wind Farm Size*

The state space model mentioned in (4.21) results in seven complex conjugate eigenvalues and one real eigenvalue. The eigenvalues for different operating conditions are depicted in Table 4.1. The oscillatory modes obtained are: i) network mode 1 and network mode 2, ii) super synchronous mode, iii) electrical mode, iv) rotor mode, v) electromechanical mode, and vi) torsional mode. The only non-oscillatory mode is represented by the real eigenvalue. For the subsynchronous resonance analysis, electrical mode, electro-mechanical mode and torsional modes are of interest. The impact of series compensation on these three modes is studied through a comprehensive eigenvalue analysis depicted in Table 4.1.

The electrical mode that is characterized by the series capacitor is largely affected by the change in series compensation level. The impact of wind farm size is also found to be substantial. Table 4.1 illustrates that for all wind farm sizes, an increase in the series compensation level causes the electrical mode to become less stable and then become unstable at a specific compensation level, known as the critical compensation level. An unstable electrical mode always indicates the potential for induction generator effect SSR in the network. On the other hand, oscillatory frequency $\left(f_{er} \right)$ associated with the electrical mode also gets reduced with increasing level of series compensation.

Now, keeping the level of series compensation constant, when size of the wind farm is increased from 100 MW to 500 MW, the electrical mode shows a unique behavior. Initially it become less stable and then becomes more stable for larger wind farms. For example, in the case of a 100 MW wind farm with 50% series compensation, the electrical mode eigenvalues are calculated as -0.415 ± 237.08i, which become 0.165 ± 202.08i and 0.1569 ± 182.46i for 200 MW and 300 MW wind farms, respectively. However, when the wind farm size increases to 400 MW and 500 MW, the electrical mode becomes stable again. The electrical mode damped frequency also decreases with

respect to the increasing size of the wind farm. Similar behavior is also observed for all series compensation levels depicted in Table 4.1. This shows that instability due to SSR can occur at a realistic level of series compensation.

A double-cage induction generator has one electromechanical mode that is represented by the eigenvalues having an oscillatory frequency in the range of 3 Hz – 8 Hz. The electromechanical mode becomes more stable with increasing level of series compensation. At a constant level of series compensation, if size of the wind farm increases, the electromechanical mode becomes less stable. However, no instability in the electromechanical mode is seemingly caused by the series capacitor, as depicted in Table 4.1.

The torsional mode becomes relatively more stable with increasing size of the wind farm. However, increase in the percent of series compensation affects the torsional mode marginally, yet without causing any concern of the torsional interaction. Hence, no potential for torsional interaction is expected.

Figure 4.2 shows the variation in the electrical mode eigenvalues for different sizes of wind farm and series compensation levels. As the series compensation increases the real part of the electrical mode eigenvalue decreases. The oscillatory frequency of this mode also decreases consistently. The crossover series compensation level, known as the critical compensation, is unique for different sizes of wind farms. Figure 4.3 shows the damping ratio of the electrical mode. It illustrates that the effective damping ratio decreases gradually with the increasing series compensation level and becomes negative beyond the critical level of series compensation. Further increase in the series compensation yields a faster rise in the negative damping. Table 4.2 shows the critical compensation level for three different commercially available double-cage induction generators [104]-[106], [112]. It is to be noted that all the analyses carried out in this chapter are based on the IG-1 data provided in Appendix-B.

Figure 4.4 shows the damping ratio of the elctromechanical mode for different sizes of wind farms. It is observed that the smaller wind farms exhibit larger damping to the electromechanical mode in comparison to the larger wind farms.

Table 4.1 System eigenvalues for different size of wind farm

Modes	100 MW	200 MW	300 MW	400 MW	500 MW
No compensation					
Network mode-1	-7.740±2599.2i	-8.947±2132.8i	-9.657±1935.4i	-10.11±1802.4i	-10.41±1677.2i
Network mode-2	-8.788±1845.2i	-11.07±1378.8i	-12.64±1181.5i	-13.86±1048.5i	-14.94±923.23i
Sup. Sync. mode	-9.800±376.59i	-10.01±376.67i	-10.15±376.73i	-10.24±376.77i	-10.31±376.79i
Electrical mode	X	X	X	X	X
Rotor mode	-62.03±2.8866i	-60.51±3.1177i	-59.54±3.3131i	-58.84±3.5633i	-58.26±3.9728i
Elect-mech. mode	-5.658±34.578i	-4.506±31.003i	-3.841±28.141i	-3.461±25.601i	-3.334±23.071i
Torsional mode	-0.552±3.5799i	-0.625±3.5629i	-0.742±3.588i	-0.890±3.7309i	-0.925±4.0691i
Non-osc. mode	-7.684	-5.464	-3.669	-2.002	-0.433
40% Series compensation					
Network mode-1	-7.703±2613.1i	-8.863±2163.5i	-9.5929±1977.5i	-10.074±1872.9i	-10.42±1797.9i
Network mode-2	-8.728±1859.1i	-10.89±1409.5i	-12.433±1223.5i	-13.539±1118.9i	-14.42±1044i
Sup. Sync. mode	-6.818±501.74i	-6.789±533.07i	-6.6586±550.61i	-6.5325±561.61i	-6.420±569.5i
Electrical mode	-1.118±251.73i	-0.762±220.39i	-0.86505±202.84i	-1.092±191.85i	-1.352±183.98i
Rotor mode	-62.80±3.0335i	-61.55±3.3139i	-60.632±3.4701i	-59.951±3.5803i	-59.40±3.6859i
Elect-mech. mode	-6.334±36.361i	-5.388±33.973i	-4.6926±31.874i	-4.1921±30.064i	-3.813±28.385i
Torsional mode	-0.530±3.5918i	-0.557±3.5761i	-0.59757±3.5653i	-0.6502±3.5647i	-0.720±3.5837i
Non-osc. mode	-8.755	-7.210	-5.8976	-4.7785	-3.7286
50% Series compensation					
Network mode-1	-7.694±2616.1i	-8.848±2168.3i	-9.575±1984.9i	-10.05±1884i	-10.41±1814.3i
Network mode-2	-8.713±1862.2i	-10.86±1414.3i	-12.38±1231i	-13.47±1130.1i	-14.34±1060.4i
Sup. Sync. mode	-6.986±516.37i	-6.939±551.31i	-6.790±570.89i	-6.649±583.18i	-6.525±592.01i
Electrical mode	-0.415±237.08i	+0.165±202.08i	+0.156±182.46i	-0.041±170.14i	-0.306±161.31i
Rotor mode	-63.02±3.0866i	-61.85±3.4067i	-60.96±3.5792i	-60.30±3.6858i	-59.75±3.7703i
Elect-mech. mode	-6.537±36.849i	-5.683±34.809i	-5.020±32.981i	-4.520±31.384i	-4.120±29.897i
Torsional mode	-0.525±3.5951i	-0.545±3.5814i	-0.572±3.5703i	-0.607±.5641i	-0.653±3.5659i
Non-osc. mode	-9.048	-7.6941	-6.525	-5.528	-4.607
55% Series compensation					
Network mode-1	-7.690±2617.6i	-8.840±2170.5i	-9.566±1988.2i	-10.05±1888.8i	-10.41±1821.2i
Network mode-2	-8.706±1863.7i	-10.85±1416.5i	-12.36±1234.3i	-13.44±1134.9i	-14.30±1067.3i
Sup. Sync. mode	-7.061±523.11i	-7.006±559.71i	-6.849±580.23i	-6.702±593.12i	-6.572±602.39i
Electrical mode	-0.061±230.32i	+0.652±193.64i	+0.709±173.05i	+0.539±160.11i	+0.281±150.82i
Rotor mode	-63.13±3.1162i	-62.01±3.4618i	-61.15±3.6484i	-60.48±3.7587i	-59.94±3.8386i
Elect-mech. mode	-6.644±37.1i	-5.847±35.25i	-5.211±33.572i	-4.719±32.095i	-4.314±30.714i
Torsional mode	-0.523±3.5967i	-0.539±3.5842i	-0.561±3.5735i	-0.589±3.5662i	-0.625±3.5638i
Non-osc. mode	-9.199	-7.947	-6.856	-5.922	-5.063
60% Series compensation					
Network mode-1	-7.685±2619.1i	-8.832±2172.6i	-9.557±1991.3i	-10.04±1893.2i	-10.40±1827.4i
Network mode-2	-8.698±1865.1i	-10.83±1418.6i	-12.34±1237.3i	-13.42±1139.2i	-14.27±1073.4i
Sup. Sync. mode	-7.130±529.54i	-7.068±567.73i	-6.903±589.14i	-6.750±602.61i	-6.616±612.28i
Electrical mode	+0.296±223.87i	+1.158±185.58i	+1.297±164.06i	+1.166±150.52i	+0.926±140.79i
Rotor mode	-63.24±3.148i	-62.181±3.5235i	-61.33±3.7288i	-60.68±3.8471i	-60.14±3.9266i
Elect-mech. mode	-6.755±37.356i	-6.023±35.706i	-5.424±34.193i	-4.948±32.849i	-4.545±31.584i
Torsional mode	-0.521±3.5984i	-0.534±3.5872i	-0.551±3.5771i	-0.573±3.5694i	-0.600±3.5646i
Non-osc. mode	-9.352	-8.209	-7.201	-6.333	-5.535

The damping ratio increases marginally with increasing series compensation until 85%, beyond which the larger wind farms show a faster rise in the damping ratio. The torsional mode-damping ratio is shown in Figure 4.5. The large wind farm offers larger damping ratio during low series compensation. The damping ratio decreases steadily with the increase in the level of series compensation.
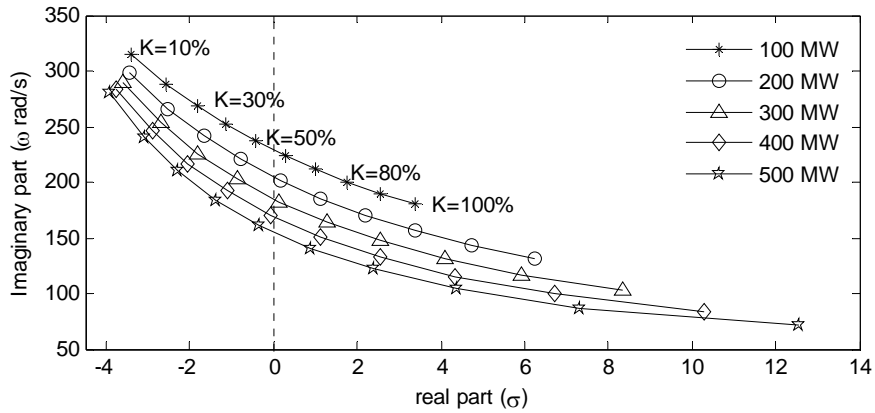
Figure 4.2 Electrical mode eigenvalues
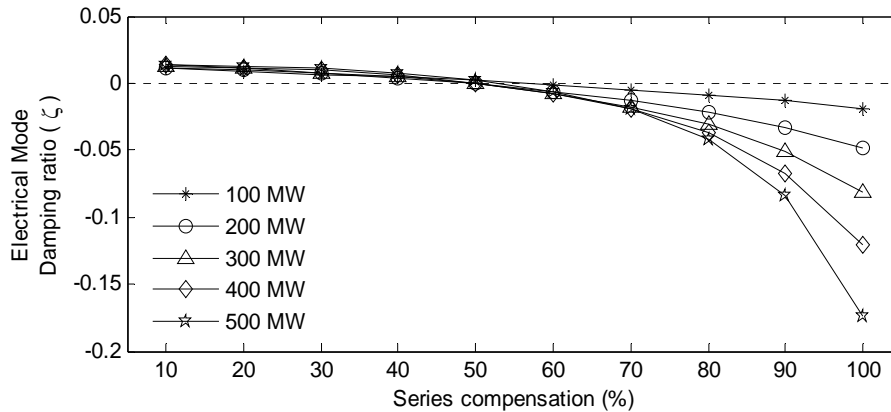
Figure 4.3 Electrical mode damping ratio

Table 4.2 Critical series compensation level (%)
for different size of wind farm

Wind farm size	IG-1	IG-2	IG-3
100 MW	56.00	57.20	71.80
200 MW	48.25	49.10	57.25
300 MW	48.60	49.20	55.20
400 MW	50.50	50.80	55.70
500 MW	52.60	53.10	57.20
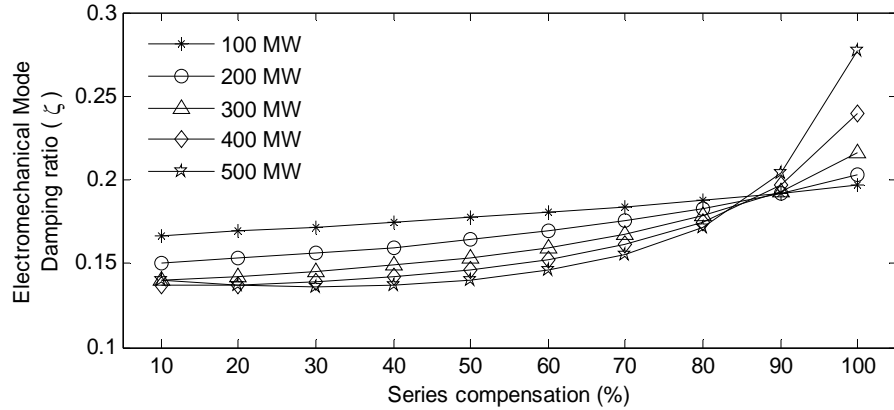
Figure 4.4 Electromechanical damping ratio
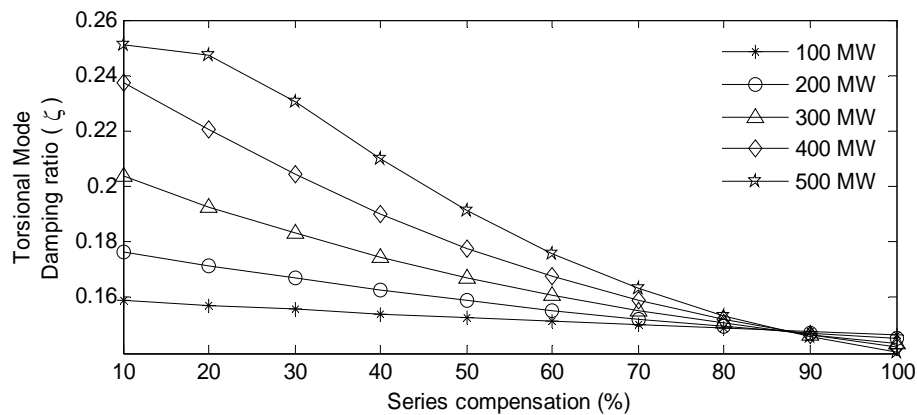
Figure 4.5 Torsional mode damping ratio

4.4.1.2   *Variation in Wind Farm Output*

In the previous section, the wind farm size has been varied by aggregating an appropriate number of wind turbines. In this section, the wind farm size is kept constant at 500 MW and the output of the wind farm is varied which is obtained by varying the mechanical torque input to the aggregated wind turbines. The eigenvalues calculated for different outputs and series compensations are depicted in Table 4.3.

It is observed that the electrical mode becomes less stable consistently with increasing series compensation level and finally becomes unstable beyond the critical compensation level. The unstable electrical mode leads to induction generator effect SSR in the wind turbine generators. Simultaneously, the damped frequency of the electrical mode is found to decrease with increased level of series compensation. Now when the compensation level is kept constant and wind farm outputs are varied, the electrical mode eigenvalues

change very little with the increase in power outputs. When the output power varies, the slip of the induction generator only varies narrowly which does not cause significant change in the rotor resistance. Since the numbers of wind turbines are kept constant, the effective equivalent impedance of the wind farm remains almost constant. Thus, variation in the output of a large wind farm is less sensitive to the issue of SSR. The critical compensation levels for different types of generators are depicted in Table 4.4.

Table 4.3 System eigenvalues with different power output

Modes	100 MW	200 MW	300 MW	400 MW	500 MW
40% Series compensation					
Network mode-1	-10.86±2408.8i	-10.8±2299.8i	-10.70±2147.4i	-10.58±1974.8i	-10.42±1797.9i
Network mode-2	-13.56±1654.9i	-13.66±1545.8i	-13.84±1393.4i	-14.08±1220.9i	-14.42±1044i
Sup. Synh. mode	-6.409±570i	-6.41±569.94i	-6.411±569.85i	-6.415±569.71i	-6.420±569.5i
Electrical mode	-1.357±183.43i	-1.363±183.48i	-1.364±183.59i	-1.360±183.75i	-1.352±183.98i
Rotor mode	-59.65±0.8033i	-59.62±1.4707i	-59.57±2.1425i	-59.50±2.8659i	-59.40±3.6859i
Elect-mech. mode	-3.142±29.967i	-3.210±29.829i	-3.331±29.531i	-3.521±29.06i	-3.813±28.385i
Tortional mode	-0.407±3.4973i	-0.43±3.4988i	-0.476±3.5033i	-0.562±3.5199i	-0.720±3.5837i
Non-osc. mode	-6.056	-5.834	-5.43	-4.775	-3.728
50% Series compensation					
Network mode-1	-10.84±2410.1i	-10.78±2301.8i	-10.69±2151.7i	-10.56±1983.9i	-10.41±1814.3i
Network mode-2	-13.53±1656.1i	-13.64±1547.8i	-13.80±1397.8i	-14.03±1229.9i	-14.34±1060.4i
Sup. Synh. mode	-6.508±592.67i	-6.510±592.6i	-6.513±592.47i	-6.518±592.28i	-6.525±592.01i
Electrical mode	-0.315±160.58i	-0.322±160.65i	-0.323±160.79i	-0.318±161.01i	-0.306±161.31i
Rotor mode	-59.98±0.95387i	-59.95±1.619i	-59.90±2.2843i	-59.84±2.9897i	-59.75±3.7703i
Elect-mech. mode	-3.518±31.191i	-3.580±31.086i	-3.691±30.844i	-3.864±30.454i	-4.120±29.897i
Tortional mode	-0.409±3.5161i	-0.428±3.5175i	-0.466±3.521i	-0.534±3.5315i	-0.653±3.5659i
Non-osc. mode	-6.593	-6.393	-6.036	-5.472	-4.607
55% Series compensation					
Network mode-1	-10.84±2410.7i	-10.78±2302.7i	-10.68±2153.7i	-10.56±1987.8i	-10.41±1821.2i
Network mode-2	-13.52±1656.8i	-13.63±1548.8i	-13.79±1399.7i	-14.01±1233.9i	-14.30±1067.3i
Sup. Synh. mode	-6.552±603.14i	-6.554±603.05i	-6.558±602.91i	-6.564±602.69i	-6.572±602.39i
Electrical mode	0.272±150i	0.264 ±150.08i	0.2629±150.24i	0.268±150.48i	0.281±150.82i
Rotor mode	-60.16±1.0498i	-60.13±1.7131i	-60.08±2.3755i	-60.02±3.0736i	-59.94±3.8386i
Elect-mech. mode	-3.745±31.882i	-3.804±31.793i	-3.911±31.576i	-4.075±31.221i	-4.314±30.714i
Tortional mode	-0.410±3.5256i	-0.427±3.527i	-0.461±3.53i	-0.521±3.5384i	-0.625±3.5638i
Non-osc. mode	-6.897	-6.708	-6.372	-5.850	-5.063
60% Series compensation					
Network mode-1	-10.83±2411.3i	-10.77±2303.7i	-10.67±2155.5i	-10.55±1991.3i	-10.40±1827.4i
Network mode-2	-13.51±1657.4i	-13.61±1549.7i	-13.77±1401.6i	-13.99±1237.4i	-14.27±1073.4i
Sup. Synh. mode	-6.593±613.13i	-6.595±613.03i	-6.600±612.87i	-6.607±612.62i	-6.616±612.28i
Electrical mode	0.9178±139.87i	0.9081±139.97i	0.9059±140.15i	0.9116±140.41i	0.9260±140.79i
Rotor mode	-60.35±1.1627i	-60.32±1.8238i	-60.28±2.4835i	-60.22±3.175i	-60.14±3.9266i
Elect-mech. mode	-4.008±32.638i	-4.064±32.565i	-4.165±32.37i	-4.320±32.048i	-4.545±31.584i
Tortional mode	-0.412±3.5351i	-0.426±3.5365i	-0.4571±3.5392i	-0.510±3.5458i	-0.600±3.5646i
Non-osc. mode	-7.229	-7.051	-6.736	-6.252	-5.535

Table 4.4 Critical series compensation level (%)
for different wind farm output

Wind farm output	IG-1	IG-2	IG-3
100 MW	52.75	53.20	57.30
200 MW	52.80	53.25	57.35
300 MW	52.85	53.30	57.40
400 MW	52.80	53.25	57.35
500 MW	52.60	53.10	57.20

Figure 4.6, Figure 4.7, and Figure 4.8 show the damping ratio of electrical mode, electromechanical mode and torsional mode, respectively, for different operating conditions. The electrical mode damping ratio remains almost constant for all of the outputs of a large wind farm, as shown in Figure 4.6. It only decreases with increased percent series compensation level. The electromechanical mode damping ratios are shown in Figure 4.7. It is observed that during a low level of series compensation the damping ratios for different outputs are different. However, as the compensation level increases the damping ratios increase and become similar. Figure 4.8 shows the variation in the torsional mode-damping ratio. With a low level of series compensation and large power output, the damping ratio remains high, but it decreases linearly with increase in the series compensation level. However, for low power output conditions the variation is negligible. After comparing Table 4.1 and Table 4.3, it is observed that the various subsynchronous modes primarily depend on the size of the wind farm rather than this power output.
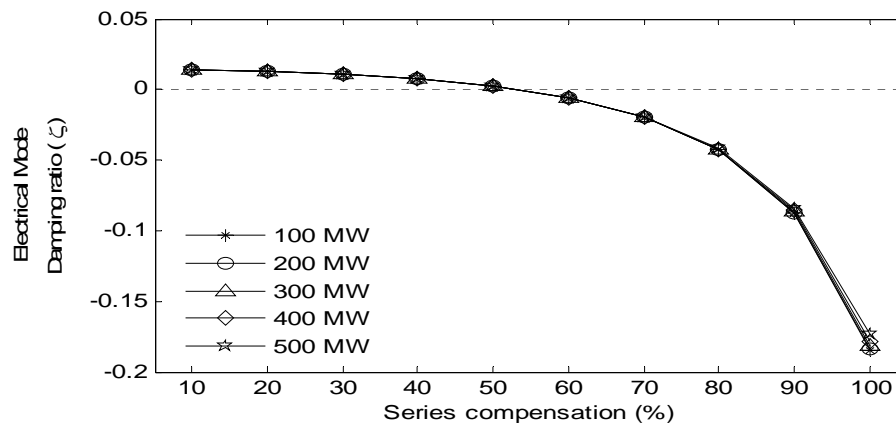
Figure 4.6 Electrical mode damping ratio
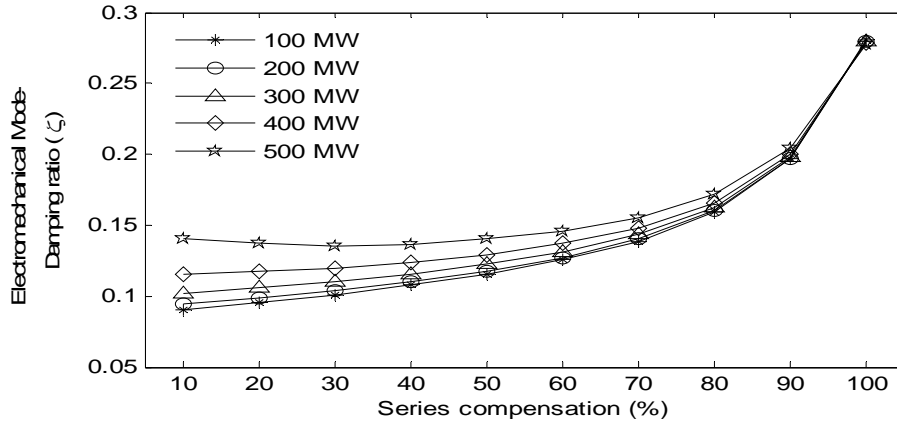
Figure 4.7 Electromechanical mode damping ratio
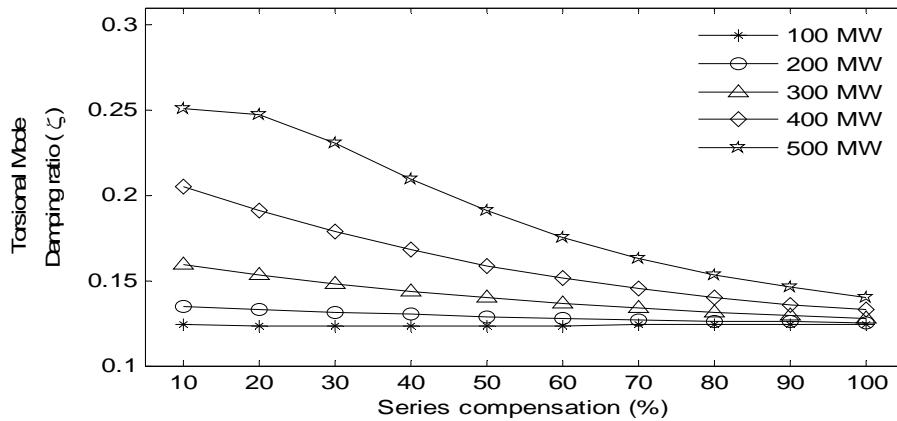
Figure 4.8 Torsional mode damping ratio

4.4.2 Participation Factor Analysis

From the eigenvalue analysis, stability of the subsynchronous modes is studied. The normalized participation factor analysis described in Chapter 2 is performed to investigate the influence of various system states on the subsynchronous modes. A 100 MW wind farm connected to a 50% series compensated line is considered to conduct the study. Figure 4.9 shows the participation factors associated with the electrical, electromechanical, torsional, and rotor mode. The participation factor associated with the electrical mode is shown in Figure 4.9 (a), which is mainly contributed by the d-q axis voltage across the series capacitor, d-q axis stator current of the induction generator and line current. Although very small, rotor circuit influence is also observed here. Figure 4.9 (b) illustrates the participation factor associated with the electromechanical mode. This shows the contribution from the generator speed, and d axis induced voltage of two rotor

cages. Similarly the torsional mode participation factor is depicted in Figure 4.9 (c), which is mostly contributed by the dynamics of the drive train system and no interaction from the electrical network is found in this case. The participation factor associated with the rotor mode is shown in Figure 4.9 (d). This mode is largely contributed by the rotor circuit parameters.

(a) Electrical mode

(b) Electromechanical mode

(c) Torsional mode

(d) Rotor mode
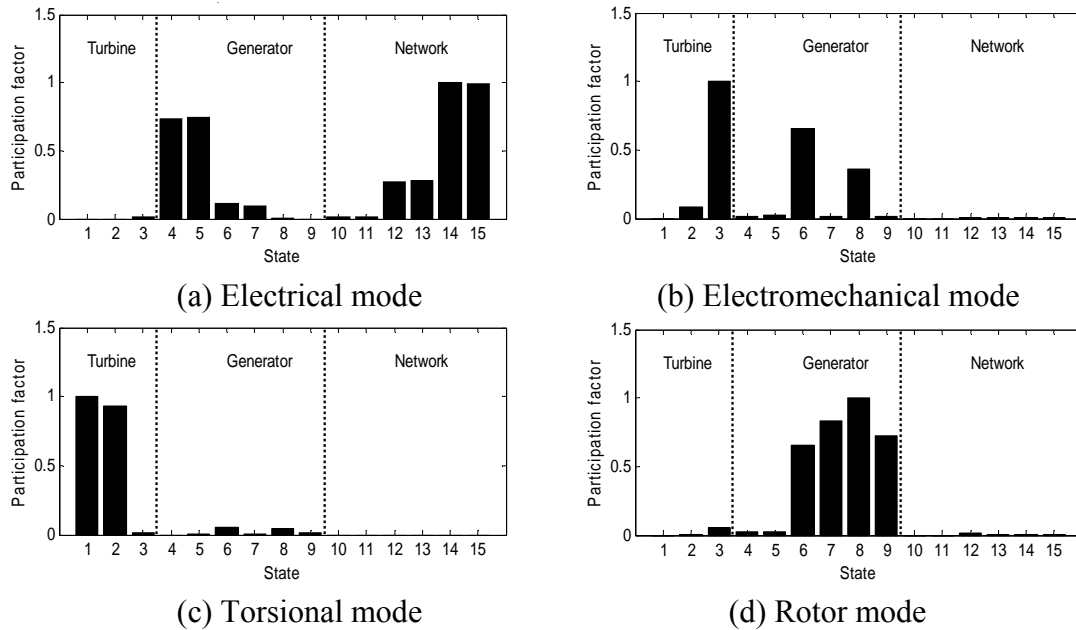
Figure 4.9 Participation factors of various modes

4.4.3   Sensitivity Analysis

Sensitivity analysis shows the change in the eigenvalues for different parameters characterizing the study system. The electrical mode, electromechanical mode, and torsional mode are considered for the sensitivity analysis which is classified into two parts: i) electrical parameter sensitivity and ii) mechanical parameter sensitivity. Two different cases are considered: i) 100 MW wind farm and ii) 100 MW output of a 500 MW wind farm. It is considered that both wind farms are connected to 40% series compensated transmission lines.

4.4.3.1   *Sensitivity to Electrical Parameters*

The electrical parameter sensitivity study primarily deals with the variation in the stator circuit resistance, unsaturated reactance, rotor circuit resistances, and unsaturated mutual reactance of the induction generator. Each chosen parameter is varied as 0.25, 0.5, 1, 1.5,

and 2 times the rated parameter value (mentioned with a zero in the subscript). Figure 4.10 shows the impact of variation in stator resistance on the damping ratio of electrical mode, electromechanical mode, and torsional mode. In Figure 4.10 (a), it is shown that the electrical mode-damping ratio of a 100 MW wind farm becomes negative when the stator resistance is reduced below the 70% of its nominal value. However when a 500 MW wind farm is considered, the variation in stator resistance is found to have less impact in comparison to a 100 MW wind farm. The electromechanical and torsional mode-damping ratios are shown in Figure 4.10 (b) and (c), respectively. The influence of the stator resistance is found to be negligible in this case. This validates the participation factor analysis that states that the electromechanical and torsional mode are least influenced by the electrical parameters of the stator.

(a) Electrical mode   (b) Electromechanical mode   (c) Torsional mode
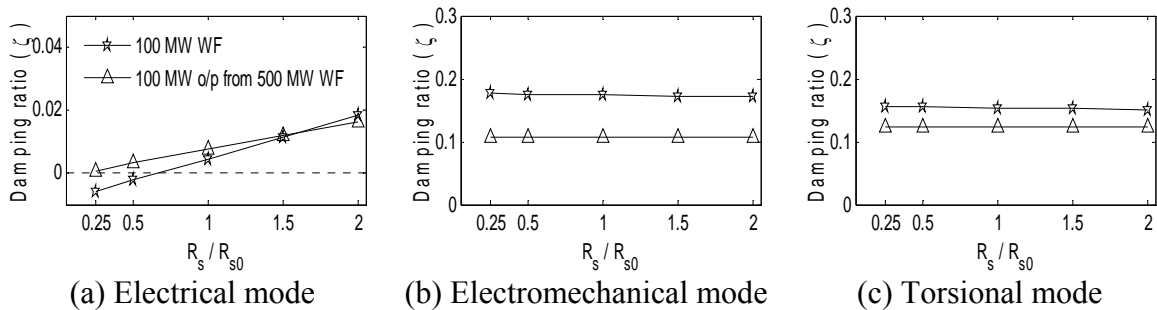
Figure 4.10 Impact of change in stator resistance

Figure 4.11 shows the variation in stator leakage reactance and its impact on the three aforementioned subsynchronous oscillatory modes. In the case of a 100 MW wind farm, as the stator reactance increases the damping ratio of the electrical mode increases and then achieves about a constant value as shown in Figure 4.11 (a). Similar behavior is also witnessed for a 500MW wind farm. However, in both cases the electromechanical mode-damping ratio remains stable for any change in reactance value, as depicted in Figure 4.11 (b). From Figure 4.11 (b) it is observed that in a 100 MW wind farm, electromechanical oscillation is better damped in comparison to the 500 MW wind farm. The variation in the torsional mode-damping ratio with respect to stator reactance is shown in the Figure 4.11 (c). In the case of a 100 MW wind farm, the torsional mode-damping ratio increases with the increase in the reactance. However, in the case of a 500 MW wind farm, the torsional mode-damping ratio remains almost constant. This

behavior is expected due to larger effective stator reactance. When less numbers of induction generators are connected, it reduces the effective series compensation. With large number of induction generators, the effective stator reactance decreases, hence, impact of series compensation increases on the torsional mode-damping.

(a) Electrical mode   (b) Electromechanical mode   (c) Torsional mode
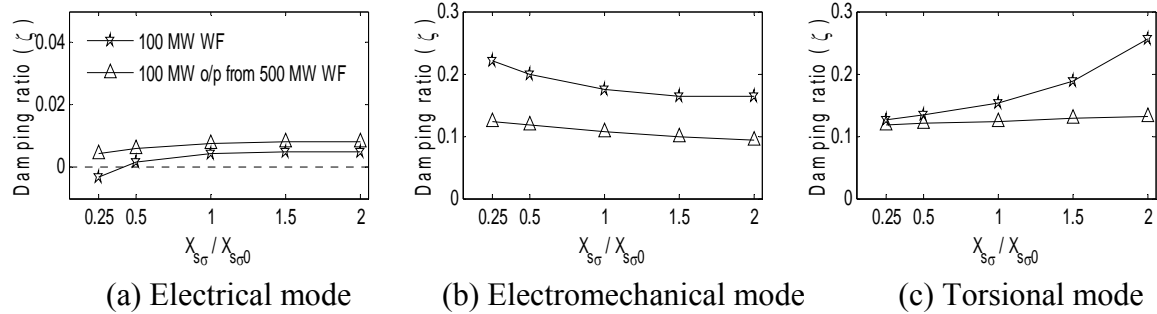
Figure 4.11 Impact of change in stator reactance

The effects of variation in both outer cage and inner cage rotor resistance on the performance of the wind farm are presented in Figure 4.12 and Figure 4.13, respectively. Figure 4.12 (a) shows decreasing electrical mode-damping ratio that becomes negative with increased outer cage resistance of the double-cage induction generator. At low resistance conditions, the 500 MW wind farm offers more damping to this mode. Impact of variation on the electromechanical mode and torsional mode are shown in Figure 4.12 (b) and Figure 4.12 (c), respectively. When the outer cage resistance increases, the damping ratio of the electromechanical mode and torsional mode also increase rapidly. This response is found to be opposite to that of the electrical mode response. Figure 4.13 shows the variation in damping ratio with respect to the variation in the inner cage rotor resistance. The electrical mode and the electromechanical mode-damping ratio are found to be least affected as seen in Figure 4.13 (a) and Figure 4.13 (b), respectively. However, the torsional mode stability increases with an increase in the inner cage resistance, shown in Figure 4.13 (c). The impact of change in the mutual reactance is shown in Figure 4.14. It is observed that the variation in the unsaturated mutual reactance does not show any significant variation in the damping ratios of the three modes. In all cases it is found that a smaller wind farm always exhibits larger damping to low frequency oscillatory modes than a large wind farm.

(a) Electrical mode (b) Electromechanical mode (c) Torsional mode
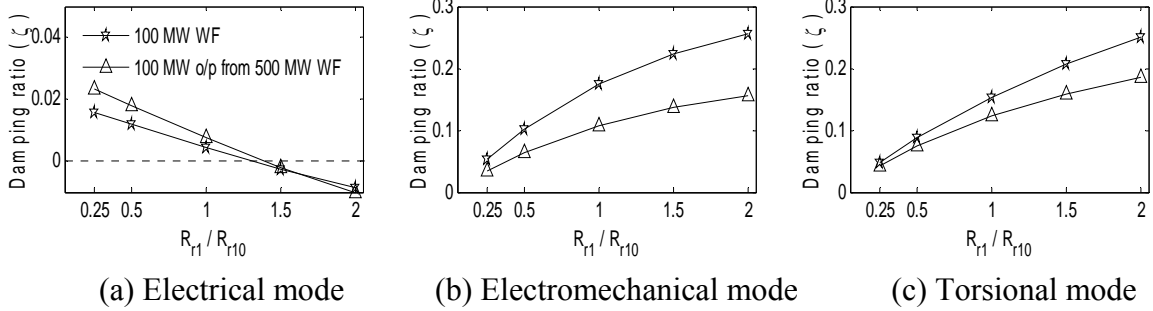
Figure 4.12 Impact of first (outer) cage rotor resistance

(a) Electrical mode (b) Electromechanical mode (c) Torsional mode
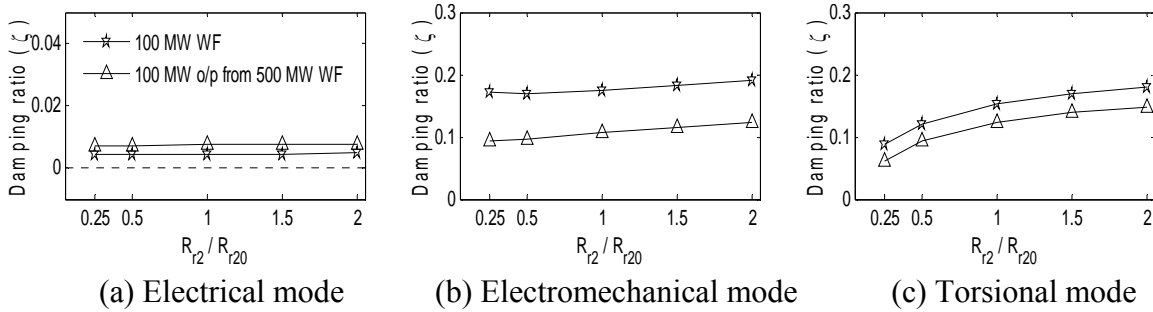
Figure 4.13 Impact of second (inner) cage rotor resistance

(a) Electrical mode (b) Electromechanical mode (c) Torsional mode
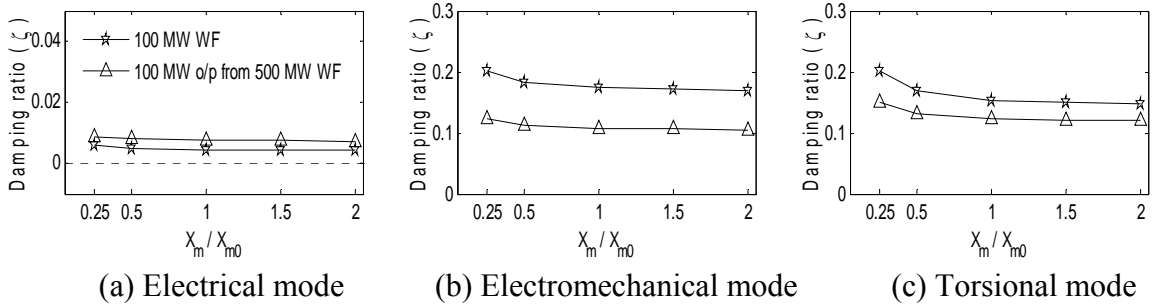
Figure 4.14 Impact of mutual reactance

4.4.3.2 *Sensitivity to Mechanical Parameters*

The wind turbine inertia constant, generator inertia constant, and shaft stiffness are considered for the mechanical parameter sensitivity study. Participation factor analysis presented in Section 4.4.2 shows that the electrical mode is entirely independent of the mechanical parameters of the wind turbine. Further, the variation in the mechanical parameters of the wind turbine has a greater effect over the electromechanical and torsional mode. Figure 4.15 and Figure 4.16 show the change in damping ratio with the change in inertia constant and shaft stiffness of the wind turbine, respectively. The electrical mode is found to be insensitive in both the cases as shown in Figure 4.15 (a) and Figure 4.16 (a). The impact on the electromechanical mode is also found to be small,

as shown Figure 4.15 (b) and Figure 4.16 (b). However, the damping ratio of the torsional mode is largely affected by the change in the inertia constant and shaft stiffness of the wind turbine. The torsional mode-damping ratio increases quite linearly with the increase in the turbine inertia constant and the shaft stiffness of the wind turbine as shown in Figure 4.15 (c) and Figure 4.16 (c).

Figure 4.17 (a) shows variation in the generator inertia constant and its impact on the electrical mode-damping ratio which is unaffected by the variation. Figure 4.17 (b) shows the increase in the damping ratio of the electromechanical mode with increase in the generator inertia constant. Figure 4.17 (c) shows the impact on the torsional mode. Being much smaller than the turbine inertia constant, the influence of the generator inertia constant on the torsional mode is found to be negligible. From these studies, it is also observed that a 100 MW wind farm offers larger damping than the 500 MW wind farm producing 100 MW output.

(a) Electrical mode   (b) Electromechanical mode   (c) Torsional mode
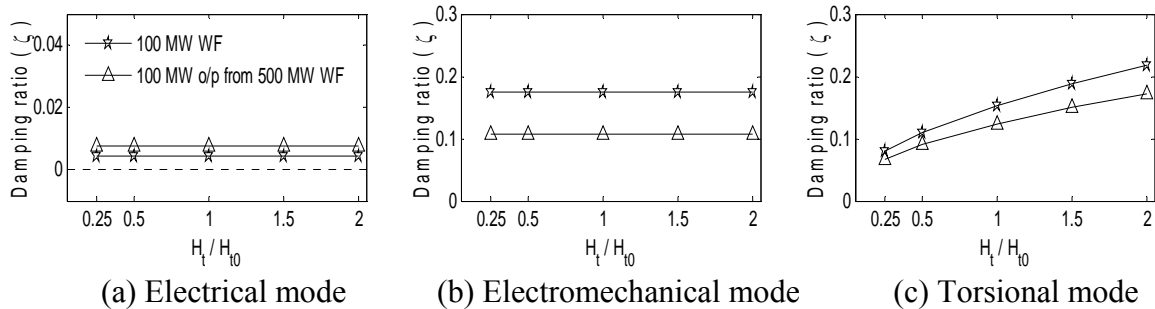
Figure 4.15 Impact of turbine inertia constant

(a) Electrical mode   (b) Electromechanical mode   (c) Torsional mode
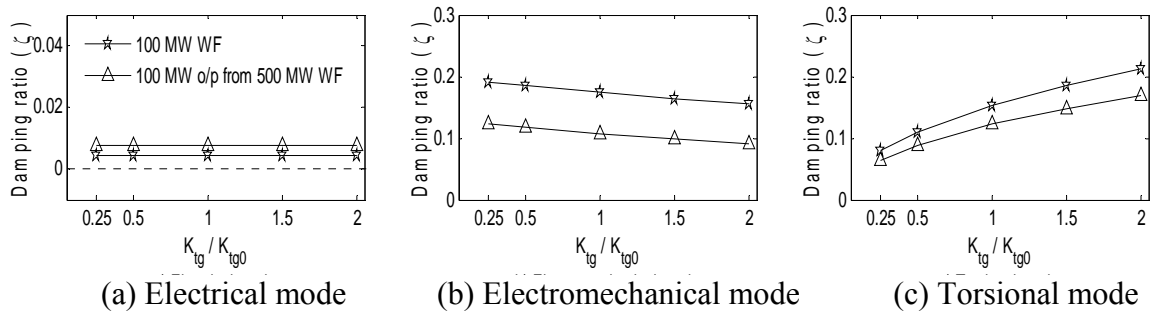
Figure 4.16 Impact of shaft stiffness

(a) Electrical mode (b) Electromechanical mode (c) Torsional mode
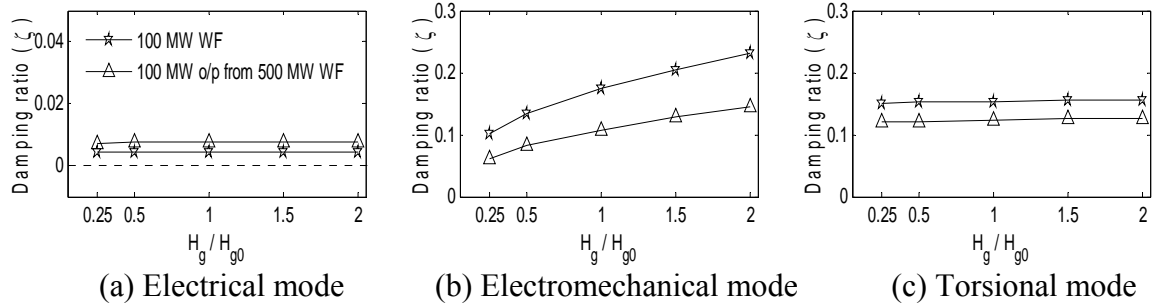
Figure 4.17 Impact of generator inertia constant

4.5 ELECTROMAGNETIC TRANSIENT SIMULATIONS

A detailed electromagnetic transient simulation study with PSCAD/EMTDC software is done to validate the small signal analysis.

4.5.1   Steady State Subsynchronous Resonance

The FFT of the time domain simulation results show the actual modal frequencies that are compared with the calculated damped frequencies of the corresponding oscillatory modes. This section presents the investigation of steady state SSR in two scenarios: i) variation in the wind farm size and ii) variation in the output of a 500 MW wind farm.

4.5.1.1   *Variation in Wind Farm Size*

Figure 4.18 shows the steady state performance of a 100MW wind farm connected to 50% and 60% series compensated lines, respectively. The motivation behind the chosen series compensation is that one is below and another is above the critical compensation level. As predicted from eigenvalues in Table 4.1, the 100 MW wind farm connected to a 50% series compensated line exhibits a stable electrical mode and no self-excited oscillations are found in the electromagnetic torque as shown in Figure 4.18 (a). However, with 60% series compensation the electromagnetic torque experiences self-excitation that grows with time. PCC voltage shown in Figure 4.18 (b) also exhibits similar behavior. Beyond the critical compensation level of 56% shown in Table 4.2, self-excitation occurs in the system. The FFT analysis of the electromagnetic torque and the PCC voltage is shown in Figure 4.18 (c). The estimated frequencies of both the oscillations are found to be 223.1 rad/s which matches very closely with the calculated value of 223.87 rad/s (damped frequency of the electrical mode at 60% series

compensation) shown in Table 4.1. Similar study is conducted for a 300 MW wind farm. In this case the compensation levels are 40% and 50% because of the lower critical compensation level (48.25%) shown in Table 4.2. No oscillation is witnessed with 40% series compensation but the electromagnetic torque and PCC voltage start oscillating when the series compensation level is increased to 50%, as shown in Figure 4.19 (a) and Figure 4.19 (b), respectively. This is predicted from the eigenvalue analysis. The FFT of the torque and voltage is shown in Figure 4.19 (c). The estimated frequency (181.6 rad/s) matches closely with the electrical mode damped frequency (182.46 rad/s) of the 300MW wind farm with 50% series compensation. Simulation with a 500 MW wind farm connected to 50% and 55% series compensation depicts similar results shown in Figure 4.20. The oscillation (with 55% series compensation) in electromagnetic torque and PCC voltage is shown in Figure 4.20 (a) and Figure 4.20 (b), respectively. Figure 4.20 (c) shows the estimated electrical mode damped frequency that matches with the calculated value shown in Table 4.1.
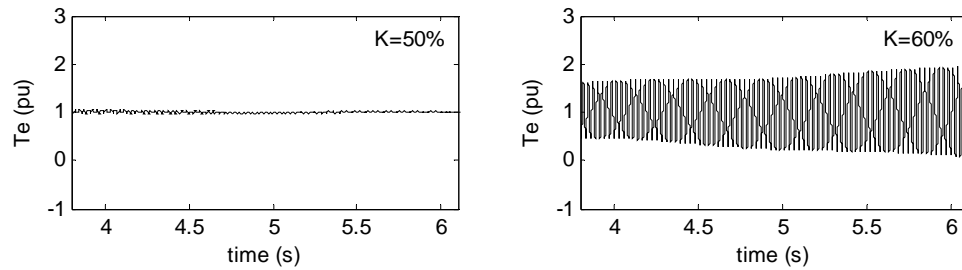
(a) Electromagnetic torque
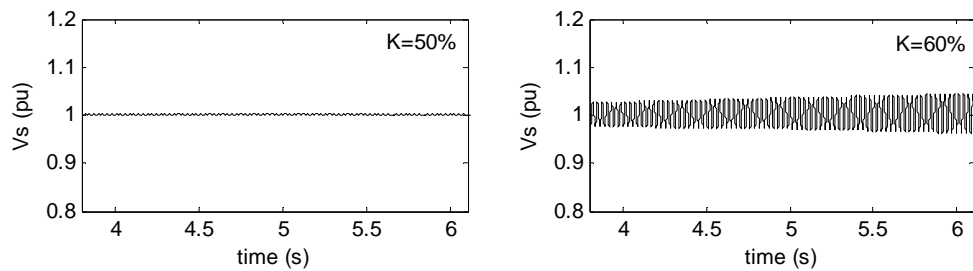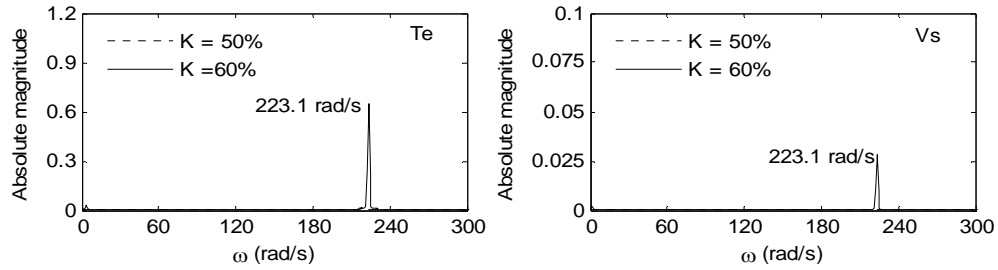
(b) PCC voltage

(c) FFT of electromagnetic torque

Figure 4.18 Steady state SSR in a 100 MW wind farm
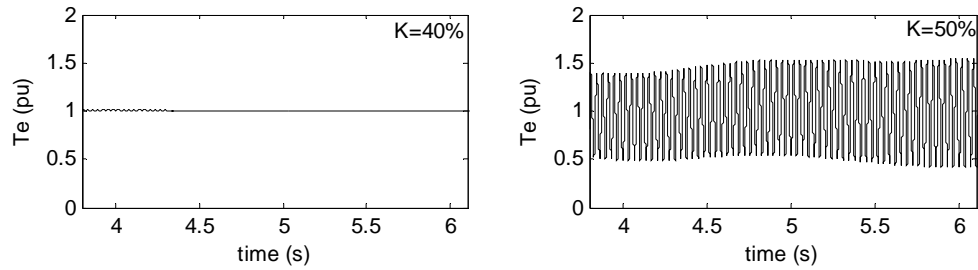
(a) Electromagnetic torque
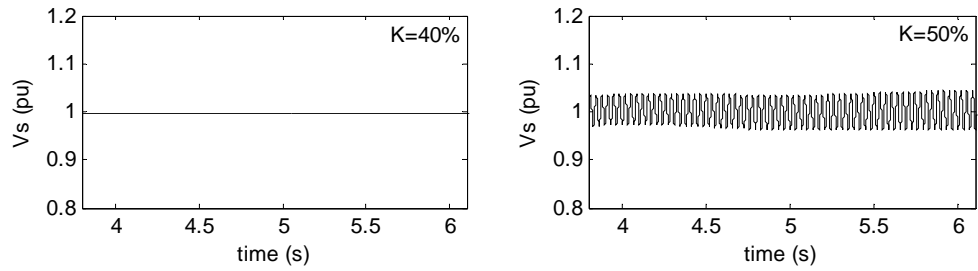
(b) PCC voltage
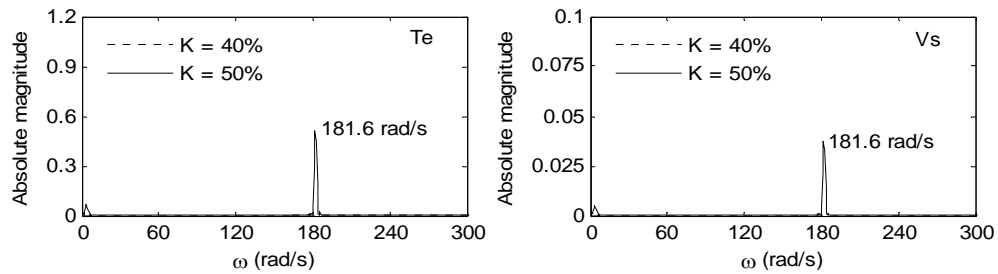
(c) FFT of electromagnetic torque

Figure 4.19 Steady state SSR in a 300 MW wind farm

(a) Electromagnetic torque

(b) PCC voltage
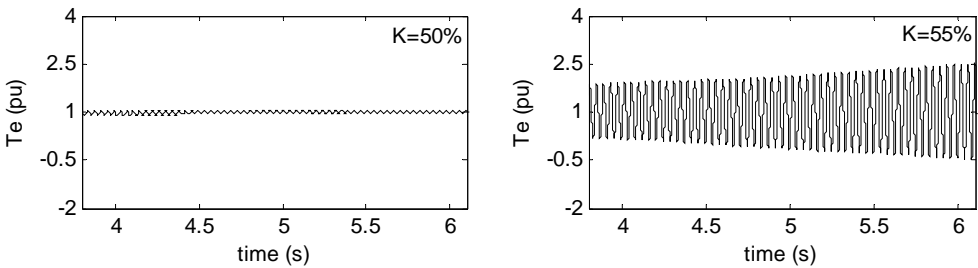
(c) FFT of electromagnetic torque and PCC voltage
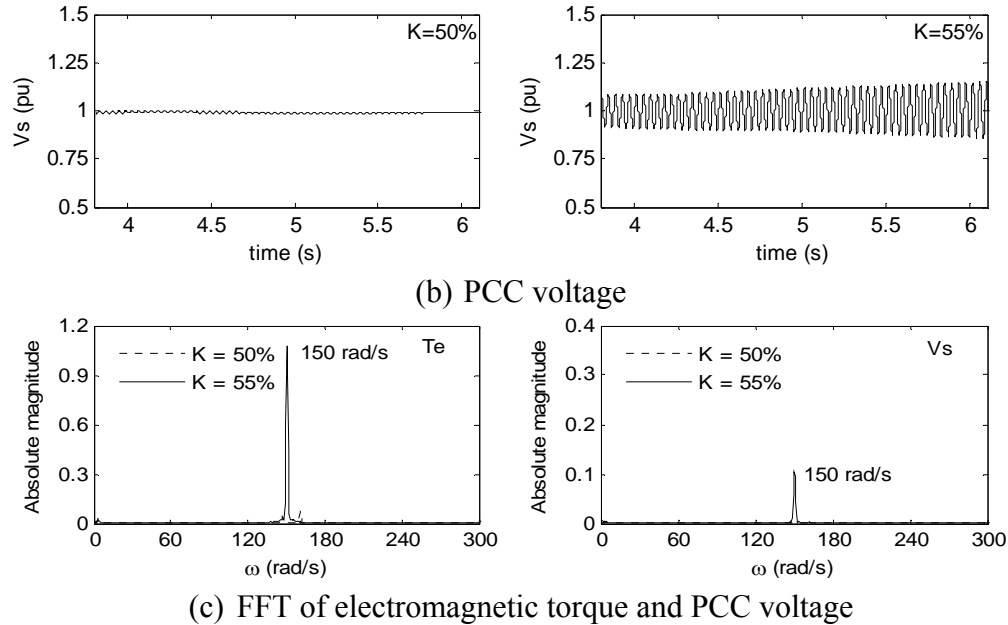
Figure 4.20 Steady state SSR in a 500 MW wind farm

4.5.1.2   *Variation in Wind Farm Output*

The study of steady state SSR is now done with a large 500 MW wind farm producing 100 MW and 300 MW output. Table 4.4 shows the critical compensation levels for different output conditions. Thus, 50% and 55% series compensation are chosen to simulate one stable and unstable operating condition. Figure 4.21 (a) shows the electromagnetic torque of 100 MW output at steady state for the two compensation levels. Similarly the PCC voltage is shown in Figure 4.21 (b). To estimate the oscillatory frequency FFT analysis of the electromagnetic torque and the PCC voltage are carried out and shown in Figure 4.21 (c). The estimated frequencies shown in Figure 4.21 (c) correspond to the 55% series compensation, which match with the calculated values shown in Table 4.3. A similar study is conducted with 300MW output. The self-excitation in electromagnetic torque and PCC voltage are observed, and shown in Figure 4.22 (a) and Figure 4.22 (b), respectively. The FFT of the two quantities are shown in Figure 4.22 (c). The estimated frequencies match with the calculated damped frequencies shown in Table 4.3.

(a) Electromagnetic torque

(b) PCC voltage

(c) FFT of electromagnetic torque and PCC voltage
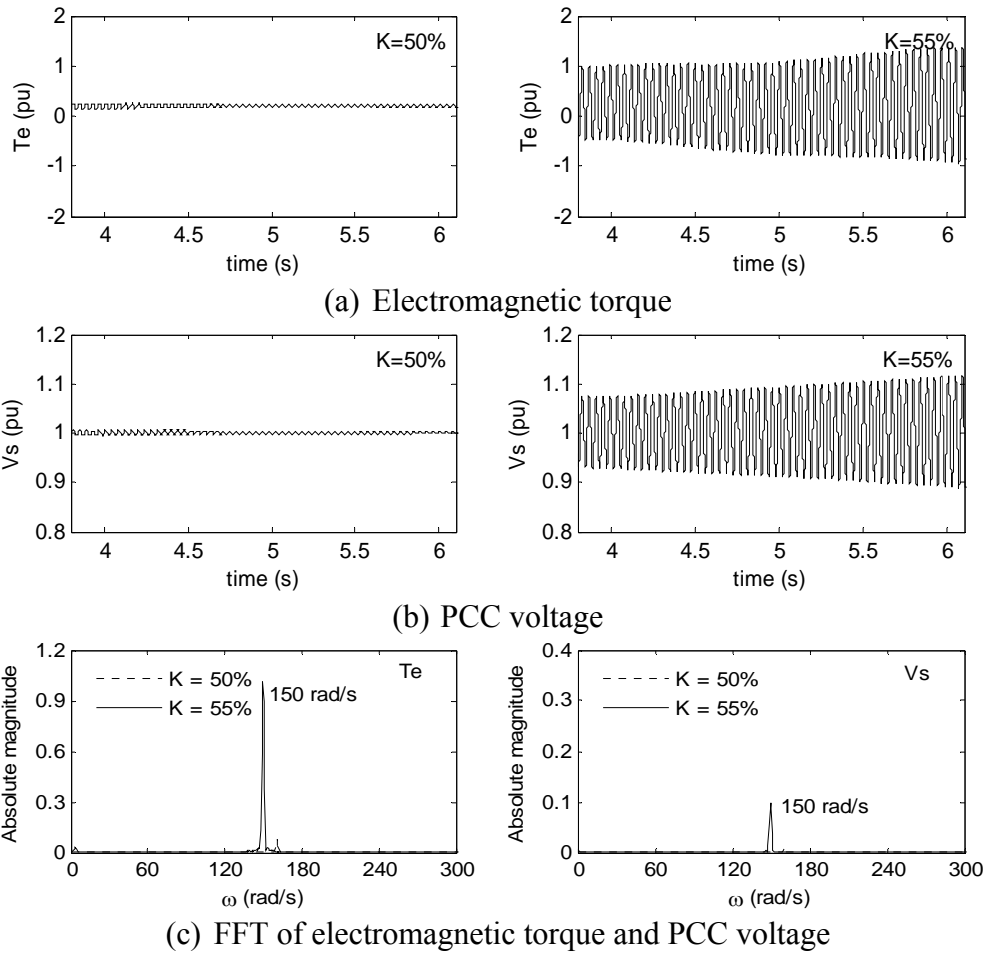
Figure 4.21 Steady state SSR in a 500 MW wind farm producing 100 MW output

(a) Electromagnetic torque

(b) PCC voltage

(c) FFT of electromagnetic torque and PCC voltage
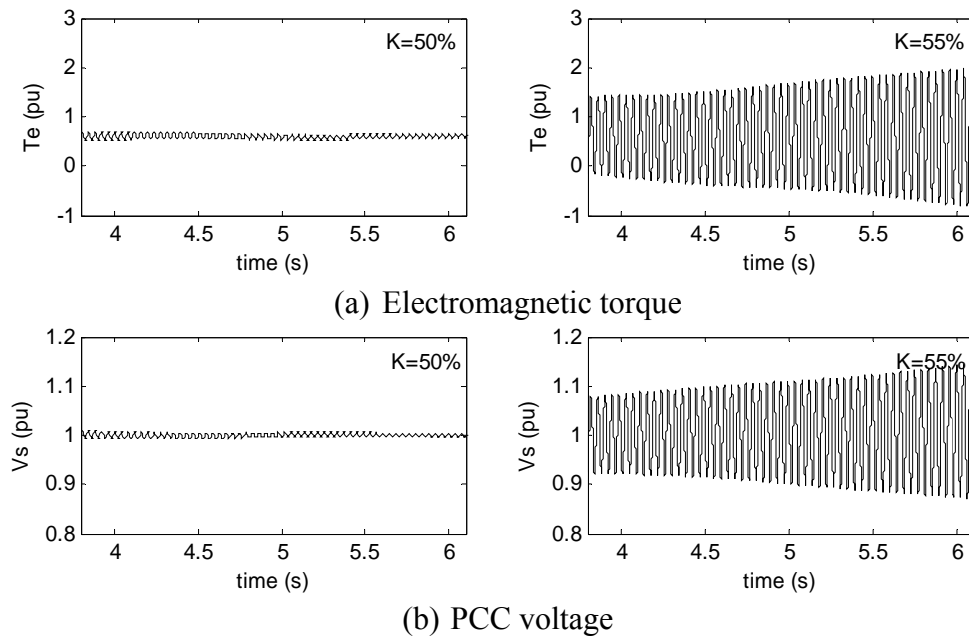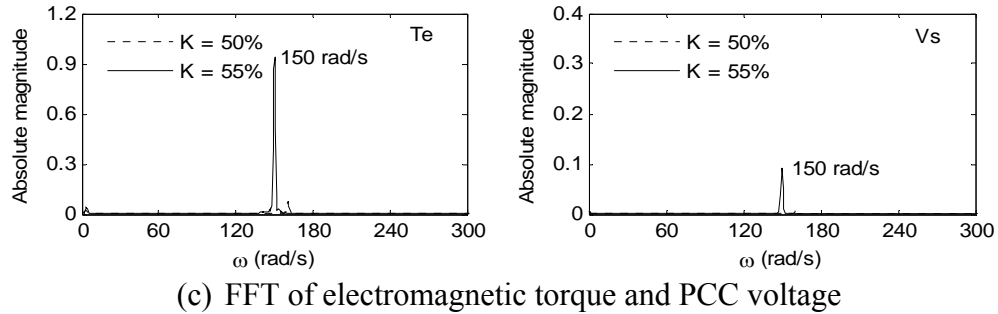
Figure 4.22 Steady state SSR in a 500 MW wind farm producing 300 MW output.

4.5.2　Transient Subsynchronous Resonance

4.5.2.1　*Variation in Wind Farm Size*

Transient SSR in wind farms may result from large disturbances such as fault, or line outages etc. To study the potential of SSR during transients in the system, a three phase fault is simulated at F_2 (Bus-2) as shown in Figure 4.1. The fault is simulated at t=4s and cleared after six cycles (100 ms). When the fault occurs, a large disturbance is experienced in the electromagnetic torque, shaft torque, speed of the generator, terminal voltage and voltage across series capacitor. Each of the mentioned variables contains multiple frequency components. Thus FFT analysis is carried out to determine the various frequency components.

A 100 MW wind farm with 50% and 60% series compensation is considered and simulation results are shown in Figure 4.23. The electromagnetic torque following the disturbance is shown in Figure 4.23 (a). Since 50% series compensation is a stable operating condition the oscillation in electromagnetic torque decays. However, with 60% series compensation the oscillation in electromagnetic torque grows gradually and becomes unstable. Corresponding shaft torque is shown in Figure 4.23 (b). With 60% series compensation, the shaft destabilizes due to the influence of the electrical mode instability. The FFT of electromagnetic torque and shaft torque is shown in Figure 4.23 (c). The frequencies: 237.1 rad/s and 223.8 rad/s corresponding to the 50% and 60% series compensation, respectively, match with the calculated frequencies of 237.08 rad/s and 223.87 rad/s, respectively, shown in Table 4.1. Similarly, the FFT of shaft torque shows the torsional mode frequency of 3.68 rad/s which corresponds to the calculated

damped frequency of ≈ 3.57 rad/s. This correlation validates the small signal analysis carried out in this Chapter. The generator speed, PCC voltage, and voltage across series capacitor are shown in Figure 4.23 (d), (e) and (f), respectively. The oscillations in the generator speed and PCC voltage contain multiple frequency components that are similar to the detected components found in electromagnetic torque and shaft torque. The series capacitor voltage contains a frequency component that is the 60 Hz compliment of the electrical mode oscillatory frequency.

(a) Electromagnetic torque

(b) Shaft torque

(c) FFT of electromagnetic and shaft torque

(d) Generator speed

(e) PCC voltage

(f) Series capacitor voltage
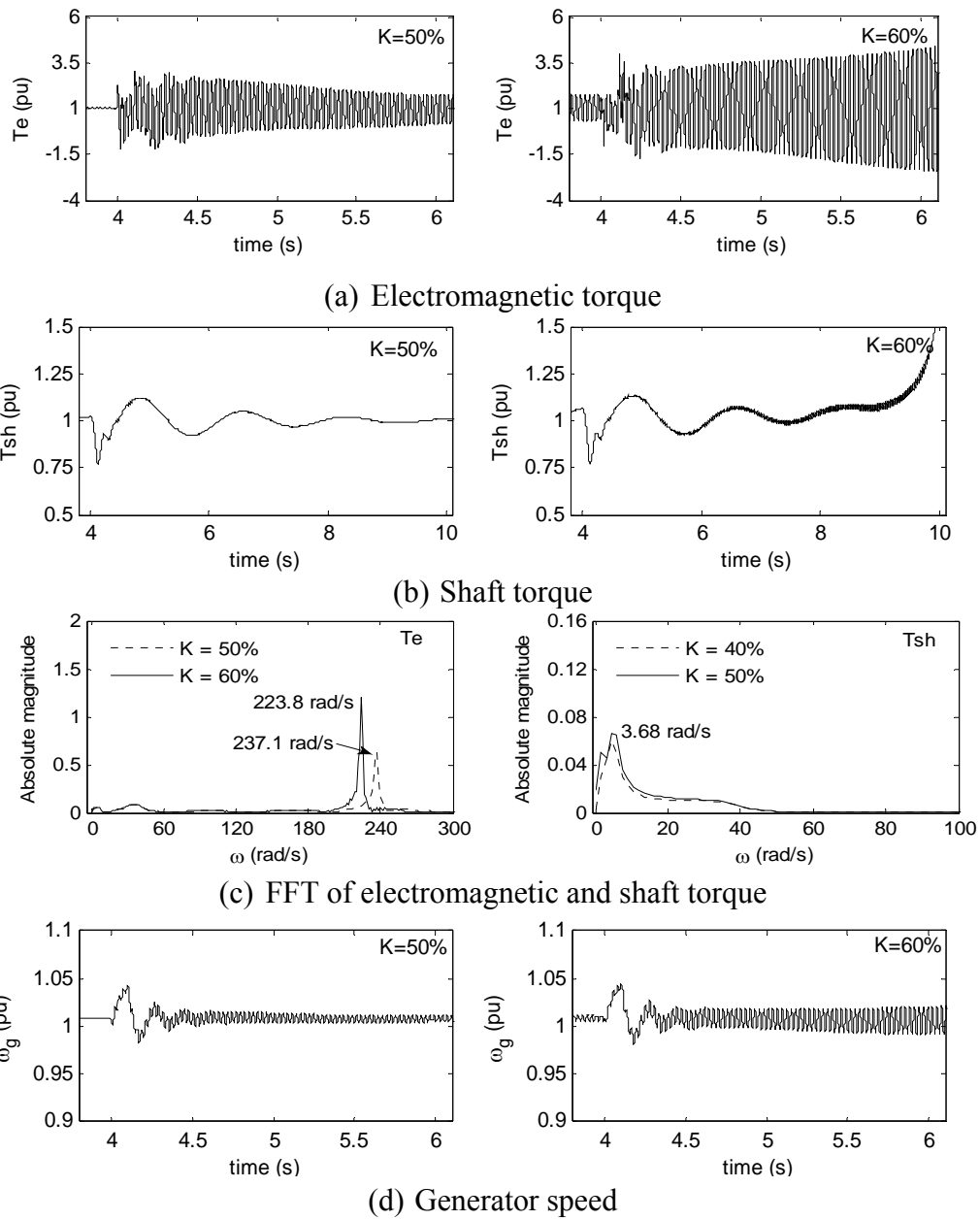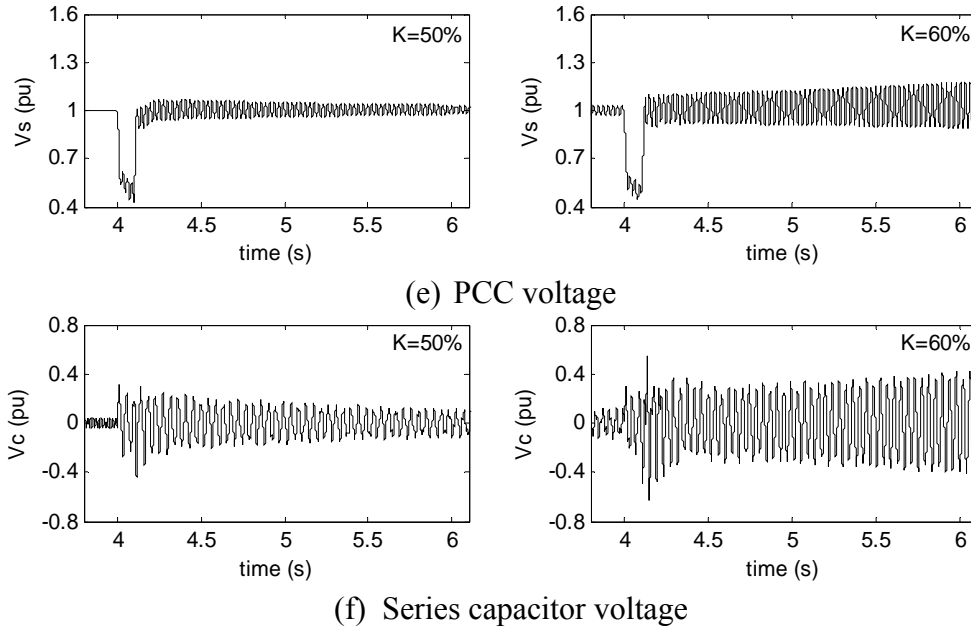
Figure 4.23 Transient SSR in a 100 MW wind farm.

Similar study is carried out with a 300 MW wind farm connected to 40% and 50% series compensated transmission line. The response of the wind farm following the three phase fault at the remote end is depicted in Figure 4.24. The electromagnetic torque oscillation shown in Figure 4.24 (a) is similar to the 100 MW wind farm illustrated in Figure 4.23 (a). Shaft torque oscillation is shown in Figure 4.24 (b). In this case since the instability does not occur within the time frame (10 sec) of simulation, the shaft torque seems to be stabilized. However, the electrical mode instability destabilizes the shaft torque after 10 sec, not shown here. The FFT of the electromagnetic torque (see Figure 4.24 (c)) shows two frequencies: 203.1 rad/s and 182.6 rad/s, corresponding to 40% and 50% series compensation, respectively. FFT of the shaft torque depicted in Figure 4.24 (c) shows a torsional mode frequency of 3.68 rad/s. All of the measured frequencies match very well with the corresponding calculated damped frequencies shown in the Table 4.1. The generator speed, PCC voltage, and series capacitor voltage also exhibit similar responses to the fault which are displayed in Figure 4.24 (d), (e) and (f).
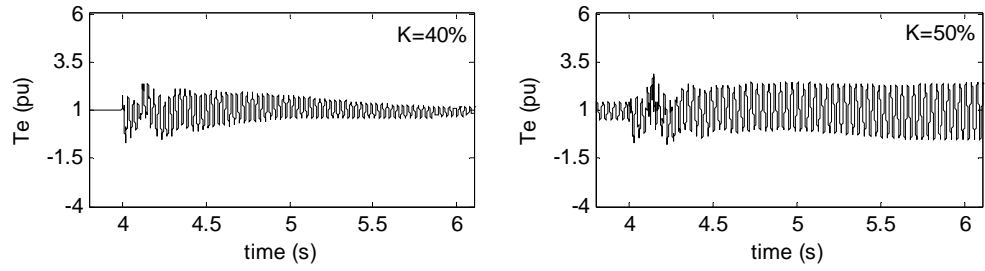
(a) Electromagnetic torque
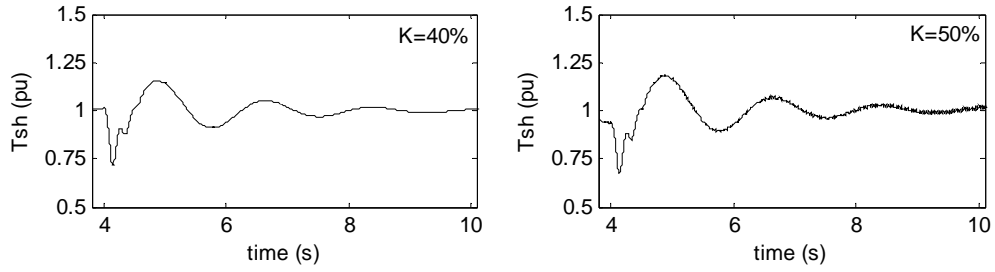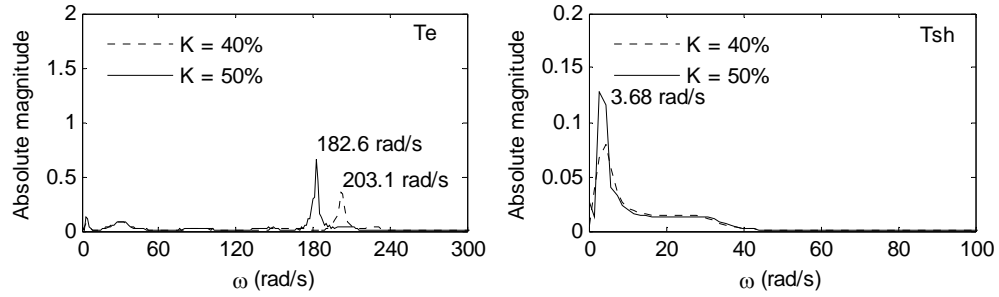
(b) Shaft torque

(c) FFT of electromagnetic and shaft torque
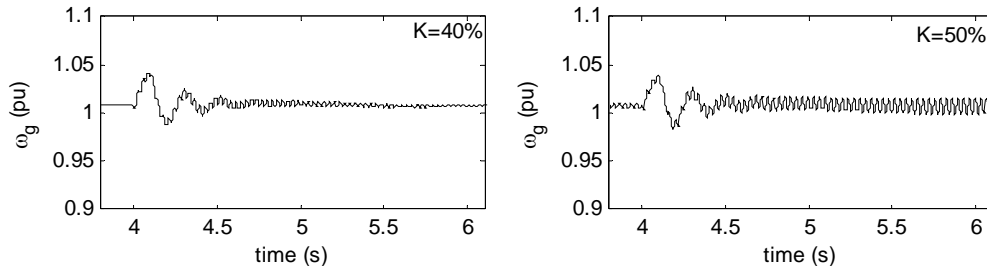
(d) Generator speed
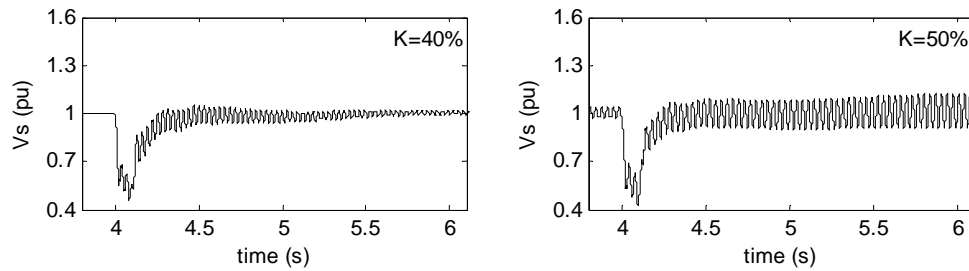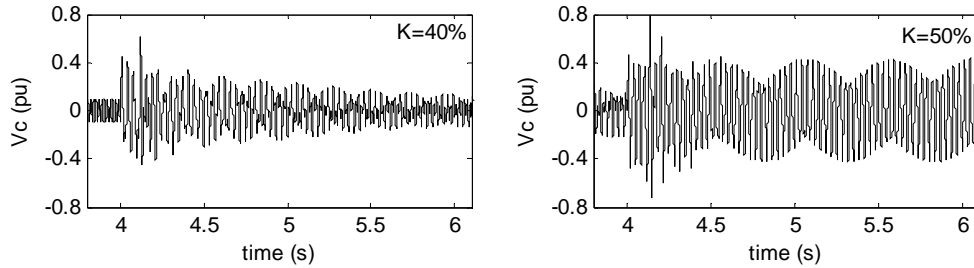
(e) PCC voltage

(f) Series capacitor voltage

Figure 4.24 Transient SSR in a 300 MW wind farm

Figure 4.25 shows the electromagnetic torque, PCC voltage, and the series capacitor voltage of a 500 MW wind farm following the three phase fault in the network. 50% and 55% series compensation are considered in this case. Since the critical compensation level is 52.60%, 55% series compensation causes induction generator effect SSR which can be seen from the gradually growing oscillations in electromagnetic torque, PCC voltage, and series capacitor voltage shown in Figure 4.25 (a) , (b) and (c), respectively. The large transmission line current builds up high voltage across the series capacitor, which further grows and becomes unstable. This may cause severe damage to the series capacitor and its auxiliary equipment.
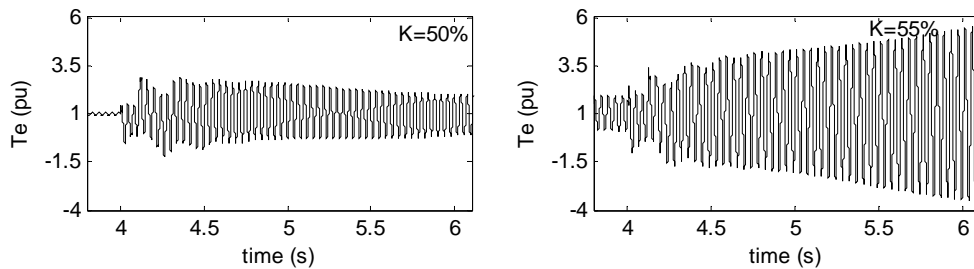
(a)   Electromagnetic torque

(b) PCC voltage
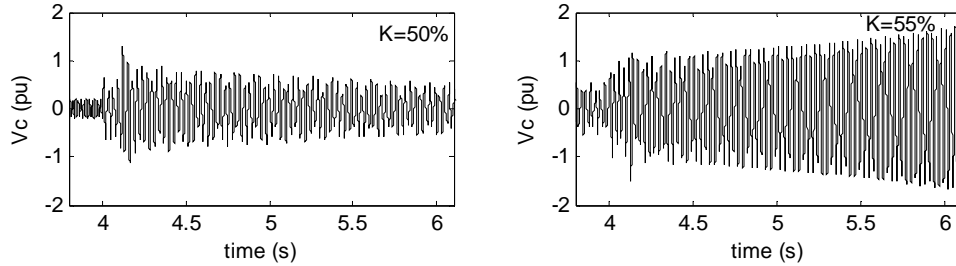
(c) Series capacitor voltage

Figure 4.25 Transient SSR in a 500 MW wind farm

4.5.2.2 *Variation in Wind Farm Output*

Due to the variation in the wind speed, variable output power from the wind farm flows through the series compensated line. To evaluate the impact of series compensation on the wind farm during the above scenario, several simulations are carried out with a 500 MW wind farm producing variable power outputs. The series compensation levels considered are 50% and 55%. Figure 4.26 shows the performance of the wind farm producing 100MW (0.2 pu) output. With 55% series compensation the electrical mode is found to be unstable as shown in Table 4.3. This is now reasonably validated through the time domain simulation shown in Figure 4.26 (a). The shaft torque for the corresponding series compensation level is shown in Figure 4.26 (b). Due to the electrical mode instability, shaft torque is also amplified and attains a very high magnitude which can potentially damage the wind turbine shafts. The FFT of electromagnetic torque and shaft torque are shown in Figure 4.26 (c). The estimated frequencies match very closely with the calculated values shown in Table 4.3. Generator speed and PCC voltage are shown in Figure 4.26 (d) and (e), respectively. With 50% series compensation, the oscillations in the speed and voltage are stabilized. However, the oscillation grows with 55% series compensation. The estimated frequencies are identical to the measured frequencies obtained from the FFT of electromagnetic torque.

Figure 4.27 illustrates the performance of the wind farm with 300MW output. The electromagnetic torque and shaft torque are shown in Figure 4.27 (a) and Figure 4.27 (b), respectively. The oscillations are almost similar to the oscillations observed with 100 MW output shown in Figure 4.26. The estimated frequencies from the FFT are depicted in Figure 4.27 (c), which match with the calculated damped frequencies. From the study

with other outputs and sizes of wind farm, it is confirmed that beyond the critical compensation, symmetrical fault in the network may cause significant rise in the electromagnetic torque and shaft torque. Repetitive high shaft torque may lead to cyclic fatigue of the shaft.
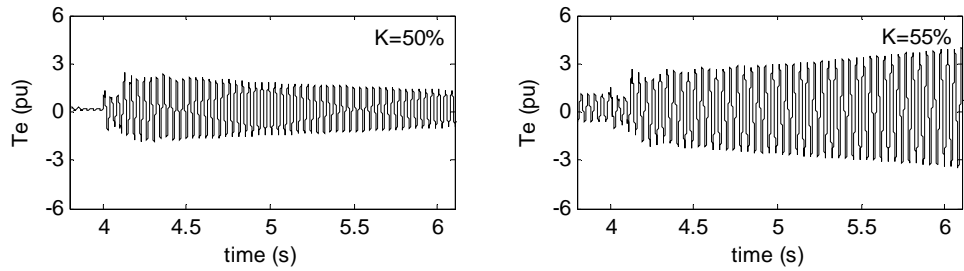
(a) Electromagnetic torque
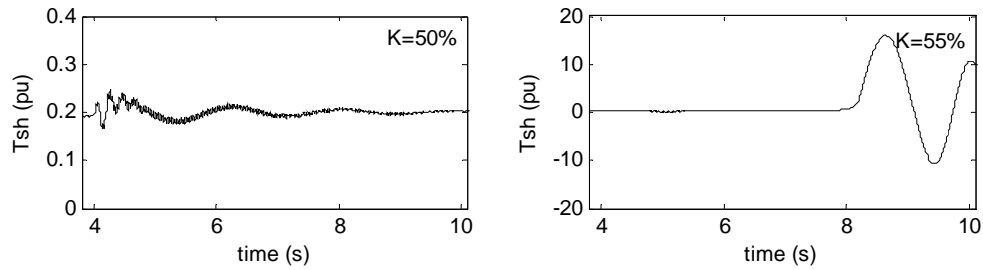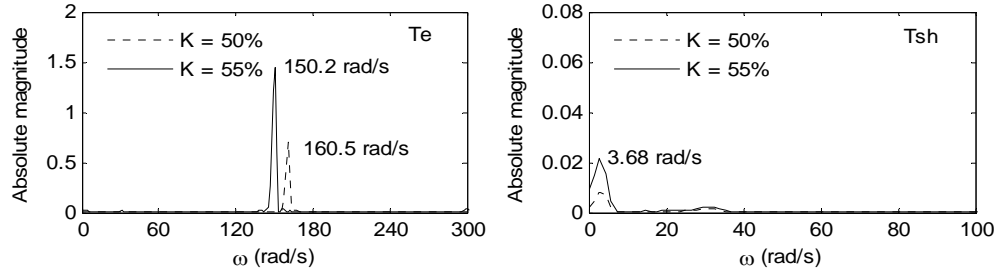
(b) Shaft torque

(c) FFT of electromagnetic torque and shaft torque
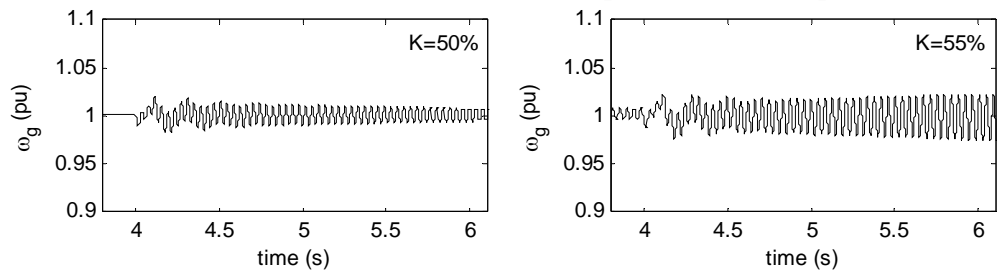
(d) Generator speed
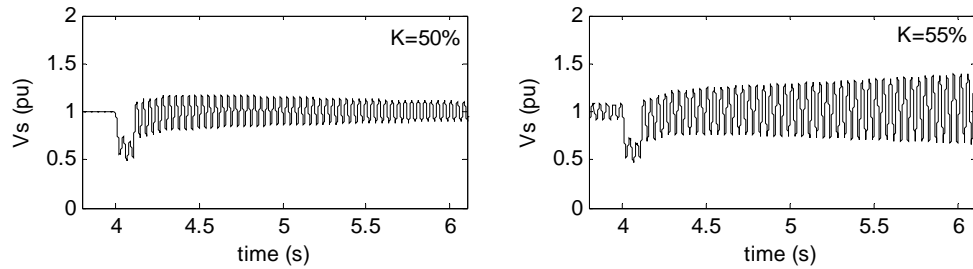
(e) PCC voltage

Figure 4.26 Transient SSR in a 500 MW wind farm producing 100 MW output
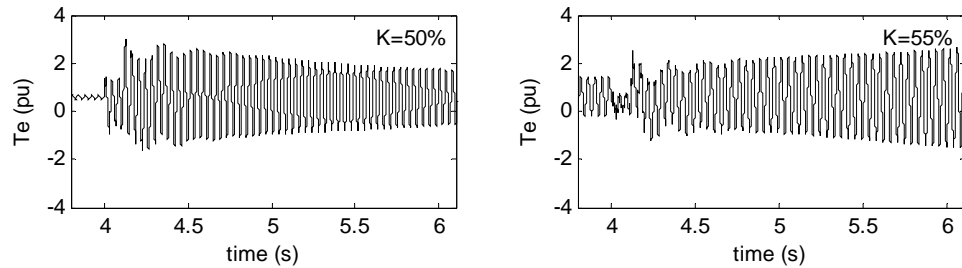
(a) Electromagnetic torque
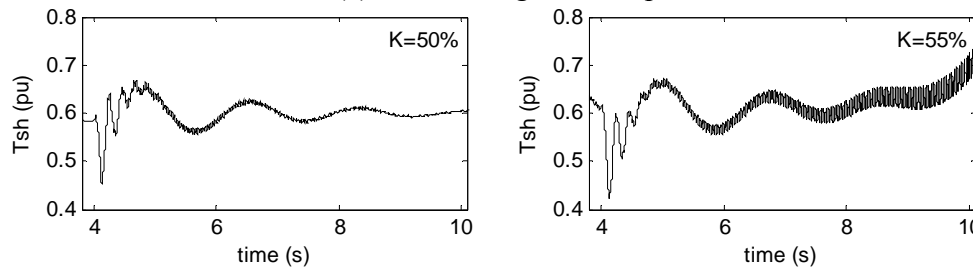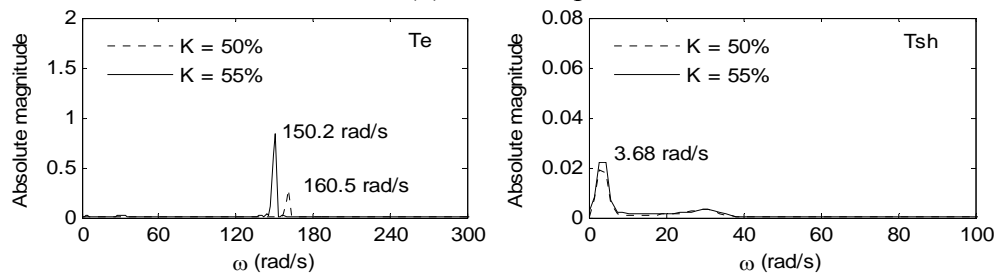
(b) Shaft torque

(c) FFT of electromagnetic torque and shaft torque

Figure 4.27 Transient SSR in a 500 MW wind farm producing 300 MW output

4.6   IMPACT OF FAULT LOCATION

Series capacitors are placed differently in lines in different jurisdictions. For instance in Sweden, several series capacitors are placed in the center of the transmission lines and one such application also exists in Canada [42]. However, several series capacitor applications in the USA comprise two capacitors placed at both the ends of a

transmission line. In some cases series capacitor banks are also placed at one-third length of the transmission line. A detailed analysis of the location of the series capacitor is provided in [42].

In the previous sections the steady state and transient SSR analysis are carried out considering the capacitor bank in the center of the line. In this section, series capacitor bank is split into two banks and each bank is placed at each end of the line, as shown in Figure 4.28. This configuration is selected to investigate the impact of fault location and position of the series capacitor on the wind farms.
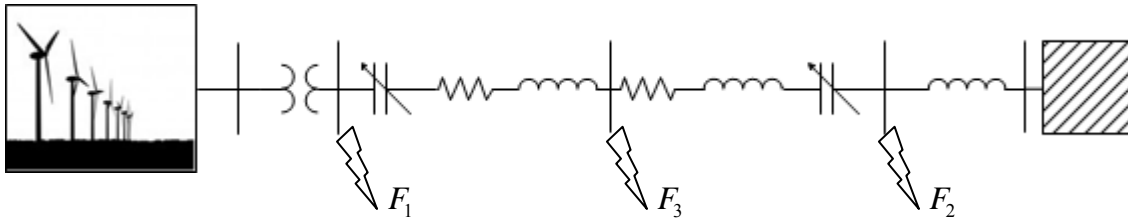
Figure 4.28 Modified study system.

4.6.1   Variation in Size of Wind Farm

The time domain simulation of the modified system is carried out with PSCAD/EMTDC software. The six cycles three phase fault is initiated at t=4s and its impact on electromagnetic torque, shaft toque, and PCC voltage of the wind farm are studied. The electromagnetic torque of a 50 MW wind farm following the fault clearance is shown in Figure 4.29 (a). The fault at location F_1 results in a large disturbance in the electromagnetic torque. The peak amplitude of the electromagnetic torque decreases as the fault location moves away from the wind farm terminal, which is also seen in the case of single-cage induction generator based wind farm. Similar trend is found with 100MW and 300 MW wind farms as shown in Figure 4.29 (b) and (c), respectively. As the size of the wind farm increases, the impact of the terminal fault on the electromagnetic torque decreases significantly. For instance, for a 50 MW wind farm the peak electromagnetic toque following the fault at F_1 is 10 pu, which is reduced to 8 pu and 2.5 pu for 100MW

and 300 MW wind farms, respectively. Similar responses are observed for the faults at other locations as well.

(a) 50 MW wind farm

(b) 100 MW wind farm

(c) 300 MW wind farm
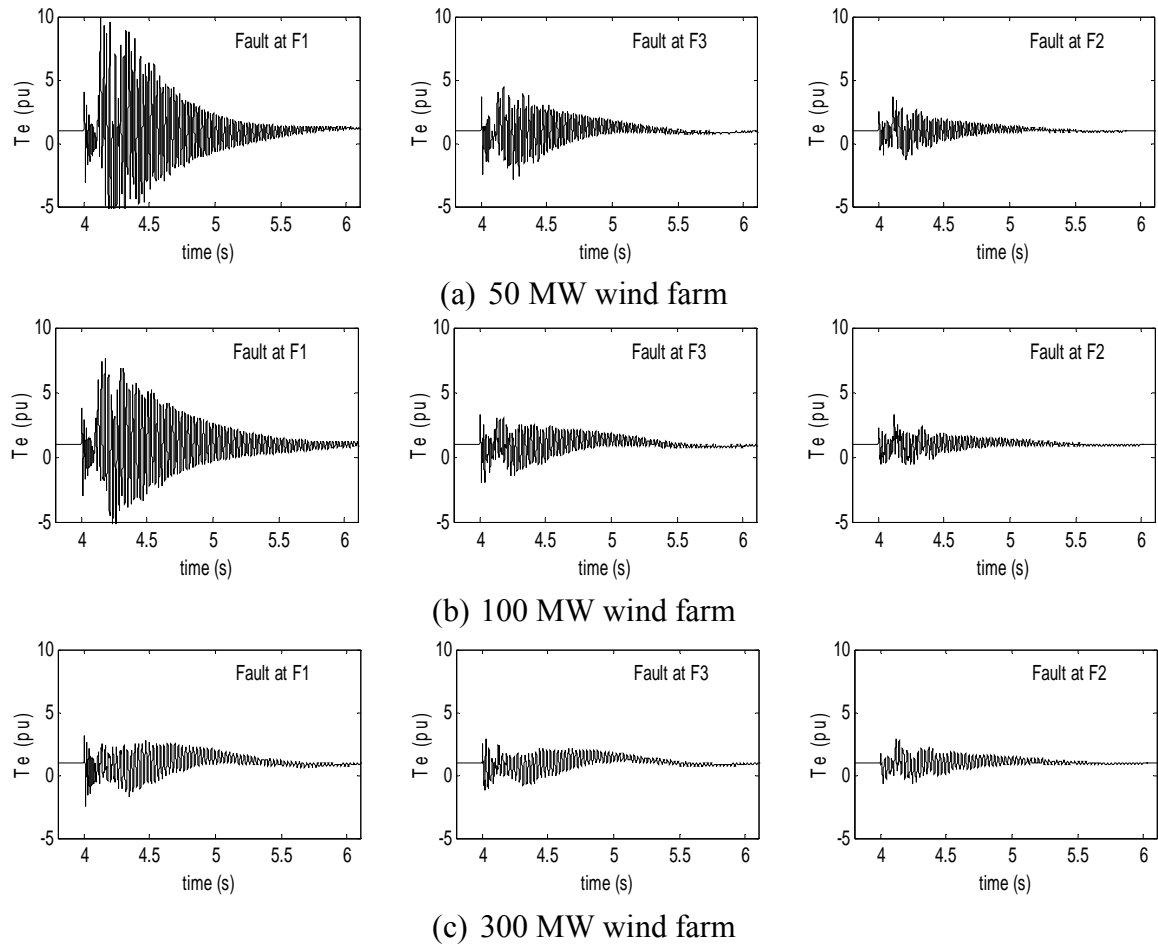
Figure 4.29 Impact of fault location on electromagnetic torque

The shaft torques of different wind farms following the fault at different locations are shown in Figure 4.30. It is shown that the shaft torque does not get amplified excessively like the electromagnetic torque for a fault at F_1. The fault at remote end (location F_2) exhibits the lowest peak overshoot in the shaft torque as shown in Figure 4.30 (a) for a 50MW wind farm. Simulation results for 100MW and 300 MW wind farms are also shown in Figure 4.30 (b) and (c), which also demonstrate a similar behavior for corresponding locations.

(a) 50 MW wind farm

(b) 100 MW wind farm

(c) 300 MW wind farm
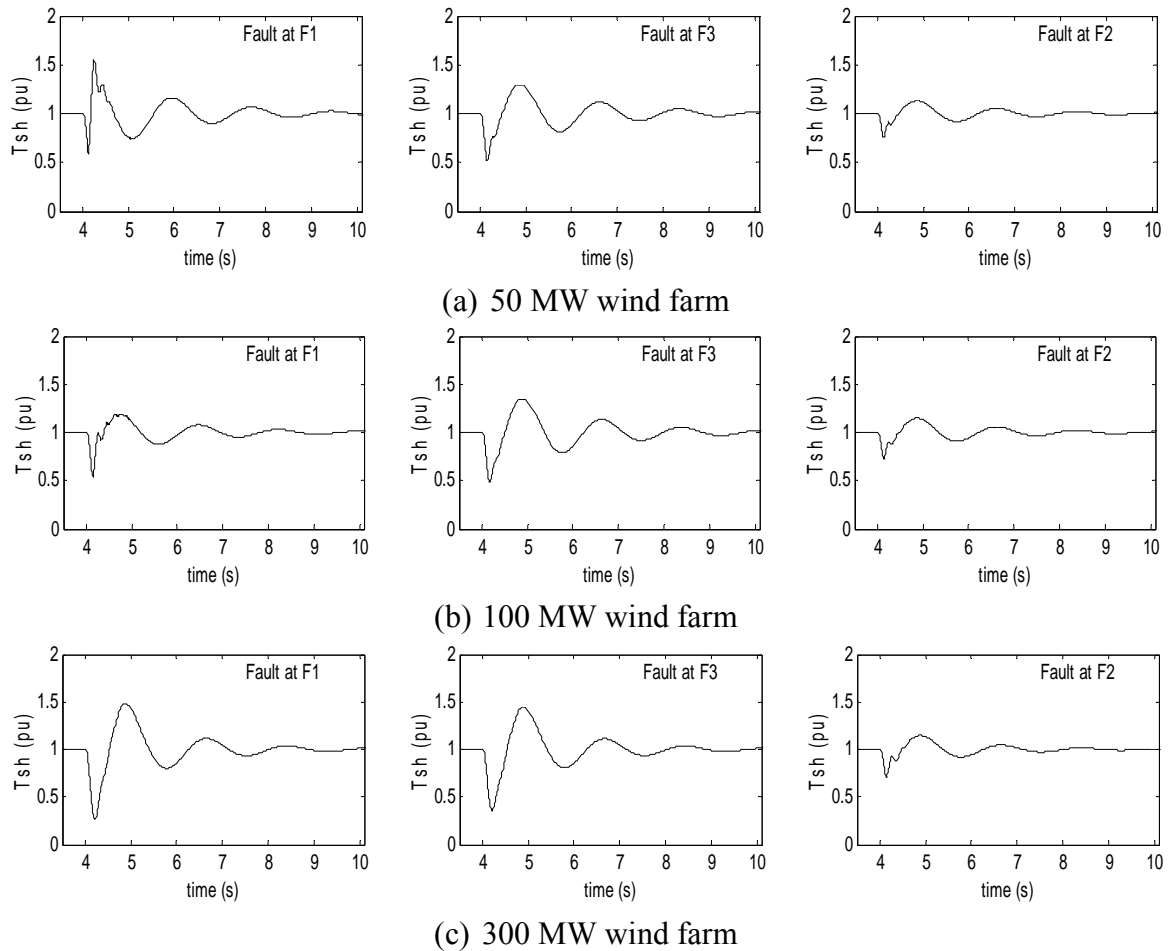
Figure 4.30 Impact of fault location on shaft torque

Since induction generators are not separately excited, their magnetization solely depends upon the reactive current drawn from the grid. Alternatively, shunt capacitor at the terminals provide adequate reactive power to generate active power at unity power factor. The impact of fault locations on the PCC voltage is shown in Figure 4.31. When the fault occurs at F_1, a large fault current flows through the series capacitor, which stores enormous amount of electrical energy. Following the fault clearance, the stored energy is released through the induction generator, which results in the sudden rise in the PCC voltage. The voltage rise is quite prominent in case of 50 MW and 100 MW wind farms as shown in Figure 4.31 (a) and (b), respectively. However, for 300 MW and larger wind farms, no such voltage rise is observed. During the midline fault (location F_3) only one capacitor bank carries the large fault current which discharges through the other end capacitor, thereby minimizing the voltage rise. Hence, fault at location F_3 may not be a

concern for the wind farms. Similarly the fault at F_2 also does not cause any significant rise in the PCC voltage. It is observed that, torsional mode oscillation is found in the PCC voltage for larger wind farms.

(a) 50 MW wind farm

(b) 100 MW wind farm
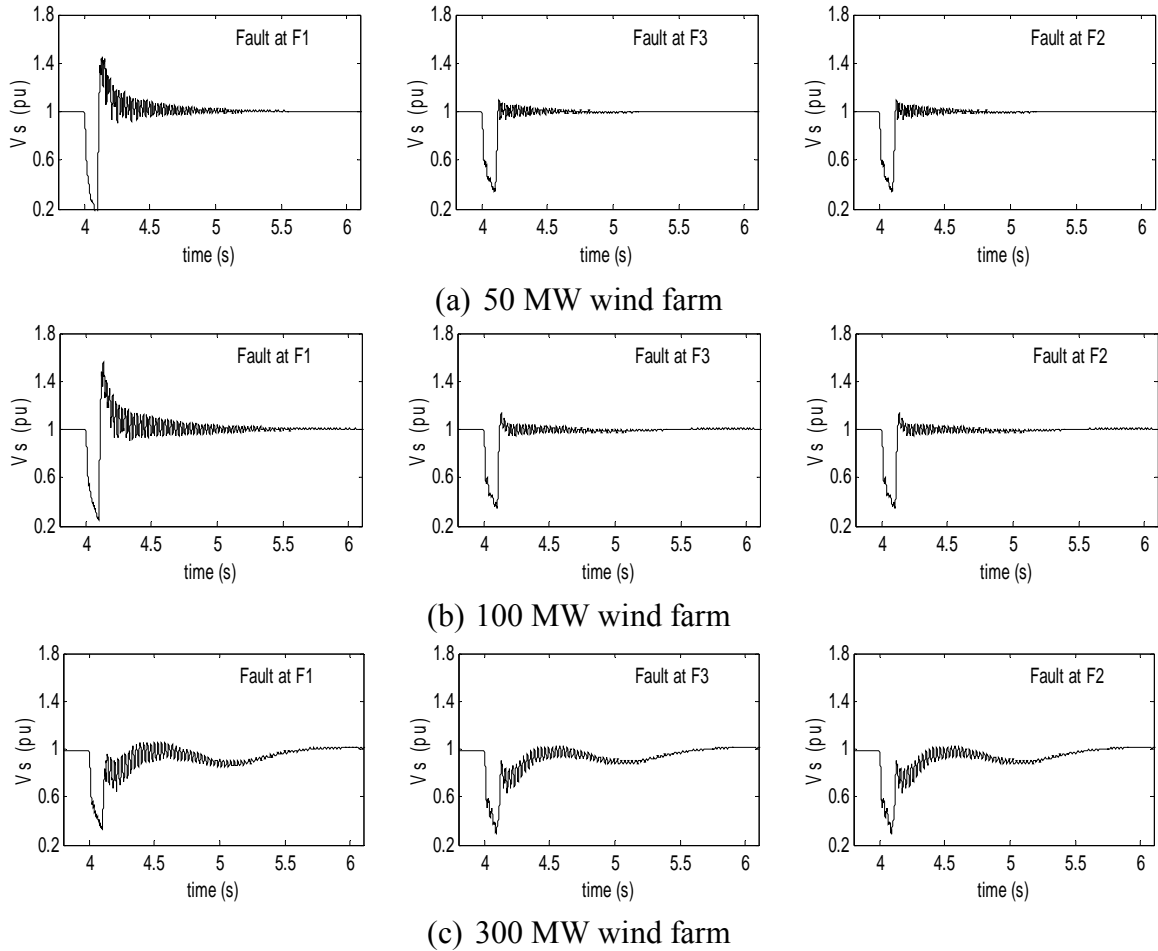
(c) 300 MW wind farm

Figure 4.31 Impact of fault location on PCC voltage

4.6.2 Variation in Wind Farm Output

In order to evaluate the impact of fault during low power output condition, a 500 MW wind farm is considered, whose output is 100 MW. The wind farm is connected to a 40% series compensated line. The fault at location F_1 causes large oscillation in the electromagnetic torque as seen in Figure 4.32 (a) in comparison to the fault at other two locations. The peak electromagnetic torque reaches 3 pu, 1.75 pu and 1.7 pu for faults at F_1, F_3 and F_2, respectively. The shaft torque following the faults is shown in Figure 4.32 (b). It is observed that the peak shaft torques observed in these cases are less than the

peak shaft torques seen in smaller wind farms producing their rated output. The PCC voltage is also found to be within the acceptable limit after the fault is cleared. The oscillations found in the electromagnetic torque are dominated by the electrical mode, whereas the shaft torque oscillation is dominated by the torsional mode. This analysis shows that the adverse impact of fault location decreases as the size of the wind farm increases. In the case of smaller wind farms, the fault near the PCC may cause severe oscillations in the wind farm.

(a) Electromagnetic torque

(b) Shaft torque

(c) PCC voltage
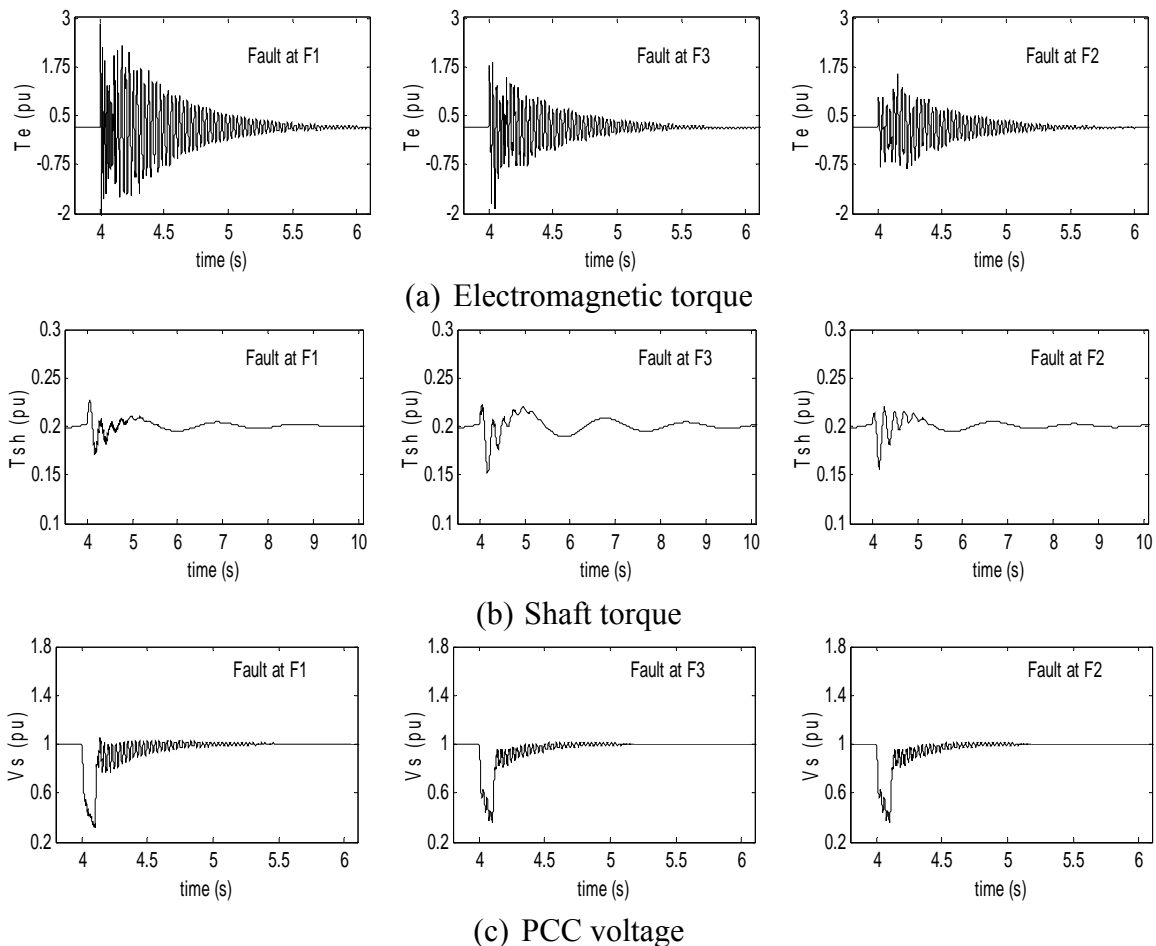
Figure 4.32 Impact of fault location on a 500 MW wind farm during 100 MW output

4.7 TRANSIENT RESPONSE OF SERIES CAPACITOR INSERTION

In this case the series compensation level is changed during the transient simulation at t=4s and the response is illustrated in Figure 4.33. The initial compensation level is chosen as 40% which represents a stable operating condition for all sizes of wind farms

ranging 100 MW-500 MW. At t=4s, when the compensation level is increased to 50%, only 200 MW and 300 MW wind farms experience growing electromagnetic torque. The response is as predicted by the eigenvalue analysis. In the case of 100 MW, 400 MW, and 500 MW wind farms, since critical compensation level is above 50%, the power output and electromagnetic torque following the transient are stabilized. However, in the case of 200 MW and 300 MW wind farms, the oscillation in the power output and electromagnetic torque grows gradually till the system is destabilized, although not shown here.
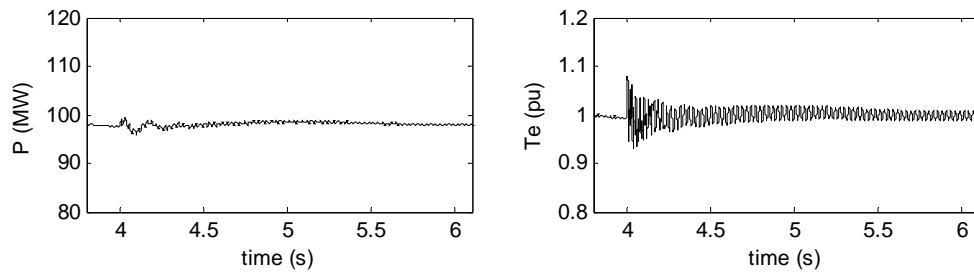
(a) 100 MW wind farm
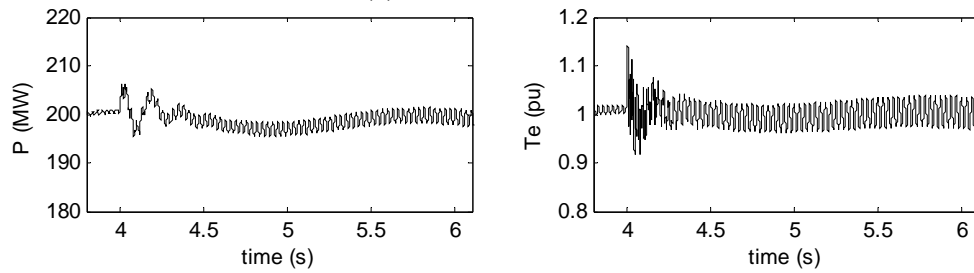
(b) 200 MW wind farm
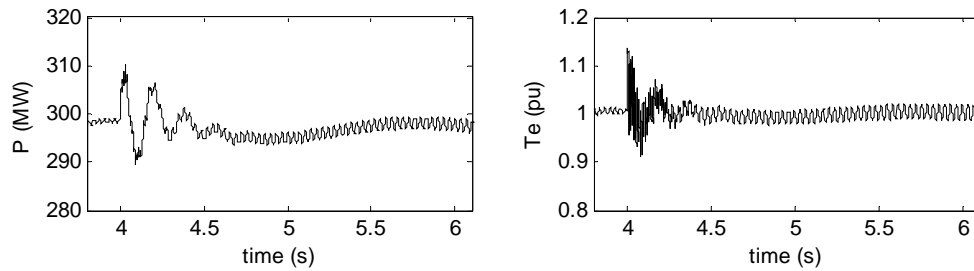
(c) 300 MW wind farm
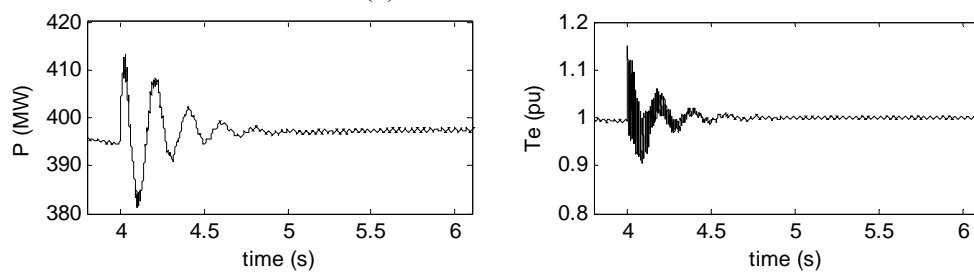
(d) 400 MW wind farm
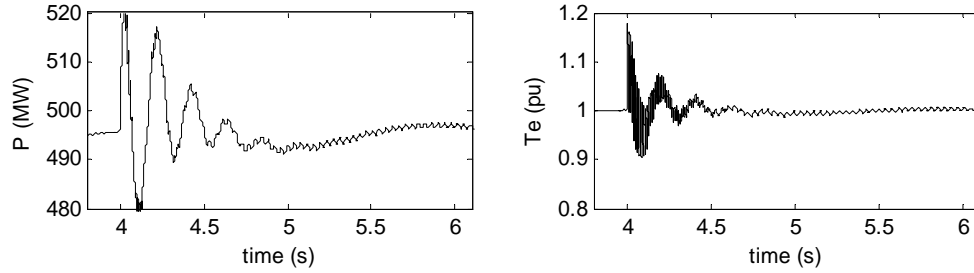
(e) 500 MW wind farm

Figure 4.33 Impact of change in compensation level on the wind farm

4.8 HIGH SHAFT TORQUE

High shaft torque rise refers to the phenomenon that relates to a fault on a series compensated transmission line. During the fault a large amount of energy is stored in the series capacitor, which is discharged through the electrical generator after the fault is cleared. This energy is discharged in the form of a current having a frequency complimentary to the electrical mode damped frequency. In this case the growth rate of the shaft torque is very high. The oscillatory shaft torque may be expected to reach a damaging level within 100ms. Each occurrence of this high amplitude transient torque can result in reduction of the shaft life due to cyclic fatigue.

4.8.1 Equivalent Circuit Analysis

Applying the equivalent circuit theory described in Chapter 2, the impact of terminal fault is examined. The series compensation level is considered as 50%.

The characteristic polynomial of the equivalent circuit is written as:

$$|Z(s)| = a_6 s^6 + a_5 s^5 + a_4 s^4 + a_3 s^3 + a_2 s^2 + a_1 s + a_0 \tag{4.30}$$
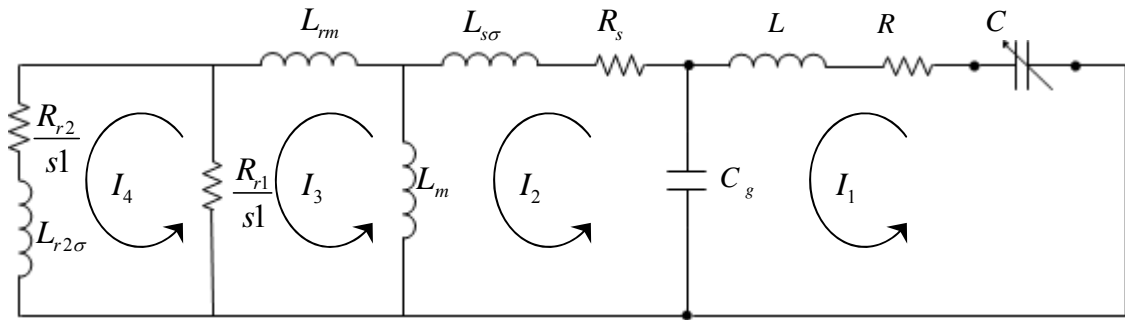
Figure 4.34 Equivalent circuit of study system with double-cage induction generator

Using the parameters of the system shown in Figure 4.34, the slip (sl) dependent roots of (4.30) are calculated. For this system there are six roots obtained by equating the characteristic polynomial to zero. Of these roots, one complex conjugate pair is quite sensitive to the slip of the machine. Keeping other system parameters constant, the loci of the sensitive root is plotted in Figure 4.35 as the slip is varied between 0.02 and -0.6 for different sizes of wind farms. As the slip increases, the roots move to the right, cross the imaginary axis, and subsequently split into two real roots. Further increase in slip causes them to rejoin into a complex pair that starts moving to the left, crosses the imaginary axis and becomes stable. Figure 4.35 shows the loci of the critical root and it is seen that the system is stable above the upper resonant speed and also below the lower resonant speed.

Figure 4.36 shows the upper resonant speed and the lower resonant speed of different sizes of wind farms and different level of series compensation. The color i.d. of each curve is the same as it defined in Figure 4.35. It is observed that as the series compensation and power rating increase, both upper and lower resonant speeds increase substantially, thereby escalating the potential of instability. This behavior of an aggregated induction generator based wind farm presented in this paper is seen to be similar to the single machine analysis shown in [54], [59].
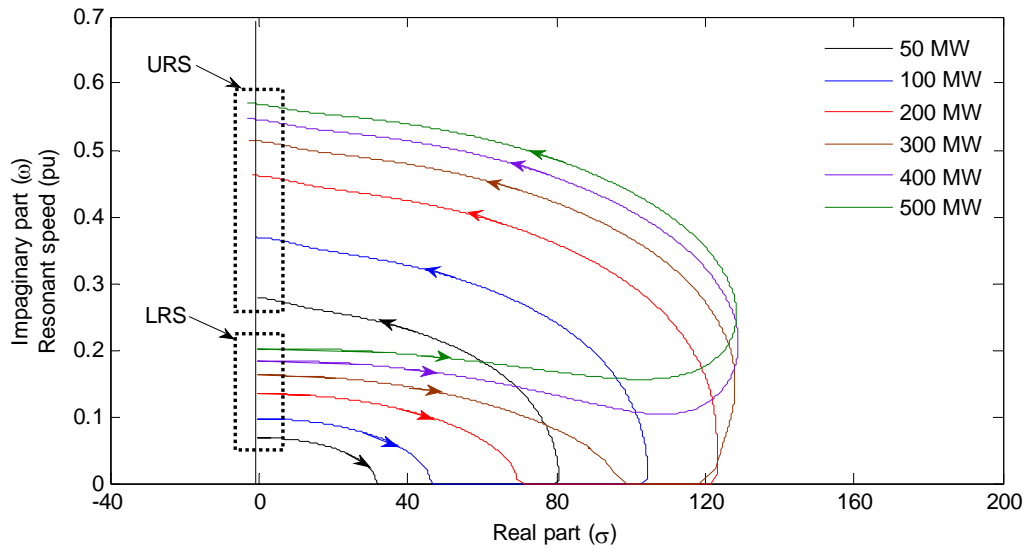
Figure 4.35 Loci of critical root with varying slip of induction generator

(a) Upper resonant speed

(b) Lower resonant speed
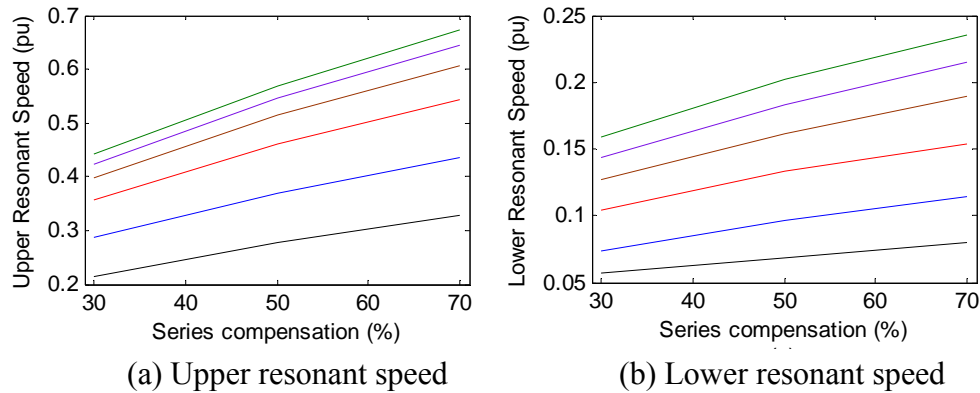
Figure 4.36 Upper and lower resonant speeds

4.8.2 Electromagnetic Transient Simulations

Time domain simulations are carried out for the validation of the equivalent circuit theory analysis that predicts the unstable band of speeds for different size of wind farm and series compensation level. Transient response of a 50 MW wind farm connected to 50% series compensated line is depicted in the Figure 4.37. Following the fault at F_1 the generator speed reaches 1.08 pu before it falls following the fault clearance. The speed falls further, and then stabilizes around the lower resonant speed, as shown in Figure 4.37 (a). When the speed falls below the upper resonant speed (0.277 pu), it cannot recover. For a fault at F_2 this behavior is not seen. Figure 4.37 (b) shows the electromagnetic

torque following the fault at two locations. Fault at F_1 causes a high magnitude and distortion in the electromagnetic torque, whereas fault at F_2 does not have such an adverse impact on the electromagnetic torque. Figure 4.37 (c) shows the significant rise in shaft torque for a fault at F_1. The peak shaft torque reaches up to 25 pu which is critical for the shaft of the wind turbine.

Simulation with a similar fault for a 100 MW wind farm shows the responses of corresponding variables of the wind farm in Figure 4.38. Following the terminal fault, the speed falls and the system becomes unstable. In this case the upper resonant speed threshold is 0.3681 pu. The generator speed for two fault locations is shown in Figure 4.38 (a). Corresponding electromagnetic torque and shaft torque are shown in Figure 4.38 (b) and Figure 4.38 (c), respectively. Figure 4.38 (c) shows a similar increase in the shaft torque. However, for 50 MW and 100 MW wind farms, the fault at location F_2 results in about 20% over shoot in the shaft torque. A single occurrence of a terminal fault as described above causing a large shaft torque may not have significant impact on the shaft. However, if faults were to reoccur over a period of time, repeated application of high torque on the shaft may cause shaft failure due to the cyclic fatigue. As a rule of thumb, it is understood that the stress level should be limited to approximately one tenth the shear limit of the particular steel being used for long shaft system [54]. The peak torque disturbance should not exceed 0.3 pu in the case of any three-phase fault in the electrical network.

Figure 4.39 and Figure 4.40 show the generator speed of a 300 MW and 500 MW wind farm, respectively, following the fault at F_1 and F_2. The 300MW wind farm with 50% series compensation represents an unstable operating condition. However, the 500 MW wind farm with 50% series compensation shows a stabilized speed for the fault at both locations. The speed does not fall below the upper resonant threshold value, and hence recovers once the fault is cleared.
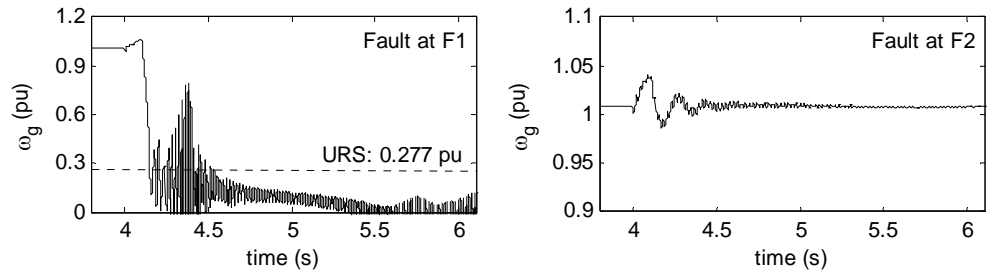
(a) Generator speed
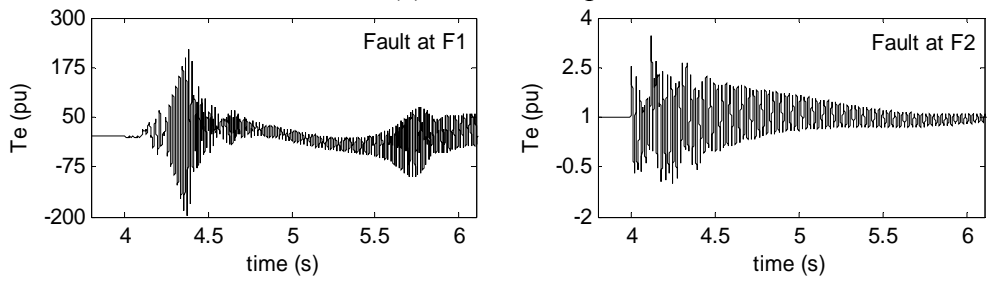
(b) Electromagnetic torque
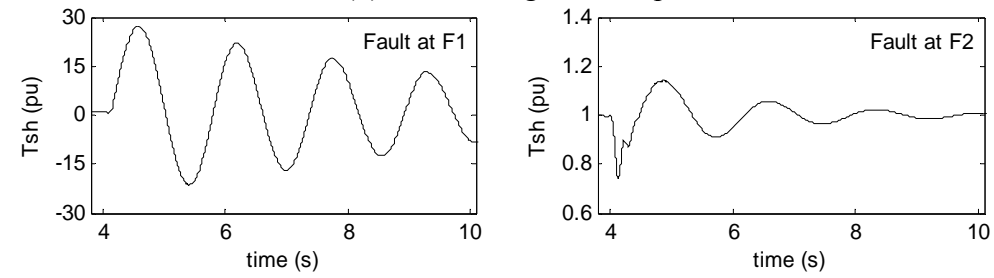
(c) Shaft torque

Figure 4.37 Impact of a terminal fault on a 50 MW wind farm
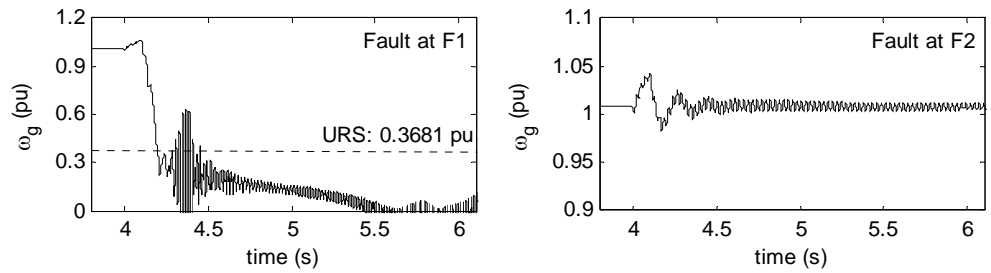
(a) Generator speed
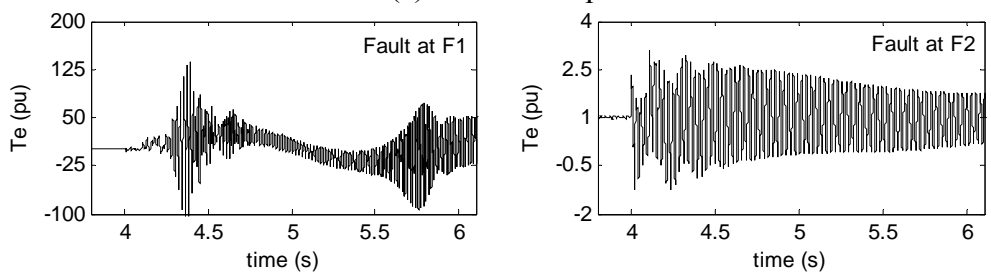
(b) Electromagnetic torque

(c) Shaft torque
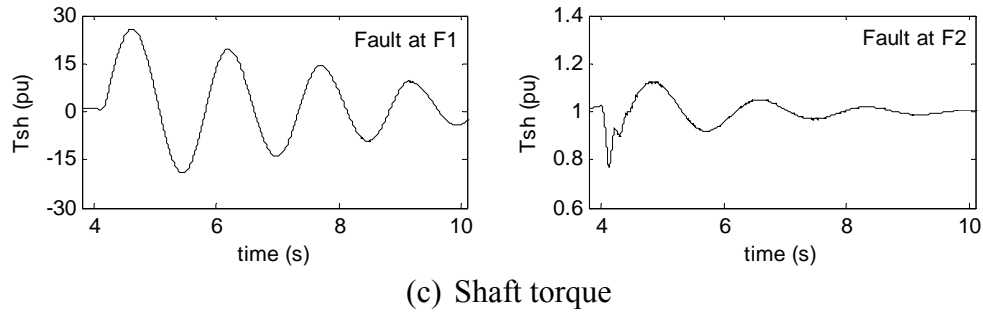
Figure 4.38 Impact of a terminal fault on a 100 MW wind farm
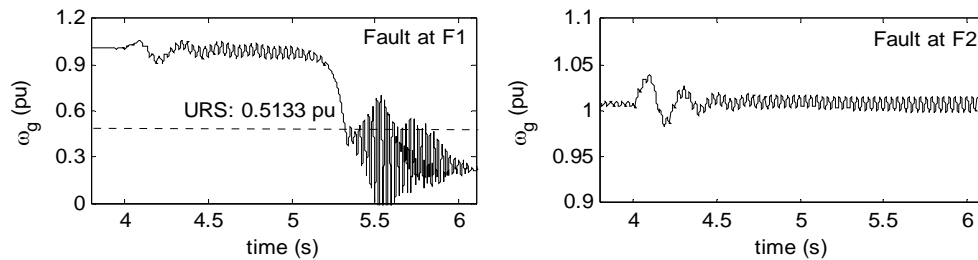
Figure 4.39 Impact of a terminal fault on a 300 MW wind
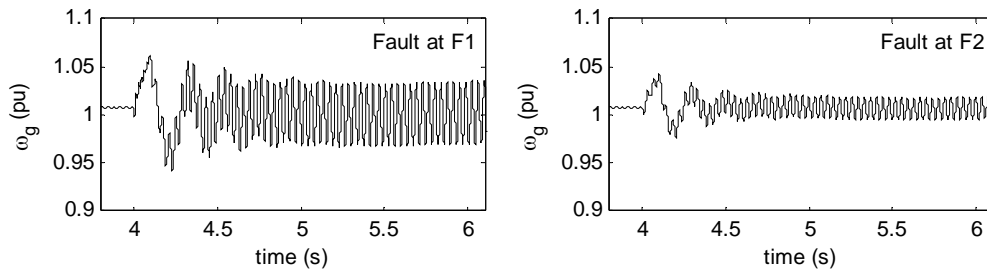
Figure 4.40 Impact of a terminal fault on a 500 MW wind

4.9 CONCLUSIONS

A detailed analysis of the potential of subsynchronous resonance (SSR) in a double-cage induction generator based wind farm connected to a series compensated transmission line is reported in this chapter. A part of this chapter is reported in [132]. In this chapter a complete mathematical model is developed for the overall wind farm including its various subsystems - the aggregated induction generator, torsional system, and ac transmission line, which is the modified IEEE First SSR Benchmark System. System eigenvalues are computed for a wide range of wind farm sizes and a broad range of series compensation levels using MATLAB software. The results are reasonably validated through detailed electromagnetic transient simulation using PSCAD/EMTDC software. The FFT analysis is used to further correlate the frequencies of the critical modes

obtained from small signal studies. The following conclusions are made with respect to the potential of SSR:

(a) Induction generator effect (i.e. the electrical mode becoming unstable) may be experienced even at realistic levels of series compensation, with large wind farms in the range of 100-500 MW.

(b) The critical levels of series compensation for SSR to occur are 56% for 100 MW, 48.25% for 200 MW, 48.6% for 300 MW, 50.5% for 400 MW and 52.6 % for 500 MW wind farms, respectively.

(c) In the case of a 500 MW wind farm, the critical levels of series compensation for SSR to occur are 52.75% for 100 MW, 52.80% for 200 MW, 52.85% for 300 MW, 52.80% for 400 MW and 52.6 % for 500 MW power output, respectively.

(d) Torsional interaction does not seem to occur for the range of wind farm sizes and series compensation levels considered.

(e) Analysis with other commercially available induction generator data reveals similar results, showing the potential for SSR oscillation in the wind farms. Critical levels of series compensation for other induction generators are presented in Table 4.2 and Table 4.4.

(f) Double-cage induction generators have two resonant speeds - an upper resonant speed and a lower resonant speed, with an unstable region of operation between them. Following a fault, if the speed of the induction generator drops below the upper resonant speed, it does not recover to its original speed. In fact, the speed continues to decrease and enters into a limit cycle that is centered around the lower resonant speed.

(g) For small sized wind farms connected to lines at realistic levels of series compensation (50%), a symmetrical fault at the terminal of the wind farm can cause high shaft torques. Although, single occurrence of such a fault event may not have significant impact on the shaft but repeated occurrences may cause shaft failure due to cyclic fatigue.

(h) Large MW rated wind farms producing small MW power outputs do not exhibit high shaft torques in response to terminal faults, as observed with the small power rated wind farms.

From the studies conducted with the study system, it appears that SSR may occur even for realistic levels of series compensation levels (typically 50%) for a 100 MW or lesser size wind farm. Since small size wind farms can be subjected to high shaft torques in response to terminal faults, detailed analysis must be performed to understand such impacts before connecting these induction generator based wind farms to a series compensated transmission line. Suitable preventive measures may also be undertaken to avoid any potential damage to the torsional system of the wind turbines.

Chapter 5

SUBSYNCHRONOUS RESONANCE ANALYSIS IN MODIFIED IEEE SECOND BENCHMARK SYSTEM

5.1 INTRODUCTION

Subsynchronous resonance analysis carried out in Chapters 3 and 4 corresponds to a radial series compensated line. This chapter presents a comprehensive study of subsynchronous resonance in induction generator based wind farms connected to non-radial series compensated networks. The analysis is carried out with induction generator based wind farms connected to modified IEEE Second Benchmark Systems. Two systems proposed in [113] are considered in this chapter. The study system-I is adapted for the study of parallel resonance; whereas the system-II is used for the study of mutual interaction between the two wind farms connected to a radial series compensated transmission line. Eigenvalue analysis is performed to predict the potential for subsynchronous resonance in wind farms, which is then reasonably validated with the PSCAD/EMTDC simulations. Fault studies are also conducted over a wide range of operating scenarios to examine the impacts of series capacitors on the performance of a wind farm. Participation factor analysis is also done to ascertain the influence of various parameters on the subsynchronous modes.

5.2 SYSTEM DESCRIPTION

The study system-I is a modified version of the IEEE Second Benchmark System-1, in which a 600 MVA synchronous generator is replaced with a 500 MW double-cage induction generator based wind farm as shown in Figure 5.1. The equivalent wind farm is modeled by the dynamic aggregation of 217 identical double-cage induction generators, each of 2.3 MW rating. The modified IEEE Second Benchmark System-2 is considered as the study system-II shown in Figure 5.2. In this system two 300 MW sized double-cage induction generator based wind farms are connected in place of synchronous generators.
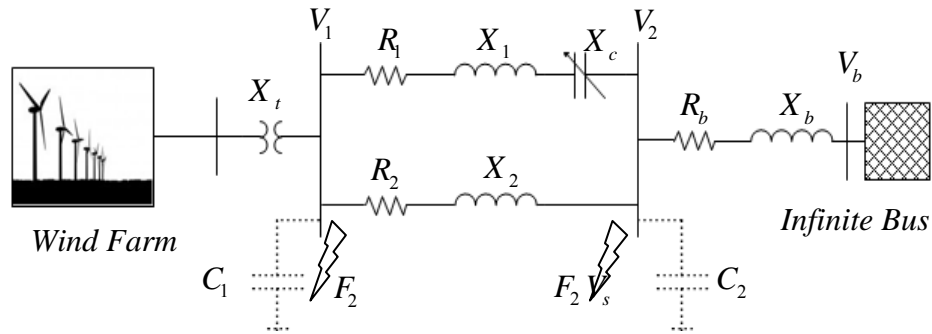
Figure 5.1 Study system-I
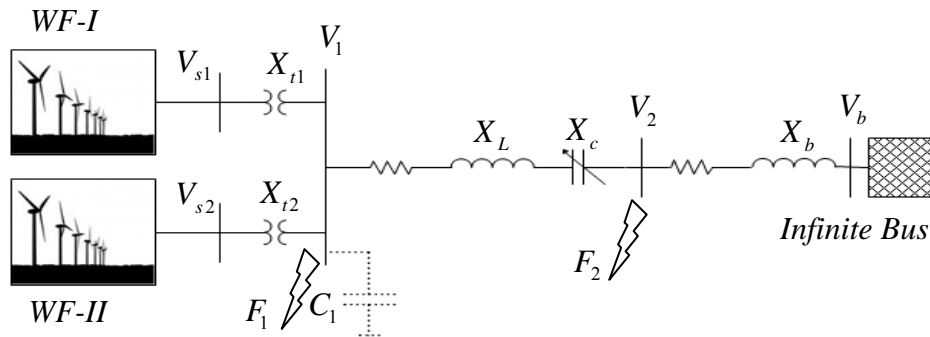
Figure 5.2 Study system-II

5.3   SYSTEM MODELING

5.3.1   Modeling of Study System-I

The dynamic models of mechanical drive train and double-cage induction generator are already presented in Chapter-2. Hence, only the network equations are presented here. In order to simplify the modeling, two fictitious capacitors are considered at Bus-1 and Bus-2. The capacitor at Bus-1 reduces the complexity involved in interfacing the wind farm with the network. Addition of such capacitors does not affect the subsynchronous resonance analysis that is discussed in Sec. 5.4. The differential equations of the network are written in synchronously rotating *d-q* reference frame.

$$C_g \frac{d}{dt}V_{ds} = I_{ds} - I_d + \omega_s C_g V_{qs} \tag{5.1}$$

$$C_g \frac{d}{dt} V_{qs} = I_{qs} - I_q - \omega_s C_g V_{ds} \tag{5.2}$$

$$L_t \frac{d}{dt} I_d = V_{ds} - R_t I_d + \omega_s L_t I_q - V_{d1} \tag{5.3}$$

$$L_t \frac{d}{dt} I_q = V_{qs} - R_t I_q - \omega_s L_t I_d - V_{q1} \tag{5.4}$$

$$L_1 \frac{d}{dt} I_{d1} = V_{d1} - R_1 I_{d1} + \omega_s L_1 I_{q1} - V_{cd} - V_{d2} \tag{5.5}$$

$$L_1 \frac{d}{dt} I_{q1} = V_{q1} - R_1 I_{q1} - \omega_s L_1 I_{d1} - V_{cq} - V_{q2} \tag{5.6}$$

$$L_2 \frac{d}{dt} I_{d2} = V_{d1} - R_2 I_{d2} + \omega_s L_2 I_{q2} - V_{d2} \tag{5.7}$$

$$L_2 \frac{d}{dt} I_{q2} = V_{q1} - R_2 I_{q2} - \omega_s L_2 I_{d2} - V_{q2} \tag{5.8}$$

$$C_1 \frac{d}{dt} V_{d1} = I_d - I_{d1} - I_{d2} + \omega_s C_1 V_{q1} \tag{5.9}$$

$$C_1 \frac{d}{dt} V_{q1} = I_q - I_{q1} - I_{q2} - \omega_s C_1 V_{d1} \tag{5.10}$$

$$C_2 \frac{d}{dt} V_{d2} = I_{d1} + I_{d2} - I_{bd} + \omega_s C_2 V_{q2} \tag{5.11}$$

$$C_2 \frac{d}{dt} V_{q2} = I_{q1} + I_{q2} - I_{bq} - \omega_s C_2 V_{d2} \tag{5.12}$$

$$L_b \frac{d}{dt} I_{bd} = V_{d2} - R_b I_{bd} + \omega_s L_b I_{bq} - V_{bd} \tag{5.13}$$

$$L_b \frac{d}{dt} I_{bq} = V_{q2} - R_b I_{bq} - \omega_s L_b I_{bd} - V_{bq} \tag{5.14}$$

$$C \frac{d}{dt} V_{cd} = I_{d1} + \omega_s C V_{cq} \tag{5.15}$$

$$C \frac{d}{dt} V_{cq} = I_{q1} - \omega_s C V_{cd} \tag{5.16}$$

where,

C_g : Power factor correction capacitor at wind turbine generator terminal (pu)

R_t : Transformer winding resistance (pu)

L_t : Transformer winding leakage inductance (pu)

C_1 : Fictitious shunt capacitance at bus-1 (pu)

C_2 : Fictitious shunt capacitance at bus-2 (pu)

R_1 : Resistance of AC transmission line-1 (pu)

L_1 : Inductance of AC transmission line-1 (pu)

R_2 : Resistance of AC transmission line-2 (pu)

L_2 : Inductance of AC transmission line-2 (pu)

C : Capacitance in series with AC transmission line-1 (pu)

V_{ds}, V_{qs} : d-q axis voltage at wind turbine terminal (pu)

V_{d1}, V_{q1} : d-q axis voltage at bus-1 (pu)

V_{d2}, V_{q2} : d-q axis voltage at bus-2 (pu)

V_{bd}, V_{bq} : d-q axis voltage at infinite bus (pu)

V_{cd}, V_{cq} : d-q axis voltage across series capacitor (pu)

I_{ds}, I_{qs} : d-q axis stator current of wind turbine generator (pu)

I_d, I_q : d-q axis current from wind farm to bus-1 (pu)

I_{d1}, I_{q1} : d-q axis current of transmission line-1 (pu)

I_{d2}, I_{q2} : d-q axis current of transmission line-2 (pu)

I_{bd}, I_{bq} : d-q axis current from bus-2 to infinite bus (pu)

Linearizing (5.1)-(5.16), the state space model of the network is obtained. The state variables are defined as:

$$x_N^t = \left[\Delta V_{ds}, \Delta V_{qs}, \Delta I_d, \Delta I_q, \Delta I_{d1}, \Delta I_{q1}, \Delta I_{d2}, \Delta I_{q2}, \Delta V_{d1}, \Delta V_{q1}, \Delta V_{d2}, \Delta V_{q2}, \Delta V_{cd}, \Delta V_{cq} \right] (5.17)$$

Wind turbine and induction generator models are taken from Chapter 2. Suitably aggregating the various sub-systems, the complete system can be expressed in the state space form as:

$$\dot{x}_{sys} = \left[A_{sys} \right] x_{sys} + \left[B_{sys} \right] u_{sys}$$
$$y_{sys} = \left[C_{sys} \right] x_{sys} \tag{5.18}$$

where,

$$x_{sys}^t = \left[x_{WT}^t \quad x_G^t \quad x_N^t \right] \tag{5.19}$$

$$x_{WT}^t = \left[\Delta\omega_t \quad \Delta\delta_{tg} \quad \Delta\omega_g \right] \tag{5.20}$$

$$x_G^t = \left[\Delta I_{ds} \quad \Delta I_{qs} \quad \Delta E_{d1} \quad \Delta E_{q1} \quad \Delta E_{d2} \quad \Delta E_{q2} \right] \tag{5.21}$$

$$u_{sys}^t = \left[\Delta T_w \quad \Delta V_{bd} \quad \Delta V_{bq} \right] \tag{5.22}$$

In this case the state matrix $\left[A_{sys} \right]$ is a 25×25 matrix, whereas $\left[B_{sys} \right]$ is a 25×3 matrix. Since $\left[C_{sys} \right]$ is not required in this study, hence it is not defined.

5.3.2   Modeling of Study System-II

In the system-II, two identical wind farms are connected to the radial series compensated line and each aggregated wind farm consists of equivalent mechanical drive train and double-cage induction generator models which have already been described in Chapter 2. Hence, this section only presents the linearized state space model of the network that includes two interfacing transformer and series compensated line. In this case, a shunt-connected capacitor C_1 is assumed at the Bus-1 which simplifies the interconnection of the state space model of the wind farm and the network. The network differential equations are written as:

$$C_{g1} \frac{d}{dt} V_{ds1} = I_{ds1} - I_{d1} + \omega_s C_{g1} V_{qs1} \tag{5.23}$$

$$C_{g1} \frac{d}{dt} V_{qs1} = I_{qs1} - I_{q1} - \omega_s C_{g1} V_{ds1} \tag{5.24}$$

$$C_{g2}\frac{d}{dt}V_{ds2} = I_{ds2} - I_{d2} + \omega_s C_{g2}V_{qs2} \qquad (5.25)$$

$$C_{g2}\frac{d}{dt}V_{qs2} = I_{qs2} - I_{q2} - \omega_s C_{g2}V_{ds2} \qquad (5.26)$$

$$L_{t1}\frac{d}{dt}I_{d1} = V_{ds1} - R_{t1}I_{d1} + \omega_s L_{t1}I_{q1} - V_{d1} \qquad (5.27)$$

$$L_{t1}\frac{d}{dt}I_{q1} = V_{qs1} - R_{t1}I_{q1} - \omega_s L_{t1}I_{d1} - V_{q1} \qquad (5.28)$$

$$L_{t2}\frac{d}{dt}I_{d2} = V_{ds2} - R_{t2}I_{d2} + \omega_s L_{t2}I_{q2} - V_{d1} \qquad (5.29)$$

$$L_{t2}\frac{d}{dt}I_{q2} = V_{qs2} - R_{t2}I_{q2} - \omega_s L_{t2}I_{d2} - V_{q1} \qquad (5.30)$$

$$C_1\frac{d}{dt}V_{d1} = I_{d1} + I_{d2} - I_d + \omega_s C_1 V_{q1} \qquad (5.31)$$

$$C_1\frac{d}{dt}V_{q1} = I_{q1} + I_{q2} - I_q - \omega_s C_1 V_{d1} \qquad (5.32)$$

$$\left(L_1 + L_b\right)\frac{d}{dt}I_d = V_d - \left(R_1 + R_b\right)I_d + \omega_s\left(L_1 + L_b\right)I_q - V_{cd} - V_{bd} \qquad (5.33)$$

$$\left(L_1 + L_b\right)\frac{d}{dt}I_q = V_q - \left(R_1 + R_b\right)I_q - \omega_s\left(L_1 + L_b\right)I_d - V_{cq} - V_{bq} \qquad (5.34)$$

$$C\frac{d}{dt}V_{cd} = I_d + \omega_s C V_{cq} \qquad (5.35)$$

$$C\frac{d}{dt}V_{cq} = I_q - \omega_s C V_{cd} \qquad (5.36)$$

where,

R_{t1}	:	Transformer-1 winding resistance
L_{t1}	:	Transformer-1 winding leakage inductance
R_{t2}	:	Transformer-2 winding resistance
L_{t2}	:	Transformer-2 winding leakage inductance
C_1	:	Fictitious shunt capacitance at bus-1
R_1	:	Resistance of AC transmission line

L_1	:	Inductance of AC transmission line
C	:	Capacitance in series with AC transmission
V_{ds1}, V_{qs1}	:	d-q axis voltage at wind turbine-1 terminal
V_{ds2}, V_{qs2}	:	d-q axis voltage at wind turbine-2 terminal
V_{d1}, V_{q1}	:	d-q axis voltage at bus-1
V_{bd}, V_{bq}	:	d-q axis voltage at infinite bus
V_{cd}, V_{cq}	:	d-q axis voltage across series capacitor
I_{ds1}, I_{qs1}	:	d-q axis stator current of wind turbine generator-1
I_{ds1}, I_{qs1}	:	d-q axis stator current of wind turbine generator-1
I_d, I_q	:	d-q axis current of series compensated transmission line

In order to obtain a state space model of the network, the differential equations presented in (5.23)-(5.36) are linearized. The complete system state space model is now obtained by combining the wind farm and the network model.

$$\dot{x}_{sys} = \left[A_{sys} \right] x_{sys} + \left[B_{sys} \right] u_{sys}$$
$$y_{sys} = \left[C_{sys} \right] x_{sys}$$

(5.37)

where,

$$x^t_{sys} = \begin{bmatrix} x^t_{WT1} & x^t_{G1} & x^t_{WT2} & x^t_{G2} & x^t_N \end{bmatrix}$$

(5.38)

$$x^t_{WT1} = \begin{bmatrix} \Delta\omega_{t1} & \Delta\delta_{tg1} & \Delta\omega_{g1} \end{bmatrix}$$

(5.39)

$$x^t_{WT2} = \begin{bmatrix} \Delta\omega_{t2} & \Delta\delta_{tg2} & \Delta\omega_{g2} \end{bmatrix}$$

(5.40)

$$x^t_{G1} = \begin{bmatrix} \Delta I_{ds1} & \Delta I_{qs1} & \Delta E_{d11} & \Delta E_{q11} & \Delta E_{d21} & \Delta E_{q21} \end{bmatrix}$$

(5.41)

$$x^t_{G2} = \begin{bmatrix} \Delta I_{ds2} & \Delta I_{qs2} & \Delta E_{d12} & \Delta E_{q12} & \Delta E_{d22} & \Delta E_{q22} \end{bmatrix}$$

(5.42)

$$x^t_N = \begin{bmatrix} \Delta V_{ds1}, \Delta V_{qs1}, \Delta V_{ds2}, \Delta V_{qs2}, \Delta I_{d1}, \Delta I_{q1}, \Delta I_{d2}, \Delta I_{q2}, \Delta V_{d1}, \Delta V_{q1}, \Delta I_d, \Delta I_q, \Delta V_{cd}, \Delta V_{cq} \end{bmatrix}$$

(5.43)

$$u^t_{sys} = \begin{bmatrix} \Delta T_{w1} & \Delta T_{w2} & \Delta V_{bd} & \Delta V_{bq} \end{bmatrix}$$

(5.44)

The system state matrix $\left[A_{sys} \right]$ is a 32×32 matrix and input matrix $\left[B_{sys} \right]$ is a 32×4 matrix.

5.4   SMALL SIGNAL ANALYSIS OF STUDY SYSTEM-I

5.4.1   Eigenvalue Analysis

Eigenvalues of the complete system state matrix $\left[A_{sys} \right]$ are calculated and depicted in Table 5.1 for a 300 MW wind farm with 50% series compensation. There are twenty-five states as can be seen from the state space model. This results in thirteen modes, out of which twelve oscillatory modes are presented by paired complex conjugate eigenvalues and the only non-oscillatory mode is represented by a real eigenvalue. The high frequency mode eigenvalues -10.948 ± 3.6751e+011i and -6.0807±2.3952e+011i are associated with the dynamics of the shunt capacitors at Bus-1 and Bus-2 and have minimal impact on the other system modes. Table 5.2 shows the calculated eigenvalues of the selected modes of system-I for different sizes of wind farm and series compensation levels. These modes are electrical, electromechanical, and torsional mode. It is observed that as the series compensation level increases, the electrical mode becomes less stable. However, change in the stability is marginal and may not cause any instability even though modal frequency decreases sharply. In another scenario, when the size of the wind farm is increased at a fixed compensation level, initially the electrical mode tends to become less stable but later becomes more stable. A decrease in the frequency is also observed here. The other modes are found to be substantially stable.

Table 5.3 shows the eigenvalues of the system-I with variable power output condition resulting from variation in the wind speed. The wind farm size chosen is 500 MW. The impact of power output on the stability of electrical mode is found to be quite negligible. However, the stability of both electromechanical and torsional mode improves with the increase in the power output. With the increase in series compensation level, although stability of the electrical mode is unaffected, the modal frequency decreases substantially. The stability of electromechanical mode and torsional mode also improve with the increase in the power output at a constant series compensation level. When series

compensation level increases at a constant power output, stability of electrical mode decreases gradually along with a substantial decrease in the modal frequency. Electromechanical mode stability and modal frequency both increase marginally. However, the torsional mode is found to be the least affected by the variation in the series compensation.

Table 5.1 Eigenvalues of system-I

Mode	Eigenvalues
Sup. Sync. mode	-15.953 ± 588.93i
Electrical mode	-14.536 ± 164.89i
Elect- mech. mode	-3.8228 ± 28.752i
Torsional mode	-0.6853 ± 3.5679i
All other modes	-10.948 ± 3.6751e+011i
	-10.948 ± 3.6751e+011i
	-6.0807 ± 2.3952e+011i
	-6.0807 ± 2.3952e+011i
	-12.272 ± 1918i
	-15.447 ± 1164.1i
	-19.703 ± 376.6i
	-59.592 ± 3.2573i
	-3.9897

Table 5.2 System-I eigenvalues with different wind farm size

Mode	100 MW	300 MW	500 MW
50% Series compensation			
Electrical mode	-15.20 ± 174.4i	-14.53 ± 164.89i	-14.54 ± 160.76i
Elect- mech. mode	-5.681 ± 34.866i	-3.822 ± 28.752i	-3.193 ± 24.062i
Torsional mode	-0.541 ± 3.5809i	-0.685 ± 3.5679i	-0.898 ± 3.8634i
70% Series compensation			
Electrical mode	-14.77 ± 137.05i	-13.97 ± 125.77i	-14.04 ± 120.87i
Elect- mech. mode	-5.822 ± 35.368i	-3.948 ± 29.746i	-3.190 ± 25.473i
Torsional mode	-0.533 ± 3.5838i	-0.639 ± 3.5587i	-0.838 ± 3.7029i
90% Series compensation			
Electrical mode	-14.18 ± 104.65i	-13.23 ± 91.659i	-13.38 ± 86.038i
Elect- mech. mode	-6.020 ± 36.193i	-4.095 ± 31.413i	-3.170 ± 27.677i
Torsional mode	-0.521 ± 3.5882i	-0.582 ± 3.5561i	-0.705 ± 3.5812i

Table 5.3 System-I eigenvalues with different wind farm output

Mode	100 MW	300 MW	500 MW
50% Series compensation			
Electrical mode	-14.57 ± 160.56i	-14.57 ± 160.61i	-14.54 ± 160.76i
Elect- mech. mode	-2.214 ± 26.754i	-2.451 ± 26.079i	-3.193 ± 24.062i
Torsional mode	-0.395 ± 3.4309i	-0.509 ± 3.4442i	-0.898 ± 3.8634i
70% Series compensation			
Electrical mode	-14.088 ± 120.57i	-14.08 ± 120.65i	-14.04 ± 120.87i
Elect- mech. mode	-2.3473 ± 27.592i	-2.567 ± 27.073i	-3.190 ± 25.473i
Torsional mode	-0.3962 ± 3.4488i	-0.488 ± 3.4592i	-0.838 ± 3.7029i
90% Series compensation			
Electrical mode	-13.45 ± 85.66i	-13.45 ± 85.756i	-13.38 ± 86.038i
Elect- mech. mode	-2.470 ± 29.079i	-2.665 ± 28.791i	-3.170 ± 27.677i
Torsional mode	-0.396 ± 3.4739i	-0.460 ± 3.4819i	-0.705 ± 3.5812i

Table 5.4 shows the calculated eigenvalues of the system-I during a contingency, i.e. uncompensated line is out of service. With this line outage, the wind farm becomes exposed to a radial system with series compensation. The electrical mode stability deceases significantly in comparison to original non-radial system, as can be seen from Table 5.4 . The impact of wind farm size and series compensation level is now comparable to the First Benchmark System described in Chapter 4. However, in this contingency the radial series compensated line does not cause any potential for SSR in the wind farm. This is primarily due to the large resistance of the radial line. It is noted that in First Benchmark System the X/R ratio of the series compensated line is 25 whereas in Second Benchmark System-1, the compensated line has an X/R ratio of 10.8. In this contingency scenario, the impact of variable output is shown in Table 5.5. The change in stability of the concern modes is comparable to the non-contingency period. However, stability of the electrical mode and electromechanical mode decreases substantially during the line contingency. From all of these eigenvalues it is thus confirmed that there is no potential for either induction generator effect or torsional interaction in a non-radial condition. This observation stands valid even during the contingency period when the uncompensated line is out of service.

Table 5.4 System eigenvalues with outage of one line for different wind farm size

Mode	100 MW	300 MW	500 MW
50% Series compensation			
Electrical mode	-4.535 ± 246.85i	-7.2 ± 207.76i	-8.637 ± 194.93i
Elect- mech. mode	-5.411 ± 34.298i	-3.515 ± 27.639i	-3.095 ± 22.328i
Torsional mode	-0.542 ± 3.5764i	-0.717 ± 3.583i	-0.842 ± 4.0648i
70% Series compensation			
Electrical mode	-3.475 ± 223.14i	-6.035 ± 176.78i	-7.636 ± 161.45i
Elect- mech. mode	-5.707 ± 35.166i	-3.785 ± 29.384i	-3.048 ± 25.001i
Torsional mode	-0.530 ± 3.5821i	-0.634 ± 3.5566i	-0.826 ± 3.7192i
90% Series compensation			
Electrical mode	-2.366 ± 202.73i	-4.663 ± 149.97i	-6.406 ± 132.37i
Elect- mech. mode	-6.048 ± 36.099i	-4.172 ± 31.358i	-3.241 ± 27.719i
Torsional mode	-0.519 ± 3.5884i	-0.571 ± 3.5555i	-0.679 ± 3.5719i

Table 5.5 System eigenvalues with outage of one line for different wind farm output

Mode	100 MW	300 MW	500 MW
50% Series compensation			
Electrical mode	-8.722 ± 194.46i	-8.708 ± 194.57i	-8.637 ± 194.93i
Elect- mech. mode	-1.906 ± 25.666i	-2.160 ± 24.915i	-3.094 ± 22.328i
Torsional mode	-0.388 ± 3.4007i	-0.520 ± 3.4195i	-0.842 ± 4.0648i
70% Series compensation			
Electrical mode	-7.736 ± 160.87i	-7.718 ± 161.02i	-7.636 ± 161.45i
Elect- mech. mode	-2.188 ± 27.108i	-2.411 ± 26.64i	-3.048 ± 25.001i
Torsional mode	-0.390 ± 3.4366i	-0.482 ± 3.4486i	-0.826 ± 3.7192i
90% Series compensation			
Electrical mode	-6.521 ± 131.67i	-6.501 ± 131.86i	-6.405 ± 132.37i
Elect- mech. mode	-2.567 ± 28.955i	-2.759 ± 28.738i	-3.240 ± 27.719i
Torsional mode	-0.394 ± 3.4734i	-0.453 ± 3.482i	-0.679 ± 3.5719i

5.4.2 Participation Factor Analysis

The participation analysis of three modes is shown in Figure 5.3. A detail procedure of the participation factor analysis is already described in Chapter 2. Figure 5.3 (a) shows a strong participation of series capacitor voltage, line current, and parallel line current on the electrical mode. The impact of stator current is very small. Similarly, the electromechanical mode is strongly influenced by the generator speed and the *d* axis induced voltage in the rotor. No influence of the network is observed, as can be seen from Figure 5.3 (b). Figure 5.3 (c) shows the participation factors associated with the torsional

mode that is highly influenced by the wind turbine inertia and shaft stiffness. Contribution of rotor circuit is found to be very small in this case.

(a) Electrical mode   (b) Electromechanical mode

(c) Torsional mode
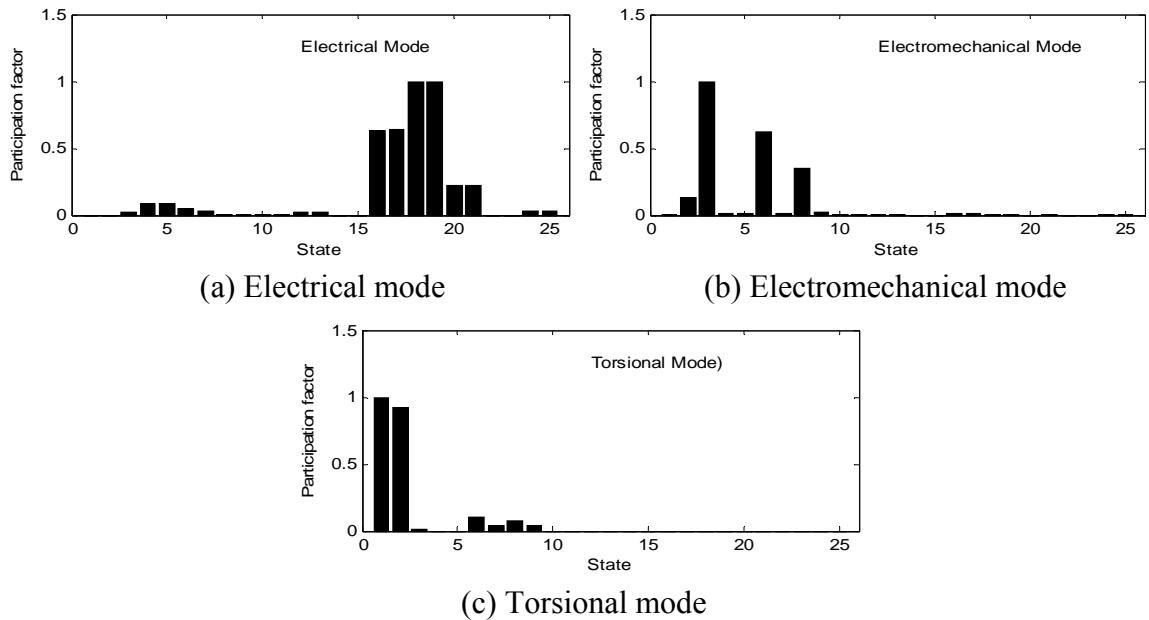
Figure 5.3 Participation factor of system-I modes

5.5   SMALL SIGNAL ANALYSIS OF STUDY SYSTEM-II

5.5.1   Eigenvalue analysis

In system-II two similar wind farms are connected to a radial series compensated transmission line. The system parameters are given in Appendix B and C. The potential of SSR is investigated through a comprehensive eigenvalue analysis. Selected eigenvalues for different sizes of wind farms are shown in Table 5.6. From the Table 5.6 no operating condition seems to indicate the potential for SSR in the wind farms. In every case all of the modes i.e. electrical, electromechanical, and torsional mode remain stable. Though the electrical mode and torsional mode become less stable with increase in the series compensation level, they do not show any instability even up to 90% series compensation.

Table 5.6 shows the eigenvalues of the system with two symmetrical wind farms. In order to see the impact of series compensation on asymmetrical size of wind farms, two more case studies are reported in Table 5.7 and Table 5.8.

Table 5.7 shows the eigenvalues of a smaller wind farm (WF-I) connected across a larger wind farm (WF-II). From the eigenvalue analysis, it is seen that individual wind farm size has negligible influence over the electrical mode stability, as long as the number of wind turbines connected to series compensated line remain constant. However, torsional mode and electromechanical modes are found to be more stable for larger wind farms. From this detailed eigenvalue analysis it is observed that no potential of SSR is found in wind farms operating in vicinity and connected to a series compensated line.

Table 5.6 Selected eigenvalues of system-II

Mode	WF-I	WF-II	WF-I	WF-II	WF-I	WF-II
	100 MW	100 MW	200 MW	200 MW	300 MW	300 MW
50% Series compensation						
Electrical mode	$-5.623 \pm 237.5i$		$-7.493 \pm 214.81i$		$-8.683 \pm 204.24i$	
Elect- mech. mode-I	$-6.534 \pm 35.947i$		$-6.102 \pm 33.701i$		$-5.743 \pm 30.977i$	
Elect- mech. mode-II	$-5.106 \pm 27.295i$		$-3.875 \pm 23.74i$		$-3.395 \pm 20.416i$	
Torsional mode-I	$-0.540 \pm 3.5827i$		$-0.632 \pm 3.5763i$		$-0.798 \pm 3.7529i$	
Torsional mode-II	$-0.374 \pm 2.9788i$		$-0.441 \pm 2.9954i$		$-0.505 \pm 3.091i$	
70% Series compensation						
Electrical mode	$-4.557 \pm 212.08i$		$-6.424 \pm 185.17i$		$-8.683 \pm 204.24i$	
Elect- mech. mode-I	$-6.529 \pm 36.294i$		$-6.065 \pm 34.302i$		$-5.743 \pm 30.977i$	
Elect- mech. mode-II	$-5.389 \pm 27.966i$		$-4.144 \pm 24.947i$		$-3.395 \pm 20.416i$	
Torsional mode-I	$-0.528 \pm 3.5866i$		$-0.582 \pm 3.5714i$		$-0.798 \pm 3.7529i$	
Torsional mode-II	$-0.365 \pm 2.9798i$		$-0.408 \pm 2.9805i$		$-0.505 \pm 3.091i$	
90% Series compensation						
Electrical mode	$-3.417 \pm 190.19i$		$-5.201 \pm 159.56i$		$-4.727 \pm 171.28i$	
Elect- mech. mode-I	$-6.546 \pm 36.697i$		$-6.023 \pm 34.909i$		$-7.340 \pm 38.746i$	
Elect- mech. mode-II	$-5.703 \pm 28.639i$		$-4.505 \pm 26.208i$		$-4.253 \pm 24.835i$	
Torsional mode-I	$-0.518 \pm 3.5907i$		$-0.546 \pm 3.5746i$		$-0.505 \pm 3.6065i$	
Torsional mode-II	$-0.357 \pm 2.9814i$		$-0.380 \pm 2.9756i$		$-0.408 \pm 2.9662i$	

Table 5.7 Selected eigenvalues of system-II for different wind farm sizes and series compensation level (Large WF-II)

Mode	WF-I	WF-II	WF-I	WF-II
	100 MW	200 MW	100 MW	300 MW
50% Series compensation				
Electrical mode	-6.652 ± 224.04i		-7.448 ± 215.9i	
Elect- mech. mode-I	-6.619 ± 36.141i		-6.634 ± 35.877i	
Elect- mech. mode-II	-4.187 ± 24.529i		-3.651 ± 22.249i	
Torsional mode-I	-0.552 ± 3.5838i		-0.580 ± 3.5854i	
Torsional mode-II	-0.424±2.9764i		-0.502 ± 3.0075i	
70% Series compensation				
Electrical mode	-5.569 ± 196.14i		-6.411 ± 186.46i	
Elect- mech. mode-I	-6.623 ± 36.551i		-6.647 ± 36.488i	
Elect- mech. mode-II	-4.449 ± 25.491i		-3.856 ± 23.431i	
Torsional mode-I	-0.533 ± 3.5875i		-0.545 ± 3.5877i	
Torsional mode-II	-0.398 ± 2.9725i		-0.451 ± 2.9792i	
90% Series compensation				
Electrical mode	-4.365 ± 172.08i		-5.228 ± 161.06i	
Elect- mech. mode-I	-6.637 ± 36.978i		-6.667 ± 37.053i	
Elect- mech. mode-II	-4.770 ± 26.505i		-4.136 ± 24.687i	
Torsional mode-I	-0.517 ± 3.5919i		-0.521 ± 3.5923i	
Torsional mode-II	-0.378 ± 2.9727i		-0.410 ± 2.9693i	

Table 5.8 Selected eigenvalues of system-II for different wind farm sizes and series compensation level (Large WF-I)

Mode	WF-1	WF-2	WF-1	WF-2
	200 MW	100 MW	300 MW	100 MW
50% Series compensation				
Electrical mode	-6.657 ± 223.99i		-7.457 ± 215.84i	
Elect- mech. mode-I	-6.160 ± 33.507i		-6.163 ± 31.703i	
Elect- mech. mode-II	-4.534 ± 26.494i		-3.938 ± 25.26i	
Torsional mode-I	-0.602 ± 3.5662i		-0.705 ± 3.5879i	
Torsional mode-II	-0.384 ± 2.9839i		-0.398 ± 2.9923i	
70% Series compensation				
Electrical mode	-5.575 ± 196.07i		-6.422 ± 186.37i	
Elect- mech. mode-I	-6.071 ± 33.968i		-6.049 ± 32.246i	
Elect- mech. mode-II	-4.893 ± 27.463i		-4.273 ± 26.588i	
Torsional mode-I	-0.569 ± 3.5678i		-0.636 ± 3.5651i	
Torsional mode-II	-0.369 ± 2.9823i		-0.377 ± 2.9861i	
90% Series compensation				
Electrical mode	-4.371 ± 171.97i		-5.241 ± 160.9i	
Elect- mech. mode-I	-5.972 ± 34.52i		-5.861 ± 32.802i	
Elect- mech. mode-II	-5.333 ± 28.423i		-4.767 ± 27.96i	
Torsional mode-I	-0.543 ± 3.5728i		-0.582 ± 3.5612i	
Torsional mode-II	-0.357 ± 2.9827i		-0.36 ± 2.9842i	

5.5.2 Participation Factor Analysis

Two identical wind farms each of 100 MW are considered for the participation factor analysis. The series compensation level is taken as 50%. Participation factors associated with the torsional mode of both wind farms are shown in Figure 5.4 (a). This mode is primarily contributed by the wind turbine drive train system. The Influence of other states appears to be negligible in both wind farms. Figure 5.4 (b) shows the participation factors associated with the electromechanical mode. This mode is contributed mainly by the generator rotor speed and d axis rotor induced voltage. However, electromechanical mode of WF-I is lightly coupled with the speed of the generator in WF-II and vice versa. This contribution is around 25%. Figure 5.4 (c) shows the participation factors of the electrical mode, which are largely contributed by the series capacitor voltage, line current, and stator current of the generators in both WF equally. However, the stator current contribution depends upon the size of the WF.

(a) Torsional mode

(b) Electromechanical mode

(c) Electrical mode
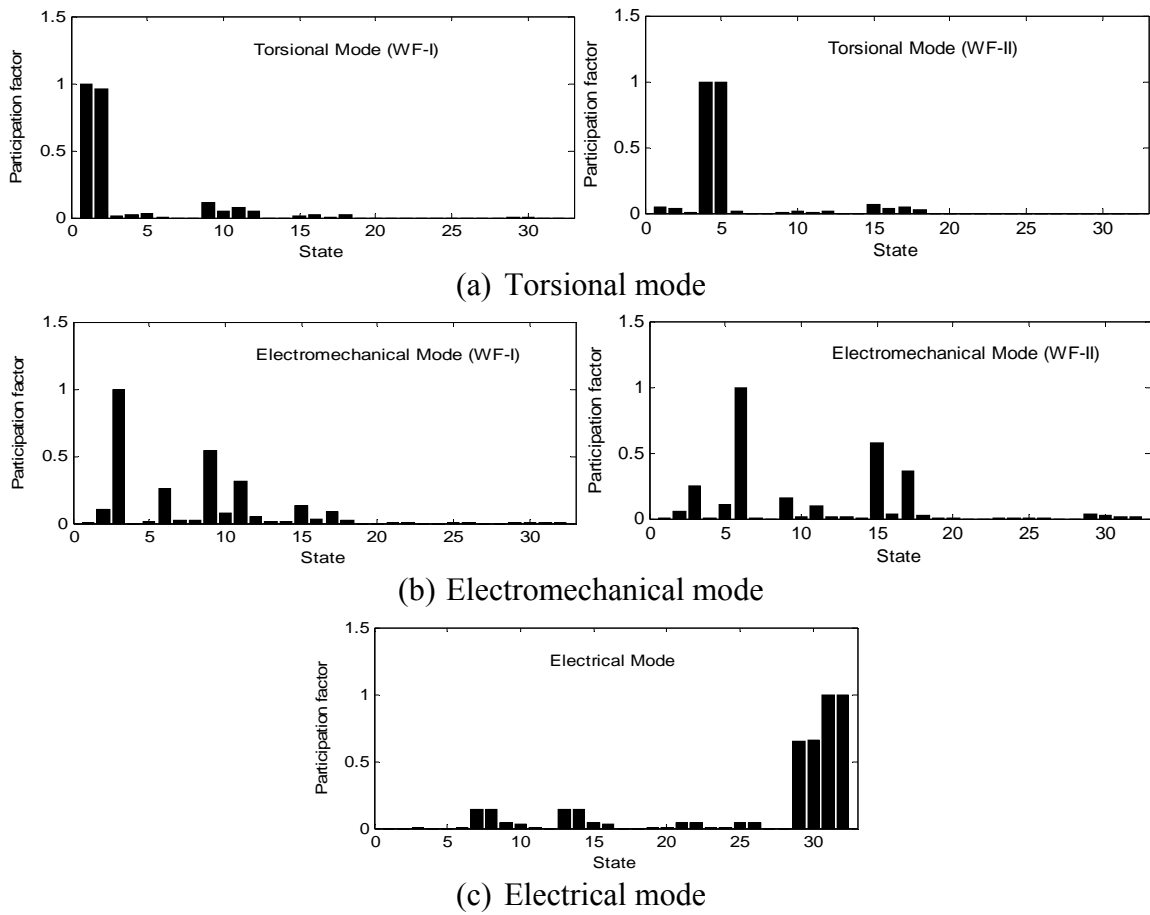
Figure 5.4 Participation factor analysis of different modes

5.6 ELECTROMAGNETIC TRANSIENT SIMULATIONS OF STUDY SYSTEM-I

In the previous section a comprehensive eigenvalue analysis is presented. To validate this small signal analysis, detailed time domain simulations of the study system are carried out with PSCAD/EMTDC. Faults at two locations F_1 (near by wind farm) and F_2 (remote end) are simulated and detailed results with FFT analysis are presented.

5.6.1 Impact of Remote End Fault

A six cycle three phase fault is simulated at the location F_2. This analysis is performed with variation in wind farm size and power output. During this study the series compensation level is kept constant at 70%.

5.6.1.1 *Variation in Wind Farm Size*

For the fault study with different size of wind farms, 100 MW, 300 MW, and 500 MW rated wind farms are chosen. The impact of a symmetrical fault at F_2 at time t=4 sec on a 100 MW wind farm is shown in Figure 5.5. Figure 5.5 (a) shows the electromagnetic torque and shaft torque following the clearance of the fault. Both torques are stabilized, as expected from the eigenvalue analysis. The FFT of the electromagnetic torque and shaft torque is shown in Figure 5.5 (b). The FFT estimated frequency of 36.05 rad/s in electromagnetic torque represents the electromechanical mode oscillatory frequency, which matches very closely with the predicted damped frequency of 35.36 rad/s shown in Table 5.2 for the corresponding operating condition. Similarly FFT estimated frequency of 3.68 rad/s in both electrical and shaft torque also matches very closely with the calculated value of 3.56 rad/s shown in Table 5.2. The response of generator speed and PCC voltage are found to quite similar to shaft torque and electromagnetic torque, respectively, and hence are not reported here.

(a) Electromagnetic torque and Shaft torque

(b) FFT of electromagnetic torque and shaft torque
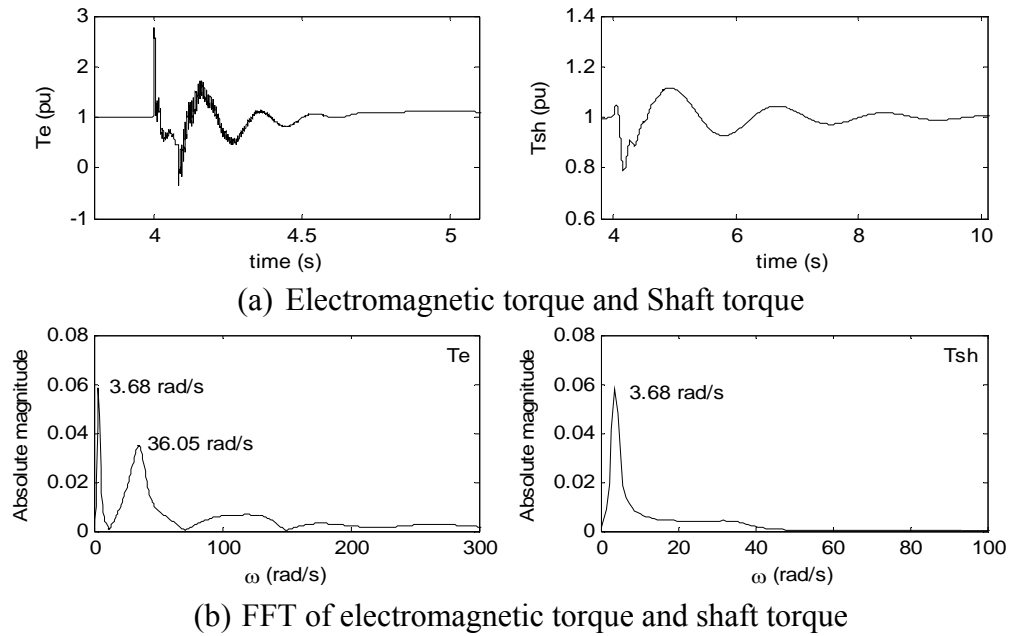
Figure 5.5 Impact of fault on a 100 MW wind farm

The study results for a 300 MW wind farm are shown in Figure 5.6. Figure 5.6 (a) shows the electromagnetic torque and shaft torque, whereas Figure 5.6(b) shows the corresponding FFT results. From the FFT analysis of electromagnetic torque, the estimated frequencies are 3.68 rad/s, 29.45 rad/s and 125.9 rad/s, which represent the torsional mode, electromechanical mode and electrical mode frequencies, respectively. The estimated frequencies match closely with the corresponding damped frequencies of 3.55 rad/s, 29.74 rad/s and 125.72 rad/s shown in Table 5.2. Similarly, the torsional mode frequency of 3.68 rad/s detected from the FFT of shaft torque matches with the calculated value of 3.55 rad/s from the eigenvalue analysis. The study is extended to a 500 MW wind farm and corresponding results are shown in Figure 5.7. The electromagnetic torque and shaft torque are shown in Figure 5.7 (a) while FFT of both the torques are shown in Figure 5.7 (b). The estimated frequencies match very closely with the calculated damped frequencies illustrated in Table 5.2. Thus the eigenvalue analysis results are reasonably validated by the electromagnetic transient simulation studies. From these studies with three different wind farms, it is observed that as the size of wind farm increases, the peak overshoot in the electromagnetic torque decreases, while that in the shaft torque remains almost same. It is confirmed from PSCAD/EMTDC studies that there is no potential for SSR in the studied system, as also predicted from eigenvalue analysis.

(a) Electromagnetic shaft and Shaft torque

(b) FFT of electromagnetic and shaft torque
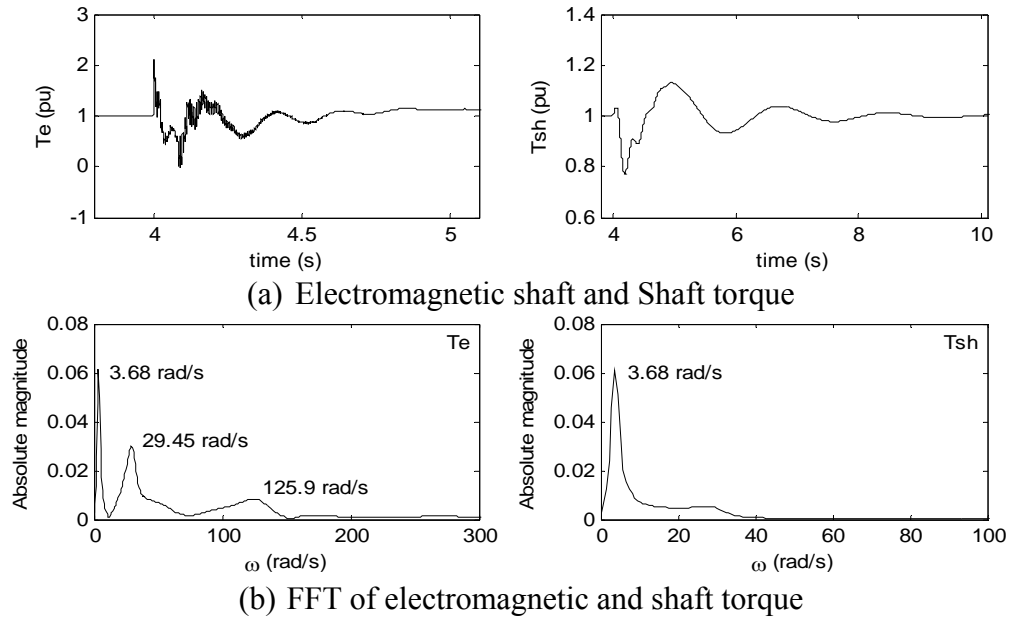
Figure 5.6 Impact of fault on a 300 MW wind farm

(a) Electromagnetic and Shaft torque

(b) FFT of electromagnetic and shaft torque
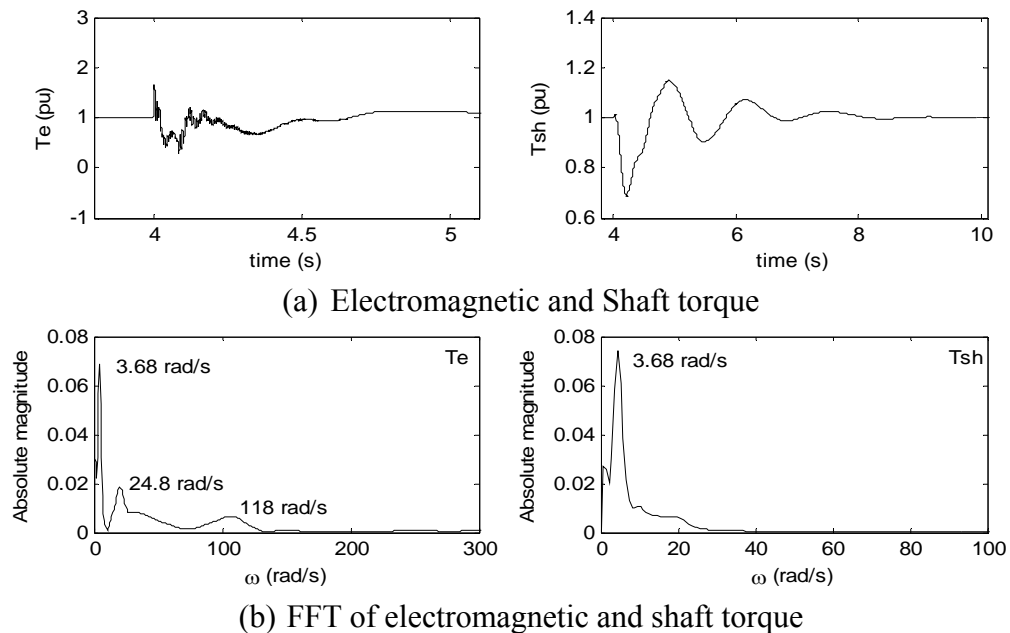
Figure 5.7 Impact of fault on a 500 MW wind farm

5.6.1.2 *Variation in Wind Farm Output*

A large wind farm of 500 MW with 70% series compensation is considered for this analysis whose output varies. The impact of fault at F_2 for 100 MW and 300 MW output conditions are shown in. Figure 5.8 and Figure 5.9, respectively. Post-fault disturbances in electromagnetic torque and shaft torque are shown in these figures. In the case of 100

MW output, the shaft torque displays electromechanical mode oscillations following the fault in the network, however the oscillations get damped out gradually. For a 300 MW output condition, the presence of electromechanical mode oscillation is reduced in comparison to 100 MW condition. In both cases, the torsional mode is excited, although the oscillation is damped out subsequently.
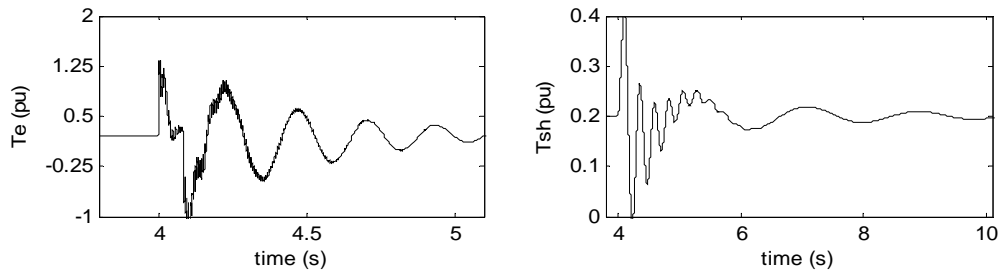
Figure 5.8 Impact of fault on a 500 MW wind farm producing 100 MW output
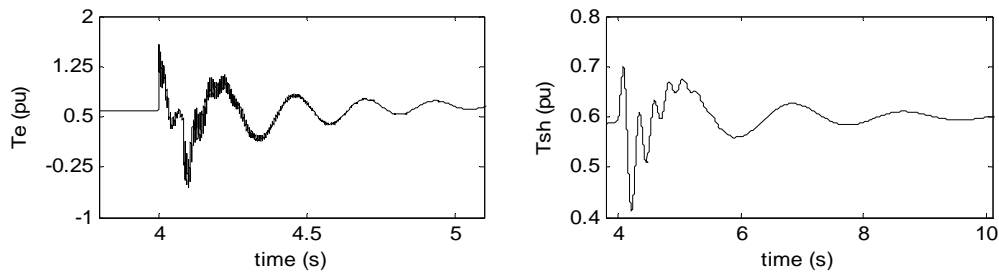
Figure 5.9 Impact of fault on a 500 MW wind farm producing 300 MW output

5.6.2   Impact of Terminal Fault

In Chapter 3 and 4 the equivalent circuit analysis is presented to predict the potential of shaft torque rise for a symmetrical fault near the PCC of a wind farm. Similar analysis is carried out here for system-I with 50% series compensation. Figure 5.10 shows the impact of a symmetrical fault at location F_1. Post fault electromagnetic torque and shaft torque are shown in Figure 5.10 (a) whereas the generator speed and PCC voltage are shown in Figure 5.10 (b). It shows no instability in the system. A similar study with a 100 MW output condition is depicted in Figure 5.11. It is seen that the terminal fault may not be a concern to wind farms under the considered network configuration and operating conditions. This is primarily due to the high resistance of the transmission line. The instability in the generator speed is contributed by the undamped oscillation caused by

the series capacitor, when the series resistance remains lower than the critical value [38], [40].

(a) Electromagnetic and Shaft torque

(b) Generator speed and PCC voltage
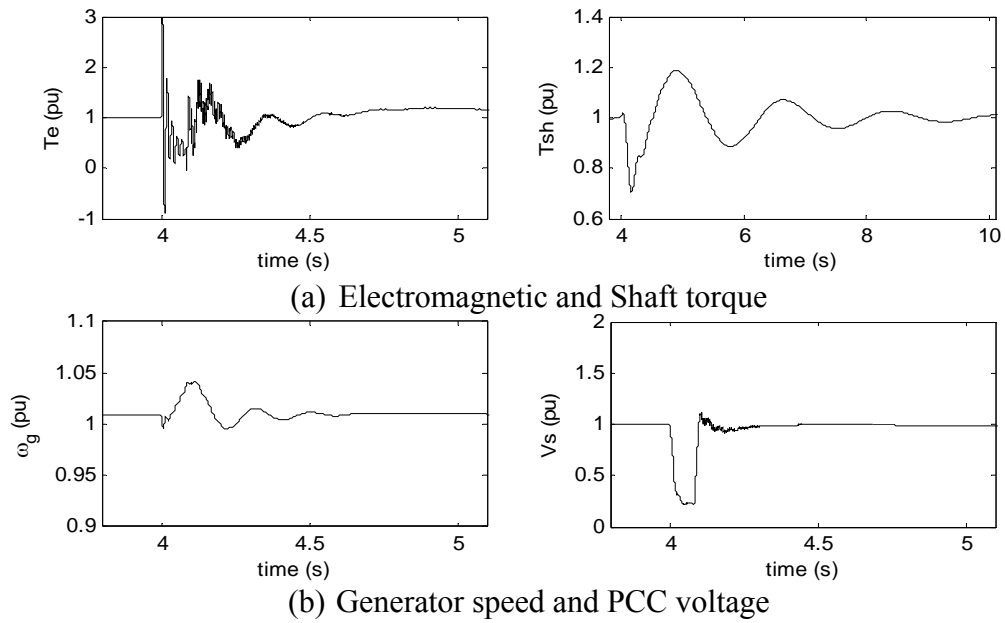
Figure 5.10 Impact of fault on a 500 MW wind farm with 100 MW output

(a) Electromagnetic and Shaft torque

(b) Generator speed and PCC voltage
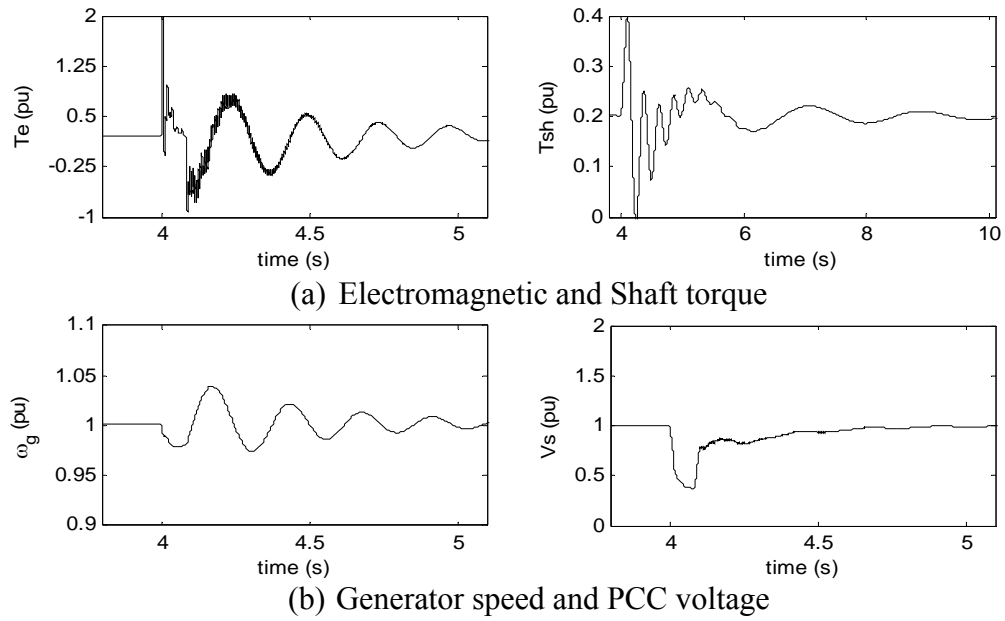
Figure 5.11 Impact of fault on a 500 MW wind farm with 300 MW output

5.7 ELECTROMAGNETIC TRANSIENT SIMULATIONS OF STUDY SYSTEM-I WITH UNCOMPENSATED LINE OUTAGE

During the outage of the uncompensated transmission line, the wind farm is exposed to a radial series compensated line. Small signal analysis is carried out for the modified network and corresponding eigenvalues are shown in Table 5.4. A time domain simulation of the modified system is now carried out with PSCAD/EMTDC that validates the small signal analysis. A six-cycle three phase fault occurs at 4s at the Bus-2 (location-F_2). During the fault the wind farm remains connected to the network.

In this section, the simulation results for 100 MW and 300 MW wind farms with 50% series compensation are presented. Figure 5.12 (a) shows the impact of fault on the electromagnetic and shaft torque of the wind turbine. The fault causes oscillations in the electromagnetic torque and shaft torque whose oscillatory frequencies are estimated from the FFT shown in Figure 5.12 (b). The electromagnetic torque oscillations contain three modal frequencies: 3.68 rad/s 33.3 rad/s and 246.6 rad/s, which correspond to torsional mode, electromechanical mode, and electrical mode, respectively. These estimated frequencies match very closely with the calculated value of 3.576 rad/s, 34.298 rad/s and 246.85 rad/s, respectively, obtained from eigenvalue analysis shown in Table 5.4. The FFT of the shaft torque shown in Figure 5.12 (b) shows the torsional mode oscillation. The estimated frequency 3.68 rad/s matches very closely with the calculated damped frequency of 3.578 rad/s. The electromagnetic transient simulation thus corroborates the small signal analysis. The impact of the fault at F_2 on the speed of the induction generator and PCC voltage is shown in Figure 5.12 (c). The oscillation in the speed is contributed by the torsional system of the wind turbine. However, oscillations in PCC voltage are quite small.

Similar fault study is conducted for a 300 MW wind farm with 50% series compensation and results are illustrated in Figure 5.13. The electromagnetic torque and the shaft torque of the wind turbine are shown in the Figure 5.13 (a), whereas Figure 5.13 (b) shows the FFT of the electromagnetic torque and the shaft torque. The estimated frequencies match

with the calculated value shown in Table 5.4. The impact of the fault on the speed and the PCC voltage are found to be similar to the case study shown with 100 MW, hence not reported here.
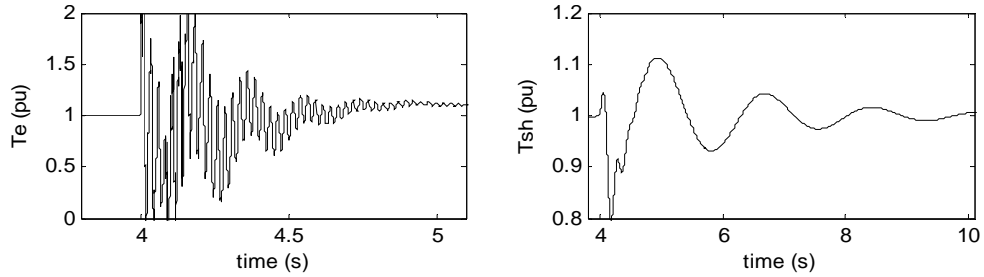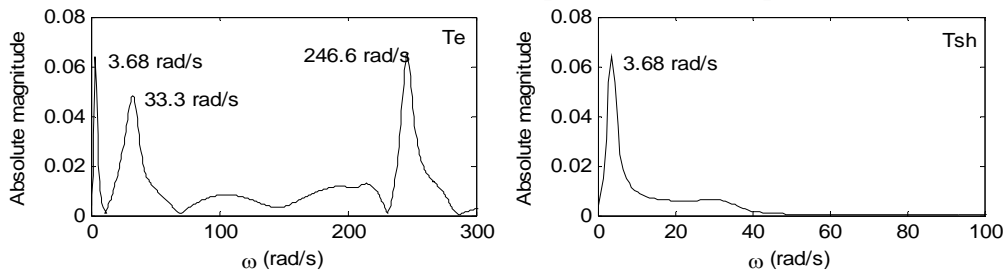
(a) Electromagnetic torque and Shaft torque

(b) FFT of electromagnetic torque and shaft torque
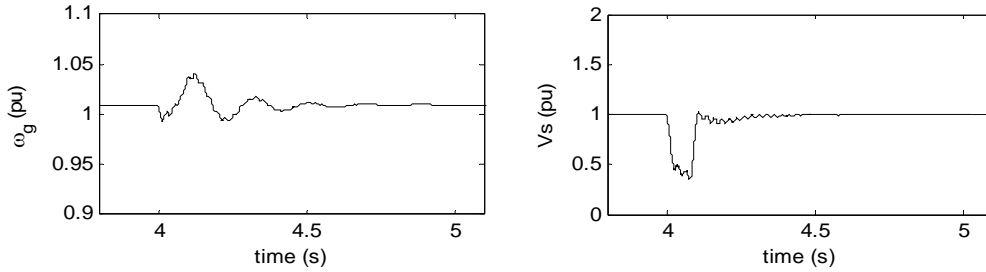
(c) Generator speed and PCC voltage

Figure 5.12 Impact of fault on a 100 MW wind farm
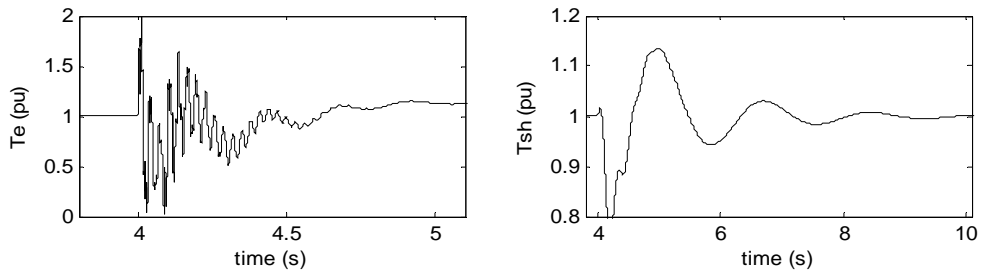
(a) Electromagnetic torque and Shaft torque
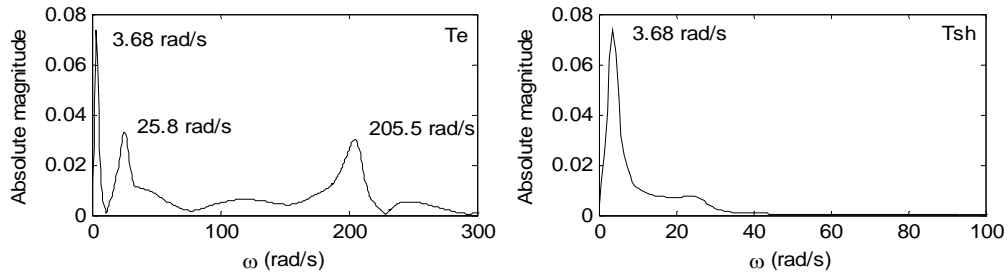
(b) FFT of electromagnetic and shaft torque

Figure 5.13 Impact of fault on a 300 MW wind farm

5.8 ELECTROMAGNETIC TRANSIENT SIMULATIONS OF SYSTEM-II

Time domain simulation is now carried out with the system-II considering two 100 MW double-cage induction generator based wind farms connected to 70% series compensated line. The LLLG fault is simulated at location F_2. The electromagnetic torque and shaft torque are shown in Figure 5.14 (a). The oscillation in electromagnetic torque in both wind farms is quite similar but the oscillation in shaft torque comprises two different frequencies. With the FFT analysis shown in Figure 5.14 (s), the multiple frequency components are identified which match with the calculated values obtained from the eigenvalue analysis. The torsional mode oscillation differs due to different torsional system parameters used for the two wind farms.
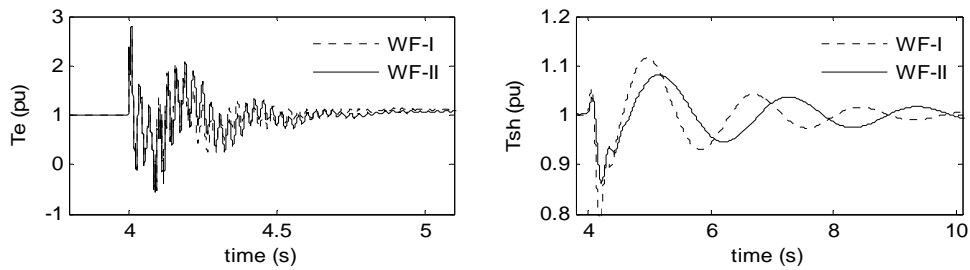
(a) Electromagnetic torque and shaft torque
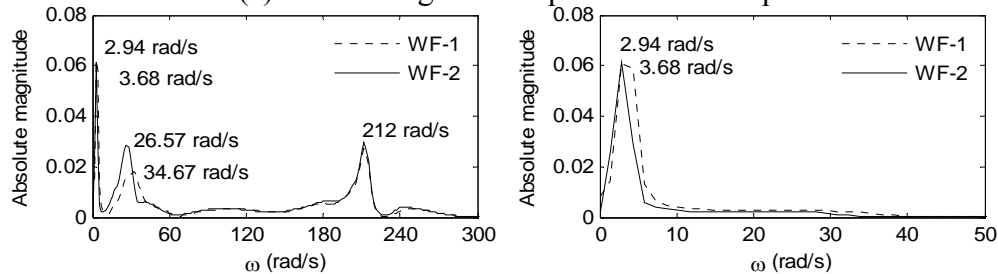
(b) FFT of electromagnetic and shaft torque

Figure 5.14 Impact of fault on two 100 MW wind farms

5.9 CONCLUSIONS

This chapter presents the SSR analysis of wind farms connected to non-radial series compensated lines. The study systems are adopted from the IEEE Second Benchmark Systems in this analysis. A detailed model of the study system comprising double-cage induction generator based wind farms and series compensated transmission lines is developed. A comprehensive eigenvalue analysis is presented for a wide range of operating conditions such as variation in wind farm size, variation in series compensation, outage of uncompensated line, etc. Participation factor analysis is utilized to determine the influence of various states on the system modes. All of the small signal analysis results are reasonably validated through electromagnetic transient simulation carried out in PSCAD/EMTDC. The following conclusions are made:

(a) In a non-radial series compensated network, a double-cage induction generator based wind farm may not experience SSR.

(b) In a contingency (outage of uncompensated line in system-I), although no potential for induction generator effect SSR is found, the level of series compensation may play a critical role in torque rise as the wind farm will be operating radially with the series compensated line.

(c) When two wind farms in close vicinity are connected to a series compensated line both wind farms may experience a common electrical mode oscillation, but a different shaft oscillation depending upon the different drive train system parameters.

(d) Terminal fault may not be a concern due to the low X/R ratio of the series compensated line that offers larger damping to the electrical mode oscillation. Due to the high series resistance, the speed of the generator never goes below the upper resonance speed threshold value following a fault in the network.

Chapter 6

MITIGATION OF SUBSYNCHRONOUS RESONANCE IN SERIES COMPENSATED WIND FARM USING STATCOM

6.1 INTRODUCTION

In Chapter 3 and 4, detailed analyses of the subsynchronous resonance in series compensated induction generator based wind farms are presented. Chapter 5 presents a similar analysis with non-radial series compensated lines. It is observed that subsynchronous resonance in wind farms may only be a concern when it operates radially with a series compensated line. The size of the wind farm and level of series compensation are the key factors affecting the subsynchronous resonances. Although no torsional interaction was found, high shaft torque may still be a threat for the cyclic fatigue in wind turbine generator shaft. The locations of fault and series capacitors also influence the subsynchronous oscillations in a wind farm. Hence, mitigation of the potential for SSR in a wind farm is the prime contribution of this chapter.

There are several countermeasures techniques, originally proposed for the mitigation of torsional interactions in large synchronous generators coupled with multi-stage turbines. [34], [35], [42], [114]-[118]. Broadly, those countermeasures can be classified in three groups: unit tripping counter measures, non-unit tripping counter measures, and conceptual counter measures. Application of FACTS controllers for the SSR mitigation comes under the conceptual mitigation. It is expected that a FACTS controller responds to the system conditions and provides positive damping to the unstable modes [119]-[123].

In this chapter a FACTS device- STATCOM is proposed for the mitigation of induction generator effect SSR in a radial series compensated wind farm. Two types of controllers are proposed and tested with an aggregated wind farm. The performance of these controllers is also assessed in presence of the collector cables. Detailed modeling of adequate STATCOM controllers is discussed. An eigenvalue analysis is carried out

which is then reasonably validated with the time domain simulations with PSCAD/EMTDC.

6.2 SYSTEM DESCRIPTION

The study system is shown in Figure 6.1. In this system a double-cage induction generator based wind farm is connected to a series compensated transmission line. This system is a modified IEEE First SSR Benchmark System [44]. The synchronous generator is replaced by an induction generator. A STATCOM is proposed at the PCC of the wind farm. The wind farm size is varied between 100 MW and 500 MW, whereas the series compensation level is varied from 10% to 90%. Symmetrical faults at two locations are simulated to examine the performance of the wind farm in the presence of the series capacitor.
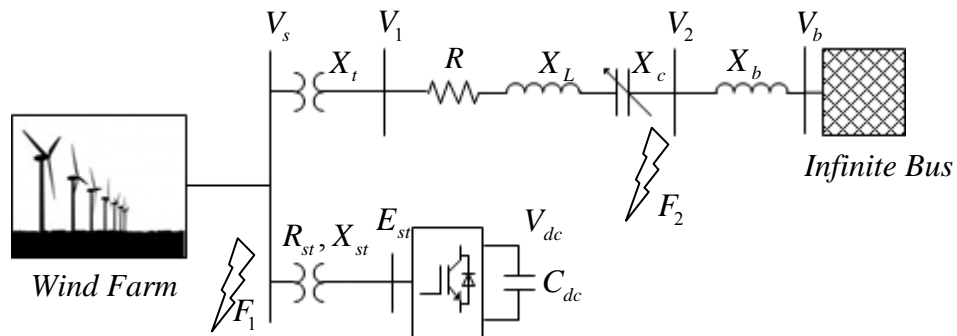
Figure 6.1 Study system with STATCOM connected at the PCC

6.3 STATCOM

The static synchronous compensator (STATCOM) was developed as an advanced var compensator. STATCOM consists of voltage source converter instead of controllable reactors and switched capacitors used in static var compensator (SVC). The self-commutated devices like GTO, IGBT, IGCT and MCT are widely used in VSCs. The first STATCOM in the world is commissioned in Japan in 1991. The STATCOM have several advantages over the SVC. Few of them are [34]:

(a)   Faster response

(b)   Less space requirement

(c) Relocatable

(d) Can be interfaced with battery, fuel cell, SMES or PV modules

(e) Superior performance during the transient

(f) Does not contribute to the short circuit current

(g) No issue related to loss of synchronism

A STATCOM is comparable to the synchronous condenser; which can supply variable reactive power and regulate the bus voltage. The STATCOM is realized as a voltage source with variable magnitude. If the STATCOM voltage magnitude is set to a higher value than the grid voltage (in pu), it injects reactive power into the grid. This mode of operation very often is referred to as the "over-excited" mode. Similarly when the STATCOM per unit voltage magnitude is lower than the grid voltage, it absorbs reactive power and is known as "under-excited" mode. In the over excited mode operation the STATCOM acts like a variable capacitor and during the under excited mode it behaves like a variable inductor. An equivalent circuit of the system with a var compensator is shown in Figure 6.2. The reactive current is derived as

$$I_{st} = \frac{E-V}{X}$$

(6.1)
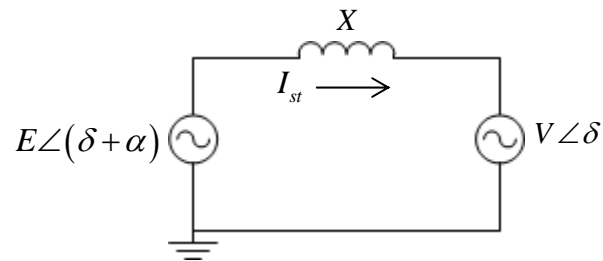
Figure 6.2 Equivalent circuit of a synchronous condenser

In recent global power scenarios, wind energy generator technology has occupied a significant space and it continuing to grow. In some countries the wind energy penetration has increased substantially. To comply with the grid code, the wind farms are expected to remain connected during the low voltage and/or fault in the gird. Significant reactive power support is therefore required for the wind farms to meet the grid code. Out of many options for the dynamic reactive power compensating devices, STATCOM leads because of its many advantages over others as mentioned earlier.   Stability of the power

system also depends upon the stability of the large wind farms, which can be improved by putting a STATCOM of suitable rating at the PCC. With increased threat of subsynchronous resonance in an induction generator based wind farm, a STATCOM is proposed. The size of the STATCOM is set as 60 MVAR/100 MW wind farm size.

6.3.1   Power Circuit Modeling

The single line diagram of the STATCOM is shown in Figure 6.3. The STATCOM bus AC voltage is directly proportional to the DC side voltage. A capacitor is connected at the DC side of the converter, whose voltage is to be kept constant [34], [123], [124]. The modeling and analysis of the STATCOM is carried out with the following:

(a)   The system voltages are balanced and sinusoidal

(b)   The switches are ideal

(c)   Transformer impedances are equal in all three phases
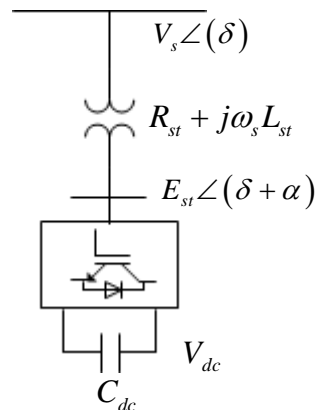
Figure 6.3 Equivalent circuit of STATCOM

Considering a six-pulse converter based STATCOM, it can be described by the differential equations:

$$L_{st} \frac{dI_{sta}}{dt} = V_{sa} - R_{st} I_{sta} - E_{sta} \tag{6.2}$$

$$L_{st} \frac{dI_{stb}}{dt} = V_{sb} - R_{st} I_{stb} - E_{stb} \tag{6.3}$$

$$L_{st} \frac{dI_{stc}}{dt} = V_{sc} - R_{st} I_{stc} - E_{stc} \tag{6.4}$$

$$C_{dc} \frac{dV_{dc}}{dt} = I_{dc} - \frac{V_{dc}}{R_{dc}} \tag{6.5}$$

where,

R_{st} :   Resistance in series with the STATCOM represents the sum of transformer winding resistance losses and the inverter conduction losses (pu)

L_{st} :   Leakage resistance of the transformer (pu)

C_{dc} :   DC side capacitor (pu)

R_{dc} :   Resistance in shunt with the capacitor C_{dc} represents the switching loss of the inverter and the power loss in the capacitor (pu)

$I_{sta}, I_{stb}, I_{stc}$:   Three phase currents of the STATCOM (pu)

V_{sa}, V_{sb}, V_{sc} :   Three phase voltages at the PCC (pu)

$E_{sta}, E_{stb}, E_{stc}$:   Three phase voltages at the STATCOM terminal (pu)

V_{dc} :   DC side voltage (pu)

I_{dc} :   DC side current (pu)

Applying Kron's transformation [34] to transform (6.2)-(6.4) to a synchronously rotating reference frame the dynamic equations are written as:

$$L_{st} \frac{d}{dt} I_{dst} = V_{ds} - R_{st} I_{dst} + \omega_s L_{st} I_{qst} - E_{dst} \tag{6.6}$$

$$L_{st} \frac{d}{dt} I_{qst} = V_{qs} - R_{st} I_{qst} - \omega_s L_{st} I_{dst} - E_{qst} \tag{6.7}$$

$$C_{dc} \frac{d}{dt} V_{dc} = I_{dc} - \frac{V_{dc}}{R_{dc}} \tag{6.8}$$

where,

V_{ds}, V_{qs} : d-q axis PCC voltage (pu)

I_{dst}, I_{qst} : d-q axis STATCOM current (pu)

E_{dse}, E_{qst} : d-q axis STATCOM terminal voltage (pu)

Assuming the switches are ideal, they are lossless and from the conservation of energy principle, in terms of d-q form,

$$V_{dc}I_{dc} = E_{dst}I_{dst} + E_{qst}I_{qst} \tag{6.9}$$

E_{dst} and E_{qst} are now expressed as the function of modulation index (m), DC voltage (V_{dc}), angle of the PCC voltage (θ) and the angular difference between the PCC voltage and the STATCOM terminal voltage (α).

$$E_{dst} = mV_{dc}\sin(\theta + \alpha) \tag{6.10}$$

$$E_{qst} = mV_{dc}\cos(\theta + \alpha) \tag{6.11}$$

$$m = \frac{\sqrt{6}}{\pi} \tag{6.12}$$

Substituting (6.10) and (6.11) in (6.9)

$$P_{dc} = mV_{dc}\sin(\theta + \alpha)I_{dst} + mV_{dc}\cos(\theta + \alpha)I_{qst} \tag{6.13}$$

Comparing (6.9) and (6.13)

$$I_{dc} = mI_{dst}\sin(\theta + \alpha) + mI_{qst}\cos(\theta + \alpha) \tag{6.14}$$

It is to be noted that

$$\tan(\theta) = \frac{V_{ds}}{V_{qs}}, \quad V_s = \sqrt{V_{ds}^2 + V_{qs}^2} \tag{6.15}$$

$$V_{ds} = V_s\sin(\theta), \quad V_{qs} = V_s\cos(\theta) \tag{6.16}$$

The active current, I_{st}^P, and reactive current, I_{st}^R, of the STATCOM can be written as:

$$I_{st}^P = \frac{V_{ds}I_{dst} + V_{qs}I_{qst}}{V_s} \tag{6.17}$$

$$I_{st}^R = \frac{-V_{ds}I_{qst} + V_{qs}I_{dst}}{V_s} \tag{6.18}$$

Using (6.16) in (6.17) and (6.18)

$$I_{st}^P = I_{dst}\sin(\theta) + I_{qst}\cos(\theta) \tag{6.19}$$

$$I_{st}^R = I_{dst}\cos(\theta) - I_{qst}\sin(\theta) \tag{6.20}$$

6.3.2 Steady State Performance of the STATCOM

The steady state performance of the proposed STATCOM when connected to the study system is presented in Figure 6.4. Variation in the PCC voltage for the different reactive power rating of the STATCOM is shown in Figure 6.4 (a). This is carried out for three different series compensation levels (K): 30%, 50% and 70%. It is seen that, with the low series compensation level the STATCOM controls the voltage more effectively and the slope decreases with the increase in the series compensation level. Similar analysis is carried out for the DC voltage that is shown in Figure 6.4 (b). Variation in DC voltage is very much similar to that of PCC voltage. Figure 6.4 (c) shows the reactive power injection from the STATCOM for different series compensation level. Variation in the slip of the induction generator is shown in Figure 6.4 (d). It is seen that in inductive mode of the STATCOM, the slip decreases faster with lower series compensation. As the series compensation level increases the variation in the slip is small.

(a) PCC voltage

(b) DC Voltage

(c) Reactive current

(d) Generator slip
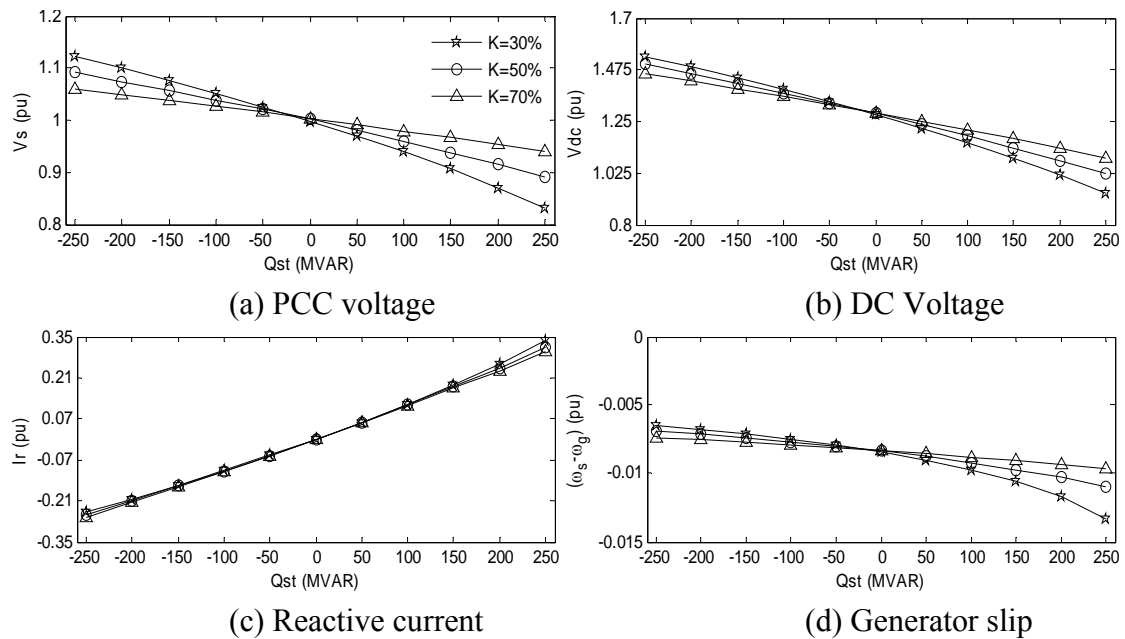
Figure 6.4 Steady state performance of STATCOM

6.4 STATCOM CONTROLLER MODELING

Two types of STATCOM controllers are proposed for the mitigation of subsynchronous resonance in wind farms. The detailed model of each controller is discussed here.

6.4.1   Controller-I

The proposed controller-I (C-I) is similar to the Type-2 controller originally proposed in [124]. In this controller DC voltage remains uncontrolled and only the angular difference between the the STATCOM terminal and the PCC bus voltage is controlled. This controller is mostly used in transmission network for dynamic reactive power support. However, the uncontrolled DC voltage may cause over voltage in the AC side bus. Figure 6.5 shows the block diagram of the controller-I.
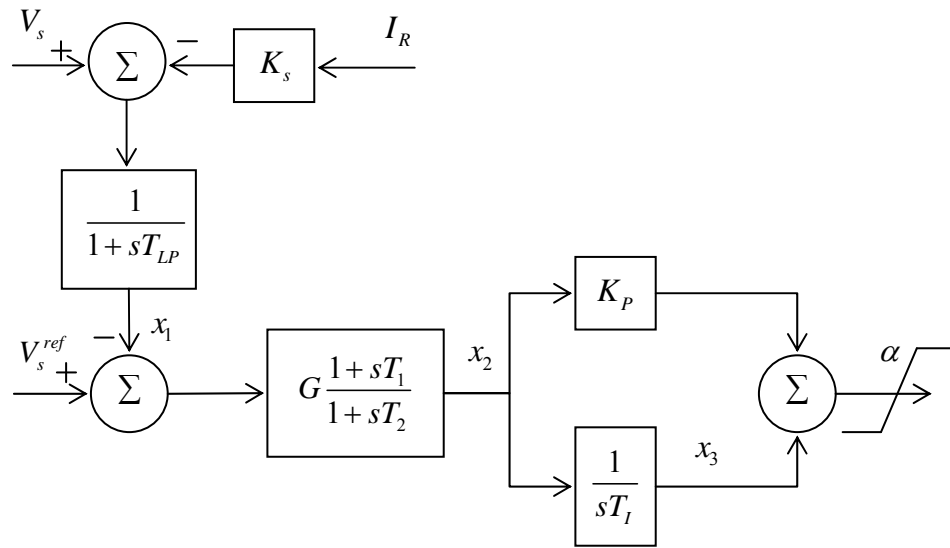
Figure 6.5 Block diagram of controller-I

The state space model of the controller is developed for small signal analysis. The linearized dynamic equations of controller-I are:

$$T_{LP}\frac{d}{dt}(\Delta x_1) = \Delta V_s - K_s\Delta I_R - \Delta x_1 \qquad (6.21)$$

$$GT_1\frac{d}{dt}(\Delta x_1) + T_2\frac{d}{dt}(\Delta x_2) = G(V_S^{Ref} - \Delta x_1) - \Delta x_2 \qquad (6.22)$$

$$T_I\frac{d}{dt}(\Delta x_3) = \Delta x_2 \qquad (6.23)$$

Arranging (6.21)-(6.23) in the state space form,

$$\dot{x}_{Ct} = [A_{Ct}]x_{Ct} + [B_{Ct}]u_{Ct} \qquad (6.24)$$

$$y_{Ct} = [C_{Ct}]x_{Ct} \qquad (6.25)$$

where,

$$x_{Ct}^{t} = \begin{bmatrix} \Delta x_1 & \Delta x_2 & \Delta x_3 \end{bmatrix}, \quad y_{Ct} = \begin{bmatrix} \Delta \alpha \end{bmatrix} \tag{6.26}$$

$$u_{Ct}^{t} = \begin{bmatrix} \Delta V_s & \Delta I_R \end{bmatrix} \tag{6.27}$$

$$\begin{bmatrix} C_{Ct} \end{bmatrix} = \begin{bmatrix} K \end{bmatrix} = \begin{bmatrix} 0 & K_P & 1 \end{bmatrix} \tag{6.28}$$

6.4.2   Controller-II

In controller-II (C-II), the DC link capacitor voltage is controlled by the phase angle difference between the STATCOM terminal and PCC bus voltage. The reactive current is controlled by regulating V_s to V_s^{ref}. In this controller, modulation index (m) and angle (α) are controlled. The proposed controller-II is shown in Figure 6.6, where both the inputs are decoupled from each other. The modulation index is derived from the voltage error, where a voltage droop characteristic is introduced for control of the voltage at the PCC. Regulating the magnitude of the converter bus voltage, now regulates the reactive power injection, or absorption by the STATCOM. The phase angle difference (α) is derived from the DC voltage error. For the damping of subsynchronous oscillations, an additional lead lag compensator is used in each control path. Since no torsional interaction is witnessed in the wind farm due to series compensation, no damping controller is required here. For the small signal analysis, the proposed controller is now modeled as a linear time invariant system that is described through a set of differential equations. The dynamic equations of the controller-II are written as:

$$T_{LP} \frac{d}{dt} \left(\Delta x_1 \right) = \Delta V_S - K_S \Delta I_R - \Delta x_1 \tag{6.29}$$

$$G_1 T_1 \frac{d}{dt} \left(\Delta x_1 \right) + T_2 \frac{d}{dt} \left(\Delta x_2 \right) = G_1 \left(V_S^{Ref} - \Delta x_1 \right) - \Delta x_2 \tag{6.30}$$

$$T_{I1} \frac{d}{dt} \left(\Delta x_3 \right) = \Delta x_2 \tag{6.31}$$

$$T_{DC} \frac{d}{dt} \left(\Delta x_4 \right) = \Delta V_{DC} - \Delta x_4 \tag{6.32}$$

$$G_2 T_3 \frac{d}{dt} \left(\Delta x_4 \right) + T_4 \frac{d}{dt} \left(\Delta x_5 \right) = G_2 \left(V_{DC}^{Ref} - \Delta x_4 \right) - \Delta x_5 \tag{6.33}$$

$$T_{I2}\frac{d}{dt}\left(\Delta x_6\right)=\Delta x_5 \tag{6.34}$$
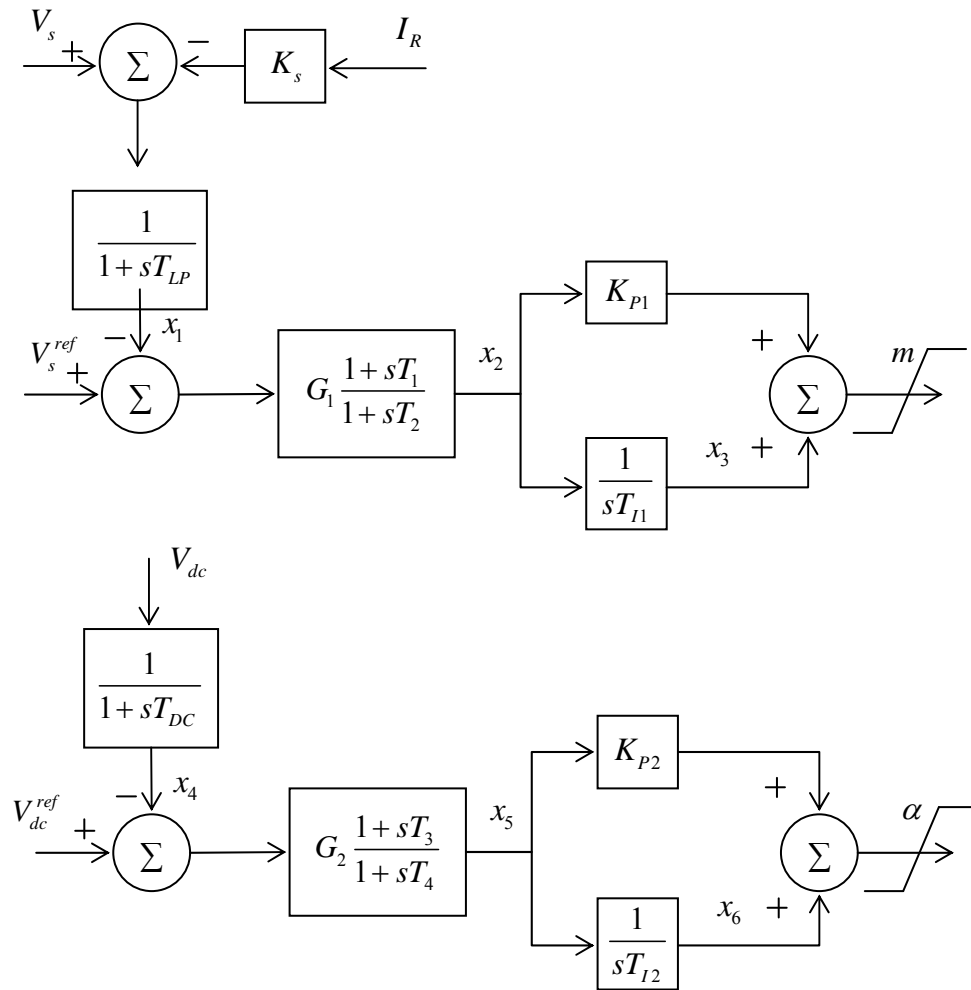
Figure 6.6 Block diagram of controller-II

Equations (6.29)-(6.34) are written in the linear state space form as

$$\dot{x}_{Ct}=\left[A_{Ct}\right]x_{Ct}+\left[B_{Ct}\right]u_{Ct} \tag{6.35}$$

$$y_{Ct}=\left[C_{Ct}\right]x_{Ct} \tag{6.36}$$

where,

$$x_{Ct}^{t}=\begin{bmatrix}\Delta x_1 & \Delta x_2 & \Delta x_3 & \Delta x_4 & \Delta x_5 & \Delta x_6\end{bmatrix} \tag{6.37}$$

$$y_{Ct}^{t}=\begin{bmatrix}\Delta m & \Delta\alpha\end{bmatrix} \tag{6.38}$$

$$[C_{Ct}] = [K] = \begin{bmatrix} 0 & K_{P1} & 1 & 0 & 0 & 0 \\ 0 & 0 & 0 & 0 & K_{P1} & 1 \end{bmatrix} \tag{6.39}$$

6.4.3 Complete System Model with Controller-I

When the STATCOM is connected at the PCC of the wind farm shown in Figure 6.1 the system equations are changed from those derived in Chapter 4. Keeping the drive train and induction generator model intact only the network models are redefined. These equations are linearized while constructing the small signal model. The differential equations are:

$$C_g \frac{d}{dt} V_{ds} = I_{ds} - (I_d + I_{dst}) + \omega_s C_g V_{qs} \tag{6.40}$$

$$C_g \frac{d}{dt} V_{qs} = I_{qs} - (I_q + I_{qst}) - \omega_s C_g V_{ds} \tag{6.41}$$

$$L \frac{d}{dt} I_d = V_{ds} - R I_d + \omega_s L I_q - V_{cd} - V_{bd} \tag{6.42}$$

$$L \frac{d}{dt} I_q = V_{qs} - R I_q - \omega_s L I_d - V_{cq} - V_{bq} \tag{6.43}$$

$$C \frac{d}{dt} V_{cd} = I_d + \omega_s C V_{cq} \tag{6.44}$$

$$C \frac{d}{dt} V_{cq} = I_q - \omega_s C V_{cd} \tag{6.45}$$

where,

V_{ds}, V_{qs} :   *d-q* axis voltage at the PCC (pu)

I_{ds}, I_{qs} :   *d-q* axis stator current of induction generator (pu)

I_d, I_q :   *d-q* axis series compensated line current (pu)

V_{cd}, V_{cq} :   *d-q* axis voltage across series capacitor (pu)

V_{bd}, V_{bq} :   *d-q* axis voltage at the infinite bus (pu)

The state space model of the drive train, induction generator and network are expressed as:

$$\dot{x}_{WT} = [A_{TT}] x_{WT} + [A_{TG}] x_G + [B_T] u_{WT} \tag{6.46}$$

$$\dot{x}_G = [A_{GT}] x_{WT} + [A_{GG}] x_G + [A_{GN}] x_N \tag{6.47}$$

$$\dot{x}_N = [A_{NG}]x_G + [A_{NN}]x_N + [A_{NSt}]x_{St} + [B_N]u_N \tag{6.48}$$

Arranging the dynamic equations of the power circuit of the STATCOM presented (6.6)-(6.8), the STATCOM model is defined in the state space form as:

$$\dot{x}_{St} = [A_{StN}]x_N + [A_{StSt}]x_{St} + [B_{St}]u_{St} \tag{6.49}$$

where,

$$u_{st} = [\Delta\alpha] \tag{6.50}$$

Combining (6.46)-(6.49) the open loop equation of the complete system is written as:

$$\dot{x}_{sys} = [A_{sys}]x_{sys} + [B_1]u_1 + [B_2]u_2 + [B_3]u_3 \tag{6.51}$$

where,

$$x_{sys}^t = \begin{bmatrix} x_{WT}^t & x_G^t & x_N^t & x_{St}^t \end{bmatrix} \tag{6.52}$$

$$x_{WT}^t = \begin{bmatrix} \Delta\omega_t & \Delta\delta_{tg} & \Delta\omega_g \end{bmatrix} \tag{6.53}$$

$$x_G^t = \begin{bmatrix} \Delta I_{ds} & \Delta I_{qs} & \Delta E_{d1} & \Delta E_{q1} & \Delta E_{d2} & \Delta E_{q2} \end{bmatrix} \tag{6.54}$$

$$x_N^t = \begin{bmatrix} \Delta V_{ds} & \Delta V_{ds} & \Delta I_d & \Delta I_q & \Delta V_{cd} & \Delta V_{cq} \end{bmatrix} \tag{6.55}$$

$$x_{St}^{'} = \begin{bmatrix} \Delta I_{dst} & \Delta I_{qst} & \Delta V_{dc} \end{bmatrix} \tag{6.56}$$

$$u_1 = [\Delta T_W], \quad u_2 = \begin{bmatrix} \Delta V_{bd} \\ \Delta V_{bq} \end{bmatrix}, \quad u_3 = u_{St} \tag{6.57}$$

The state space model of controller-I defined in (6.24) is rewritten as:

$$\dot{x}_{Ct} = [A_{Ct}]x_{Ct} + [B_{Ct}][M]x_{sys} \tag{6.58}$$

where,

$$[M]x_{sys} = u_{Ct} \tag{6.59}$$

From (6.28), (6.50) and (6.57)

$$u_3 = [K]\Delta x_{Ct} \tag{6.60}$$

The combined equation of the system including controller-I is now expressed as:

$$\begin{bmatrix} \dot{x}_{sys} \\ \dot{x}_{Ct} \end{bmatrix} = \begin{bmatrix} A_{sys} & B_3K \\ B_{Ct}M & A_{Ct} \end{bmatrix} \begin{bmatrix} x_{sys} \\ x_{Ct} \end{bmatrix} + B_1u_1 + B_2u_2 \tag{6.61}$$

The total number of states of the closed loop system is 21.The detailed eigenvalue analysis of the close loop system defined in (6.61) is presented in Sec. 6.5.

6.4.4 Complete System Model with Controller-II

The augmentation of the controller-II is carried out in a similar way as it is described for controller-I. The closed loop state space model of the system is developed as mentioned in (6.61). With controller-II the total number of states becomes 24.

6.4.5 Singular Value Decomposition (SVD)

A controllability analysis is performed using the singular value decomposition (SVD) technique to determine the effectiveness of the control inputs m and α given in (6.61). Considering the electrical mode of the system, singular values of two matrices $\left[A_{sys} - \lambda I, B_2(:,1)\right]$ and $\left[A_{sys} - \lambda I, B_2(:,2)\right]$ are calculated [125], [126]. Table 6.1 shows the minimum singular values for both inputs for different wind farm sizes at 50% series compensation. From each case it is seen that the electrical mode can be effectively controlled through the modulation index m. Further, as the size of the wind farm increases, modulation index m becomes more effective as compared to the phase angle difference α. Similar observations are also made for different compensation levels considering a 500 MW wind farm as shown in Table 6.2.

Table 6.1 Minimum singular value for different wind farm size

WF Size (MW)	100	200	300	400	500
SVD (m)	1.17	0.909	0.745	0.637	0.557
SVD (α)	1.019	0.650	0.432	0.299	0.210

Table 6.2 Minimum singular value for different compensation

K (%)	40	50	60	70	80
SVD (m)	0.537	0.557	0.546	0.497	0.410
SVD (α)	0.266	0.210	0.119	0.046	0.176

Once it is determined that modulation index is more effective in stabilizing the electrical mode oscillation, emphasis is given to the tuning of gains of the corresponding control loop. The initial values of the two PI controller parameters $\left(K_{p1}, K_{p2}, T_{i1}, T_{i2}\right)$ are chosen based on the STATCOM controller design criteria described in [34]. The lead-lag

compensator gains and time constants $\left(G_1,G_2,T_1,T_2,T_3,T_4\right)$ are adapted from typical values given in [99]. Eigenvalue analysis is performed to determine the best parameter values that can stabilize the electrical mode the most. These parameters are further improvised through fault studies with PSCAD/EMTDC software with the objective of reducing the overshoot in AC voltage and decreasing the settling time as well. This iterative process is followed until reasonably good PI controller gains are obtained. These parameters are then used for all the SSR studies.

6.5 EIGENVALUE ANALYSIS

The eigenvalue analysis of the study system is carried out for a wide range of operating conditions. The wind farm size is varied from 100 MW to 500 MW, while the series compensation is varied in between 10% and 90%. The size of STATCOM is chosen as 60 MVA/100 MW. The choice of STATCOM size is based on the previous study conducted in [26] and STATCOMs used in integration of wind farm. Table 6.3 shows all the eigenvalues of the systems (300 MW wind farm with 50% series compensation) including controller-I and controller-II.

Table 6.4 shows the comprehensive eigenvalue analysis of the study system with and without the proposed STATCOM. Only three oscillatory modes that are useful for the analysis of SSR are shown explicitly. In the absence of STATCOM (Table 6.4) as the compensation level increases, the electrical mode becomes less stable and then becomes unstable for all sizes of wind farm considered. Now when the STATCOM with proposed controller-I is employed at the PCC, the system eigenvalues are calculated and shown in Table 6.5. Being the most sensitive mode, the electrical mode is studied thoroughly.It is found that with the controller-I the electrical mode becomes unstable for all wind farm sizes. For example, the electrical mode eigenvalues for 300 MW wind farm with 50% series compensation are $0.156 \pm 182.46i$ without STATCOM. With STATCOM these eigenvalues become $2.188 \pm 176.68i$.

Table 6.6 shows the system eigenvalues with STATCOM controller-II that shows a further enhancement in the electrical mode stability in comparison to the controller-I. The proposed controller-II also improves the stability of electromechanical modes of the wind

turbine generator. For instance, without STATCOM the electromechanical mode eigenvalues for a 100 MW wind farm with 50% series compensation are -6.537 ± 36.849i. With controller-I and controller-II these eigenvalues change to -6.4289 ± 36.927i and -6.892 ± 36.733i, respectively. The torsional mode is not much affected by the two impacts of STATCOM controllers. The stable eigenvalues of the torsional mode indicates there is no potential of torsional instability.

Table 6.3 Complete system eigenvalues

Mode	Without STATCOM	With STATCOM	
		Controller-I	Controller-II
Sup. Sync. mode	-6.790 ± 570.89i	-6.752 ± 539.98i	-5.470 ± 605.57i
Electrical mode	+0.156 ± 182.46i	-2.188 ± 176.68i	-2.233 ± 175.88i
Elect- mech. mode	-5.020 ± 32.981i	-4.743 ± 33.079i	-5.127 ± 33.076i
Torsional mode	-0.572 ± 3.5703i	-0.502 ± 3.5372i	-0.522 ± 3.5515i
Other modes	-9.575 ± 1984.9i	-5.808 ± 2537.7i	-2.213 ± 2507.4i
	-12.38 ± 1231i	-9.801 ± 1466.4i	-8.526 ± 1456i
	-60.96 ± 3.5792i	-3.558 ± 660.37i	-5.491 ± 605.81i
	-6.525	-167.3 ± 59.511i	-11.25 ± 478.25i
		-61.49 ± 3.3024i	-5.159 ± 128.56i
		-8.919 ± 5.5316i	-62.04 ± 2.596i
		-2.071	-245.0,-178.39
			-8.649,-2.7203
			-0.0062,-0.031231

Table 6.4 System eigenvalues without STATCOM

Modes	100 MW	200 MW	300 MW	400 MW	500 MW
40% Series compensation					
Electrical mode	-1.118 ± 251.73i	-0.762 ± 220.39i	-0.865 ± 202.84i	-1.092 ± 191.85i	-1.352 ± 183.98i
Elect- mech. mode	-6.334 ± 36.361i	-5.388 ± 33.973i	-4.692 ± 31.874i	-4.192 ± 30.064i	-3.813 ± 28.385i
Torsional mode	-0.530 ± 3.5918i	-0.557 ± 3.5761i	-0.597 ± 3.5653i	-0.650 ± 3.5647i	-0.720 ± 3.5837i
50% Series compensation					
Electrical mode	-0.415 ± 237.08i	+0.165 ± 202.08i	+0.156 ± 182.46i	-0.041 ± 170.14i	-0.306 ± 161.31i
Elect- mech. mode	-6.537 ± 36.849i	-5.683 ± 34.809i	-5.020 ± 32.981i	-4.520 ± 31.384i	-4.120 ± 29.897i
Torsional mode	-0.525 ± 3.5951i	-0.545 ± 3 .5814i	-0.572 ± 3.5703i	-0.607 ± .5641i	-0.653 ± 3.5659i
55% Series compensation					
Electrical mode	-0.061 ± 230.32i	+0.652 ± 193.64i	+0.709 ± 173.05i	+0.539 ± 160.11i	+0.281 ± 150.82i
Elect- mech. mode	-6.644 ± 37.1i	-5.847 ± 35.25i	-5.211 ± 33.572i	-4.719 ± 32.095i	-4.314 ± 30.714i
Torsional mode	-0.523 ± 3.5967i	-0.539 ± 3.5842i	-0.561 ± 3.5735i	-0.589 ± 3.5662i	-0.625 ± 3.5638i
60% Series compensation					
Electrical mode	+0.296± 223.87i	+1.158± 185.58i	+1.29 ± 164.06i	+1.166 ± 150.52i	+0.926 ± 140.79i
Elect- mech. mode	-6.755 ± 37.356i	-6.023 ± 35.706i	-5.424 ± 34.193i	-4.948 ± 32.849i	-4.545 ± 31.584i
Torsional mode	-0.521 ± 3.5984i	-0.534 ± 3.5872i	-0.551 ± 3.5771i	-0.573 ± 3.5694i	-0.600 ± 3.5646i

Table 6.5 System eigenvalues with STATCOM controller-I

Modes	100 MW	200 MW	300 MW	400 MW	500 MW
40% Series compensation					
Electrical mode	-2.462 ± 238.74i	-2.391 ± 212.56i	-2.372 ± 198.02i	-2.410 ±188.41i	-2.483 ± 181.42i
Elect- mech. mode	-6.201 ± 36.437i	-5.123 ± 34.018i	-4.355 ± 31.965i	-3.777 ± 30.133i	-3.327 ± 28.423i
Torsional mode	-0.506 ± 3.5829i	-0.503 ± 3.5534i	-0.503 ± 3.5229i	-0.506 ± 3.4899i	-0.512 ± 3.4523i
50% Series compensation					
Electrical mode	-2.732 ± 221.71i	-2.402 ± 192.82i	-2.188 ± 176.68i	-2.091 ± 166i	-2.074 ± 158.2i
Elect- mech. mode	-6.429 ± 36.927i	-5.463 ± 34.868i	-4.743 ± 33.079i	-4.182 ± 31.465i	-3.729 ± 29.953i
Torsional mode	-0.506 ± 3.5872i	-0.503 ± 3.5625i	-0.502 ± 3.5372i	-0.503 ± 3.5104i	-0.505 ± 3.4807i
55% Series compensation					
Electrical mode	-2.959 ± 213.81i	-2.482 ± 184.15i	-2.132 ± 166.78i	-1.947 ± 155.59i	-1.867 ± 147.42i
Elect- mech. mode	-6.547 ± 37.183i	-5.665 ± 35.36i	-4.960 ± 33.681i	-4.412 ± 32.189i	-3.962 ± 30.785i
Torsional mode	-0.507 ± 3.5894i	-0.503 ± 3.5676i	-0.502 ± 3.5443i	-0.502 ± 3.5204i	-0.503 ± 3.4942i
60% Series compensation					
Electrical mode	-3.249 ± 206.24i	-2.585 ± 174.87i	-2.098 ± 157.28i	-1.805 ± 145.6i	-1.650 ± 137.07i
Elect- mech. mode	-6.669 ± 37.447i	-5.842 ± 35.794i	-5.194 ± 34.32i	-4.667 ± 32.963i	-4.224 ± 31.677i
Torsional mode	-0.507 ± 3.5916i	-0.504 ± 3.5716i	-0.502 ± 3.5514i	-0.501 ± 3.5303i	-0.502 ± 3.5075i

Table 6.6 System eigenvalues with STATCOM controller-II

Modes	100 MW	200 MW	300 MW	400 MW	500 MW
40% Series compensation					
Electrical mode	-3.566 ±227.06i	-2.804 ± 207.5i	-2.511 ± 195.29i	-2.418 ± 187.05i	-2.417 ± 180.81i
Elect- mech. mode	-6.632 ±36.256i	-5.529 ± 34i	-4.698 ± 31.997i	-4.085 ± 30.255i	-3.603 ± 28.631i
Torsional mode	-0.508 ±3.5852i	-0.516 ± 3.5623i	-0.529 ± 3.5383i	-0.549 ± 3.5139i	-0.579 ± 3.4879i
50% Series compensation					
Electrical mode	-3.600 ± 209.54i	-2.628 ± 188.83i	-2.233 ± 175.88i	-2.079 ± 167.08i	-2.033 ± 160.35i
Elect- mech. mode	-6.892 ± 36.733i	-5.909 ± 34.818i	-5.127 ± 33.076i	-4.525 ± 31.538i	-4.034 ± 30.096i
Torsional mode	-0.508 ± 3.5893i	-0.513 ± 3.5708i	-0.522 ± 3.5515i	-0.536 ± 3.5323i	-0.556 ± 3.5122i
55% Series compensation					
Electrical mode	-3.652 ± 201.87i	-2.635 ± 180.94i	-2.257 ± 167.95i	-2.142 ± 159.2i	-2.141 ± 152.51i
Elect- mech. mode	-7.031 ± 36.983i	-6.122 ± 35.256i	-5.377 ± 33.663i	-4.788 ± 32.242i	-4.297 ± 30.901i
Torsional mode	-0.508 ± 3.5913i	-0.512 ± 3.575i	-0.519 ± 3.558i	-0.530 ± 3.5412i	-0.546 ± 3.5237i
60% Series compensation					
Electrical mode	-3.736 ± 194.93i	-2.733 ± 174.08i	-2.446 ± 161.38i	-2.437 ± 152.97i	-2.544 ± 146.65i
Elect- mech. mode	-7.179 ± 37.242i	-6.355 ± 35.718i	-5.658 ± 34.289i	-5.090 ± 33i	-4.604 ± 31.772i
Torsional mode	-0.507 ± 3.5934i	-0.511 ± 3.5791i	-0.517 ± 3.5644i	-0.525 ± 3.5499i	-0.537 ± 3.5349i

The improvement of the electrical mode stability with STATCOM is illustrated in Figure 6.7, which shows the variation in the electrical mode eigenvalues with series compensation level and wind farm size. As observed in Figure 6.7 (a), the electrical mode eigenvalues become less stable with increase in the series compensation and cross the

imaginary axis at critical compensation level. Figure 6.7 (b) shows the improvement in the electrical mode stability with the proposed STATCOM controller-I. Only at a very high unrealistic series compensation level the electrical mode of 500 MW wind farm tends to be unstable. The trend of the variation in the electrical mode eigenvalues with the controller-II is quite similar to the controller-I, though not reported here.

(a) Without STATCOM   (b) With STATCOM (C-I)
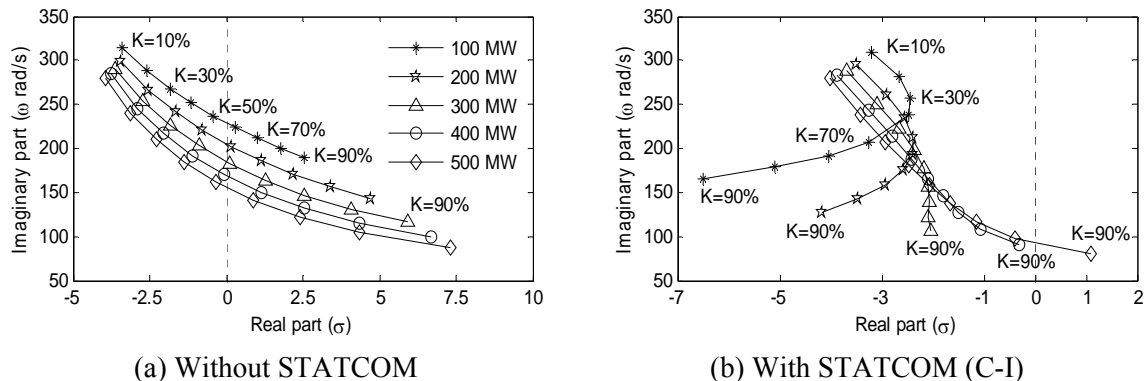
Figure 6.7 Electrical mode eigenvalues

6.6 ELECTROMAGNETIC TRANSIENT SIMULATIONS

This section presents the time domain simulations of the study system carried out with PSCAD/EMTDC software. The detailed model of the wind farm, series compensated line, and STATCOM with two proposed controllers are implemented with PSCAD/EMTDC. The time domain simulations are done in steady state and transient condition. The small signal analysis results are correlated with the time domain simulation results.

6.6.1 Steady State SSR

Steady state SSR refers to the self-excitation due to induction generator effect. This is indicated by an unstable electrical mode. The imaginary part of the electrical mode eigenvalue predicts the oscillatory frequency of the self-excitation in the wind farm. From the eigenvalue analysis it is observed that only the electrical mode becomes unstable beyond a critical compensation level for different sizes of wind farms. Therefore, beyond this compensation level, occurrence of self-excitation is expected. Figure 6.8 (a) shows the self-excitation of the electromagnetic torque and its mitigation with a 60 MVA STATCOM for a 100 MW wind farm connected to 60% series

compensated line. The size of the STATCOM is determined from the PSCAD/EMTDC studies to be most adequate to stabilize the electrical mode. The PCC voltage is shown in Figure 6.8 (b). In steady state since both the proposed controllers behave identically, performance with only controller-I is shown. Figure 6.9 and Figure 6.10 show the self-excitation of the PCC voltage and its mitigation through the STATCOM for a 300 MW and 500 MW wind farm, respectively, connected to 50% and 55% series compensation, respectively. For a 300 MW wind farm the critical compensation level is 48.60%, thus 50% series compensation presents a marginally unstable operating condition which can be seen from a slowly growing oscillations in the PCC voltage depicted in Figure 6.9. However, in the case of a 500 MW wind farm with 55% series compensation, the electrical mode is unstable, therefore the oscillations in the PCC voltage grow faster. Similar responses are seen with the electromagnetic torque, though not shown here. The STATCOM controllers effectively stabilize the electrical mode oscillations.

a) Electromagnetic torque
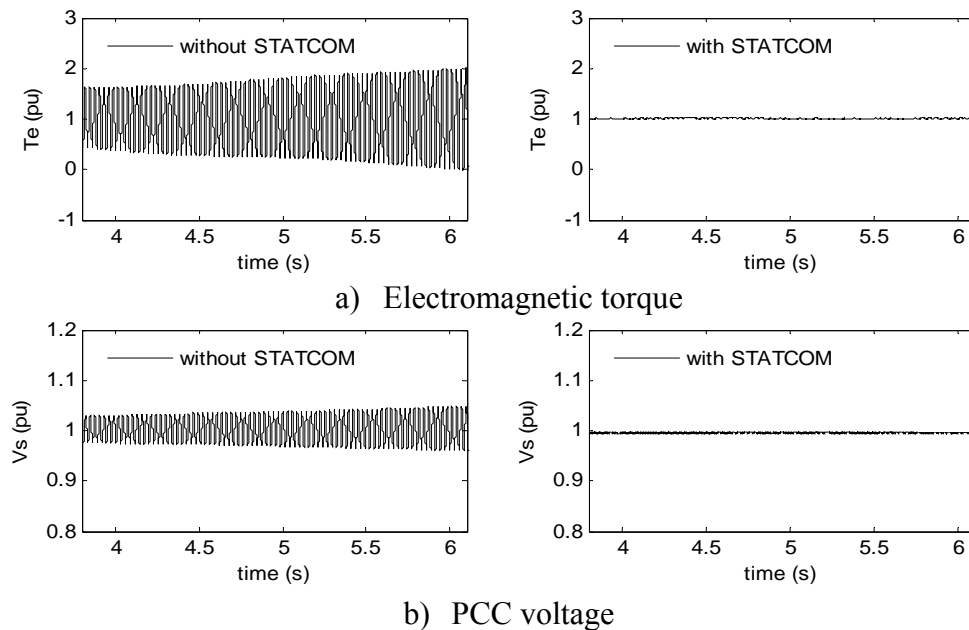
b) PCC voltage

Figure 6.8 Steady state performance of a 100 MW wind farm
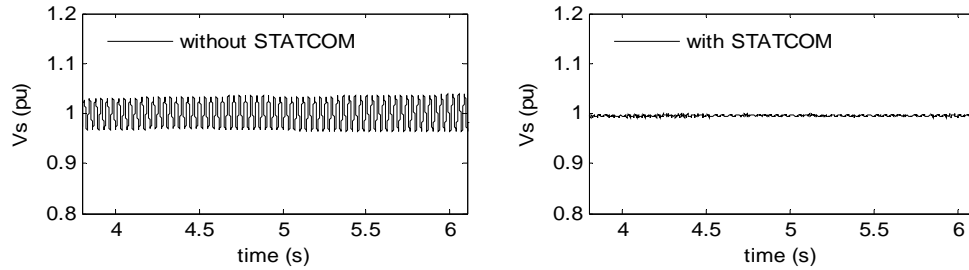
Figure 6.9 Steady state PCC voltage of a 300 MW wind farm
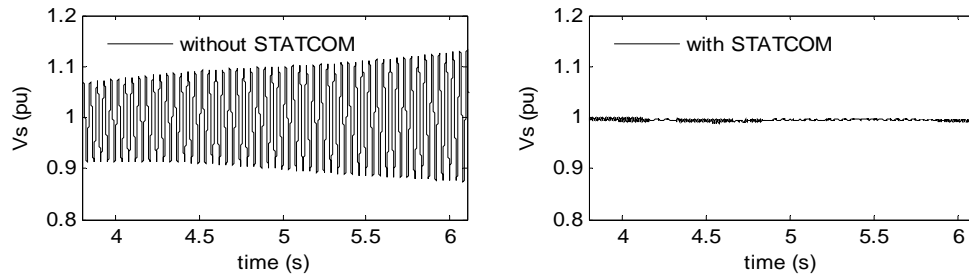
Figure 6.10 Steady state PCC voltage of a 500 MW wind farm

6.6.2   Transient SSR with Remote Fault

This section presents the performance of STATCOM during systems faults for various cases that includes variation in the size of wind farm, variation in the output of a wind farm, and variation in the series compensation level.

6.6.2.1   *Variation in wind farm size*

Wind farm sizes from 100 MW to 500 MW are considered for the transient SSR analysis. Performances of both the controllers are reported together. For each wind farm the series compensation level is chosen marginally above its critical series compensation level. Figure 6.11 shows the performance of the 100 MW wind farm with 60% series compensation and effectiveness of the proposed controllers in damping the SSR oscillations. The electromagnetic torque without STATCOM and with STATCOM is shown in Figure 6.11 (a). In the absence of the STATCOM, fault in the network causes induction generator effect SSR. The electromagnetic torque grows and attains large value. With the proposed controller C-I though the oscillation is damped out successfully, it takes approximately 2s. Meanwhile, the controller C-II offers improved performance and the SSR oscillation is damped out successfully within 0.6s.

The shaft torque for the corresponding operating condition is shown in Figure 6.11 (b). The peak shaft torque reaches upto 1.2pu after the fault is cleared. However, influence of the unstable electromagnetic torque continues and later destabilizes the shaft torque. The proposed controllers now avoid the destabilisation. The peak overshoot is reduced and oscillation in the shaft torque is stabilized rapidly. The performance of both controllers is quite similar in this case. FFT analysis of the electromagnetic torque and shaft torque is shown in Figure 6.11 (c). The FFT of electromagnetic torque shows the estimated frequency of 225.3 rad/s without STATCOM, which matches with the electrical mode frequency shown in

Table 6.4. The estimated frequency of 204.1 rad/s matches with the calculated damped frequency (206.24 rad/s) of the electrical mode with controller I have shown in Table 6.5. With a STATCOM controller–II no electrical mode oscillation is detected in the electromagnetic torque. The electromechanical mode frequency detected at 35.34 rad/s match very closely with the calculated values of 37.55 rad/s, 37.44 rad/s and 37.24 rad/s which are the electromechanical mode eigenvalues of the wind turbine generators without STATCOM, with STATCOM controller-I and STATCOM controller-II, respectively. The torsional mode frequency in all cases is found to be approximately 3.6 rad/s, which matches closely with the FFT estimated value of 3.68 rad/s. Figure 6.11 (d) and (e) depict the generator speed and PCC voltage, respectively. The generator is stabilized faster with controller C-II than with controller C-I. With C-II, the over voltage following the fault clearance is also reduced significantly. The reactive power output of the STATCOM and the DC voltage are shown in Figure 6.11 (f). The negative reactive power output of the STATCOM indicates the capacitive mode of operation. The DC voltage is stabilized faster with C-II and the overshoot also gets reduced. During transients STATCOM injects large (two times of rating) reactive power for few cycles only which can be seen from Figure 6.11 (f).
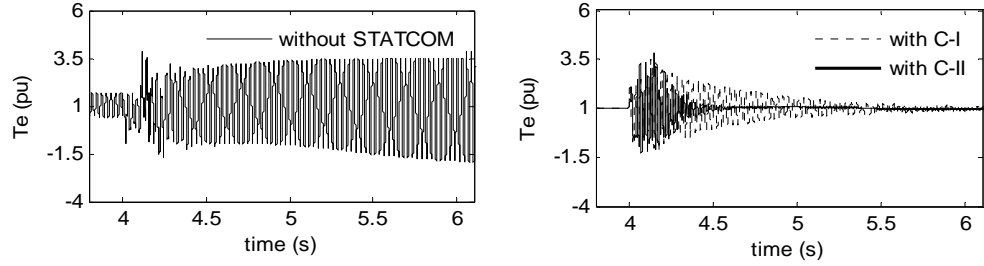
(a) Electromagnetic torque
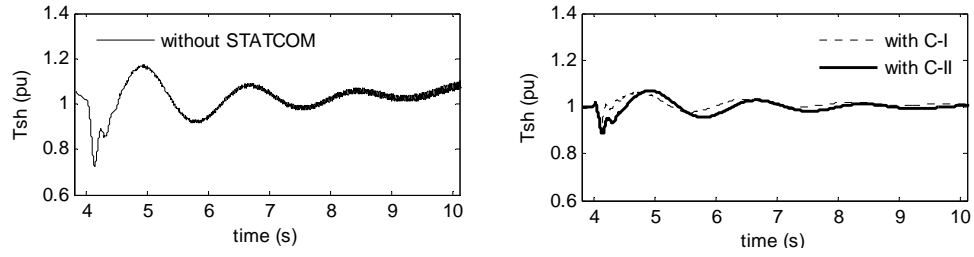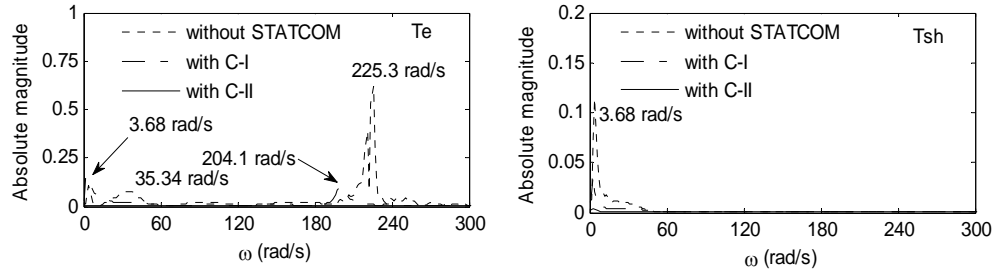
(b) Shaft torque

(c) FFT of electromagnetic and shaft torque
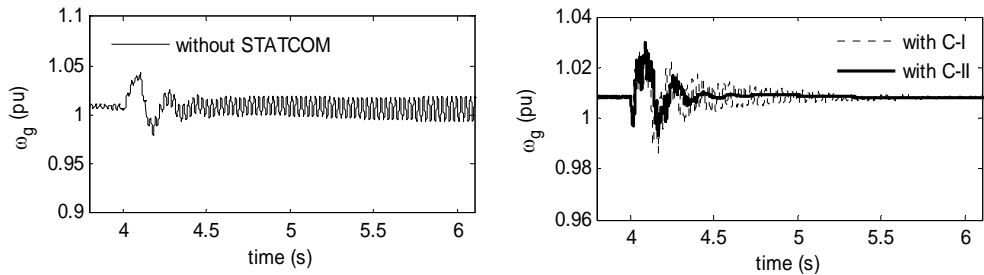
(d) Generator speed
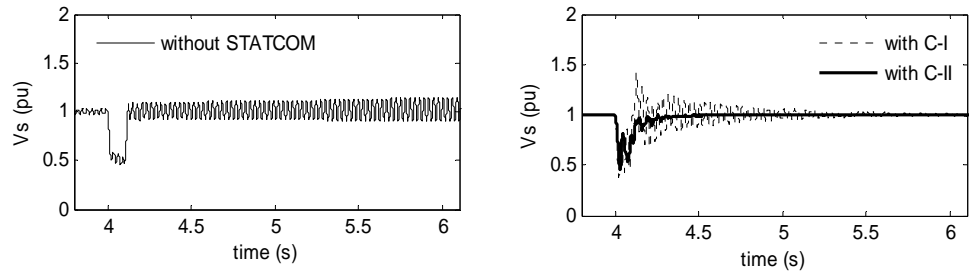
(e) PCC voltage
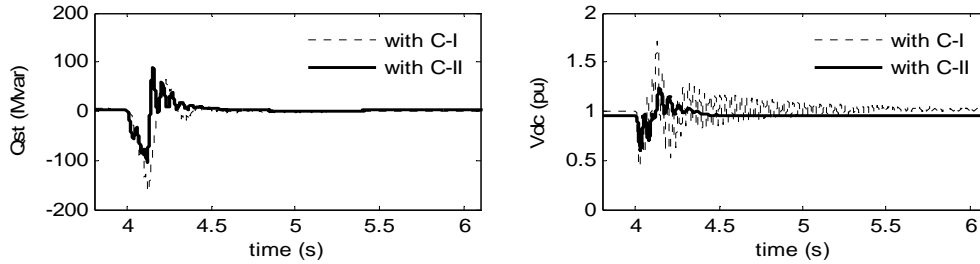
(f) STATCOM reactive power and DC link voltage

Figure 6.11 Transient SSR and its mitigation in a 100 MW wind farm

Transient simulation results of a 300 MW wind farm with 50% series compensation are shown in Figure 6.12. The electromagnetic torque, shaft torque, generator speed, and PCC voltage with and without the STATCOM is shown in Figure 6.12 (a) - (d), respectively. Figure 6.12 (e) shows the reactive power output and DC voltage of the STATCOM. It is observed that controller C-II reduces the post fault oscillations in electromagnetic torque, generator speed, and PCC voltage more effectively than the controller C-I. DC voltage is also now controlled effectively. The estimated frequencies of electromagnetic torque and shaft torque match very closely with the calculated values shown in Table 6.3 to Table 6.5. With controller C-II, reactive power output of the STATCOM is also reduced which is an added benefit. This indicates the reduced use of the MVA capacity of the STATCOM.

Now the performance of the 500 MW wind farm with 55% series compensation is shown in Figure 6.13. The growing oscillation of the electromagnetic torque is successfully stabilized by the proposed controllers. Also in this case, performance of the C-II is found to be superior over of that of C-I. The STATCOM substantially reduces the peak over shoot in the shaft torque following the fault.
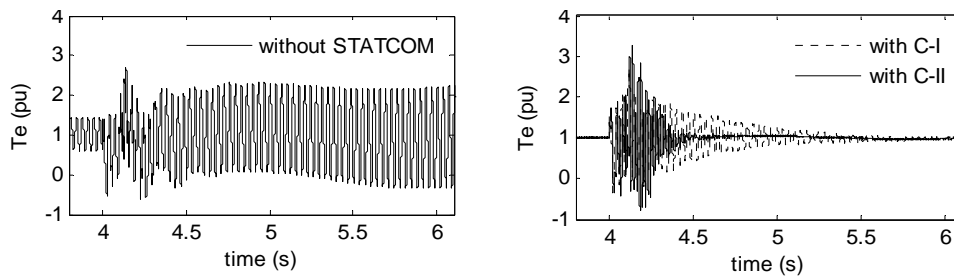
(a) Electromagnetic torque
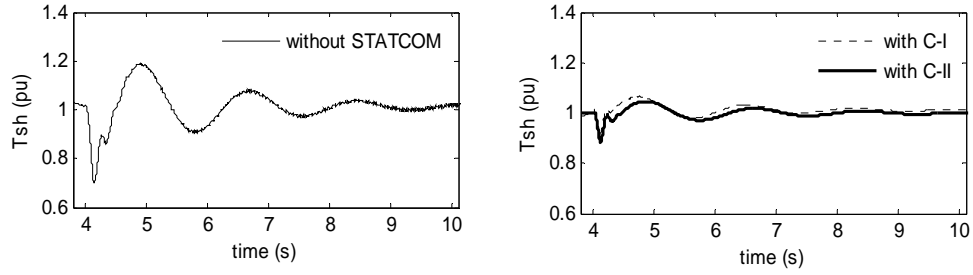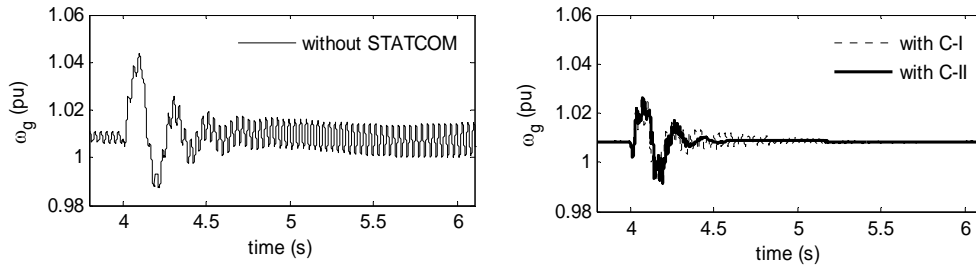
(b) Shaft torque

(c) Generator speed
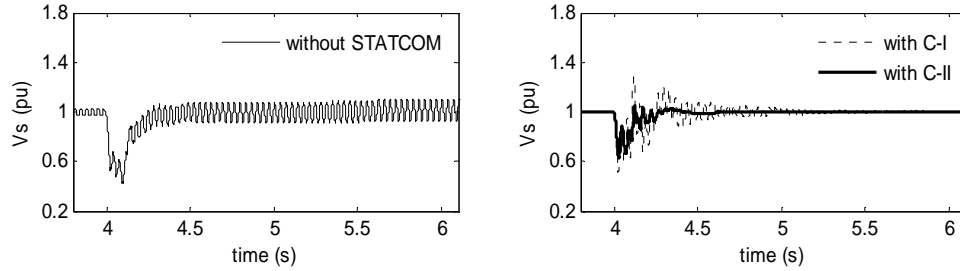
(d) PCC voltage
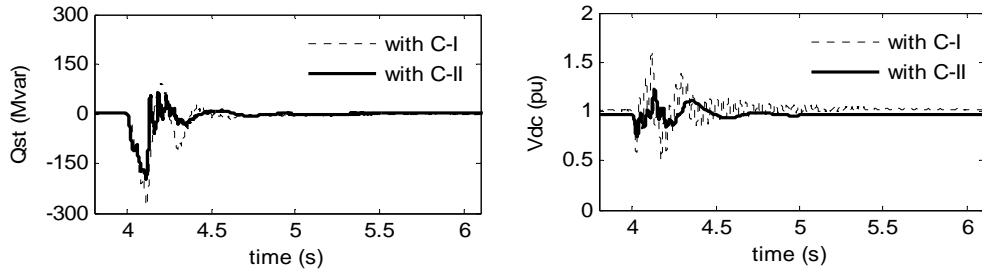
(e) STATCOM reactive power and DC link voltage

Figure 6.12 Transient SSR and its mitigation in a 300 MW wind farm
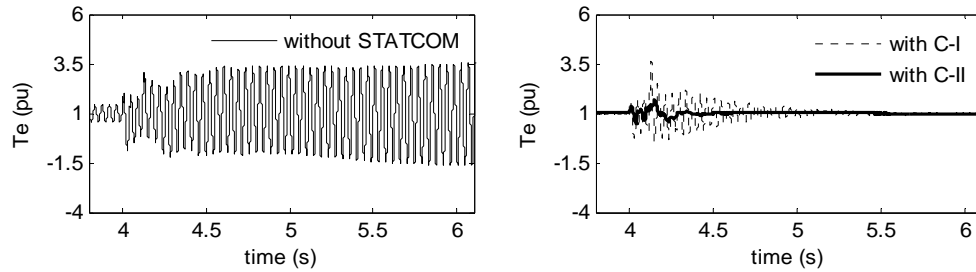
(a) Electromagnetic torque
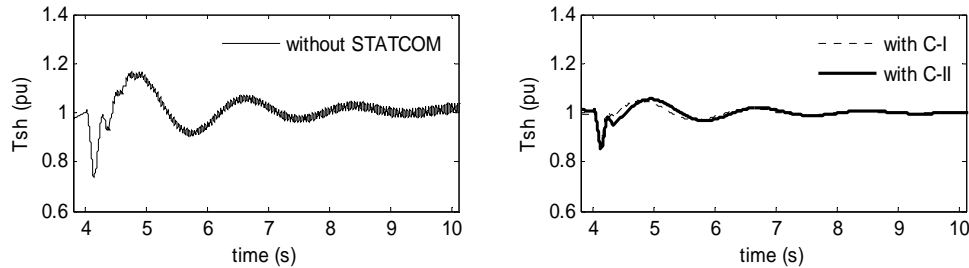
(b) Shaft torque

Figure 6.13 Transient SSR and its mitigation in a 500 MW wind farm

6.6.2.2 *Variation in wind farm output*

In the previous section different sizes of wind farms were considered. This section deals with different output of a large wind farm. A 500 MW wind farm is considered and keeping the series compensation level constant at 55%, the study is conducted with 100 MW and 300 MW output of a wind farm. A symmetrical six-cycles fault is created at the remote end (location-F_2) of the series compensated line and the simulation results are shown in Figure 6.14. The 100 MW (0.2 pu at 500 MW base) output with 55% series compensation represents an unstable electrical mode scenario that can be seen from the growing oscillation in the electromagnetic torque and the PCC voltage of the wind farm. The unstable electrical mode is damped out by the proposed controllers C-I and C-II. The electromagnetic torque with and without the STATCOM is shown in Figure 6.14 (a). The PCC voltage is shown in Figure 6.14 (b), which is also stabilized following the fault clearance. Reactive power and DC voltage of the STATCOM shown in Figure 6.14 (c) shows a significant improvement in the performance with controller C-II over the performance with controller C-I. Particularly controller C-II reduces the peak over shoot in the DC voltage that reflects as a reduced overshoot in the AC voltage at the PCC. The reactive power output of the STATCOM is also reduced with C-II without compromising the aim of stabilizing the unstable electrical mode oscillation.

Figure 6.15 shows the performance of the wind farm at a 300 MW output condition, which is quite similar to the 100 MW output case. The electromagnetic torque and the PCC voltage, both are stabilized successfully with the proposed STATCOM controllers and the potential for the SSR is mitigated.

The case studies presented validate the proposed controllers for the mitigation of subsynchronous resonance in a double-cage induction generator based wind farm. With the control of the modulation index, the DC voltage is controlled smoothly, which then minimizes the voltage overshoot at the PCC. Dynamic response of the STATCOM is also improved noticeably with controller C-II. From the transient simulations no torsional interaction is found which corroborates the small signal analysis. Accurate correlation of the FFT estimated frequencies and calculated damped frequencies validates the small signal model of the study system and the proposed controllers of the STATCOM.

(a) Electromagnetic torque

(b) PCC voltage

(c) STATCOM reactive power and DC link voltage
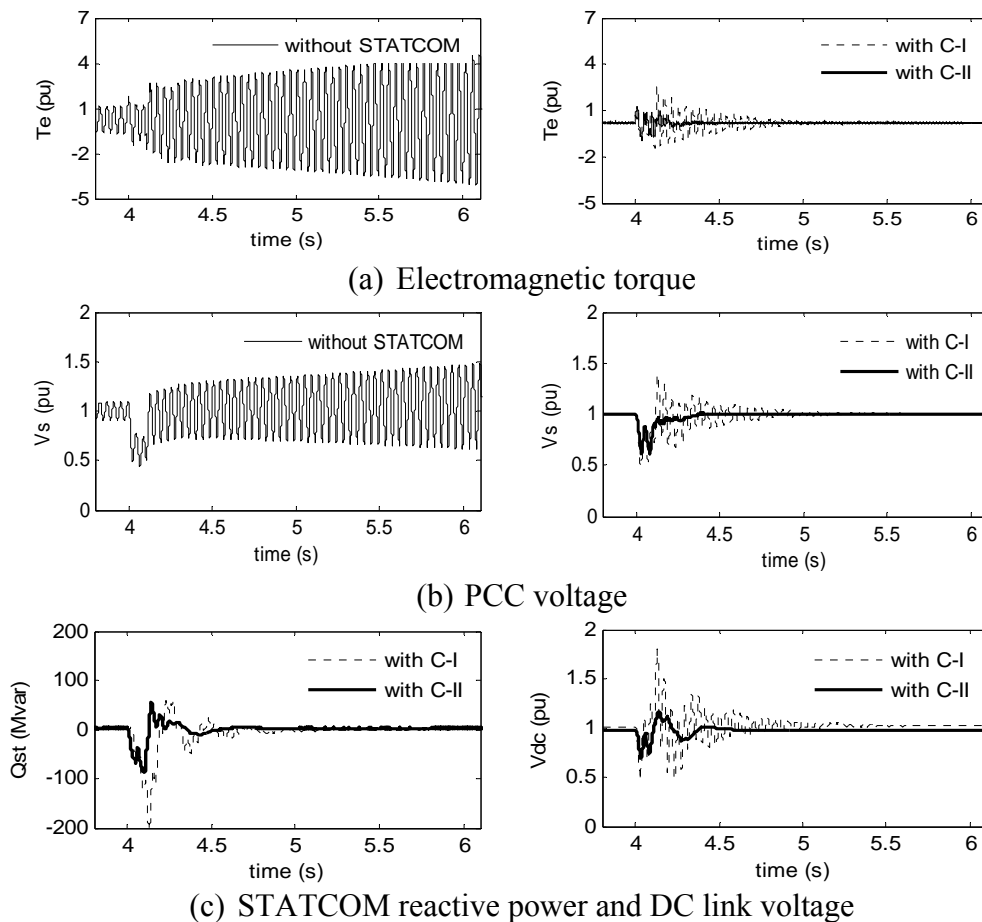
Figure 6.14 Transient performance of a 500 MW wind farm producing 100 MW

(a) Electromagnetic torque

(b) PCC voltage
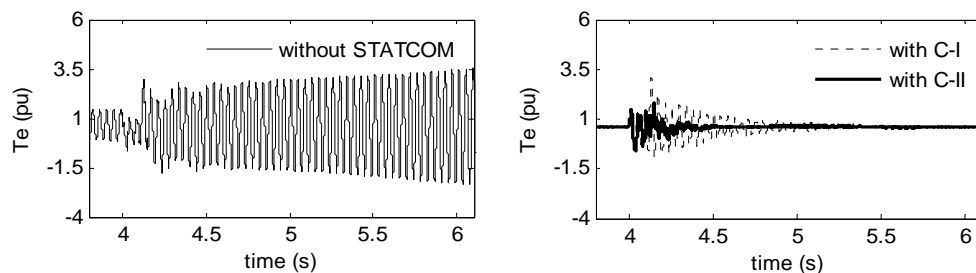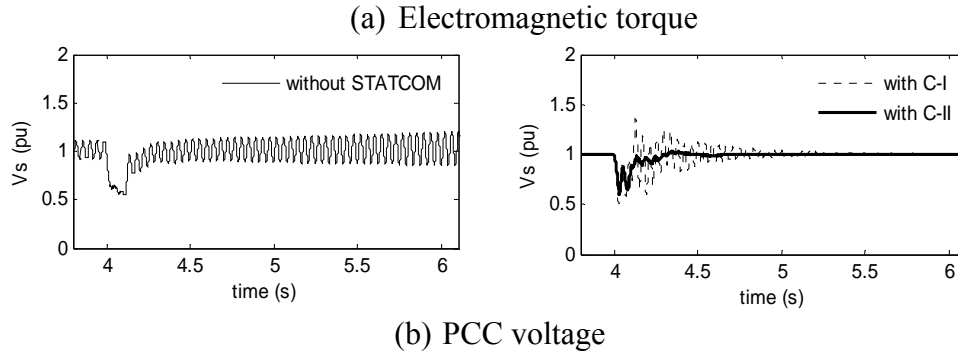
Figure 6.15 Transient performance of a 500 MW wind farm producing 300 MW

6.6.3 Transient SSR with Terminal Fault

A fault is created at the wind farm terminal and performance of the wind farms is examined with the two STATCOM controllers. The terminal fault study is carried out in two sets: one deals with the variable size of wind farm, whereas the other deals with the variable output of a large wind farm. In both cases the series compensation level is kept constant at 50%.

6.6.3.1 *Variation in Wind Farm Size*

Wind farms of 100 MW and 300 MW ratings are considered in this section. The impacts of the fault at the location F_1 on the wind farms are discussed in detail with the proposed STATCOM controllers. Figure 6.16 shows the impacts of a terminal fault on a 100 MW wind farm.

Without the STATCOM, the equivalent wind turbine generator speed falls below the upper resonant speed threshold value of 0.337 rad/s and the speed does not recover after the fault is cleared, as shown in Figure 6.16 (a). However STATCOM with the proposed controllers successfully stabilizes the generator speed. The shaft torque is shown in Figure 6.16 (b). The peak shaft torque is reduced and the maximum overshoot lies within the stress limit of 1.3pu. It is seen that with controller C-I the shaft torque sees a peak immediately after the fault is cleared, whereas with C-II this is not seen. However, the settling time remains quite similar for both controllers. The PCC voltage grows to an unacceptable magnitude as seen from Figure 6.16 (c). With the STATCOM, the PCC voltage is restored after the fault is cleared. Though the PCC voltage peak is reduced to

1.8pu, it is still not acceptable. However, C-II reduces the peak overshoot in the PCC voltage substantially to 1.17pu. The STATCOM reactive power and the DC voltage for the corresponding operating condition are shown in Figure 6.16 (d). Figure 6.17 shows the performance of the 300 MW wind farm for a similar fault at the location F_1. In this case, the speed also falls below the upper resonant speed of 0.42 pu, as depicted in Figure 6.17 (a). However, the speed is restored with the STATCOM. The corresponding shaft torque is shown in see Figure 6.17 (b). The high shaft torque is also reduced to an acceptable value of 1.2pu. It is concluded that for a fault very close to the wind farm, the peak overshoot in the PCC voltage may be a concern and it can be addressed through the STATCOM with a suitable controller. The equivalent circuit analysis very accurately predicts the threshold values of the speed that may cause the instability in the system.

(a) Generator speed

(b) Shaft torque

(c) PCC voltage
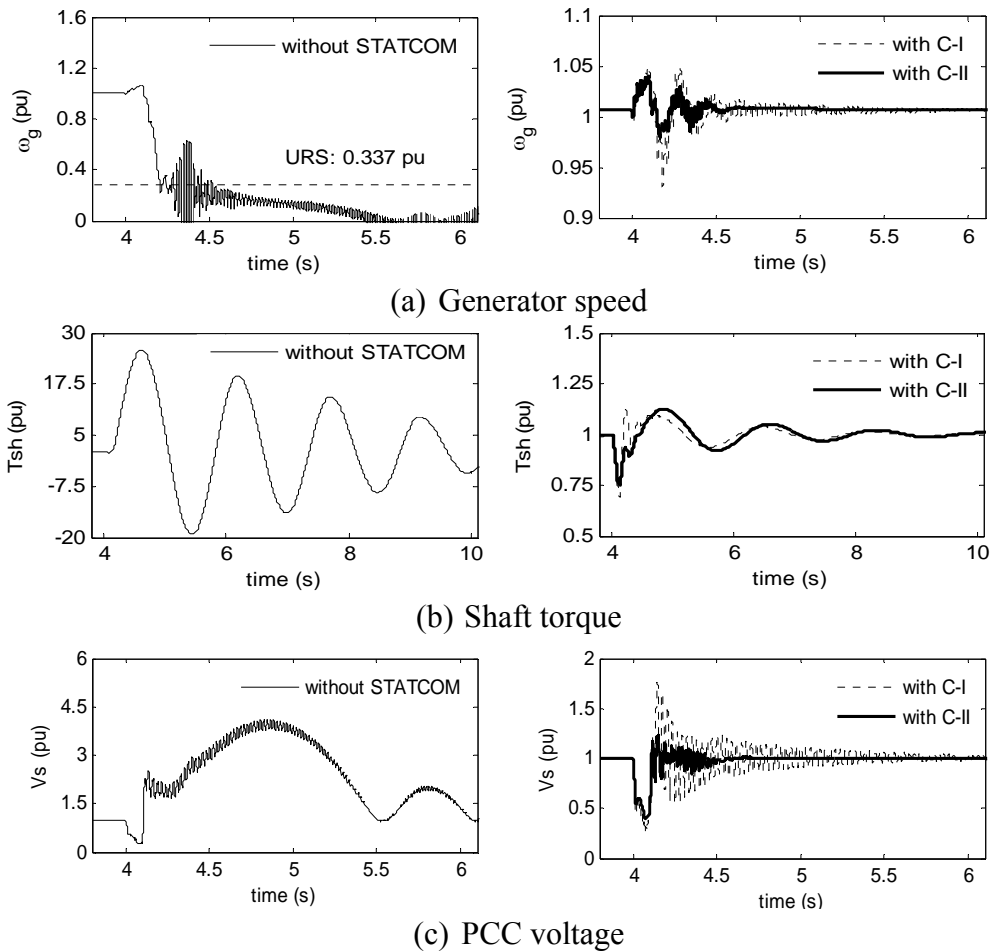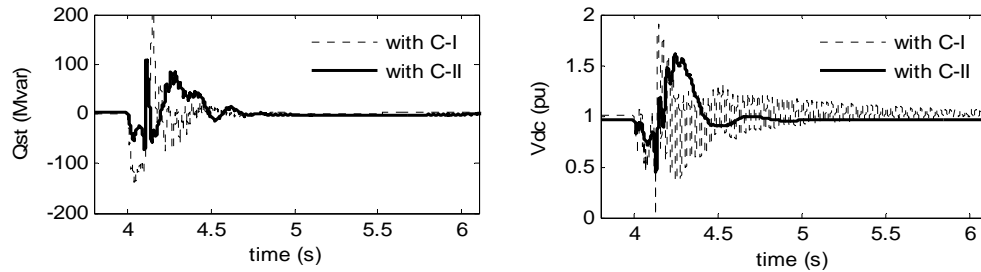
(d) STATCOM reactive power and DC link voltage

Figure 6.16 Transient performance of a 100 MW wind farm
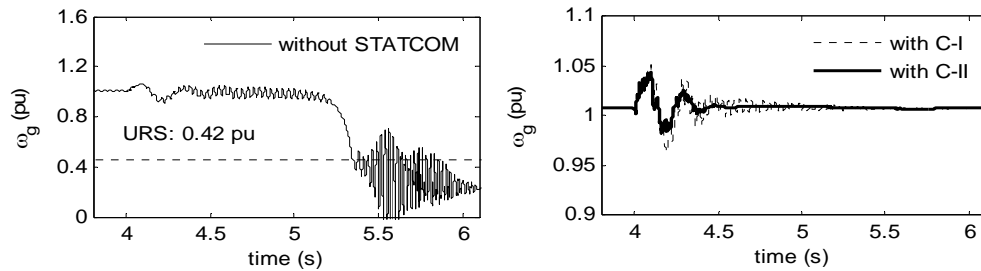
(a) Generator speed
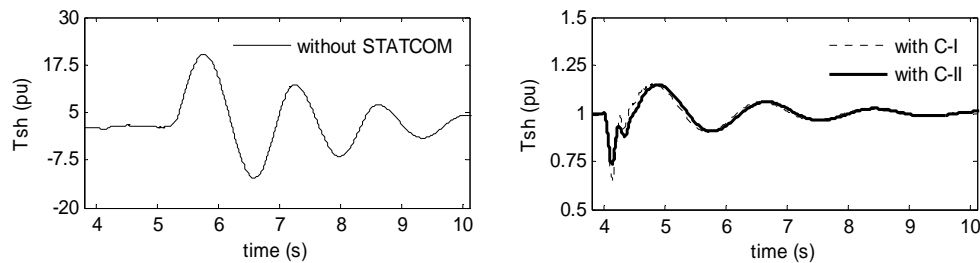
(b) Shaft torque

Figure 6.17 Transient performance of a 300 MW wind farm

6.6.3.2 *Variation in Wind Farm Output*

The study is now extended to a 500 MW wind farm producing variable power output connected to the 50% series compensated line. This section presents the fault response of the wind farm following a symmetrical fault at the wind farm terminal (location F_1) when the power output is 100 MW. Figure 6.18 (a) shows the generator speed. It is seen that the terminal fault causes only a small drop in the speed, which does not destabilize the system as it does with a wind farm of 100 MW size shown in Figure 6.16 (a). Figure 6.18 (b) shows the shaft torque and Figure 6.18 (c) shows the PCC voltage. Following the wind farm terminal fault, the overshoot in the shaft torque and PCC voltage are also found to be small. The shaft torque is stabilized rapidly with both the STATCOM

controllers. The oscillations in the PCC voltage are stabilized much faster with controller C-II in comparison to controller C-I. Simulations for other output conditions reveal the similar results though not shown.

(a) Generator speed

(b) Shaft torque

(c) PCC voltage
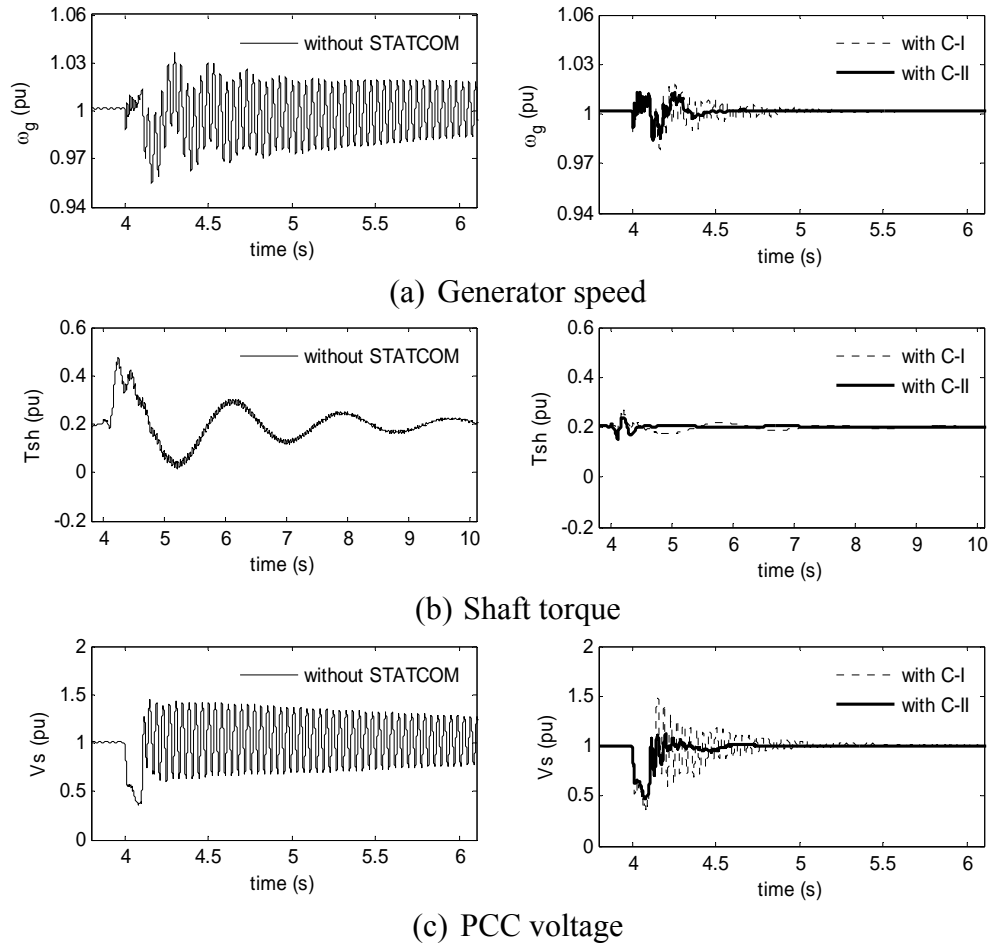
Figure 6.18 Transient performance with 100 MW output

6.7 TRANSIENT SSR STUDIES WITH WIND FARM COLLECTOR CABLE

The effectiveness of the STATCOM with controller C-II is investigated for a more realistic wind farm of 300 MW size with collector cable. The wind farm is split into three groups named as Group-I, Group-II, and Group-III. Each group consists of identical double-cage induction generators and is connected to the PCC through the collector cables. The Group-I collector cable is assumed to be the longest and the collector cable for Group-III is assumed to be the shortest. For the fault analysis, 60% and 70% series compensation levels are considered and a six-cycle symmetrical fault at the remote

terminal (location F_2) is simulated at 4s. Figure 6.19 shows the performance with 60% series compensation. The electromagnetic torques with and without STATCOM are shown in Figure 6.19 (a) and (b), respectively. It is seen that the oscillations without STATCOM in the electromagnetic torque sustain longer in the case of Group-III, in comparison to the Group-I and Group-II. However, with the STATCOM controller C-II the oscillations in all three groups are damped out within 0.2s after the fault is cleared, as seen from Figure 6.19 (b). Figure 6.19 (c) and Figure 6.19 (d) shows the shaft torque of each group with and without the STATCOM, respectively. It is observed that with STATCOM controller C-II, peak overshoot in the shaft torque is reduced substantially, irrespective of the cable length.

To demonstrate another case, series compensation level is increased to 70% and simulation results are depicted in Figure 6.20. Following the fault at the remote end, oscillations without STATCOM in the electromagnetic torque of each group grow and become unstable as seen from Figure 6.20 (a). These oscillations are damped out successfully with the STATCOM controller C-II shown in Figure 6.20 (a). The large shaft torque shown in Figure 6.20 (c) are also successfully alleviated by STATCOM controller C-II that is shown in Figure 6.20 (d).
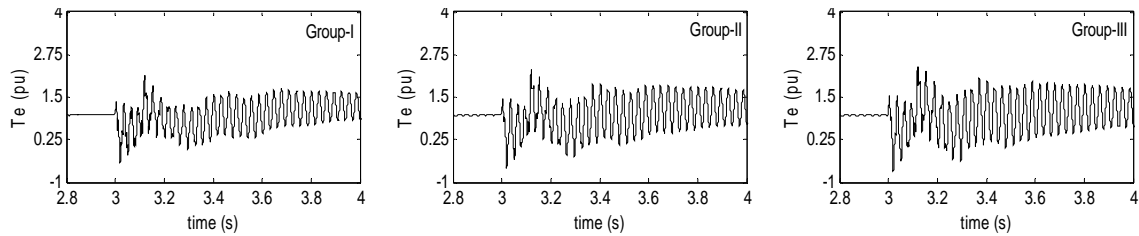
(a) Electromagnetic torque without STATCOM
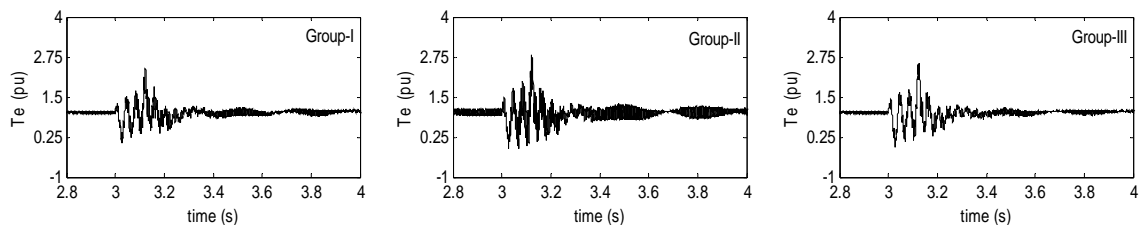
(b) Electromagnetic torque with STATCOM (C-II)
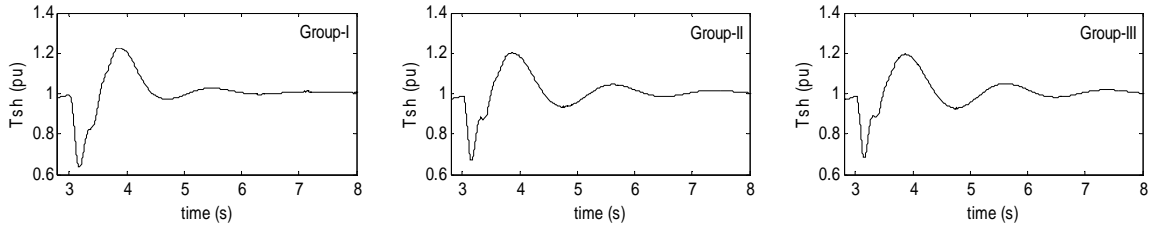
(c) Shaft torque without STATCOM
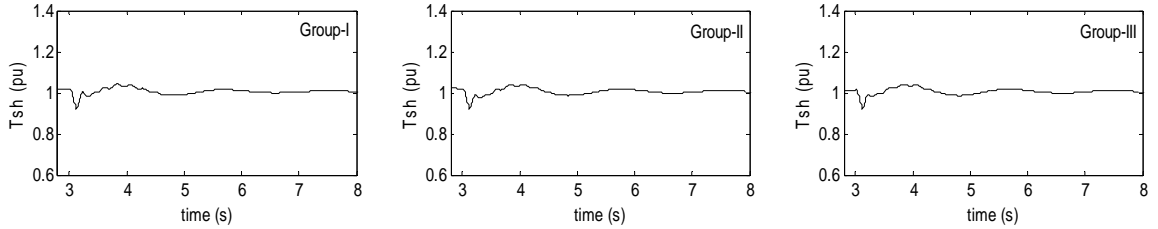
(d) Shaft torque with STATCOM (C-II)

Figure 6.19 Transient response of a 300 MW wind farm with collector cable with 60% compensation
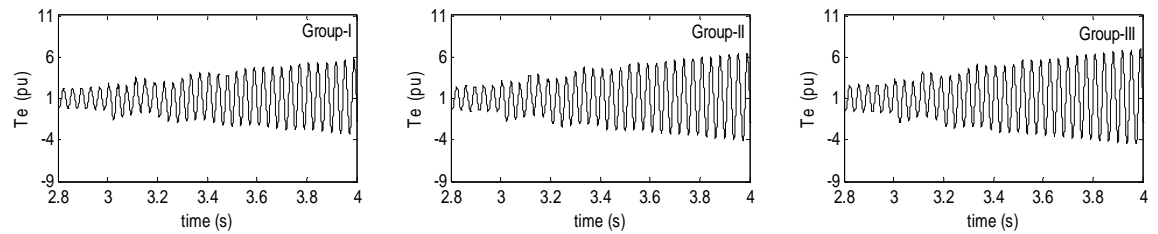
(a) Electromagnetic torque without STATCOM
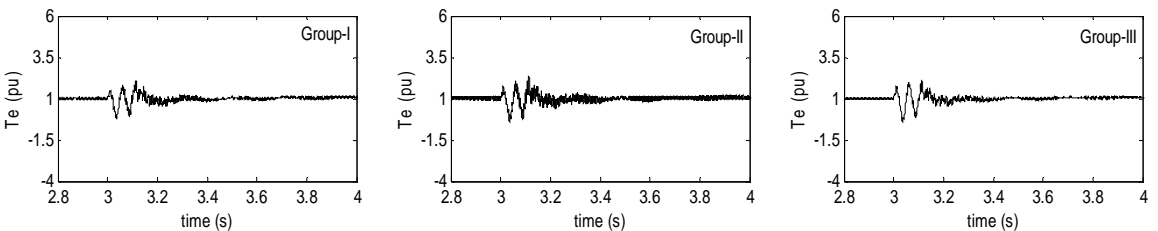
(b) Electromagnetic torque with STATCOM (C-II)
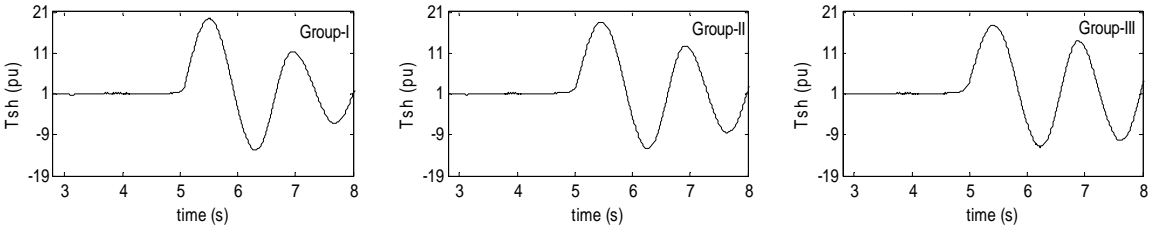
(c) Shaft torque without STATCOM
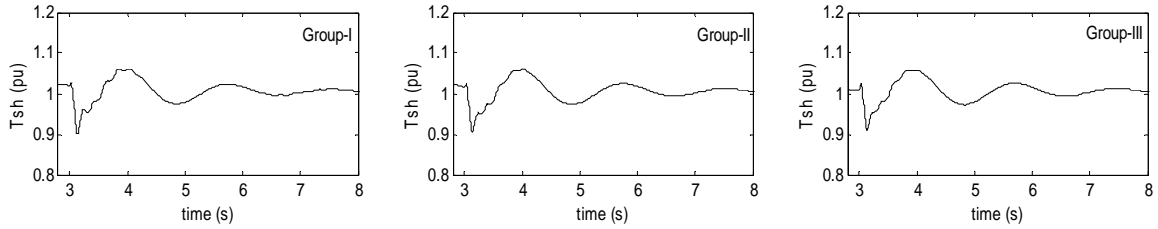
(d) Shaft torque with STATCOM (C-II)

Figure 6.20 Transient response of a 300 MW wind farm with collector cable with 70% compensation

6.8 SRR MITIGATION IN A SINGLE-CAGE INDUCTION GENERATOR BASED WIND FARM

In this section, the SSR mitigation in a single-cage induction generator based wind farm with a STATCOM is presented. In Chapter 3 a detailed SSR analysis is carried out at various operating conditions. The critical series compensation levels are found to be above 75% for different sizes of wind farms, which are beyond realistic levels of compensation. However, a fault at the terminal of the wind farm, then with a realistic compensation (50%) level may cause severe shaft torque rise resulting in the shaft fatigue.

The study system shown in Figure 6.1 is now considered by replacing the double-cage induction generator by single-cage induction generator. A 300 MW wind farm with 80% series compensation is chosen to simulate an unstable operating condition. Figure 6.21 shows the impact of the remote end fault on the wind farm. The fault causes growing oscillations in electromagnetic torque, shaft torque, PCC voltage, and generator speed. With the proposed STATCOM controllers, the unstable electromagnetic torque is now stabilized as shown in Figure 6.21 (a). Similarly, the shaft torque is also stabilized with the proposed controllers, as shown in Figure 6.21 (b). The stabilized PCC voltage and generator speed are shown in Figure 6.21 (c) and (d), respectively. In all cases, it is found that the performance of C-II is better than the performance of C-I.

(a) Electromagnetic torque

(b) Shaft torque

(c) Generator speed

(d) PCC voltage
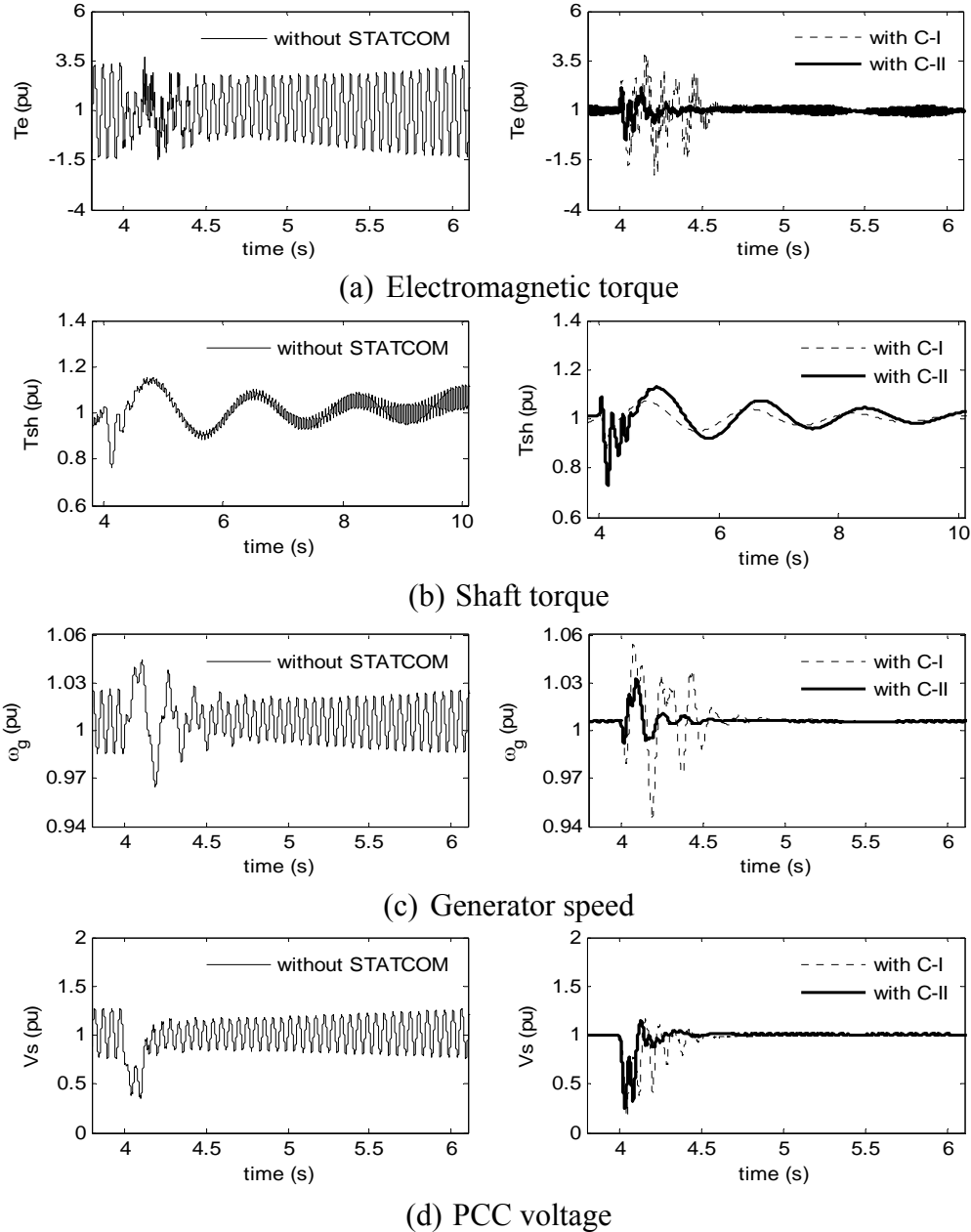
Figure 6.21 Impact of remote fault on a 300 MW wind farm with 80% compensation

Figure 6.22 shows the impacts of a terminal fault on the 300 MW wind farm. In this case a realistic 50% series compensated line is considered. Without the STATCOM the electromagnetic torque continues to oscillate for a longer period and it is damped out with the proposed STATCOM. This is depicted in Figure 6.22 (a). Following the fault clearance, the high shaft torque is witnessed in Figure 6.22 (b). The proposed controllers are able to minimize the rise in the shaft torque that increases the shaft life. Figure 6.22 (c) shows the impact of fault on generator speed that is stabilized within 2s. High

magnitude of PCC voltage is experienced without the STATCOM as shown in Figure 6.22 (d). This is minimized successfully by the proposed STATCOM controllers. However, controller-II performance is better than the controller-I. This analysis validates the performance improvement using the STATCOM at the PCC irrespective of the type of induction generators used in the wind farm.

(a) Electromagnetic Torque

(b) Shaft torque

(c) Generator speed

(d) PCC voltage
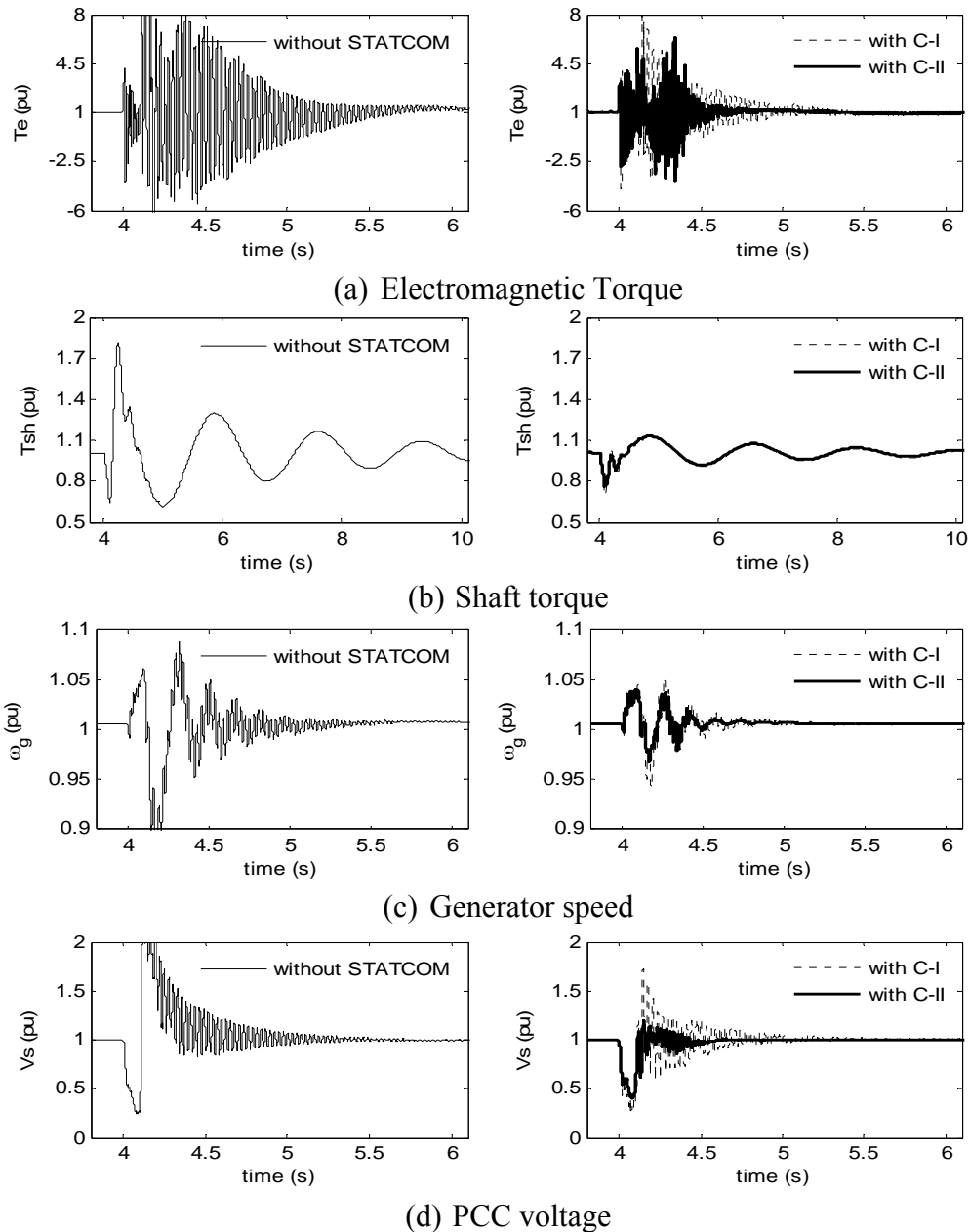
Figure 6.22 Impact of terminal fault on a 300 MW wind farm with 50% compensation

6.9 CONCLUSIONS

A STATCOM based strategy to mitigate the potential for the SSR oscillations in the wind farm is presented in this chapter. A part of this chapter is reported in [133]. Two controllers are proposed in this chapter for the STATCOM. The controller C-I is not equipped with the DC voltage control, whereas controller C-II employs DC voltage control. From the detailed eigenvalue analysis and electromagnetic transient simulation it is concluded that a STATCOM employed at the PCC alleviates the potential of SSR. A voltage controller can mitigate the SSR oscillation and increase the stability of the system. Instability due to the fault at the terminal can also be successfully addressed by the proposed controller. The STATCOM controller is also effective for the single induction generator based wind farms.

Chapter 7

SUBSYNCHRONOUS RESONANCE STUDY OF WIND FARM CONNECTED TO LINE COMMUTATED CONVERTER BASED HVDC LINES

7.1 INTRODUCTION

A study of subsynchronous resonance in a wind farm connected to a line-commutated converter (LCC) based HVDC line is presented in this chapter. Subsynchronous interactions between HVDC current controllers and turbine-generator shaft of synchronous generators have been observed in past. Previous analysis shows that the HVDC converter has the potential to create subsynchronous torsional oscillations in the turbine-generator that is connected to the same bus as the HVDC converter [38]-[41]. The potential of torsional interaction reduces as the impedance between the two increases or as additional AC circuits are connected.

As the application of HVDC for the wind farm interconnection grows, a threat of SSR interaction also intensifies. However, SSR interaction of the wind farm with HVDC lines has not yet been fully explored. Parallel AC and HVDC study system is also considered for the analysis. Thus, this chapter illustrates a very compressive study of the SSR in wind farms connected to LCC HVDC systems. Small signal analysis and its validation through the time domain simulation is carried out to investigate the potential of subsynchronous resonance. Various sensitivity studies are also carried out to evaluate the impact of parameter variation and its potential impact on the sensitive oscillatory modes.

7.2 SYSTEM DESCRIPTION

The study system considered is presented in Figure 7.1. An aggregated IG based wind farm is connected to a LCC HVDC line and series compensated parallel AC transmission line. The wind farm size is varied between 500 MW and 700 MW. The HVDC line considered here is the CIGRE Benchmark System proposed in [127]. For simplicity, the

multiple AC filter banks at each station are presented by a single capacitor bank. AC shunt filters yield oscillatory modes which are above the synchronous frequency, hence simplified AC filter representations would not affect the SSR analysis. This has been a common practice for the study of SSR [34], [78].
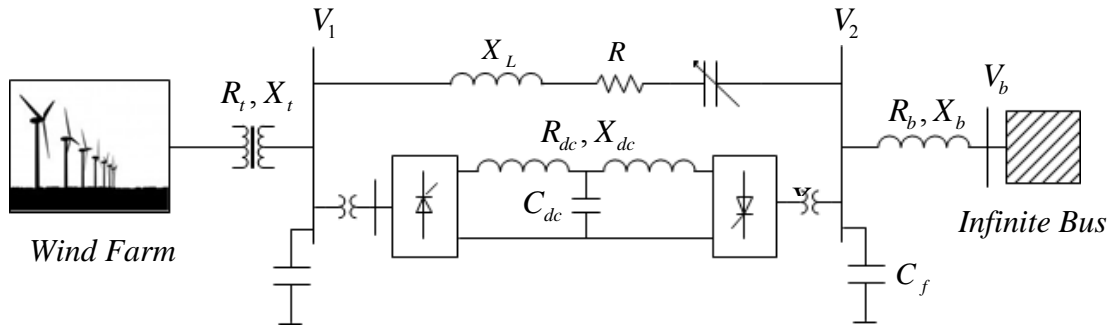
Figure 7.1 Study system

7.3 STUDY SYSTEM MODELING

The study system is divided into four sub-systems: i) mechanical drive train, ii) induction generator, iii) AC network, and iv) HVDC system. The drive train and induction generator models are taken from Chapter 2.

7.3.1   AC Network

The AC network in this system includes the shunt capacitor at generator terminal, interfacing transformer, AC filter at rectifier bus and series compensated transmission line. The dynamic equations of the network are written as:

$$C_g \frac{d}{dt} V_{ds} = I_{ds} - I_d + \omega_s C_g V_{qs} \qquad (7.1)$$

$$C_g \frac{d}{dt} V_{qs} = I_{qs} - I_q - \omega_s C_g V_{ds} \qquad (7.2)$$

$$L_t \frac{d}{dt} I_d = V_{ds} - R_t I_d + \omega_s L_t I_q - V_{d1} \qquad (7.3)$$

$$L_t \frac{d}{dt} I_q = V_{qs} - R_t I_q - \omega_s L_t I_d - V_{q1} \qquad (7.4)$$

$$C_f \frac{d}{dt} V_{d1} = I_d - I_{rd} - I_{d1} + \omega_s C_f V_{q1} \qquad (7.5)$$

$$C_f \frac{d}{dt}V_{q1} = I_q - I_{rq} - I_{q1} - \omega_s C_f V_{d1} \tag{7.6}$$

$$L\frac{d}{dt}I_{d1} = V_{ds} - RI_{d1} + \omega_s LI_{q1} - V_{cd} - V_{bd} \tag{7.7}$$

$$L\frac{d}{dt}I_{q1} = V_{qs} - RI_{q1} - \omega_s LI_{d1} - V_{cq} - V_{bq} \tag{7.8}$$

$$C\frac{d}{dt}V_{cd} = I_{d1} + \omega_s CV_{cq} \tag{7.9}$$

$$C\frac{d}{dt}V_{cq} = I_{q1} - \omega_s CV_{cd} \tag{7.10}$$

where,

C_g	:	Power factor correction capacitor at wind turbine generator terminal (pu)
R_t	:	Transformer winding resistance (pu)
L_t	:	Transformer winding leakage inductance (pu)
C_f	:	AC filter capacitance at rectifier bus (pu)
R	:	AC transmission line resistance (pu)
X_L	:	AC transmission line inductance (pu)
C	:	Capacitance in series with AC transmission line (pu)
V_{ds}, V_{qs}	:	*d-q* axis wind turbine terminal voltage (pu)
I_{ds}, I_{qs}	:	*d-q* axis generator stator current (pu)
I_d, I_q	:	*d-q* axis transformer current (pu)
V_{d1}, V_{q1}	:	*d-q* axis rectifier bus voltage (pu)
I_{d1}, I_{q1}	:	*d-q* axis series compensated line current (pu)
V_{cd}, V_{cq}	:	*d-q* axis voltage across series capacitor (pu)
I_{rd}, I_{rq}	:	*d-q* axis rectifier current (pu)
V_{bd}, V_{bq}	:	*d-q* axis infinite bus voltage. (pu)

7.3.2 HVDC Transmission System

The HVDC converters are equipped with constant current (CC) and constant extinction angle (CEA) controllers. The DC line can be modeled as an equivalent T network: two series impedance placed on both sides of the lumped charging capacitance that is put at the midpoint of the line. The base values for the AC and DC quantities should be chosen such that the per unit values of any DC quantities will remain unchanged when converted to the reference frame of the AC system [34], [78], [128]. The differential equations of the DC transmission line are written as:

$$L_{dc} \frac{d}{dt} I_{dr} = V_{dr} - R_{dc} I_{dr} - V_{dc} \tag{7.11}$$

$$C_{dc} \frac{d}{dt} V_{dc} = I_{dr} - I_{di} \tag{7.12}$$

$$L_{dc} \frac{d}{dt} I_{di} = V_{dc} - R_{dc} I_{di} - V_{di} \tag{7.13}$$

The equivalent voltage at rectifier (V_{dr}) and inverter (V_{di}) are derived as:

$$V_{dr} = \frac{3\sqrt{2}}{\pi} V_1 \cos(\alpha) - \frac{3X_{tr}}{\pi} I_{dr} \tag{7.14}$$

$$V_{di} = \frac{3\sqrt{2}}{\pi} V_2 \cos(\gamma) - \frac{3X_{ti}}{\pi} I_{di} \tag{7.15}$$

where,

L_{dc}	:	DC transmission line inductance (pu)
R_{dc}	:	DC transmission line resistance (pu)
C_{dc}	:	DC link capacitance (pu)
V_{dr}	:	Rectifier station DC bus voltage (pu)
V_{di}	:	Inverter station DC bus voltage (pu)
V_{dc}	:	DC link capacitor voltage (pu)
I_{dr}	:	DC current injected from rectifier (pu)
I_{di}	:	DC current absorbed by inverter (pu)
V_1	:	Rectifier station AC bus voltage (pu)

V_2 :   Inverter station AC bus voltage (pu)

7.3.3 HVDC Current Regulator

The current regulator at each station is modeled as shown in Figure 7.2and Figure 7.3 [78].
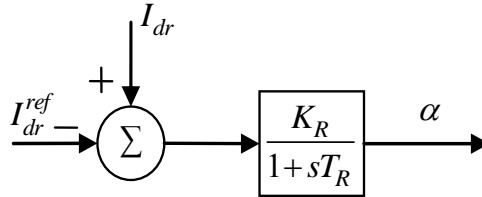
Figure 7.2 Rectifier station current regulator
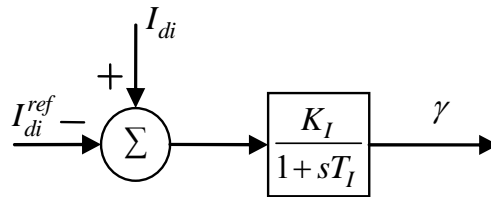
Figure 7.3 Inverter station current regulator

The differential equations of the current regulator are now written as:

$$\frac{d}{dt}(\alpha) = \frac{K_r}{T_r}\left(I_{dr} - I_{dr}^{ref}\right) - \frac{1}{T_r}(\alpha) \tag{7.16}$$

$$\frac{d}{dt}(\gamma) = \frac{K_i}{T_i}\left(I_{di} - K_m I_{dr}^{ref}\right) - \frac{1}{T_i}(\gamma) \tag{7.17}$$

7.3.4 Complete System Model

The differential equations of each subsystem are linearized. The state space model of the study system is then developed by aggregating all the linearized sub-systems. The complete state space model of the system is written as:

$$\dot{x}_{sys} = \left[A_{sys} \right] x_{sys} + \left[B_{sys} \right] u_{sys} \tag{7.18}$$

where,

$$x_{sys}^t = \left[x_{WT}^t \quad x_G^t \quad x_N^t \quad x_{DC}^t \right] \tag{7.19}$$

$$x_{WT}^t = \left[\Delta\omega_t \quad \Delta\delta_{tg} \quad \Delta\omega_g \right] \tag{7.20}$$

$$x_G^t = \left[\Delta I_{ds} \quad \Delta I_{qs} \quad \Delta E_{d1} \quad \Delta E_{q1} \quad \Delta E_{d2} \quad \Delta E_{q2} \right] \tag{7.21}$$

$$x_{DC}^t = \left[\Delta I_{dr} \quad \Delta V_{dc} \quad \Delta I_{di} \quad \Delta\alpha \quad \Delta\gamma \right] \tag{7.22}$$

When AC line is not series compensated:

$$x_N^t = \left[\Delta V_{ds} \quad \Delta V_{qs} \quad \Delta I_d \quad \Delta I_q \quad \Delta V_{d1} \quad \Delta V_{q1} \quad \Delta I_{d1} \quad \Delta I_{q1} \right] \tag{7.23}$$

When AC line is series compensated:

$$x_N^t = \left[\Delta V_{ds} \quad \Delta V_{qs} \quad \Delta I_d \quad \Delta I_q \quad \Delta V_{d1} \quad \Delta V_{q1} \quad \Delta I_{d1} \quad \Delta I_{q1} \quad \Delta V_{cd} \quad \Delta V_{cq} \right] \tag{7.24}$$

The state space models of the drive train and the induction generator remain same as it is described in Chapter 2.

7.4   SMALL SIGNAL ANALYSIS

7.4.1   Eigenvalue Analysis

The system eigenvalues are calculated at several operating points using the state space model of the study system. To simplify the analysis, the inverter station voltage is assumed to be constant [34]. Table 7.1 and Table 7.2 show the eigenvalues of the AC-DC system without and with series compensation, respectively. Table 7.1 shows the eigenvalues of the AC-DC system with a 500 MW wind farm. To evaluate the mutual interaction between the rectifier station current regulator and the wind farm without series compensation, no series compensation is applied in this case. Without an HVDC system, six pairs of complex conjugates and one real eigenvalue are obtained, whereas with HVDC system ten pairs of complex conjugates and one real eigenvalue are obtained. All of the oscillatory and non-oscillatory modes are shown in Table 7.1.

Table 7.1 presents the calculated eigenvalues of the study system without series compensation. It is seen that the electromechanical mode is influenced by the HVDC

system. The electromechanical mode eigenvalues obtained with only AC system are -3.444 ± 25.619i, which are changed to -3.059 ± 23.949i when HVDC system is considered. The stability of the torsional mode is also found to be weakened a little. Table 7.2 shows the eigenvalues of the AC-DC system with 50% series compensated AC transmission line. The calculated electrical mode eigenvalues are -0.851 ±169.94i without HVDC, which change to -15.777 ± 188.67i when HVDC system is considered. HVDC system interconnection shows a substantial improvement in the electrical mode stability. It is mentioned in Chapters 3, 4 and 5 that the induction generator effect, SSR, in wind farms is typically caused by the unstable electrical mode. It is seen from Table 7.2 that the stability of the electromechanical mode is reduced slightly with HVDC system.

Table 7.1 AC-DC System eigenvalue without series compensation

Mode	AC System	AC-DC System
Elect-mech. mode	-3.444 ± 25.619i	-3.059 ± 23.949i
Torsional mode	-0.882 ± 3.7232i	-0.787 ± 3.4081i
Other modes	-10.66 ± 1804.6i	-112.4 ± 3233.5i
	-14.40 ± 1050.6i	-103.8 ± 2618.6i
	-11.88 ± 376.73i	-141.1 ± 1477.2i
	-58.83 ± 3.5293i	-43.21 ± 856.89i
	-2.015	-13.87 ± 376.73i
		-42.20 ± 315.04i
		-90.50 ± 102.05i
		-58.95 ± 2.8489i
		-3.785

Table 7.2 AC-DC System eigenvalues with series compensation

Mode	AC System	AC-DC System
Sup.-syn. mode	-7.444 ± 583.3i	-21.57 ± 568.78i
Electrical mode	-0.851 ± 169.94i	-15.77 ± 188.67i
Elect-mech. mode	-4.494 ± 31.44i	-3.957 ± 28.044i
Torsional mode	-0.601 ± 3.563i	-0.675 ± 3.5127i
Other modes	-10.61 ± 1886.4i	-106.9 ± 3251.3i
	-14.03 ± 1132.5i	-97.03 ± 2648.5i
	-60.30 ± 3.6407i	-138.6 ± 1488i
	-5.541	-34.61 ± 879.78i
		-47.53 ± 323.38i
		-47.53 ± 323.38i
		-71.24 ± 103.71i
		-59.64 ± 3.3395i
		-4.803

Comparing Table 7.1 and Table 7.2 it is also found that the stability of electromechanical mode declines with HVDC system in both cases; without series compensation and with series compensation. However, series compensation improves the stability of the electromechanical mode of an induction generator based wind farm. Moreover, it is seen that the stability of the torsional mode is improved with the rectifier station current regulator. All other modes shown in able 7.2 are substantially damped, hence not discussed.

A detailed eigenvalue analysis is carried out for the variation in wind farm size, series compensation level and power output. Table 7.3 presents the selected eigenvalues of the study system for three different sizes (500 MW, 600 MW, and 700 MW) of wind farms and series compensation levels. The DC line power flow is set at 400 MW. With 50% series compensation, as the wind farm size increases the electrical mode stability decreases slightly. The oscillatory frequency of the electrical mode also decreases with the increase in the size of the wind farm. Similarly, the electromechanical mode eigenvalues also become less stable with a larger wind farm. However, the behavior of the torsional mode is opposite to the above trend.

As the wind farm size increases, keeping series compensation level constant at 50% the torsional mode becomes more stable. However, as the series compensation level increases, the electrical and electromechanical modes become more stable, but the torsional mode becomes less stable. The study is extended to investigate the impacts of variable power outputs of a 700 MW wind farm. Table 7.4 illustrates the calculated eigenvalues for different operating conditions. It is observed that at a constant compensation level when the wind farm output increases, all the aforementioned modes become more stable.

Table 7.3 AC-DC system eigenvalues with different wind farm sizes

Mode	500 MW	600 MW	700 MW
50% series compensation			
Sup. syn. mode	-21.572 ± 568.78i	-19.933 ± 574.7i	-18.781 ± 579.32i
Electrical mode	-15.777 ± 188.67i	-15.5 ± 182.26i	-15.252 ± 177.18i
Elect-mech. mode	-3.9572 ± 28.044i	-3.6507 ± 26.667i	-3.4147 ± 25.318i
Torsional mode	-0.6750 ± 3.5127i	-0.7388 ± 3.5149i	-0.8286 ± 3.5446i
70% series compensation			
Sup. syn. mode	-26.223 ± 603.1i	-23.88 ± 610.21i	-22.14 ± 615.79i
Electrical mode	-29.351 ± 157.16i	-29.412 ± 147.93i	-29.198 ± 140.14i
Elect-mech. mode	-4.576 ± 30.604i	-4.2401 ± 29.457i	-3.9536 ± 28.351i
Torsional mode	-0.6098 ± 3.542i	-0.6397 ± 3.5366i	-0.6785 ± 3.5372i
90% series compensation			
Sup. syn. mode	-30.724 ± 632.27i	-27.716 ± 640.43i	-25.428 ± 646.88i
Electrical mode	-50.116 ± 144i	-53.635 ± 136.89i	-56.544 ± 132.03i
Elect-mech. mode	-5.4154 ± 34.189i	-5.0899 ± 33.421i	-4.787 ± 32.661i
Torsional mode	-0.5542 ± 3.5693i	-0.5642 ± 3.5637i	-0.5763 ± 3.5589i

Table 7.4 AC-DC system eigenvalues with different wind farm outputs

Mode	500 MW	600 MW	700 MW
50% series compensation			
Sup. syn. mode	-18.138 ± 580.42i	-18.378 ± 580.01i	-18.781 ± 579.32i
Electrical mode	-15.042 ± 177i	-15.128 ± 177.08i	-15.252 ± 177.18i
Elect-mech. mode	-3.0108 ± 26.47i	-3.1742 ± 25.98i	-3.4147 ± 25.318i
Torsional mode	-0.5431 ± 3.4407i	-0.6481 ± 3.4607i	-0.8285 ± 3.5446i
70% series compensation			
Sup. syn. mode	-21.49 ± 617.22i	-21.744 ± 616.66i	-22.14 ± 615.79i
Electrical mode	-29.253 ± 139.85i	-29.236 ± 139.97i	-29.198 ± 140.14i
Elect-mech. mode	-3.6139 ± 29.124i	-3.7588 ± 28.791i	-3.9536 ± 28.351i
Torsional mode	-0.5079 ± 3.4931i	-0.5745 ± 3.5048i	-0.6785 ± 3.5372i
90% series compensation			
Sup. syn. mode	-24.733 ± 648.71i	-25.012 ± 647.97i	-25.428 ± 646.88i
Electrical mode	-56.678 ± 132i	-56.621 ± 132.02i	-56.544 ± 132.03i
Elect-mech. mode	-4.4777 ± 33.181i	-4.6137 ± 32.961i	-4.787 ± 32.661i
Torsional mode	-0.4770 ± 3.5403i	-0.5176 ± 3.5465i	-0.5763 ± 3.5589i

7.4.2   Participation Factor Analysis

From the eigenvalue analysis, different modes of the AC-DC system have been identified. The influence of different states on any particular mode is now studied through the participation factor analysis. Figure 7.4 (a) shows the participation factors associated with the super synchronous mode. This mode is largely impacted by the series capacitor and the transmission line current. Stator currents of the induction generator influence this

mode only slightly, as seen in Figure 7.4 (a). Figure 7.4 (b) shows the participation factors of the electrical mode of AC-DC system. This mode is seen to be affected by the DC line current and rectifier current regulator along with a series capacitor and line current. Figure 7.4 (c) shows the participation factors associated with the electromechanical mode, which is contributed by the generator speed and rotor induced *d*-axis voltages. This mode is also seen to be sensitive to generator inertia constant and rotor circuit parameters. Similarly Figure 7.4 (d) shows the participation factors associated with the torsional mode. This mode does not have any contribution from the electrical network. Hence, no interaction with the rectifier station current controller is anticipated.

(a) Super-synchronous mode

(b) Electrical mode

(c) Electromechanical mode

(d) Torsional mode
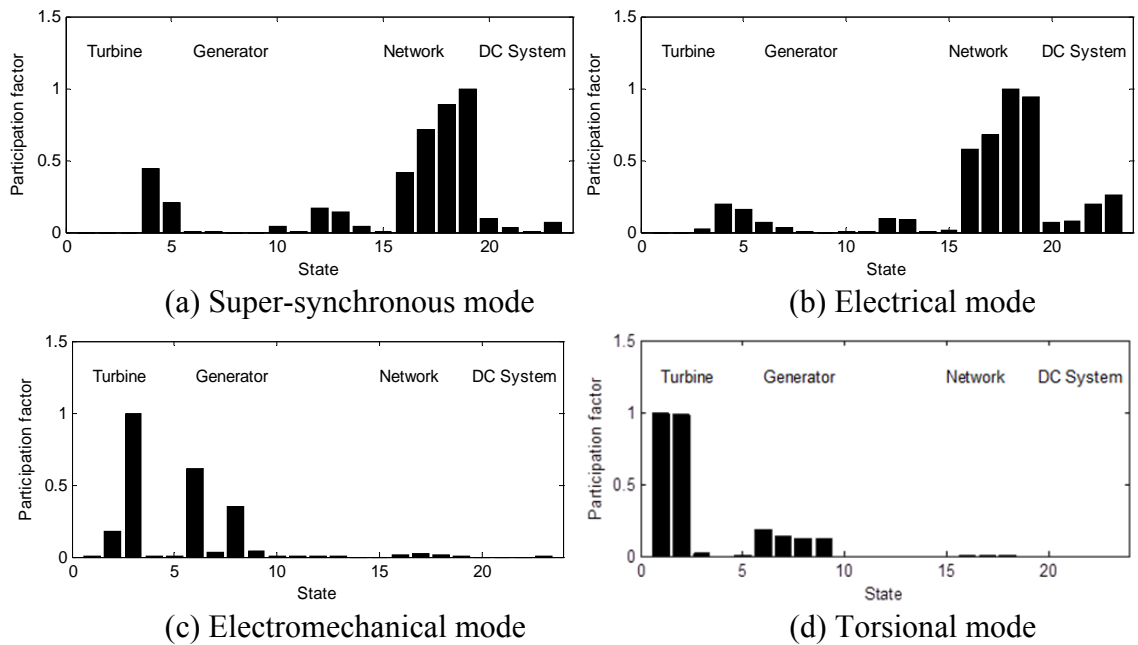
Figure 7.4 Participation factor of selected modes

7.4.3   Sensitivity Analysis

In this section, sensitivity analysis is carried out by varying different system parameters of the study system. The important parameters which may affect the performance of the wind farm and HVDC stations are: i) level of series compensation, ii) rectifier firing angle, iii) DC line power flow, and iv) Rectifier station current controller gain and time constant.

7.4.3.1 *Variation in Series Compensation*

The impact of series compensation is tested with AC system and AC-DC system. Three modes (as discussed above) are considered. When the compensation level increases from 20% to 90%, the electrical mode eigenvalue of the AC system moves towards origin and crosses the imaginary axis at critical series compensation level as shown in Figure 7.5 (a). For a 700 MW wind farm the critical series compensation level is found to be around 55% without the HVDC line. In the case of an AC-DC system, although the electrical mode stability is reduced, this mode may never become unstable, as depicted in Figure 7.5 (a). This indicates that there will be no potential for the SSR due to induction generator effect. Figure 7.5 (b) and (c) show the impact of series compensation level on the electromechanical mode and torsional mode, respectively, with AC and AC-DC system, respectively. Neither of these modes are found to become unstable with increase in the series compensation level.
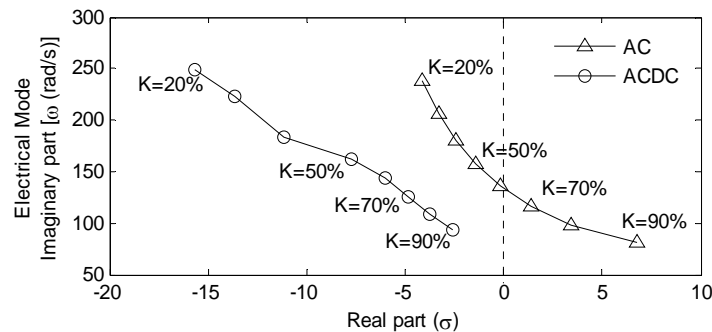
(a) Electrical mode
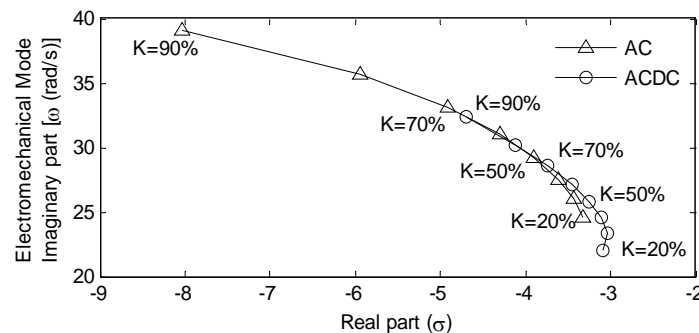
(b) Electromechanical mode
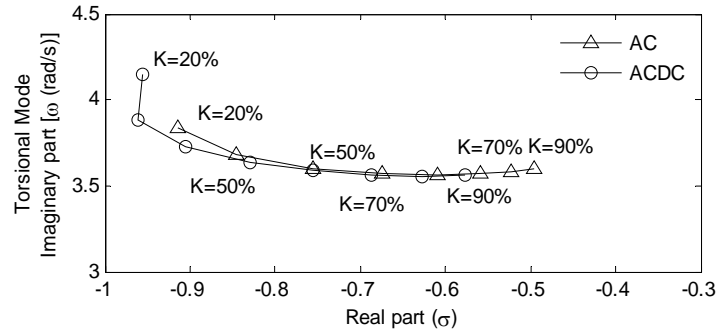
(c) Torsional mode

Figure 7.5 Impact of series compensation

7.4.3.2 *Variation in Rectifier Firing Angle*

The firing angle (α) is varied between 10º to 20º keeping all other system parameters unchanged. The rated firing angle is taken as 18º [13]. The DC line power flow is set at 400 MW and the series compensation level is chosen as 50%. As the firing angle increases, the rectifier absorbs more reactive power as shown in Figure 7.6, which results in a reduction in the voltage of the wind farm interconnection bus. The impact of variation in firing angle on the electrical mode, electromechanical mode, and the torsional mode is shown in Figure 7.7 (a), (b) and (c), respectively. It is observed that with the increase in firing angle, the electrical mode becomes less stable. The electromechanical mode becomes less stable until 16º but subsequently it becomes more stable. The torsional mode however becomes more stable with the increased firing angle. Thus, the firing angle variation has no destabilizing impact on induction generator based wind farm as all the low frequency modes tend to become more stable with higher value of firing angle.
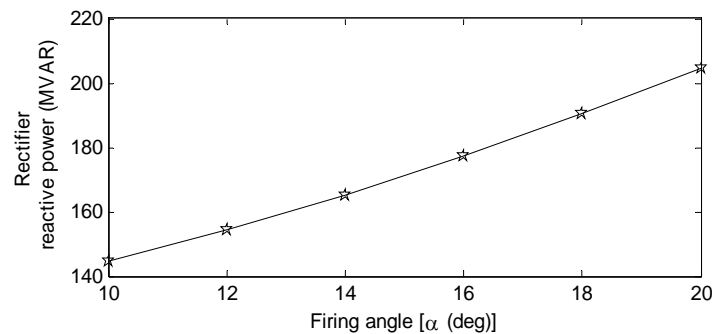
Figure 7.6 Variation in reactive power of the rectifier with firing angle

(a) Electrical mode

(b) Electromechanical mode
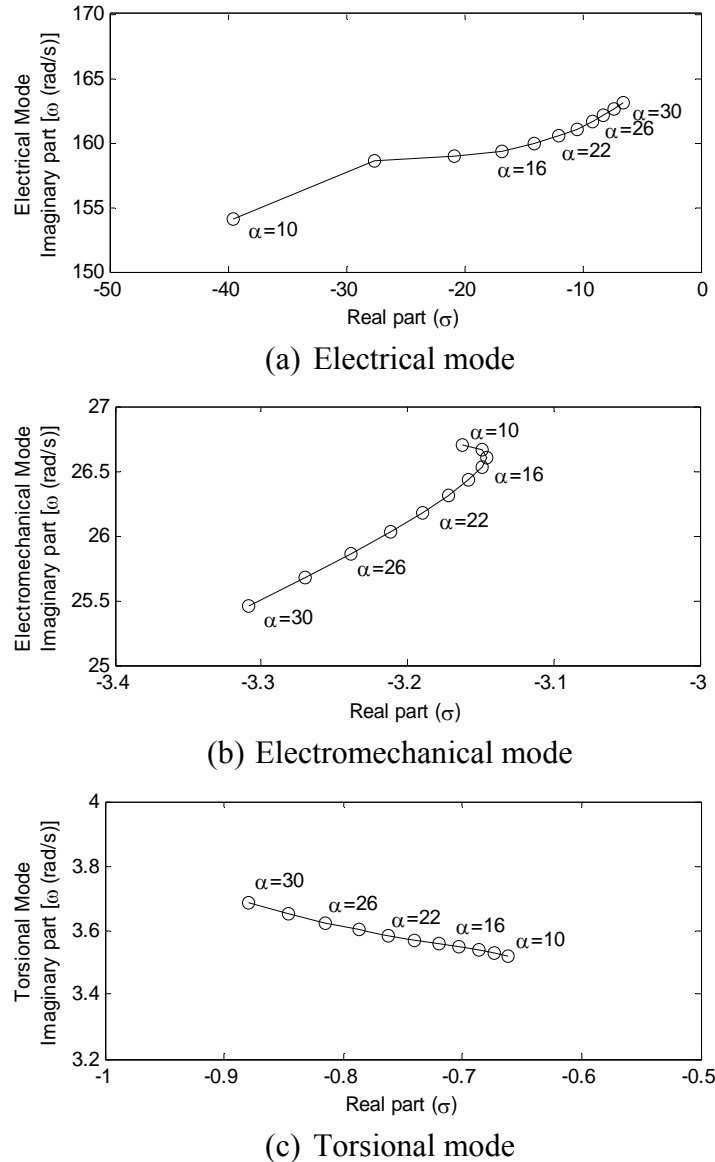
(c) Torsional mode

Figure 7.7 Impact of rectifier firing angle

7.4.3.3 *Variation in DC Power Flow*

The DC line power flow is varied from 100 MW to 600 MW and its impact on the electrical mode, the electromechanical mode, and the torsional mode eigenvalues are studied. Figure 7.8 (a) shows the decrease in the electrical mode stability with increase in the DC power flow. The electrical mode oscillatory frequency also gets reduced concurrently. Stability of the electromechanical mode is found to be varying within a small range that is depicted in Figure 7.8 (b). However, the torsional mode stability

increases with increase in the DC line power flow. The oscillatory frequency of the torsional mode remains quite constant.

(a) Electrical mode

(b) Electromechanical mode

(d) Torsional mode
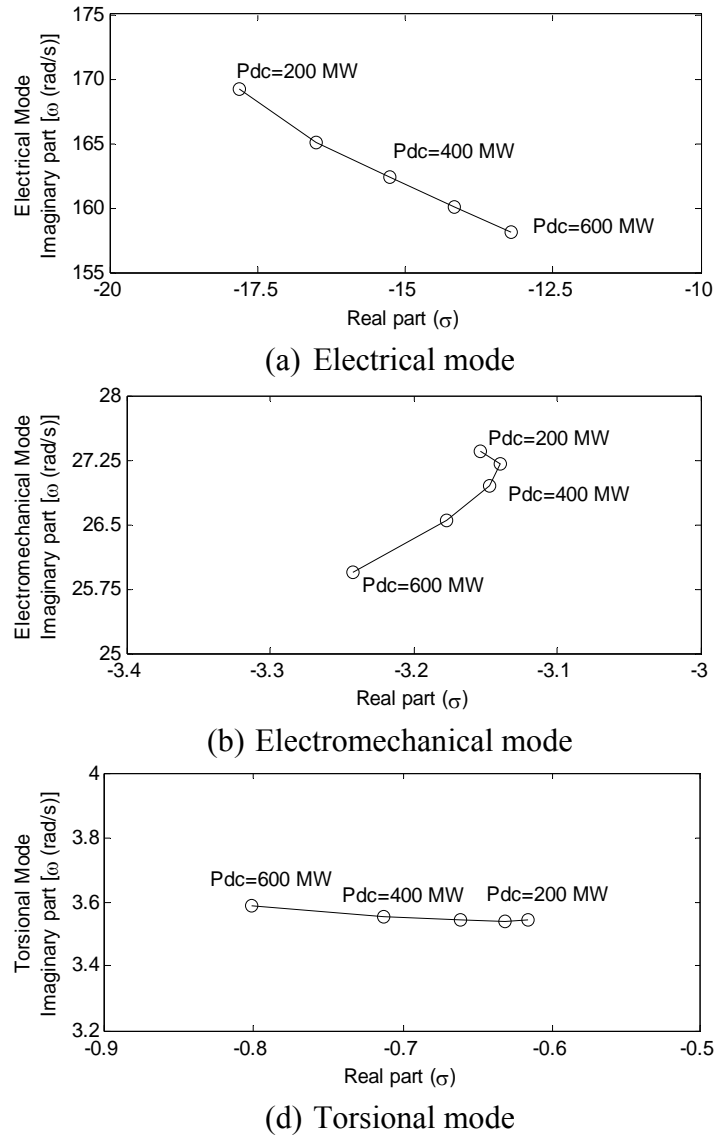
Figure 7.8 Impact of DC line power flow

7.4.3.4 *Variation in Current Regulator Gain*

A simple controller is now considered to demonstrate the modal analysis. Since the inverter dynamics are ignored and the DC link voltage at the inverter station is kept constant, only one controller at the rectifier station is considered. For sensitivity analysis, the controller gain K_R is varied between 0.1 and 100, and the corresponding electrical, electromechanical, and torsional mode eigenvalues are shown in Figure 7.9 (a), (b) and

(c), respectively. Figure 7.9 (a) shows that the stability of the electrical mode declines with the increased regulator gain. However, this mode remains stable even with a gain of 100. The electromechanical mode also becomes less stable, but the oscillatory frequency increases nominally which is illustrated in Figure 7.9 (b). The torsional mode becomes slightly more stable with increase in the controller gain as shown in Figure 7.9 (c).
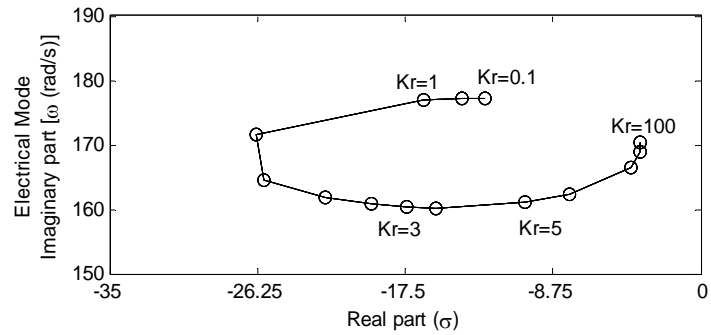
(a) Electrical mode
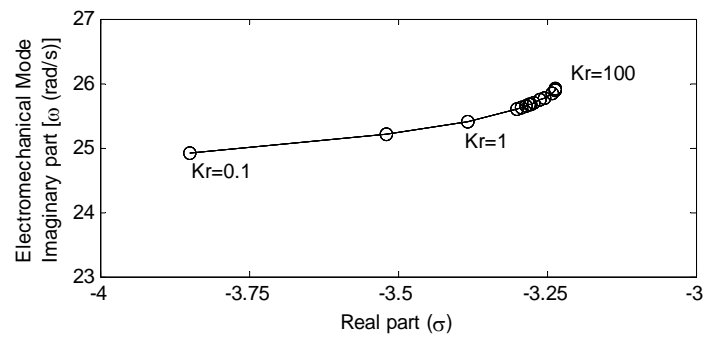
(b) Electromechanical mode
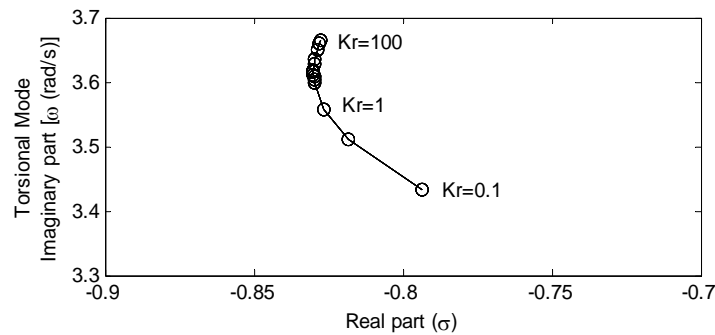
(c) Torsional mode

Figure 7.9 Impact of current regulator gain

7.4.3.5 *Variation in Current regulator time constant*

The time constant of the current controller at the rectifier station is varied between 0.0001 and 2 sec., while the nominal value is taken as 0.01. As the time constant increases, the

electrical mode stability increases until the time constant attains a value of 0.01 sec. as seen from the Figure 7.10 (a). Thereafter, a rise in the electrical mode damped frequency is observed and then the stability decreases. However, this mode does not become unstable within the range of variation considered in this case. Figure 7.10 (b) and (c) show the variation in the time constant and its impact on the electromechanical and torsional modes. The stability of the electromechanical mode is seen to be improving, whereas the torsional mode stability declines in a narrow band. Within the range of variation of the time constant, no potential for subsynchronous resonance interaction is seen. This concludes that there may not be any adverse interaction between the current regulator time constant and the wind turbine generator modes, which would cause instability.
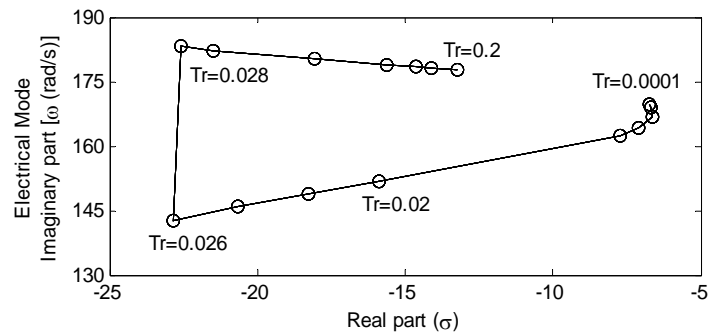
(a) Electrical mode
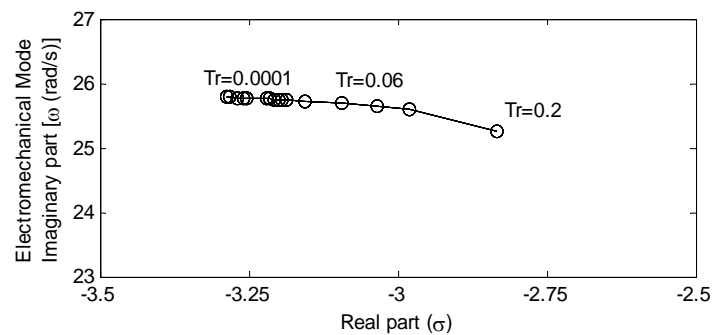
(b) Electromechanical mode
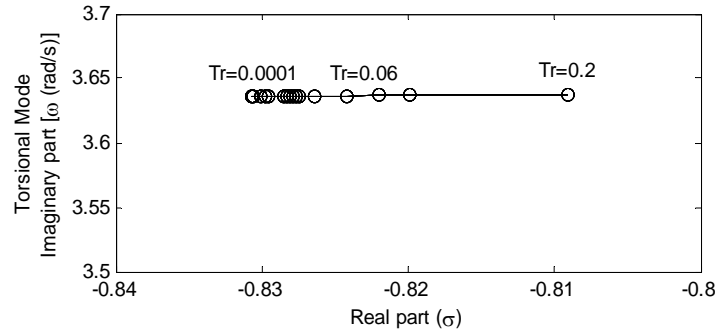
(c) Torsional mode

Figure 7.10 Impact of current regulator time constant.

7.5 ELECTROMAGNETIC TRANSIENT SIMULATIONS

The small signal analysis presented in the Sec. 7.4 is concerned with the prediction of the system stability for small perturbations utilizing the linearized state space model. It is therefore essential to validate these results and study the performance of the AC-DC system under large disturbances using detailed time domain simulation where different nonlinearities and switching actions are considered. The study system is thus modeled in an electromagnetic transient simulation program PSCAD/EMTDC. The transient simulations are carried out for various operating scenarios and the results are discussed below.

7.5.1 AC-DC System with Uncompensated AC line

The study system without series compensation is considered to examine the potential for subsynchronous resonance interaction between the wind farm and rectifier current regulator. An LLLG fault is created at Bus-2 (location F_2) shown in Figure 7.1 and the post-fault performances of the HVDC line and wind farm are analyzed. The output of the wind farm is assumed to be 500 MW, out of which 400 MW power flows through the HVDC line. Figure 7.11 (a) shows the power output of the wind farm and the power flowing through the DC line following a fault in the AC transmission network. It shows a low frequency oscillation in the output power and DC line power flow. The electromagnetic torque and shaft torque are shown in Figure 7.11 (b) which also show a similar low frequency oscillation in both torques. The generator speed and the PCC voltage are shown in Figure 7.11 (c). The DC link capacitor voltage and rectifier firing

angle are shown in Figure 7.11 (d), whereas the rectifier station DC voltage and current are shown in Figure 7.11 (e). A low frequency oscillation is observed in all the aforementioned parameters which are then damped out subsequently within 2 sec. after the fault is cleared. To estimate the oscillatory frequency, an FFT analysis of the electromagnetic torque and shaft torque is carried out, which is depicted in Figure 7.11 (f). Two estimated frequencies are found as 3.51 rad/s and 24.3 rad/s, which represent the torsional mode and electromechanical mode damped frequencies, respectively. These FFT estimated frequencies match very closely with the calculated values of 3.408 rad/s and 23.949 rad/s provided in Table 7.1. From the system eigenvalues depicted in Table 7.1, it is seen that the electromechanical mode and the torsional mode both remain stable at the operating condition considered for this study. This is now reasonably validated with the time domain simulation result. All other modes shown in Table 7.1 are also found to be stable from the small signal analysis which is reasonably validated with the time domain simulations.

(a) Wind farm power output and DC power flow

(b) Electromagnetic torque and shaft torque

(c) Generator speed and PCC voltage

(d) DC link capacitor voltage and firing angle

(e) Rectifier DC voltage and DC current

(f) FFT of Electromagnetic and shaft torque
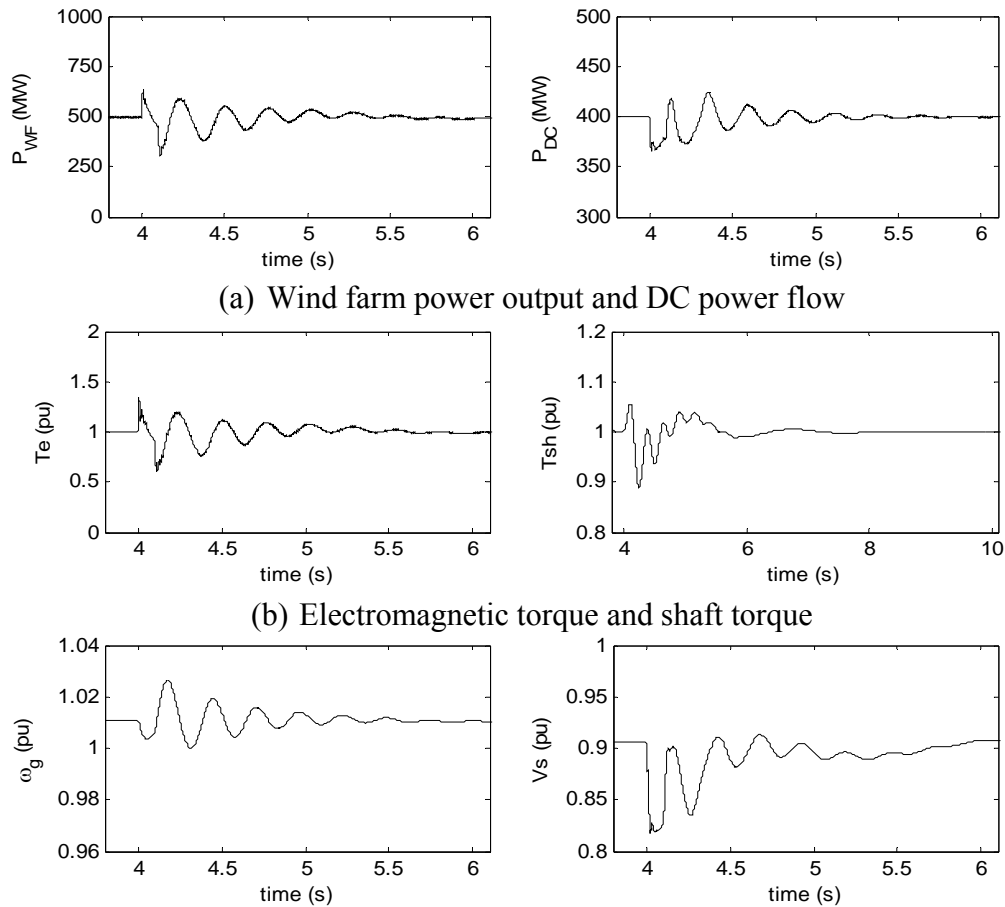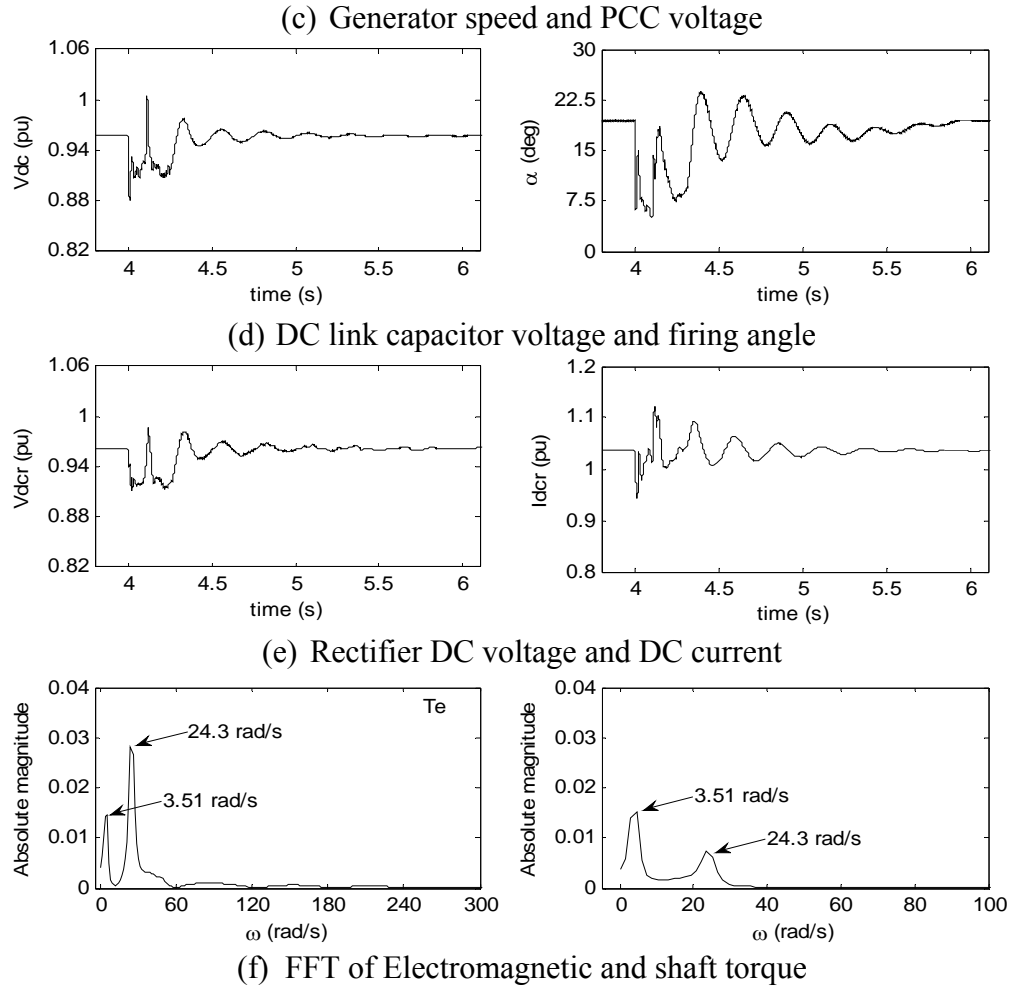
Figure 7.11 Impact of fault at F_2 on 500 MW wind farm with uncompensated AC line and HVDC line

7.5.2 AC-DC System with Series Compensated AC Line

In order to validate the small signal analysis presented in Sec. 7.4, time domain simulations of the study system are performed considering the series compensated AC line. The electromagnetic transient simulation results with 70% series compensation are discussed below.

Figure 7.12 shows the performance of the AC-DC system comprising a 500 MW wind farm during a remote terminal fault in the presence of series compensation. The DC line power flow is set at 400 MW and 100 MW power flows through the series compensated line. The impacts of the fault on the wind farm power output and DC line power flow are shown in Figure 7.12 (a), which shows the multiple frequency components. The

electromagnetic torque and shaft torque following the fault clearance are shown in Figure 7.12 (b). The generator speed and the PCC voltage corresponding to the remote end fault are shown in Figure 7.12 (c), whereas Figure 7.12 (d) shows the DC link voltage and firing angle of the rectifier station. The results show the presence of multiple low frequency components which can be seen from the oscillations in power flow, torque, and generator speed. The FFT of electromagnetic and shaft torque is shown in Figure 7.12 (e). This shows that the oscillation in electromagnetic torque is dominated by the electromechanical, electrical, and torsional modes. Similarly, the oscillation in the shaft torque is dominated by the torsional system dynamics, although a small influence of the electromechanical mode is present. The estimated modal frequencies match very closely with the calculated damped frequencies shown in Table 7.3. The stability of all modes predicted in Table 7.3 is reasonably validated with the time domain simulation results. There is no potential for the induction generator effect SSR obtained here. No interaction between the current regulator and the torsional system is found.
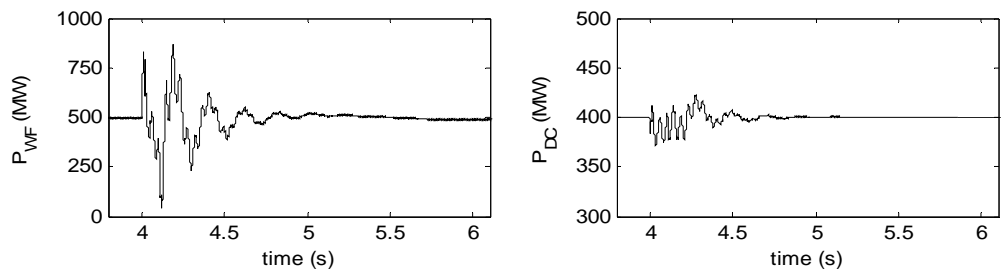
(a) Wind farm power output and DC power flow

(b) Electromagnetic and shaft torque

(c) Generator speed and PCC voltage

(d) DC link voltage and firing angle
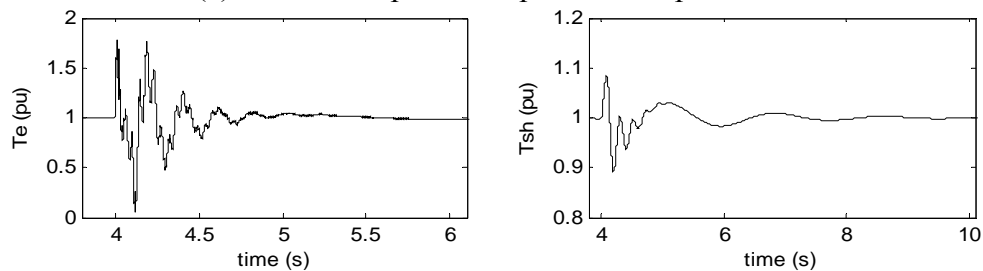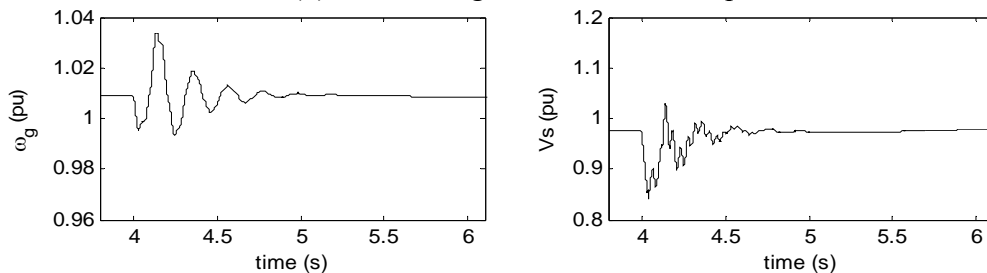
(e) FFT of Electromagnetic and shaft torque
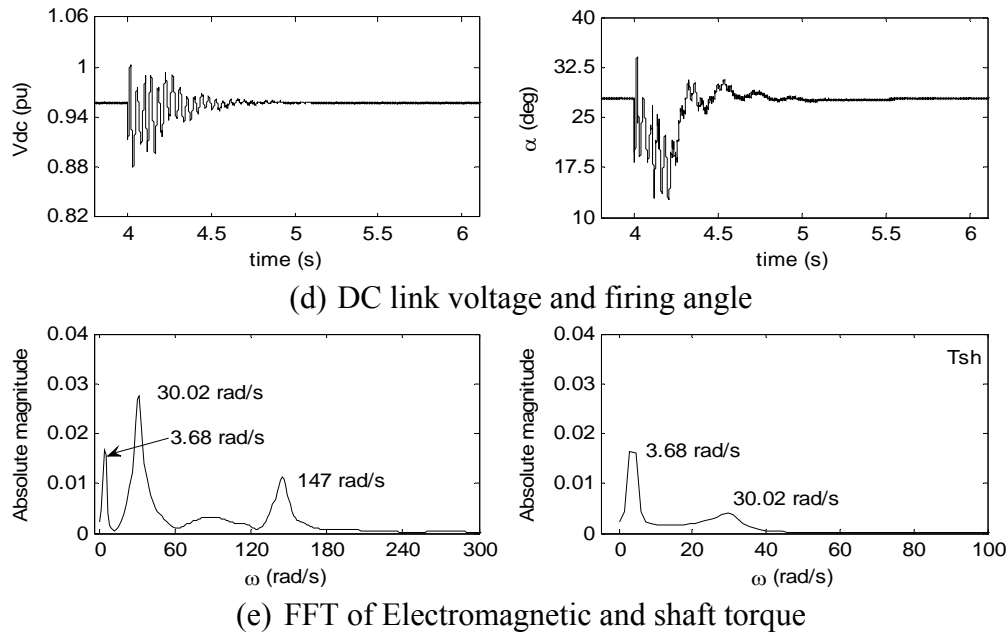
Figure 7.12 Impact of fault at F_2 on 500 MW wind farm with series compensated AC line and HVDC line

Figure 7.13 shows the performance of a 700 MW wind farm for a symmetrical fault in the AC network. The wind farm power output and DC line power flow are shown in Figure 7.13 (a), which are similar to the case study with the 500 MW wind farm depicted in Figure 7.12 (a). In both cases the fault results in a high overshoot in the power output of the wind farm. However, the DC line power flow variation remains within 30 MW. The electromagnetic torque and shaft torque are shown in Figure 7.13 (b). The peak electromagnetic torque is found to be less in comparison to the corresponding torque seen with a 500 MW wind farm. The post fault oscillations in the shaft torque are damped out gradually, and the response is comparable with the response of the shaft torque of a 500 MW wind farm. The electromagnetic torque and shaft torque return to pre-fault condition after the fault is cleared, which is predicted by the eigenvalue analysis. It is noted that the electromechanical mode and torsional mode are found to be substantially stable from the eigenvalues shown in Table 7.3. The oscillations in all other parameters such as generator speed, AC voltage, DC voltage, etc. are also found to be similar to the corresponding values shown in Figure 7.12 and as such, are not shown here. The FFT of electromagnetic and shaft torque shows the modal frequencies which match with the calculated values depicted in Table 7.3. Simulations with variation in the output of a wind

farm are also carried out, which shows similar results and are, therefore not reported here. In all cases, there is a close correlation between the time domain study and small signal analysis which validates the small signal analysis.

(a) Wind farm power output and DC power flow

(b) Electromagnetic and shaft torque
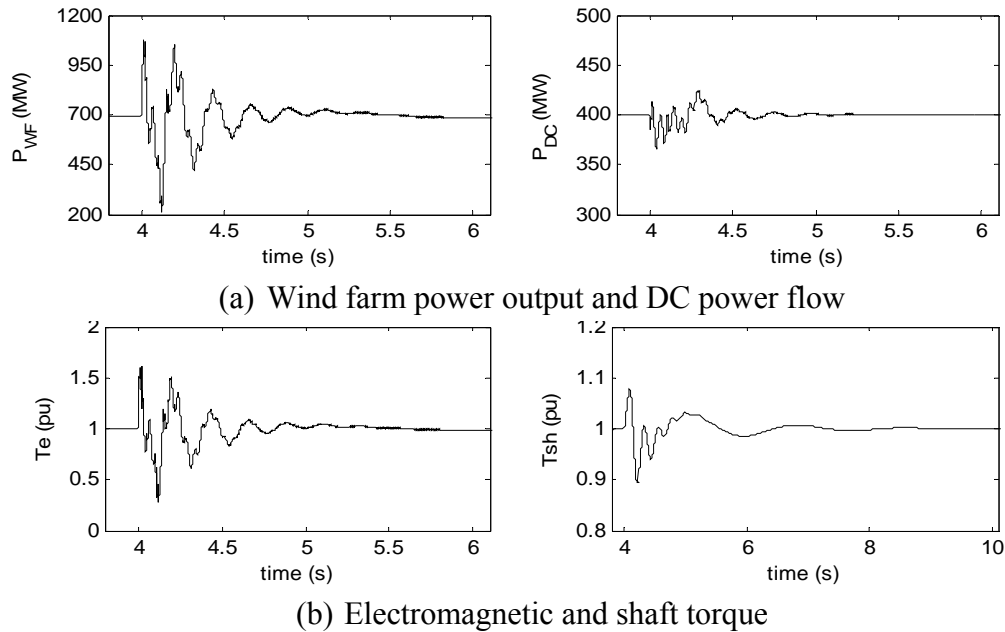
Figure 7.13 Impact of fault at F_2 on the 700 MW wind farm

7.5.3   DC Line Fault

The scenario of a DC line fault is created by simulating a fault of 100ms duration at the receiving end of the DC line. The fault in the DC line causes the cessation of the power flow through the DC line; hence, all power is transferred through the series compensated line. The impacts of the fault in the wind farm output and DC line power flow are shown in Figure 7.14 (a). It is found that the DC fault results in an electrical mode oscillation in the wind turbine generator which can be also be seen from the power output of the wind farm. The electromagnetic torque and shaft torque of the wind farm are shown in Figure 7.14 (b). Although a large overshoot is seen in the electromagnetic torque, the shaft torque remains stable with almost negligible variations.   Similarly the generator speed and the PCC voltage are depicted in Figure 7.14 (c). The oscillations in the speed contain electrical mode and electromechanical mode damped frequency components, whereas the voltage oscillation is largely characterized by the electrical mode oscillation. The stable shaft torque shows no interaction between the current regulator and the torsional system.

However, this operating condition is shown to be stable from the eigenvalue analysis illustrated in Table 7.3, and is now reasonably validated with the PSCAD/EMTDC studies. The corresponding DC link capacitor voltage and the firing angle of the rectifier station are shown in Figure 7.14 (d). The DC voltage falls rapidly after the occurrence of the fault and then recovers to normal value gradually following the fault being cleared. However, the firing angle increases up to 100 degree during the fault.

(a) Wind farm power output and DC power flow

(b) Electromagnetic and shaft torque

(c) Generator speed and PCC voltage

(d) DC link voltage and firing angle
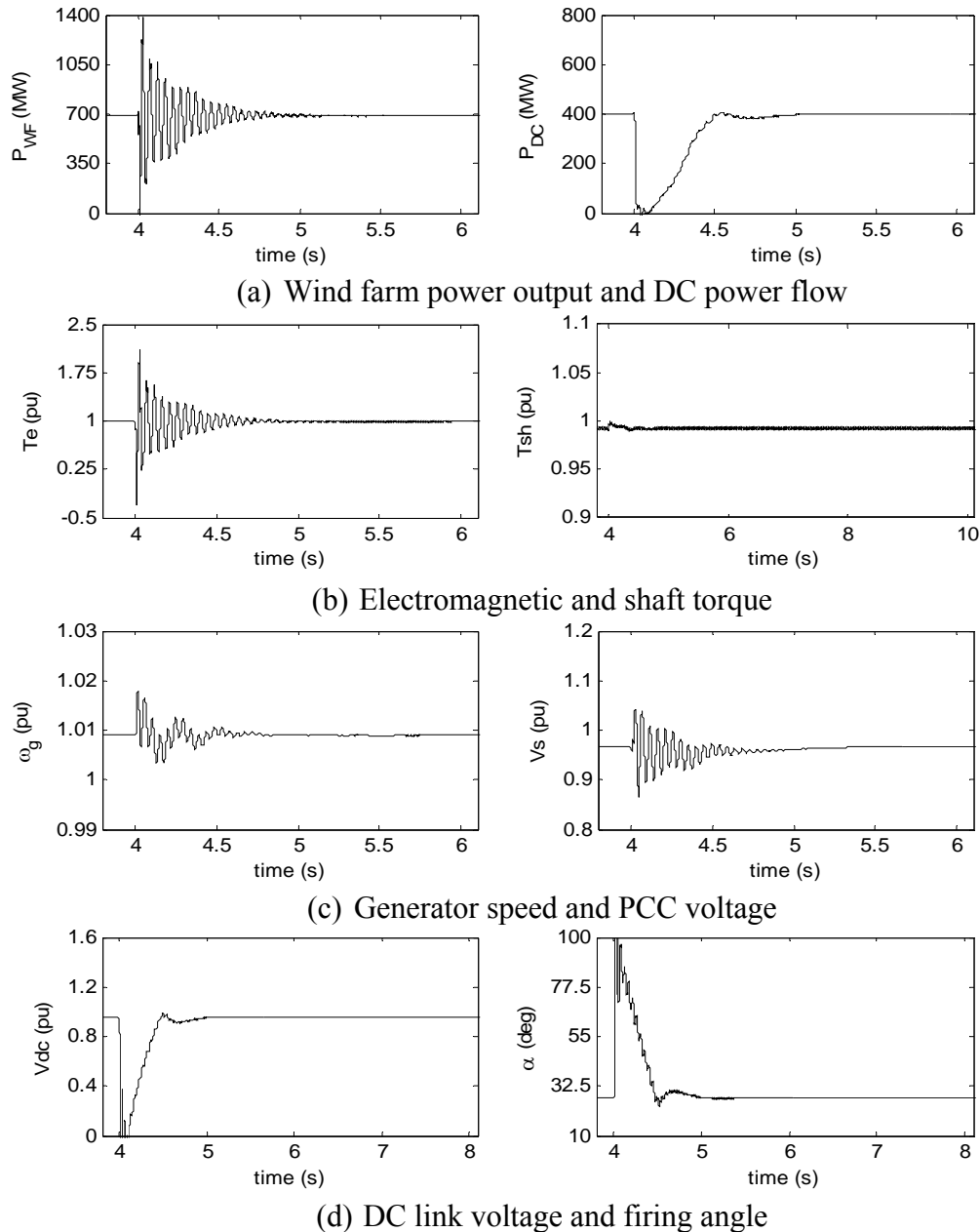
Figure 7.14 Impact of DC line fault

7.5.4   Blocked HVDC Line

During a contingency, the HVDC line may be blocked for some time. In this scenario all the power output of the wind farm flows through the series compensated AC transmission line. To simulate such a scenario, an HVDC line which is connected to 700 MW wind farm is blocked. Hence, the 700 MW power flows through the 70% series compensated line. The electromagnetic torque and shaft torque following a LLLG fault at the remote end of the line are shown in Figure 7.15. From the small signal analysis it is predicted that 70% series compensated line may experience the induction generator effect SSR which is also found in the time domain simulations. The electromagnetic torque following the fault grows steadily and gets destabilized. The corresponding shaft torque also shows subsynchronous oscillations. It is noted that even though the shaft torque oscillation involves multiple frequency components, the instability in the shaft torque is only caused by the unstable electrical mode oscillation in the electromagnetic torque. Therefore, no torsional interaction is seen here. This correlates with the results presented in chapters 3, 4 and 5 which has suggested that series compensated line does not cause torsional interaction in an IG based wind farm.
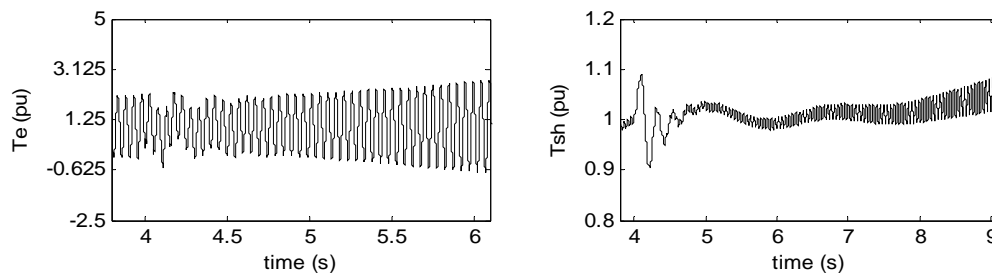
Figure 7.15 Impact of fault during blocked HVDC system

7.5.5   Overloaded DC Line

Figure 7.16 shows a condition where all of the power output of the wind farm is scheduled to flow through the DC line. This makes the series compensated AC line remain idle except for a very small charging current flow in the line. In this condition, an LLLG fault is simulated at the remote end of the series compensated AC line. The fault starts at t=4s and is cleared after 6 cycles. Figure 7.16 (a) shows the electromagnetic torque and shaft torque following the fault clearance. From the FFT, it is found that the oscillation in the electromagnetic torque contains the electromechanical and torsional

mode frequency components, whereas, the shaft torque oscillates primarily at torsional mode frequency. Figure 7.16 (b) shows the DC line power flow and the DC voltage following the fault being cleared. The system remains stable, which is also found in the eigenvalue analysis.

(a) Electromagnetic torque and shaft torque

(b) DC line power flow and DC voltage
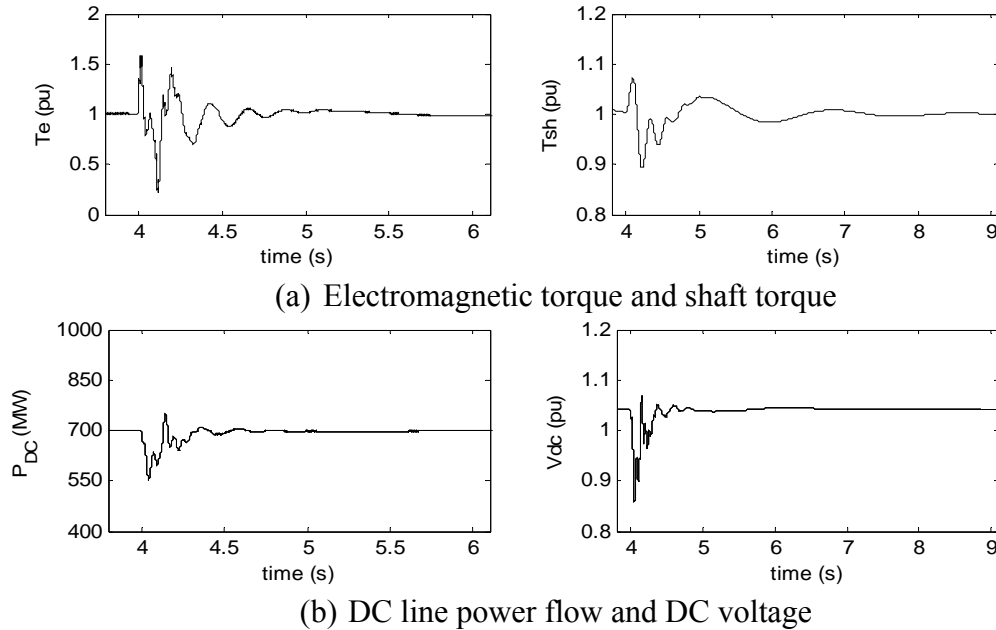
Figure 7.16 Impact of fault during DC line carrying 700 MW

7.6 CONCLUSIONS

The modal analysis of an induction generator based wind farm connected to a series compensated line in parallel with an HVDC line is presented in this chapter. A part of this chapter is reported in [133]. In this chapter a detailed study of the potential for SSR is carried out through small signal analysis. Eigenvalue analysis, participation factor analysis, and sensitivity studies are conducted to investigate the impact of series compensated line and HVDC system on the stability of an induction generator based wind farm. Time domain simulations of the study system are subsequently carried out in PSCAD/EMTDC which validates the small signal analysis. The following conclusions are drawn:

(a) Induction generator based wind farms may experience potential SSR due to the induction generator effect, only when radially connected to a series compensated transmission line.

(b)   The critical compensation level in such condition for a 700 MW wind farm is around 55%, which is a realistic level of compensation, currently used in power systems.

(c)   When the wind farm is connected to the LCC HVDC transmission system along with the series compensated line, no subsynchronous resonance interaction is observed.

(d)   No interaction between a rectifier station current regulator and torsional system is found.

Based on the system studies conducted, it is thus concluded that an LCC HVDC controller may not cause the potential for subsynchronous resonance in an induction generator based wind farm. However, subsynchronous resonance instability may be experienced if the HVDC line is blocked during a contingency and the wind farm is exposed to only an AC line with series compensation greater than its critical compensation level.

Chapter 8

HARMONIC RESONANCE IN WIND FARM

8.1 INTRODUCTION

The use of shunt capacitor banks at the terminal of the wind turbine generator is very common to achieve a power factor in the range of 0.95 lagging (under-excited) to 0.90 leading (over-excited). These capacitances are also needed to offset reactive power losses within the wind farm generating facilities and to react to sudden momentary dips in voltage commonly seen in gusty wind conditions which could in turn add stress to the Grid. However, the amount of reactive power support depends upon the grid code which introduces the constraints over the choice of capacitor size to be connected. Typically these capacitor banks are deployed in the 34.5 kV or 27.6 kV collector systems and/or at the generating substation. In the transmission level also, large switched shunt capacitors are connected for steady state voltage support. However, the presence of multiple shunt capacitors in the network increases the risk of parallel and series resonance in the power system [80], [84].

In 2010, wind turbine generators from a 101.2 MW full converter based wind farm connected to Hydro One 230 kV Chatham-Lauzon C23Z and C24Z circuits tripped on transient overvoltage whenever the 220 Mvar capacitor bank located upstream of the wind farm switched on line in the morning for voltage support. Tripping did not occur when the capacitor bank switched off in the evening.

The above incident continued for months, causing substantial revenue losses. Corrective measures were immediately taken which consisted of increasing the threshold voltage and time-delaying the overvoltage trip settings on the turbines.

The transmission capacitor connected to the system and owned by Hydro One is equipped with a synchronous control unit (SCU) to ensure zero crossing for both closing

and opening of the circuit breakers. This SCU was overhauled to ensure that it was working properly and to remove any doubts that it could cause the turbines to trip.

Henceforth, no further incidents were reported. However, the reasons for the overvoltage tripping of wind turbines were still undefined and a project was undertaken to determine the causes and suggest mitigate reasons. This chapter presents a result of the study. A comprehensive analysis of the turbine tripping incidents is performed by examining the fault recorder data. The Fast Fourier Transform (FFT) analyses of the recorded voltage and current signals are used to show the presence of harmonic components before, during, and after the switching of the capacitor banks.

An extensive frequency scan analysis is conducted to characterize the system equivalent impedance at the interconnecting bus, as a function of frequency. Thus, frequency scan analysis reveals a potential for harmonic resonance in the wind farm.

In 2011 a second 101.2 MW wind farm was connected to the same line-tap connections thereby doubling the generating capacity. The scope of the study was then extended to determine the potential for harmonic resonances in both wind farms and recommendations were made to avoid wind turbines from tripping under the new scenario.

8.2   HARMONIC RESONANCE

Network resonance phenomena in wind farms are typically caused by the presence of inductive sources in parallel and/or in series with capacitive network elements [80]. Long underground cables can additionally cause series and parallel resonance in the interconnected system along with the power factor correction capacitors.

There are two types of harmonic resonances: series and parallel resonances. In a series resonant circuit the inductive reactance and capacitive reactive components appear in series with a source of harmonic current. Series resonance points are identified by the dips in the network impedance versus frequency plot on the high voltage side of the interconnection transformer at the wind farm. In a parallel resonant circuit the capacitive and inductive components appear in parallel to a harmonic current source. Parallel

resonance is associated with high impedance at resonance frequency which results in an increased voltage distortion and harmonic current. The parallel resonance points are identified as the peaks in the driving point impedance measured at the low voltage side of the interconnection transformer. If the harmonic currents from the wind farm align with the resonant modes, significant voltage rise may result. Since the studied wind farm employs power electronic converters for grid interfacing, a characteristic harmonics current emission may cause parallel resonance with the network elements at certain resonant frequencies.

8.3 STUDY SYSTEM DESCRIPTION

In this chapter, harmonic resonance analyses are carried out for a 101.2 MW wind farm tapping Hydro One 230 kV Chatham-Lauzon C23Z and C24Z circuits. This wind farm was connected to the grid in early 2009. The simplified study system of this wind farm is shown in Figure 8.1 consisting of 44 Siemens SWT-2.3-93, 60 Hz wind turbines totaling 101.2 MW. The wind turbines are connected to 4 x 34.5 kV collectors at a Wind Generating Substation (WGS) arranged in four groups (G-1, G-2, G-3 and G-4) and located approximately 12 km from a single 230 kV circuit line-tap. These wind turbines are Siemens 2.3 MW, 690V asynchronous generators connected through a four quadrant full bridge converter (AC/DC - DC/AC).
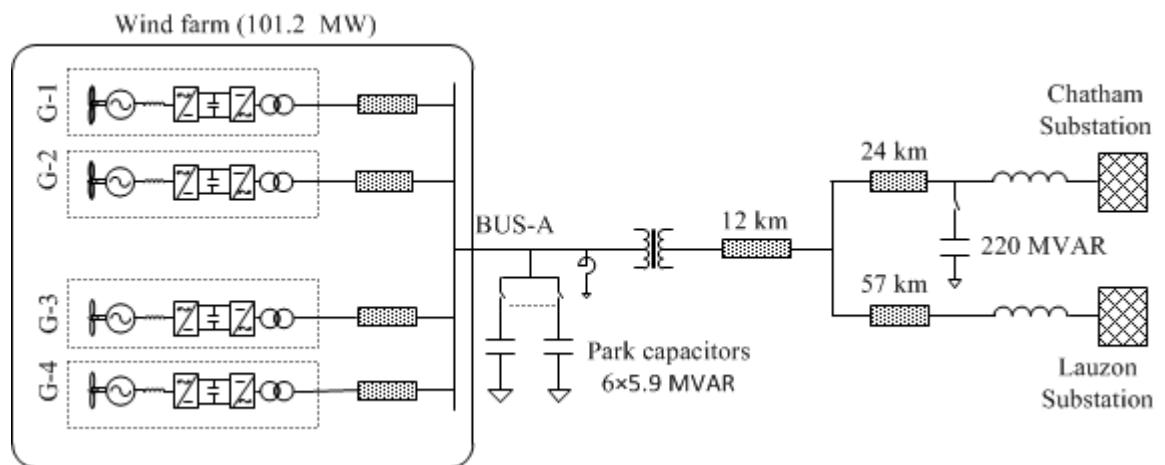
Figure 8.1 Grid connected wind farm

The Wind Farm also has 6 x 5.9 Mvar capacitor banks in-service at 34.5 kV bus primarily to provide from 0.95 lag to 0.9 lead requirements. There is a 220 MVAR capacitor bank at Chatham substation approximately 36 km from the Point of Common Coupling (PCC) to the wind farm. Each group in the wind farm is connected to the PCC through underground 34.5 kV cables.

8.4 IMPEDANCE SCAN

The driving point impedance is obtained from the frequency scan of the equivalent circuit of the network. The peaks in this impedance at different frequencies indicate network resonant modes. Voltage amplification may occur if the injected harmonics current aligns with any of the resonant mode frequencies which lead to a large harmonic current through the capacitor banks. The harmonic impedance of a transmission system is dependent on the system configuration and system strength. Hence, this analysis of the wind farm harmonic performance is performed for a comprehensive construction of all reactive components and all possible ranges of system strength.

The impedance scan is performed at the low voltage side of the interfacing transformer shown in Figure 8.1**.** Initially when the project was undertaken, a simplified model of the system was available in which the grid was represented by a single equivalent circuit. Later, a more realistic network configuration was supplied by Hydro One which presented the grid as two sections. Figure 8.2 and Figure 8.3 show the two equivalent circuits of the study system utilized for the impedance scan. Since all the wind farm power factor correction capacitors are connected at the PCC, the driving point impedance of the system is calculated at the 34.5 kV bus to investigate the potential for parallel resonance. The wind farm is treated as a harmonic current source.
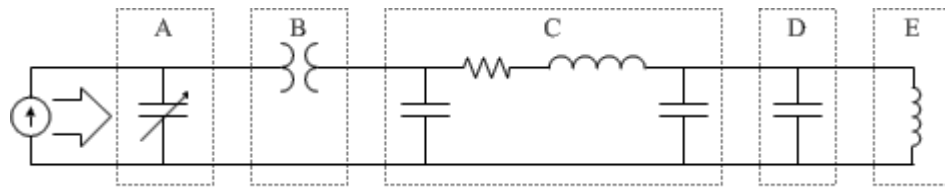
A: Wind farm capacitor bank (0-35.4 Mvar)
B: Interconnecting transformer
C: Overhead line (12 km)
D: Hydro One capacitor bank (220 Mvar)
F: Equivalent Hydro One network

Figure 8.2 Equivalent system-I
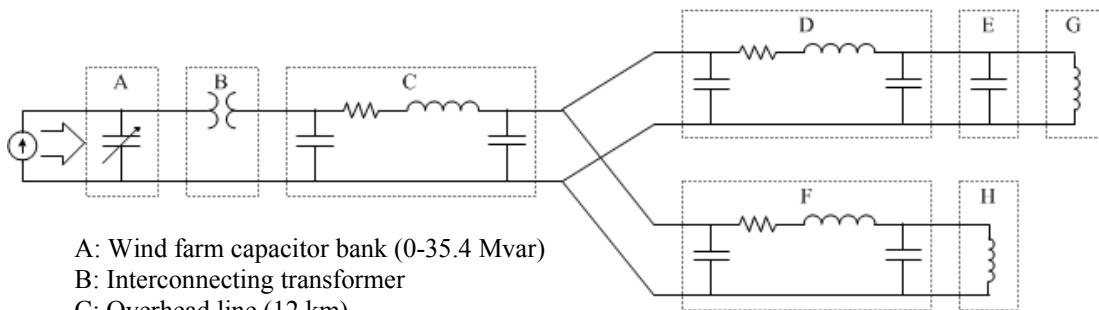
A: Wind farm capacitor bank (0-35.4 Mvar)
B: Interconnecting transformer
C: Overhead line (12 km)
D: Overhead line (24 km)
E: Hydro One capacitor bank (220 Mvar)
F: Overhead line (57 km)
G: ChathamSS
H: Lauzon SS

Figure 8.3 Equivalent system-II

According to the IEEE standard 519-1992, the parallel resonance in a system can be approximately calculated from the short level of the system at the capacitor bus, as:

$$h_R = \sqrt{\frac{MVA_{SC}}{MVAR_{CAP}}} \tag{8.1}$$

where, h_R is the parallel resonant frequency harmonic order, such as 5th or 7th, MVA_{SC} is the short circuit level at the bus of interest, and $MVAR_{CAP}$ is the rating of the capacitor bank.

From the data provided, the system strength at the PCC is found to be 627 MVA and 578 MVA corresponding to the configurations shown in Figure 8.2 and Figure 8.3, respectively. Figure 8.4 shows the variation in the calculated harmonic order with respect to the size of the park capacitor bank installed at the wind farm. There are six capacitor banks; each rated 5.9 MVAR at 34.5 kV. It is found that as the capacitor bank size increases, the harmonic order of parallel resonance decreases. System-II shows lower resonance frequencies in comparison to the System-I, as shown in Figure 8.4. Although this method is simplistic, it gives an indication of the resonance order. More accurate resonant frequencies can be obtained through the impedance scan.
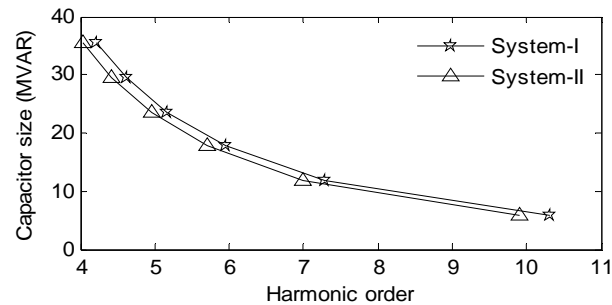
Figure 8.4 Capacitor bank size and harmonic order

The impedance scan is now performed at the LV side of the interconnecting transformer at the PCC with equivalent network systems developed in PSCAD/ EMTDC. Two equivalent systems shown in Figure 8.2 and Figure 8.3 are considered here.

8.4.1 Impedance Scan with Equivalent System-I

The impedance scan is carried out with the equivalent system-I and the results are shown in Figure 8.5. In this system the grid is represented by an equivalent voltage source behind the reactance which represents the grid strength. During this study the grid strength is kept constant at 7290 MVA as provided by Hydro One. The driving point impedance is measured across the wind farm shunt capacitor bank (A), and the wind farm is modeled as a harmonic current source.

8.4.1.1 *Impact of Park Capacitors*

Figure 8.5 shows the driving point impedance measured at the PCC for different sizes of park capacitor while the transmission network capacitor (D) remains connected. The

number of capacitors is indicated in Figure 8.1 and each capacitor is rated 5.9 Mvar. For one park capacitor bank there are two resonant peaks: one around the 6th harmonic and the other around 11th harmonic. The 6th harmonic resonance is caused by the 220 MVAR capacitor bank, whereas the 11th harmonic resonance is caused by the park capacitor. The magnitude of the impedance at the 11th harmonic is much higher than the impedance at the 6th harmonic. As the number of park capacitors increase the resonant harmonic orders and corresponding magnitude of the impedance is decreased. For a specific set of capacitors, the resonance frequencies are found around 5th and 7th harmonic orders. Incidentally, there is also the characteristic harmonic current of the wind farm voltage source converter. Thus, if the harmonic currents injected by the wind farm align with any of the resonance order, a substantial harmonic over voltage may occur at the PCC due to voltage magnification.
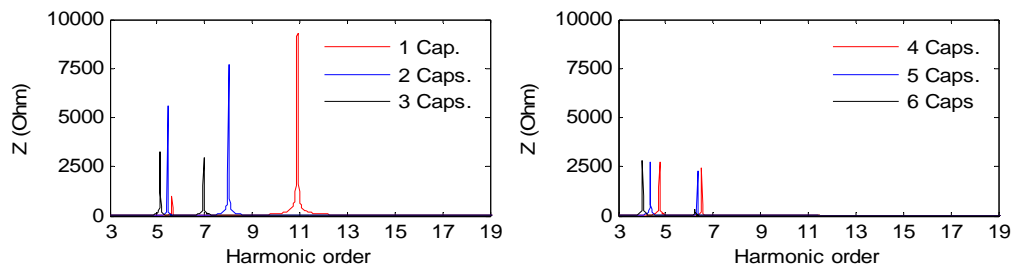
Figure 8.5 Driving point at PCC with system-I

8.4.1.2   *Impact of Short Circuit Level*

Figure 8.6 shows the driving point impedance at different short circuit level varying between 4000 MVA and 10000 MVA. Figure 8.6 (a) shows the impact of short circuit level when only one park capacitor is connected. It is found that the resonance caused by the transmission network capacitor is substantially influenced by the system short circuit level and it varies between 4th and 7th harmonic. In contrast, the short circuit level has little impact on the resonance mode caused by the park capacitor. The influence of the short circuit level with two park capacitors is depicted in Figure 8.6 (b). This illustrates a similar influence on resonance due to the transmission network capacitor. Table 8.1 summarizes the exact resonance order with respect to the change in short circuit level. In Table 8.1 'lower' represents the resonance caused by the transmission network capacitor and 'higher' represents the harmonic resonance caused by the park capacitors.

(a) One park capacitor (b) Two park capacitors
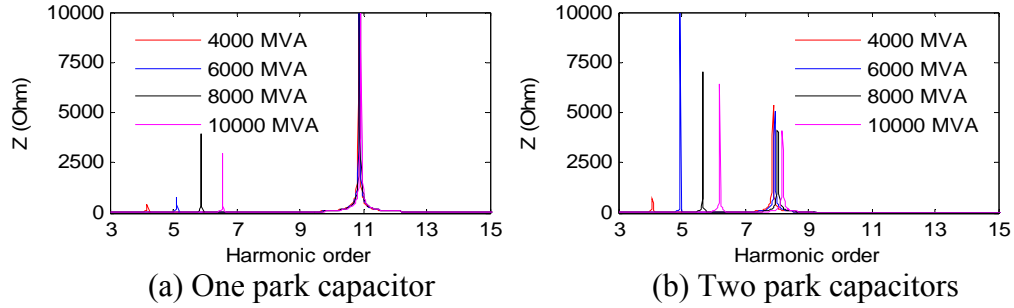
Figure 8.6 Impact of short circuit level on driving point impedance with system-I

Table 8.1 Impact of short circuit level on harmonic resonance order

SCL (MVA)	With one park capacitor		With two park capacitors	
	Lower	Higher	Lower	Higher
4000	4.17	10.87	4.08	7.883
6000	5.10	10.88	4.97	7.95
8000	5.88	10.90	5.67	8.03
10000	6.56	10.92	6.27	8.18

8.4.2   Impedance Scan with Equivalent System-II

The impedance scan is now carried out with the equivalent system-II in which the numbers (size) of the park capacitor bank is varied sequentially.

8.4.2.1   *Impact of Park Capacitors*

The driving point impedance at the PCC is shown in Figure 8.7 for the rated short circuit level of 7200 MVA and 2600 MVA at Chatham SS and Lauzon SS, respectively. Two resonant frequencies are obtained with one park capacitor and the large transmission network capacitor. One resonance occurs around 10th harmonic, whereas another resonance is observed around the 6th harmonic with a relatively small magnitude of the peak driving point impedance. This indicates the potential for the parallel resonance if the grid or wind farm has an ambient harmonic of 10th or 6th order, or the wind turbine inverters inject harmonic currents of similar order.

The harmonic resonance orders are changed when two park capacitors are switched on. The lower order resonance is obtained at a frequency very close to the 6th order harmonic and the higher order resonance appears at the frequency close to the 7th harmonic. Since the 7th harmonic is a characteristic harmonic of the wind farm grid side inverter, its

injection in the network may lead to harmonic voltage amplification due to the resonance. With three park capacitors, these resonance orders further shift towards lower order harmonics. In this case the peak magnitude of the driving point impedance is found to be higher at lower resonance order in comparison to the same with one and two park capacitors. At the same time, the peak magnitude of the impedance corresponding to the higher resonant frequencies is decreased significantly. Similarly, with more capacitors at the wind farm, higher order harmonic resonance disappears and resonance is seen between the 4th and 5th harmonic, which is mainly caused by the large transmission capacitor connected at 230 kV bus. The peak magnitude of the impedance remains almost the same for four, five, and six park capacitors. From the calculated driving point impedance with different wind farm capacitors, it is found that the resonance order is reduced substantially with the increase in the size of park capacitors. This matches very well with the predicted harmonic orders shown in Figure 8.4.
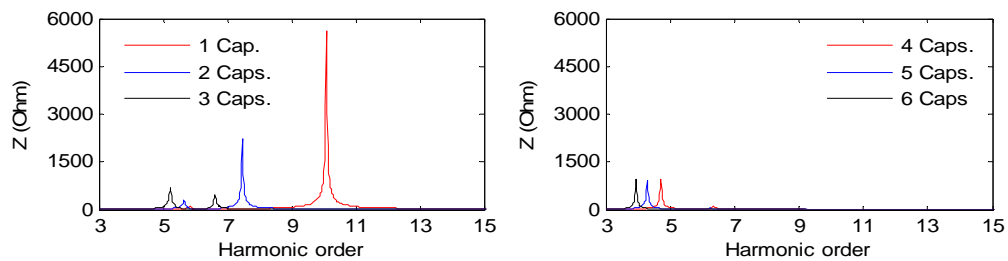
Figure 8.7 Driving point impedance at PCC

8.4.2.2 *Impact of Short Circuit Level*

The short circuit level of the power system plays a critical role in the parallel resonance as shown in(8.1). Hence, to investigate the impact of grid strength on the wind farm in view of parallel resonance, the short circuit level at each substation is varied. This study is carried out with one park capacitor and then extended to two park capacitors. Figure 8. (a) shows the effect of change in grid strength on the resonance with one park capacitor. It is found that the higher order resonance is least affected, whereas the lower order resonance is substantially affected. The lower order resonance frequency increases with the grid strength and varies between the 4th and 7th harmonic. The peak magnitude of the impedance is seen to be large corresponding to the higher resonance order, and small corresponding to the lower resonance order. A similar study done with two park

capacitors is shown in Figure 8. (b). With two park capacitors, the peak magnitude of the impedance at higher order resonance decreases to half in comparison to the same with one capacitor. However, the resonance order varies between the 7th and 8th harmonic for an increase in the grid short circuit level at Chatham SS. The change in the lower resonance order is found to be similar as it seen with one park capacitor.

Figure 8.9 shows similar studies with the change in short circuit level of the grid at Lauzon SS. Since the operating strength at this substation was 2600 MVA, the investigation is carried out with a variation between 1000 MVA and 4000 MVA. Figure 8.9 (a) shows the impact with one park capacitor which is found to be negligible on the higher resonance order, whereas lower resonance order varies within a narrow range of frequency. The magnitude of the impedances also does not vary. The effect of grid strength on the resonance with two wind farm capacitors is shown in Figure 8.9 (b). The resonance due to the wind farm capacitors is found to be unaffected by the change in short circuit level. The resonance due to the transmission network capacitor is found to change within a small range of frequencies. Table 8.2 and Table 8.3 summarize the impact of short circuit level on the resonance. The exact resonance orders are listed in these tables.

(a) One park capacitor   (b) Two park capacitors
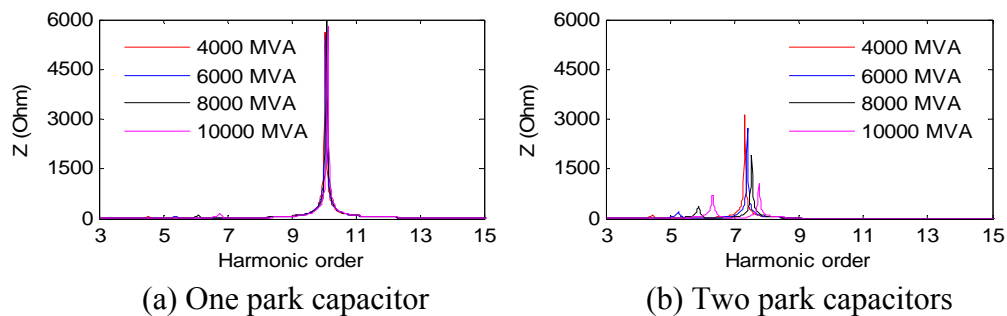
Figure 8.8 Impact of short circuit level at Chatham SS on parallel resonance

(a) One park capacitor　　　　　(b) Two park capacitors
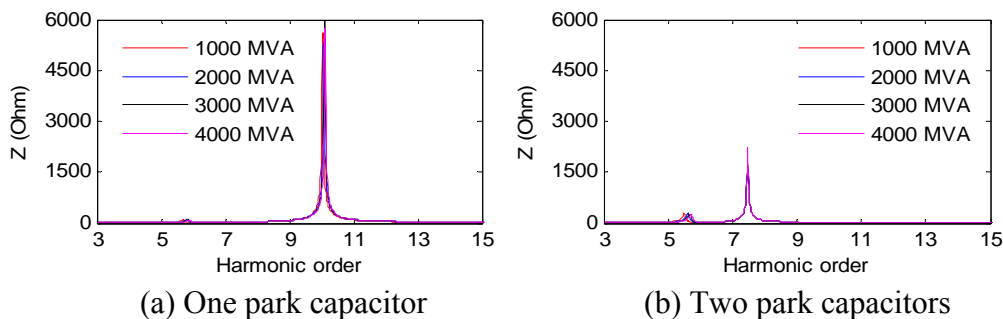
Figure 8.9 Impact of short circuit level at Lauzon SS

Table 8.2 Impact of short circuit level at Chatham SS

SCL (MVA)	With one park capacitor		With two Park capacitors	
	Lower	Higher	Lower	Higher
4000	4.58	10.05	4.47	7.32
6000	5.42	10.08	5.27	7.40
8000	6.11	10.10	5.88	7.53
10000	6.75	10.13	6.32	7.75

Table 8.3 Impact of short circuit level at Lauzon SS

SCL (MVA)	With one park capacitor		With two Park capacitors	
	Lower	Higher	Lower	Higher
1000	5.7	10.03	5.5	7.47
2000	5.81	10.08	5.61	7.47
3000	5.86	10.10	5.68	7.47
4000	5.9	10.12	5.71	7.47

8.5   FIELD DATA ANALYSIS

Five events of wind turbines tripping in this large wind farm were experienced when the transmission side capacitor was switched on in the morning. To investigate the reason behind the turbines tripping, field data for all five events were obtained and waveforms were analyzed through Fast Fourier Transform analyses.

Figure 8.10 shows the typical event logging meter set up at the wind farm substation which recorded the waveforms during the switching events that tripped the wind turbines. The monitoring meter used was TESLA 3000. It has the capacity to record the data at a rate of 32-384 samples per cycle. However, in this case the data was recorded at a rate of 96 samples per cycle. The meter recorded the 34.5 kV bus voltage and current at the PCC

of the wind farm. The 230 kV bus voltage and current are also recorded. Figure 8.11 shows the front panel of the measurement units at the wind farm.

Figure 8.10 Event logger devices

Figure 8.11 Front panel of the wind farm measurement unit

8.5.1   Event-A (14th Jan. 2010)

This event occurred in the morning when the wind farm was producing 95 MW from its 101.2 MW installed capacity. When the Chatham capacitor and two of six park capacitors

went into service, large distortion in voltage and current at the PCC were experienced as shown in Figure 8.12. Fourteen wind turbines tripped due to temporary over voltage (TOV). The PCC voltage and corresponding FFT plots are shown in Figure 8.12 (a) and (b), respectively. Similarly PCC current and its FFT plots are shown in Figure 8.12 (c) and (d), respectively. From the FFT a large peak in the magnitude of both voltage and current are observed at the 7th harmonic. Another peak at the 6th harmonic is also detected in both voltage and current. However, the impact of the 6th harmonic is larger in the case of voltage than the current. The FFT of all three phases showed almost identical behavior. This observation is now correlated with the impedance scanning results shown in Figure 8.7. Two park capacitors cause a network resonance around the 7th harmonic which is also found from correlation with field measurement. Thus it appears that the over voltage that caused the relay to trip the turbines was caused due to a resonance at the 7th harmonic.

(a) Voltage at PCC   (b) FFT of PCC voltage

(c) Current at PCC   (d) FFT of PCC current
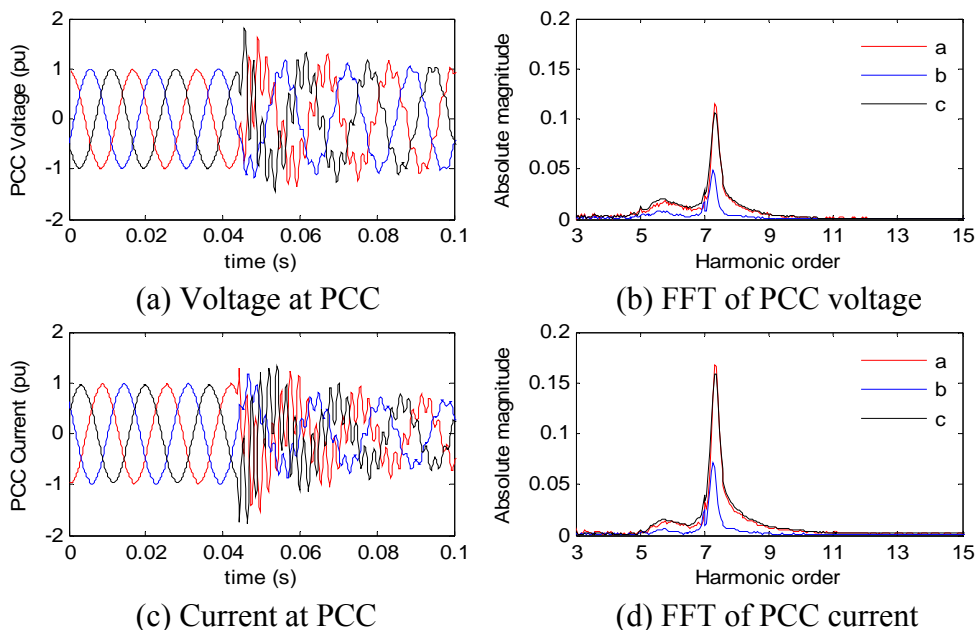
Figure 8.12 PCC voltage and current for event-A

8.5.2 Event-B (20th Jan. 2010)

Event-B relates to turbines tripping for a similar capacitor switching during a low wind power output condition. The power output of the wind farm was 24 MW, when the transmission network capacitor switching took place. Due to this switching, four turbines

tripped. The voltage and current at the PCC are shown in Figure 8.13. The FFT of PCC voltage shows peaks at the 10th and 6th harmonics. The FFT of the current also shows a peak at the 10th harmonic. Correlating with the impedance scan result in Figure 8.7 it is observed that the peaks are quite close to the predicted value with one park capacitor. The peak around the 6th harmonic is indicative of a resonance caused by the capacitor at the Chatham SS.

(a) Voltage at PCC	(b) FFT of PCC voltage
(c) Current at PCC	(d) FFT of PCC current
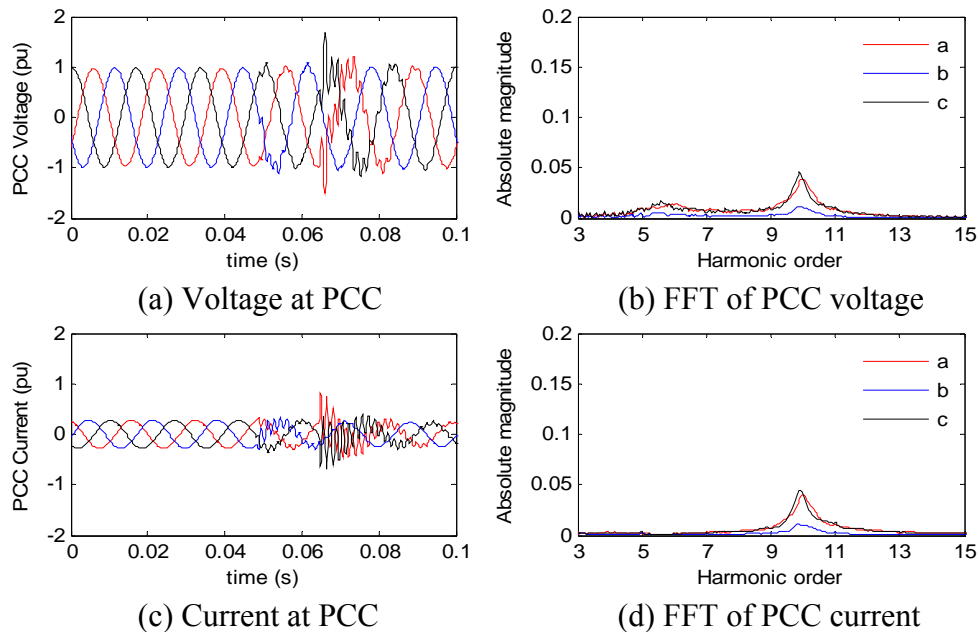
Figure 8.13 PCC voltage and current for event-B

8.5.3   Event-C (21st Jan. 2010)

Event-C presents the case of an operating condition when the wind farm power output was 84 MW. When the transmission network capacitor was put into service, thirteen turbines tripped due to the voltage amplification shown in Figure 8.14 (a). The FFT of the voltage depicted in Figure 8.6 (b) shows two peaks: one at the 10th harmonic and another at the 6th harmonic. The PCC current and its FFT are shown in the Figure 8.14 (c) and Figure 8.14 (d), respectively. The magnitude peak at the 10th harmonic in the FFT of voltage waveform matches well with the prediction from the frequency scan with one capacitor. The magnitude peak at the 6th harmonic also matches with the frequency scan which shows that this resonance is caused by the transmission network capacitor at Chatham SS.

(a) Voltage at PCC

(b) FFT of PCC voltage

(c) Current at PCC

(d) FFT of PCC current
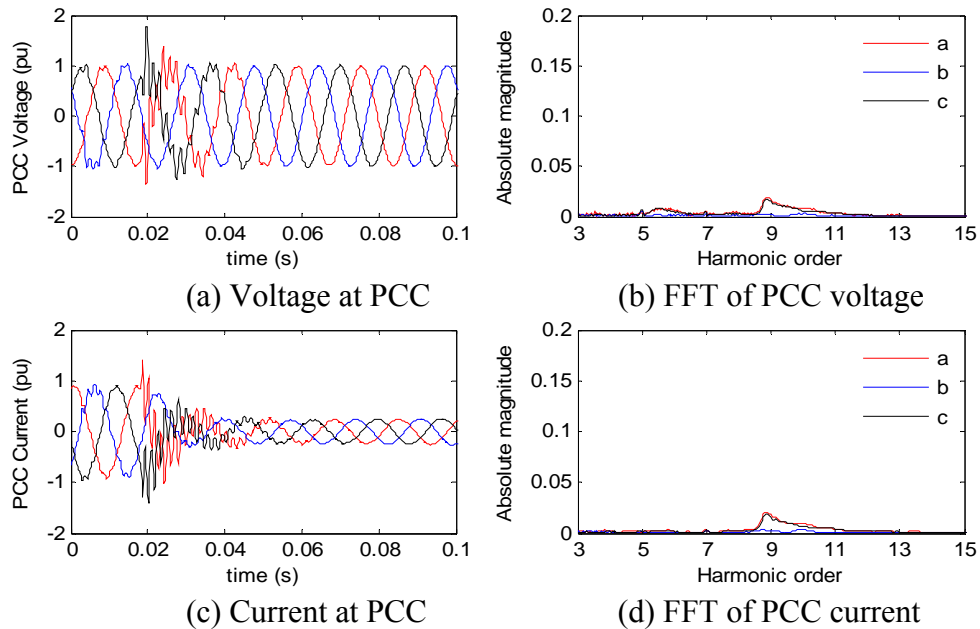
Figure 8.14 PCC voltage and current for event-C

8.5.4   Event-D (22nd Jan. 2010)

The event-D represents the case of an operating condition when the power output of the wind farm was at about 35 MW. The switching of capacitor in the networks resulted in the tripping of 33 wind turbines. The PCC voltage, current, and their FFT are shown in Figure 8.15. From the FFT of voltage shown in Figure 8.15 (b), voltage amplification is observed at the 9th and 6th harmonics. The network is already seen to be resonant at the 10th harmonic with one park capacitor. It is therefore anticipated that the overvoltages are seen due to harmonic resonances at the 9th and 10th harmonics.

(a) Voltage at PCC

(b) FFT of PCC voltage

(c) Current at PCC

(d) FFT of PCC current
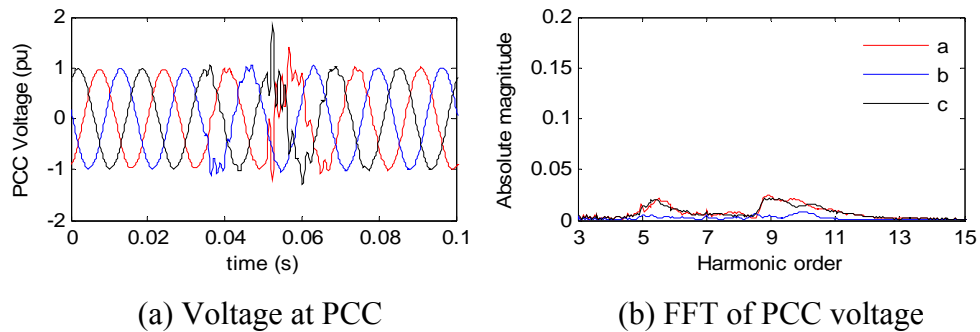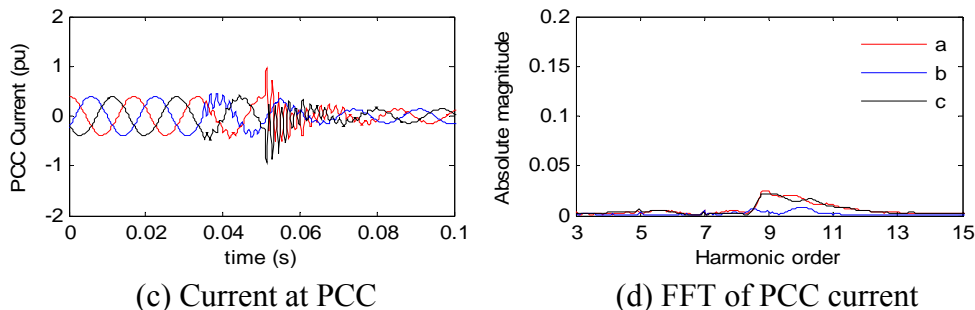
Figure 8.15 PCC voltage and current for event-D

8.5.5   Event-E (23rd Jan. 2010)

Event-E reports tripping 19 wind turbines following the switching of the transmission capacitor bank at Chatham SS. This occurred when the wind farm output was 95 MW. Distorted voltage and current at the PCC are shown in Figure 8.16. The FFT of the PCC voltage is shown in Figure 8.16 (b) showing resonant peaks at the 6th and between the 9th and 10th harmonics. From the frequency scan study it is found that these harmonic resonances are due to the combination of one park capacitor and one large transmission network capacitor. Since the FFT of voltage wave form matches very closely with the frequency scan result, it can be concluded that the overvoltage caused by the harmonic resonance in turn, caused the wind turbines to trip.

(a) Voltage at PCC

(b) FFT of PCC voltage

(c) Current at PCC

(d) FFT of PCC current
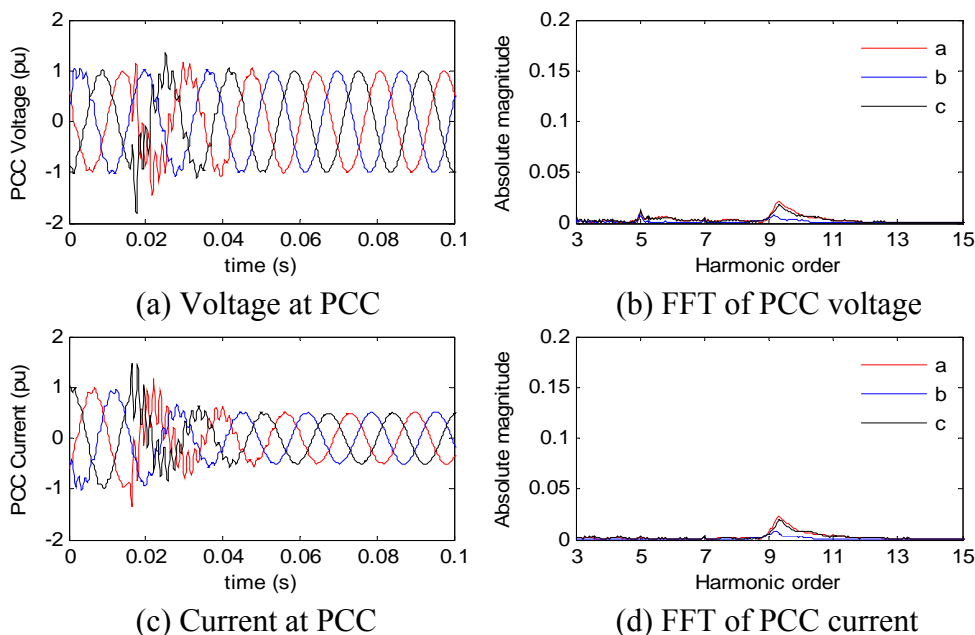
Figure 8.16 PCC voltage and current for event-E

8.6 CAPACITOR SWITCHING

It was noted that replacing the synchronization unit of the transmission capacitor at Chatham SS prevented any further turbines tripping. Hence, it was decided to perform a detailed analysis of the capacitor switching when capacitors in the three phases are not synchronized properly. This study is represented in this section.

It is known that energizing a shunt capacitor bank at or near a voltage peak produces high voltage and current transients or surges. These surges produced from the capacitor bank propagate to the remote end of an interconnected network and may cause over voltages in medium and low voltage networks [129]. Inrush current associated with the capacitor switching is in the order of 5 pu of the rated current of the capacitor bank, and at frequencies of 200-600 Hz depending upon the source impedance and size of the capacitor bank.

In the study system there is a large 220 MVAR capacitor bank at Chatham SS and this capacitor bank is put into service every morning for voltage support. In order to investigate the impact of asynchronous switching of this capacitor bank, time domain simulation is carried out. Figure 8.17 shows a typical reference signal used for capacitor switching. It is always expected that all three phases are switched on at the zero crossing of the corresponding phase voltage. Any delay towards the right of the ideal switching point is referred to as the positive delay and delay towards the left of the ideal zero crossing point is termed the negative delay in switching. In a 60 Hz system, positive peak occurs at +4.16ms delays and negative peak occurs at -4.16ms delays from the zero crossing of the phase voltage.

Figure 8.18 shows the PCC voltage (34.5 kV Bus) and capacitor bank (230 kV Bus) terminal voltage when the three poles of the capacitor banks are switched synchronously, i.e. at zero crossing, of the corresponding phase voltage. The 'A' phase of the capacitor bank is switched on at 5 sec, 'B' phase and 'C' phase are switched on after 120 degree and 240 degrees shift respectively. It is seen that there is no distortion in the voltages due to synchronous switching. The distortion seen in the 34.5 kV bus voltage is due to the

ambient harmonic in the network injected by the grid side voltage source converter of the wind turbines.
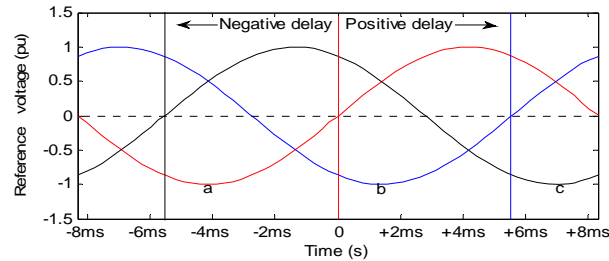
Figure 8.17 Reference signal for capacitor switching
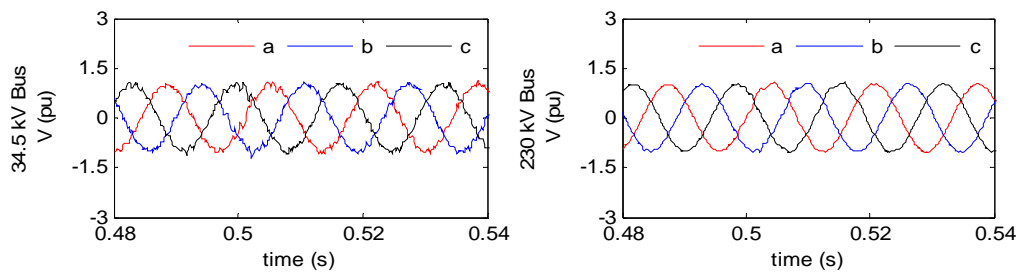
Figure 8.18 Synchronized switching of capacitor

In the synchronous control units (SCU) that are commercially used for the switching of capacitor banks in a switching, a delay of ±1ms is considered acceptable. Figure 8.17 depicts the typical switching sequence of the large capacitors. The switching delay depends upon the inherent variation of the operating time of the circuit breaker [129].

A detailed investigation into the impact of switching delay in the capacitor switching on the wind farm is now performed. Figure 8.19 (a) shows the voltage at both 34.5 kV and 230 kV buses when there is a +1ms delay in the switching of phase 'A' breaker. Figure 8.19 (b) shows the FFT of the voltages. It is observed that depending on the network condition, switching of the large capacitor causes distortion in the voltage between the 6th – 7th harmonic. As mentioned earlier, the disturbance propagates to the PCC of the wind farm. The distortion at the 34.5 kV bus is comparatively larger and may cause over voltage at the wind turbine terminals.

(a) Voltage
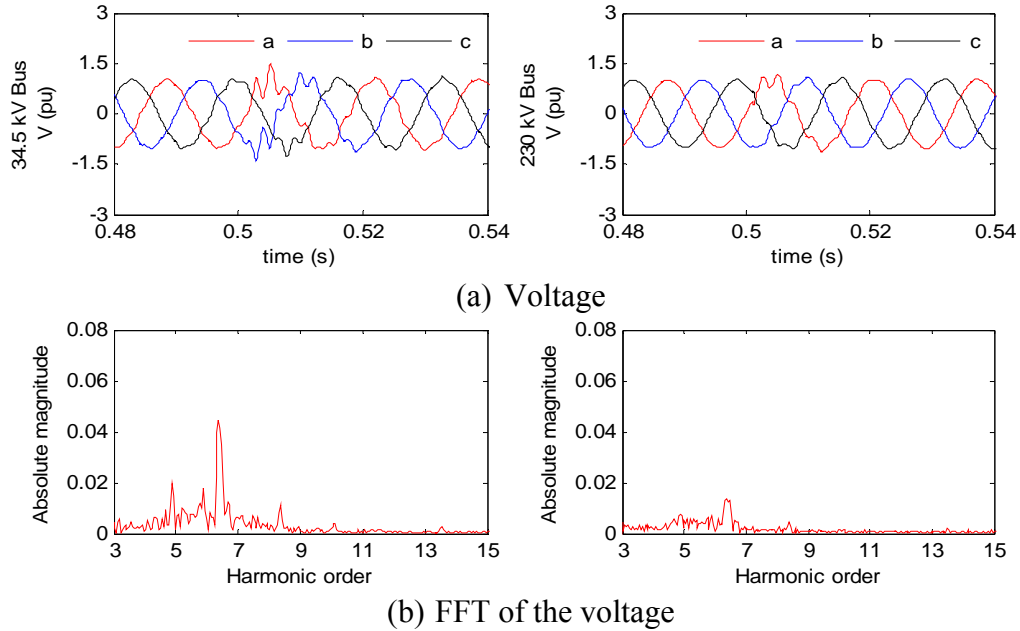
(b) FFT of the voltage

Figure 8.19 Impact of +1ms delay in switching of phase 'A'

Figure 8.20 (a) shows the voltages at both 34.5 kV and 230 kV buses for a +1ms delay in the switching of all three phases of the circuit breaker. The distortion in the voltages is found to be identical due to the simultaneous delay in the switching. The impact of a -1ms delay on the bus voltages is shown in Figure 8.20 (b). The 34.5 kV bus voltage distortions with negative switching delay are found to be more than the positive switching delay. Figure 8.21 shows the impact of a +5ms delay on the voltage and its FFT. With the +5ms delay all phases are switched on very close to the positive peak of the voltage at the capacitor bank. This voltage of 34.5 kV bus is found to be severely distorted. The FFTs of the voltage at both 34.5 kV and 230 kV buses show a high harmonic content at the 6th harmonic frequency. Figure 8.22 shows the impact of a -5ms delay on the voltage. With a -5ms delay, the 'A' phase and 'B' phase pole of the circuit breaker are switched on at maximum negative magnitude of the voltage, whereas the 'C' phase is switched on at the positive maximum voltage magnitude. Here again, a high harmonic content at the 6th harmonic is observed. Further, it is found that the voltage distortion is higher at the 34.5 kV bus side, i.e. at the terminals, of the wind farms. This harmonic over voltage could potentially cause the turbines to trip.
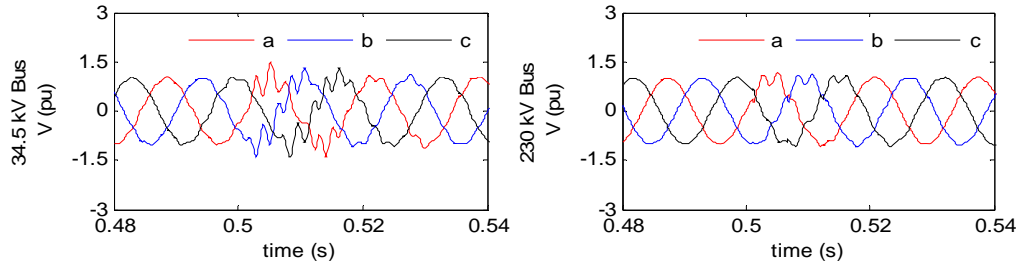
(a) Impact of +1 ms delay
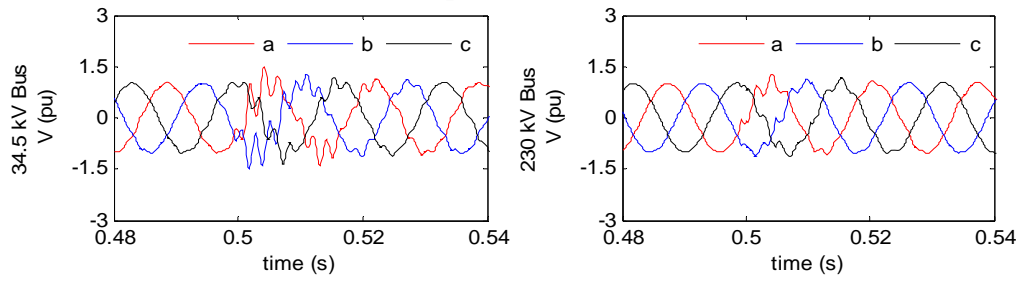
(b) Impact of -1 ms delay

Figure 8.20 Impact of ±1ms delay in three phase switching
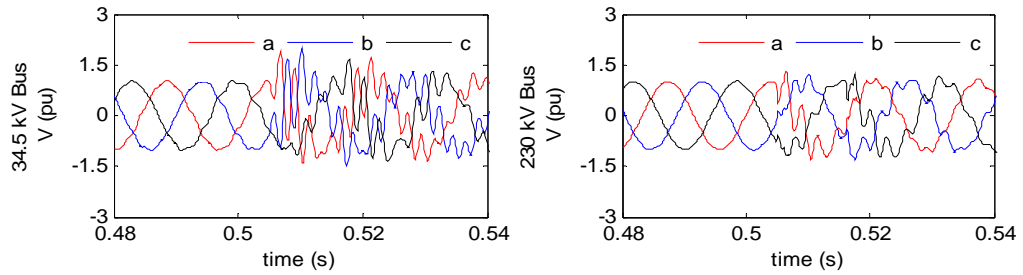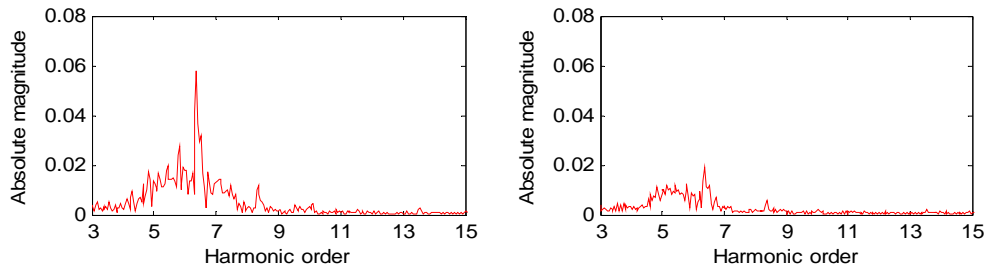
(a) Voltage

(b) FFT of voltage

Figure 8.21 Impact of +5ms delay in three phase switching.
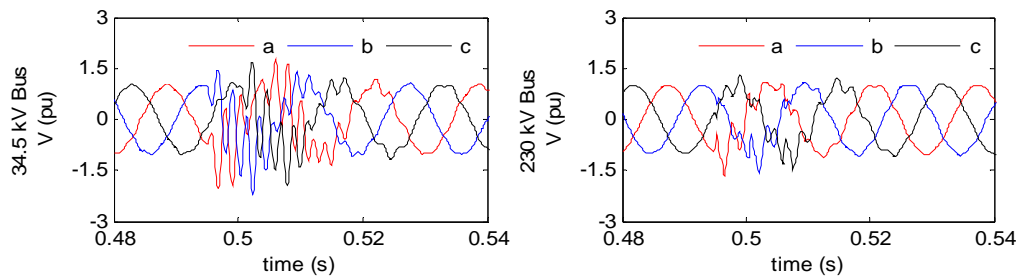
(a) Voltage
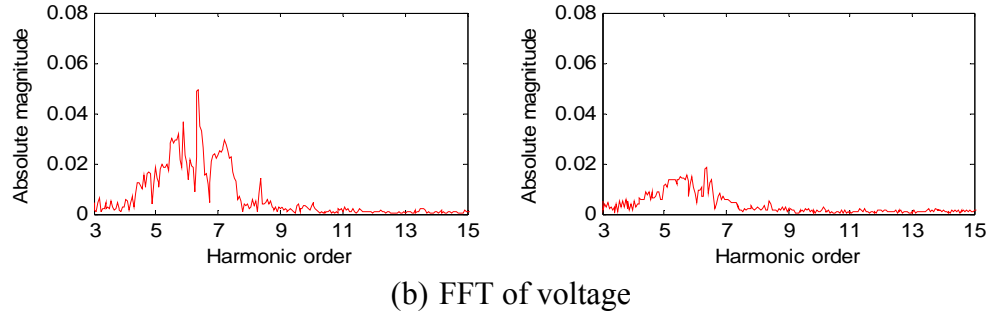
(b) FFT of voltage

Figure 8.22 Impact of -5ms delay in three phase switching

From the FFT of the 34.5 kV bus voltage for different wind turbine tripping events shown in Figure 8.12 to Figure 8.16, it is evident that there is an over voltage around the 6th harmonic. Now, from the FFT of simulated 34.5 kV bus voltages with unsynchronized switching of transmission capacitor, a high generation of 6th harmonic is also noted. The network impedance plots already demonstrate a resonant mode around the 6th harmonic. It is therefore concluded that one of the reasons for turbine trip is the overvoltage caused by unsynchronized switching of the transmission capacitor. This is further confirmed by the fact that when the SCU was repaired and synchronized switching was reestablished, no turbine trips occurred after that point.

8.7   IMPEDANCE SCAN WITH TWO IDENTICAL WIND FARMS

The study system in Figure 8.1 showed a single wind farm connected to the transmission network. Later in 2011 another wind farm of identical size was connected to the 230 kV line. The new wind farm also has six park capacitors connected at the PCC. The new configuration of the system is shown in Figure 8.23. Considering the potential for harmonic resonance and its impact on the wind turbines, a comprehensive analysis is now carried out with the second wind farm.

8.7.1   Impact of Park Capacitors

The impedance scan is carried out at two points: point-A and point-B, which are the PCCs of both the wind farms, as shown in Figure 8.23. Since there are six capacitors at each WF, seventy two combinations of the capacitors are likely. Due to the symmetry of the circuit, similar performance of both wind farms is anticipated. Hence, the number of

capacitors is sequentially varied in both wind farms and corresponding network driving point impedance are obtained.
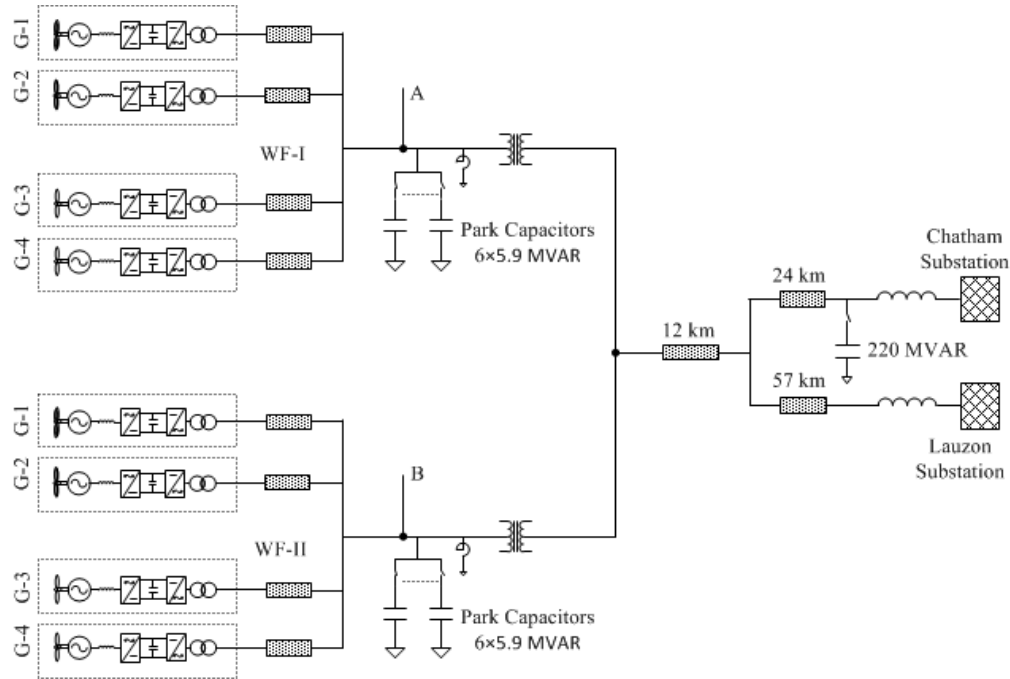
Figure 8.23 Two wind farms connected to grid

Figure 8.24 shows the driving point impedance at the PCC of each wind farm for different combinations of park capacitors. In this case, one out of six capacitors at WF-I is connected while all six capacitors at WF-II are switched in sequence. With one capacitor at each WF the impedance peaks are obtained at the 9th and 11th harmonics as shown in Figure 8.24 (a) and (b). As the number of capacitors increase at WF-II, resonance peaks of WF-II shifts towards lower harmonic order. However, the resonance at PCC of the WF-I remains constant at the 10th harmonic and the peak magnitude of the driving point impedance corresponding to the resonant frequency remains very high. However, the peak magnitude of the impedance corresponding to the resonant frequencies at PCC of the WF-II is reduced with the increase in the number of park capacitors. Only during the symmetrical combination of capacitors, both wind farms are exposed to a parallel resonance of identical characteristic.

Figure 8.25 shows the driving point impedance for two park capacitors at WF-I and one to six capacitors switched in sequence at WF-II. Two capacitors at each WF results in a resonance close to the 7th harmonic which, incidentally, is a characteristic harmonic

injected by wind turbines. The peak magnitude of the impedance is also found to be large in both cases. As the number of park capacitor at WF-II increases, the peak magnitude of the impedance decreases as does the resonance order.

(a) WF-I

(b) WF-II
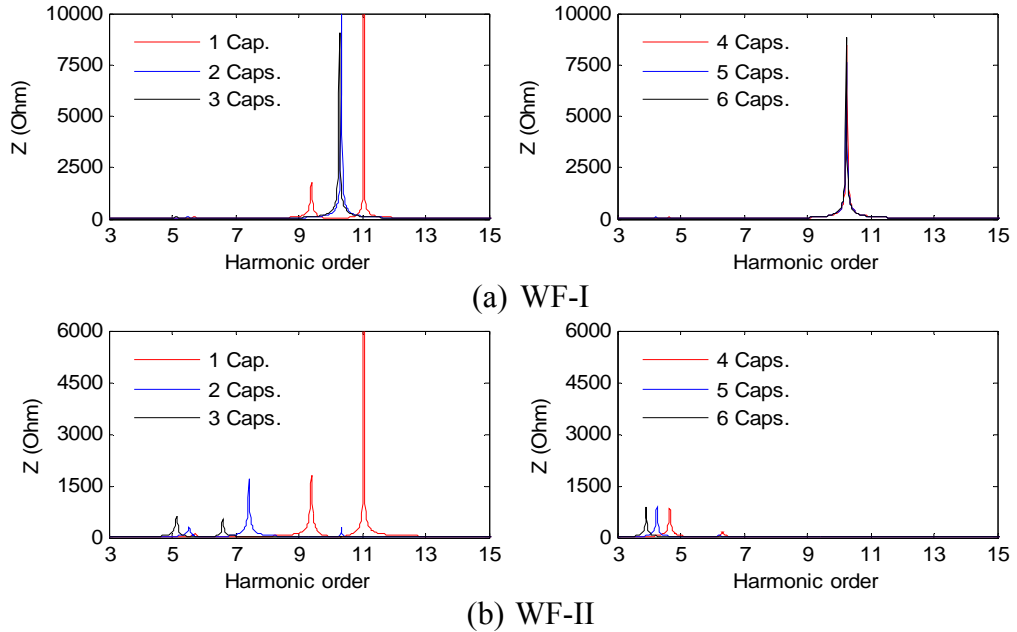
Figure 8.24 Impedance with one capacitor at WF-I and six capacitors sequentially switched at WF-II

(a) WF-I

(b) WF-II
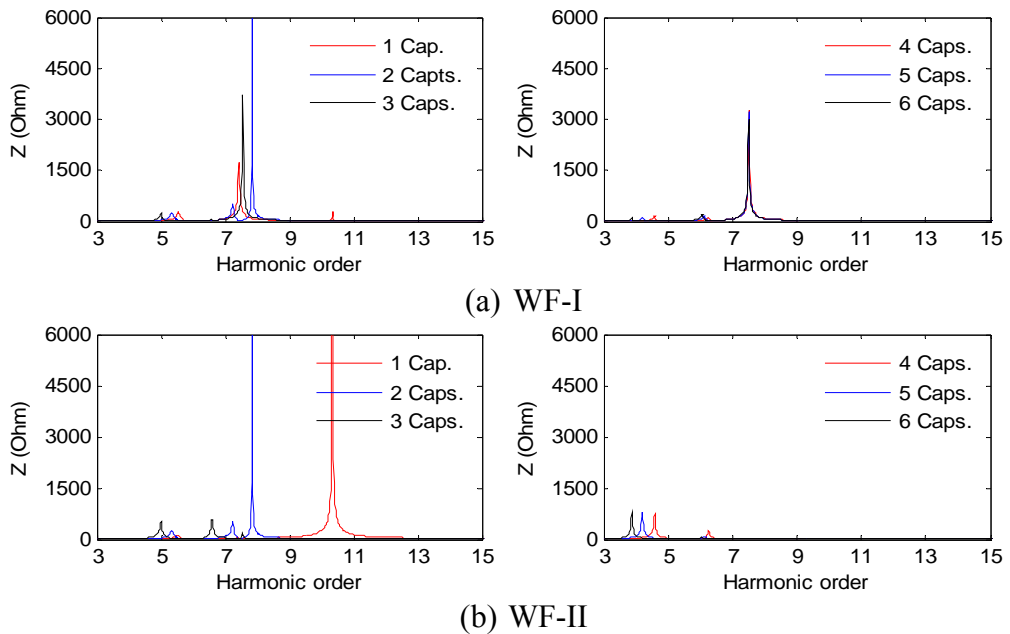
Figure 8.25 Impedance with two capacitors at WF-I and six capacitors sequentially switched at WF-II

The driving point impedance of WF-I and WF-II with three park capacitors at WF-I and six sequentially switched capacitors at WF-II is shown in Figure 8.26. The harmonic order reduces with the increase in the size of park capacitors. The peak amplitude of the corresponding impedance is also reduced. With three capacitors at each wind farm, the potential for harmonic resonances are found at the 5th and 6th harmonics, as shown in Figure 8.26 (a). The resonance at the 5th harmonic is caused by the transmission network capacitor, whereas the resonance at the 6th harmonic is originated from the park capacitors. The two resonances close to each other indicate a larger risk of voltage distortion as these resonances may be magnified by the harmonic current injection from the wind farm converter and switching harmonic produced by the large transmission network capacitor. The impedance scan results with four park capacitors at WF-I and six capacitors sequentially switched at the WF-II are presented in Figure 8.27 where Figure 8.27 (a) depicts the scanned impedance at the PCC of WF-I and Figure 8.27 (b) shows the same at the PCC of WF-II. The resonance orders at WF-I are limited within the 4th and 6th harmonics. However, these vary from 4th to 10th harmonic at the PCC of WF-II.

(a) WF-I

(b) WF-II
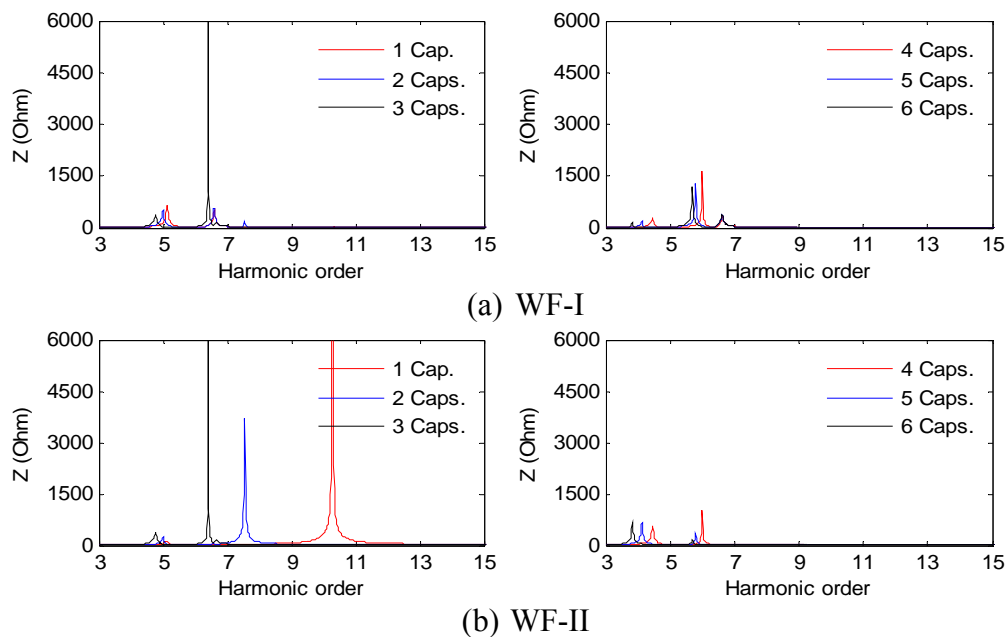
Figure 8.26 Impedance with three capacitors at WF-I and six capacitors sequentially switched at WF-II

(a) WF-I

(b) WF-II
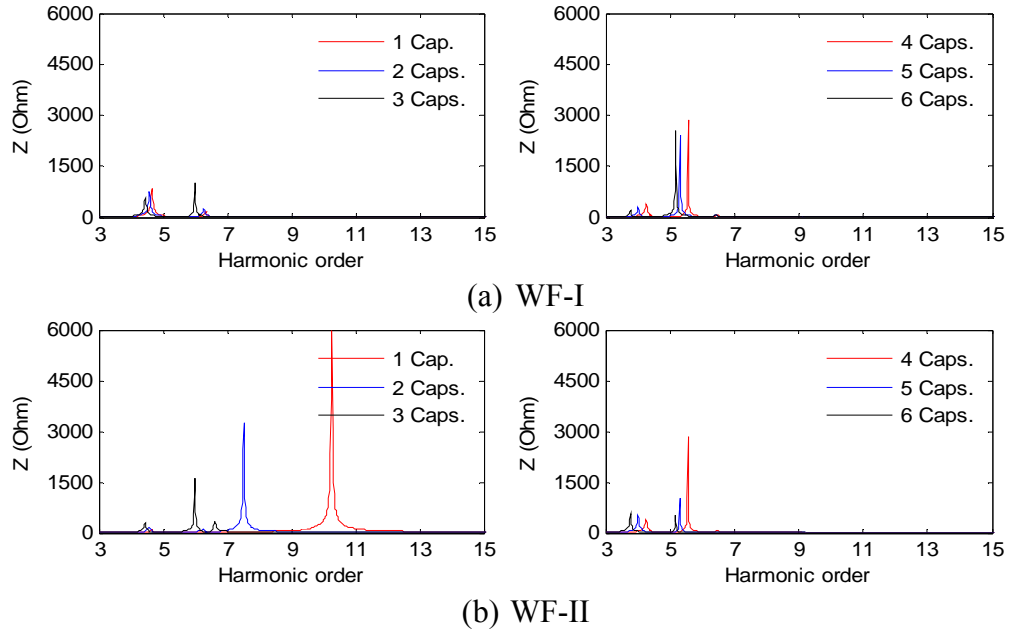
Figure 8.27 Impedance with four capacitors at WF-I and six capacitors sequentially switched at WF-II

Figure 8.28 shows the impedance scan for five capacitors at the PCC of WF-I and one to six capacitors connected sequentially at the PCC of WF-II. With five capacitors WF-I sees the network impedance peaks at the 4th and 5th harmonics. Figure 8.29 shows the driving impedance with six capacitors at WF-I and one to six capacitors at WF-II. The resonances in both wind farms are found to be similar. It is observed that the peak magnitude of the driving point impedance is reduced with the increase in the number of park capacitors.

(a) WF-I

(b) WF-II
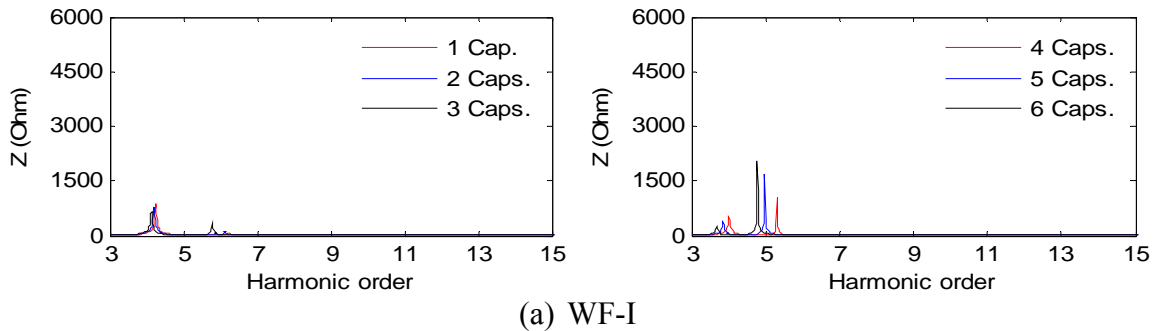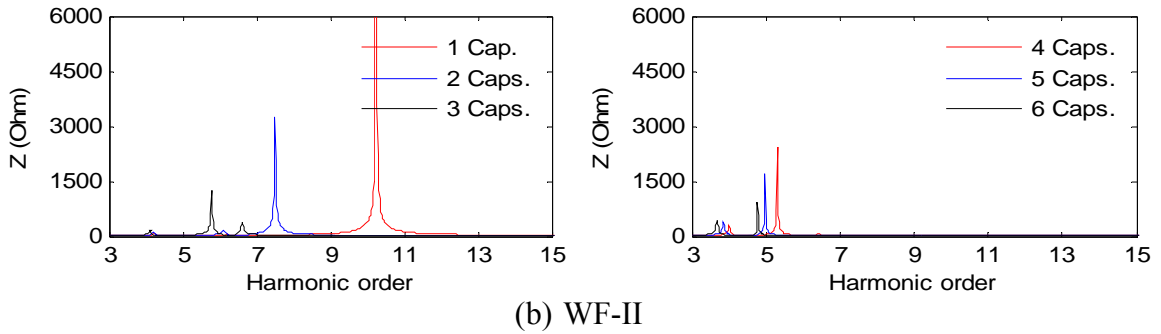
Figure 8.28 Impedance with five capacitors at WF-I and six capacitors sequentially switched at WF-II

(a) WF-I

(b) WF-II
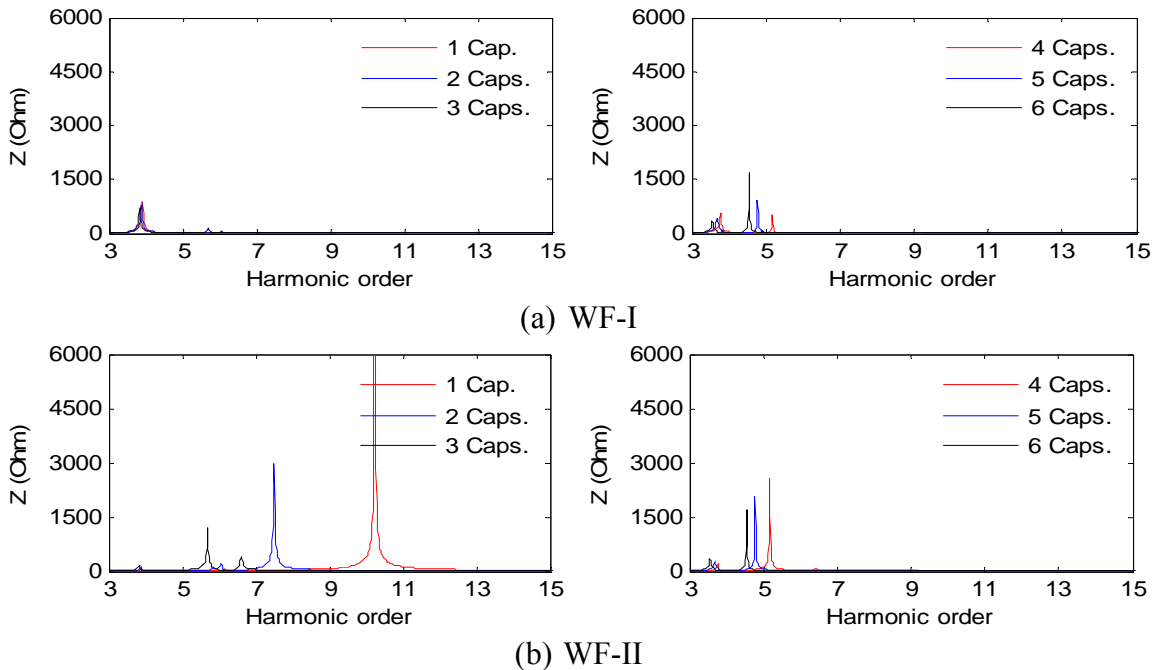
Figure 8.29 Impedance with six capacitors at WF-I and six capacitors sequentially switched at WF-II

From the detailed impedance scan with two identical wind farms, it is observed that park capacitors along with the large transmission network capacitor develop the potential for parallel resonance in the wind farms. If the harmonic current injection from the wind farm converters align with any of these network resonances, voltage magnification is anticipated, which may trip the turbines. With the increased number of park capacitors, both resonance orders come very close to each other thereby increasing the risk of parallel resonance. Hence, it is recommended to avoid the symmetrical energization of the park capacitors in both wind farms. Particularly with one and two capacitors, the adverse impact of the parallel resonance increases due to the fact that the resonance

occurs around a harmonic order which is very close to the characteristic harmonic of the converter current injected into the grid.

8.7.2 Impact of Short Circuit Level

It is seen from the impedance scan with one wind farm that the short circuit level of the Hydro One network plays a critical role in parallel resonance at the PCC. Hence, a detailed study is conducted in which the short circuit level of the Hydro One network at Chatham SS is varied between 4000 MVA and 16000 MVA. The short circuit level of the network at Lauzon SS is kept constant at the rated value of 2600 MVA. The driving point impedance with a few selected combinations of the park capacitors are chosen and discussed in this section.

Figure 8.30 shows the impedance at the PCCs of both wind farms with one park capacitor at each wind farm. It is found that the lower order resonance frequency is largely affected by the system short circuit level, whereas the resonance around the 11th harmonic remains almost stable. Due to symmetry of the circuit, the driving point impedance at both the PCC seems to be identical. Figure 8.31 shows a similar study with two park capacitors at each wind farm. The lower order resonance frequency varies between the 5th and 8th harmonic order, whereas the resonance around 8th harmonic remains quite constant, irrespective of the system short circuit level. From the field experience of wind turbines tripping, it is anticipated that these two combinations may pose a greater risk of harmonic voltage amplification in the system at low voltage side of the transformer. Another case study with two park capacitors at WF-I and five park capacitors at WF-II is shown in Figure 8.32. Within the range of short circuit level considered, the resonance frequency at WF-I varies between the 5th and 8th harmonic order, whereas, at WF-II it varies between the 4th and 6th harmonic order.
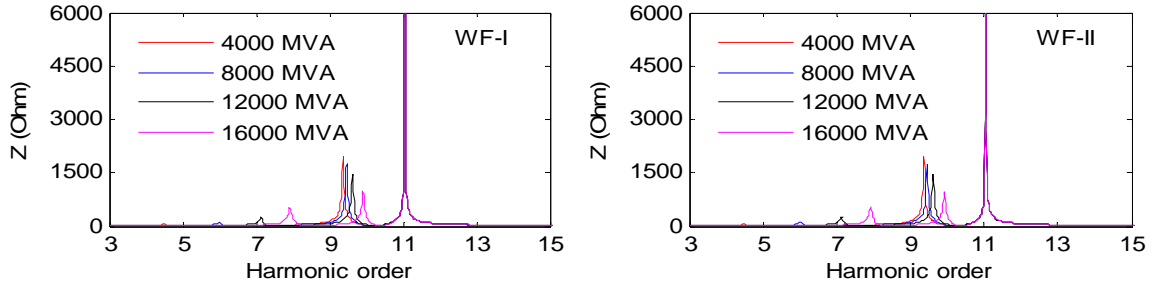
Figure 8.30 Driving point impedance at the PCC with one park capacitor at each wind farm
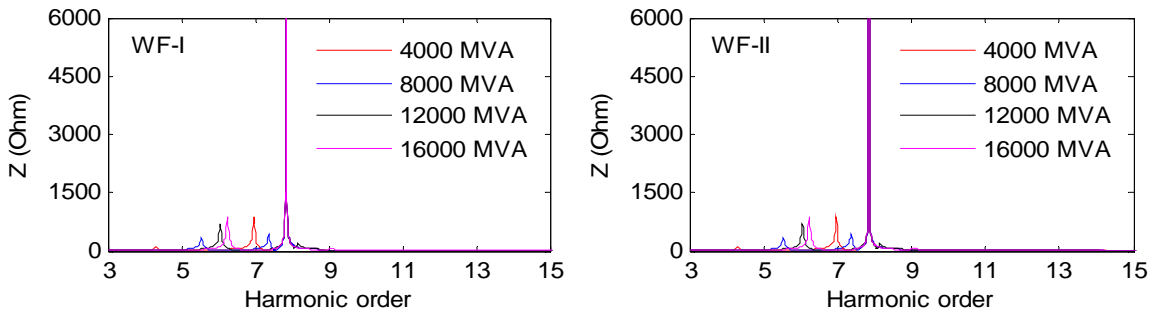
Figure 8.31 Driving point impedance at the PCC with two park capacitors at each wind farm
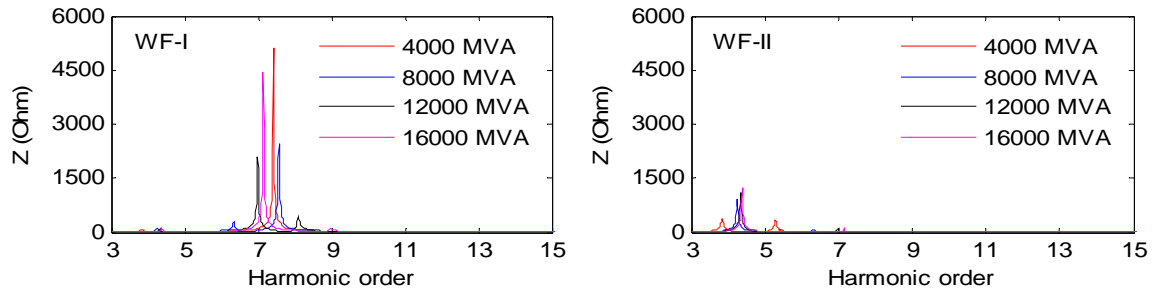
Figure 8.32 Driving point impedance at the PCC with two park capacitors at WF-I and five park capacitors at WF-II.

From the impedance scan results, several recommendations are made for the two wind farms. Table 8.4 shows the combinations of the park capacitors which are safe for the WF-I and where no potential for voltage distortion due to the parallel resonance is anticipated. These are indicated by the '√' marks. Similarly, Table 8.5 shows the combinations of the park capacitors which may not cause any risk of parallel resonance at the WF-II. With the recommended combinations, although parallel resonance may occur, they are at frequencies different from the characteristic harmonic orders of the current injected by the grid connected inverter of the wind turbines.

Table 8.4 Recommended combinations of capacitors for WF-I

	Number of capacitors at WF-I					
	1	2	3	4	5	6
1	×	×	×	√	√	√
2	×	×	×	×	√	√
3	×	×	×	×	×	√
4	×	×	×	×	×	×
5	×	×	×	×	×	×
6	×	×	×	×	×	×

(Row labels 1–6 under "Number of capacitors at WF-II")

Table 8.5 Recommended combinations of capacitors for WF-II

	Number of capacitors at WF-I					
	1	2	3	4	5	6
1	×	×	×	×	×	×
2	×	×	×	×	×	×
3	×	×	×	×	×	×
4	√	×	×	×	×	×
5	√	√	×	×	×	×
6	√	√	√	×	×	×

(Row labels 1–6 under "Number of capacitors at WF-II")

8.8   HARMONIC CURRENT INJECTION STUDY

To evaluate the impacts of harmonic current injection under the resonance conditions, a study is conducted by injecting the characteristic harmonic currents into the network at the PCC of wind farm. The maximum harmonic currents obtained from the manufacturer specification of the wind turbine inverter are injected into the network. This information is confidential and hence not provided in the thesis. The wind farm is therefore modeled as a controlled current source. All harmonic components are first injected individually, and then injected simultaneously. The percent of Total Harmonic Distortion (THD) of the PCC voltage is calculated for all cases. Although all maximum harmonics will not be injected together, this study is still conducted to determine the impact during a worst case

scenario. The study is conducted first with one wind farm, and then followed with both wind farms.

8.8.1 One Wind Farm

Considering only one wind farm, the characteristic harmonic currents are injected into the network. Figure 8.33 shows the PCC voltage with injection of all (3rd, 5th, 7th, 11th and 13th) harmonic currents from the wind farm at different short circuit levels. The THD of the corresponding PCC voltages are calculated and depicted in Table 8.6, which shows the THD at different short circuit levels for different harmonic current injections. Since one capacitor results in a resonance around the 11th harmonic order, the 11th harmonic current injection substantially increases the THD in the PCC voltage which violates the IEEE 519 regulation of 5% [130]. Irrespective of the short circuit level, the THD remains above 10% when all of the harmonic currents are injected simultaneously. As stated earlier, all of the maximum harmonic currents will never be injected simultaneously in real life. However, this study predicts the relative impact of injection of various harmonics.
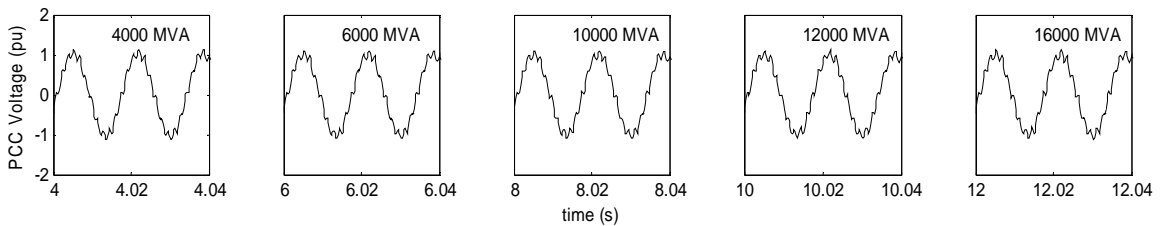
Figure 8.33 PCC voltage with one park capacitor.

Table 8.6 PCC voltage THD (%) with one park capacitor at wind farm

SCL (MVA)	I_3^{max}	I_5^{max}	I_7^{max}	I_{11}^{max}	I_{13}^{max}	$\sum_{n=3,5,7,11,13} \left(I_n^{max} \right)$
4000	0.37	0.84	1.09	**10.59**	1.59	**10.98**
6000	0.40	2.25	0.90	**11.09**	1.64	**11.66**
10000	0.35	2.11	0.27	**11.33**	1.64	**11.84**
12000	0.36	2.06	2.29	**11.66**	1.64	**12.37**
16000	0.41	2.02	1.57	**12.65**	1.69	**13.22**

Figure 8.34 shows a similar study's results with two park capacitors at the PCC. From the impedance scan it is evident that two park capacitors along with a transmission

capacitor result in resonances between the 6th and 8th order harmonic. It is found that the distortions in the PCC voltage at 4000 MVA and 16000 MVA short circuit levels are higher than other short circuit levels. Injection of the maximum 7th harmonic alone for these SCLs can cause voltage THD in excess of that specified by IEEE 519 standard. The THD of the PCC voltage for different short circuit levels are summarized in Table 8.7.

Figure 8.35 and Table 8.8 show the voltage waveforms with three park capacitors at the PCC and THD of the PCC voltage for the corresponding short circuit level, respectively. It is noted that with three park capacitors the resonance orders are found between the 5th and 7th order of harmonics, the 5th being the dominant. Voltage THDs at the wind farm with maximum 5th harmonic current injection alone can be much higher than the level prescribed by IEEE 519, for a wide range of system short circuit levels.

It is concluded that harmonic resonance in the Port Alma wind farm is substantially influenced by the number of park capacitors connected at the PCC and the short circuit level of the Hydro One network at the Chatham SS. Out of the three cases discussed here, the resonance issue with one capacitor and three capacitors is more severe than the two capacitors, found from the study over a wide range of short circuit levels.
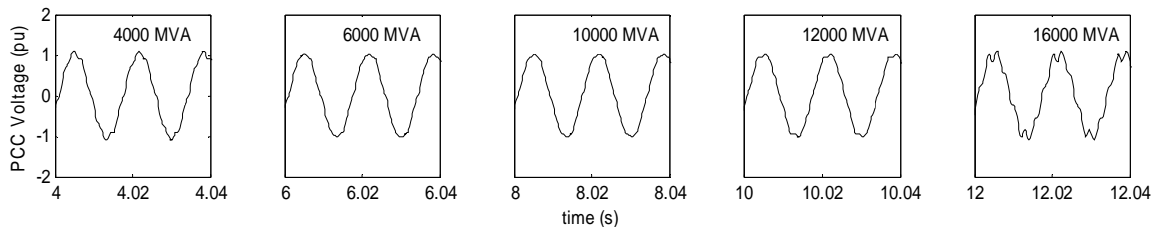
Figure 8.34 PCC voltage with two park capacitors.

Table 8.7 PCC voltage THD **(%)** with two park capacitors at wind farm

$\vec{I}_h$ SCL (MVA)	I_3^{max}	I_5^{max}	I_7^{max}	I_{11}^{max}	I_{13}^{max}	$\sum_{n=3,5,7,11,13} \left(I_n^{max} \right)$
4000	0.42	0.97	**6.40**	1.62	0.47	**6.82**
6000	0.41	3.62	2.40	1.65	0.50	4.77
10000	0.38	3.28	0.22	1.67	0.49	3.80
12000	0.38	3.15	3.30	1.68	0.49	4.98
16000	0.42	3.02	**12.11**	1.71	0.53	**12.81**
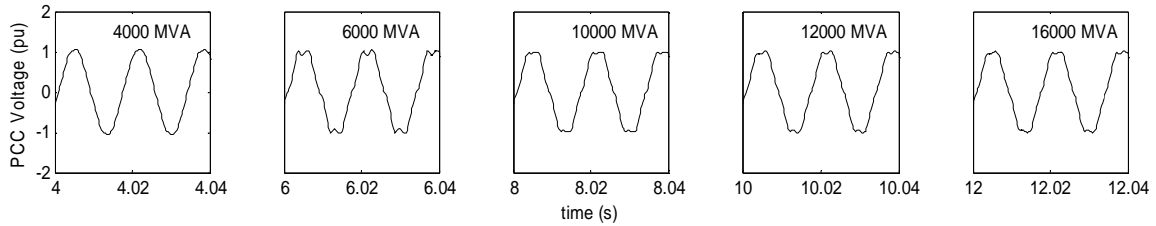
Figure 8.35 PCC voltage with three park capacitors.

Table 8.8 PCC voltage THD (%) with three park capacitors at wind farm

$\dfrac{\vec{I}_h}{\text{SCL (MVA)}}$	$I_3^{\max}$	$I_5^{\max}$	$I_7^{\max}$	$I_{11}^{\max}$	$I_{13}^{\max}$	$\displaystyle\sum_{n=3,5,7,11,13}\left(I_n^{\max}\right)$
4000	0.47	1.16	1.63	0.86	0.27	2.29
6000	0.43	**9.82**	2.88	0.88	0.28	**10.45**
10000	0.43	**7.55**	0.21	0.89	0.28	**7.75**
12000	0.43	**6.90**	0.96	0.90	0.29	**7.16**
16000	0.48	**6.21**	1.23	0.92	0.36	**6.51**

8.8.2   Two Wind Farms

When two wind farms are connected to the Hydro One transmission network, potential for parallel resonance increases as witnessed from the impedance scanning results shown in previous section. To examine the impact of resonance in terms of THD of the PCC voltage, several characteristic harmonic currents are injected into the network, and corresponding voltage THDs are calculated.

Figure 8.36 shows the PCC voltage of both wind farms with all characteristic harmonic current injection. The voltage wave forms depicted in Figure 8.36 (a) and Figure 8.36 (b) are identical due to the symmetrical circuit configuration. Table 8.9 shows THD of the PCC voltages at both wind farms. It is seen that injection of the 11th harmonic alone increases the THD beyond acceptable limits. At the 12000 MVA short circuit level, injection of the 7th harmonic alone also causes substantial rise in the THD.

Harmonic currents are now injected to the network with one park capacitor at WF-I and two park capacitors at WF-II. The simulation results are shown in Figure 8.38 and the corresponding THD of the PCC voltages are illustrated in Table 8.10.

(a) WF-I

(b) WF-II
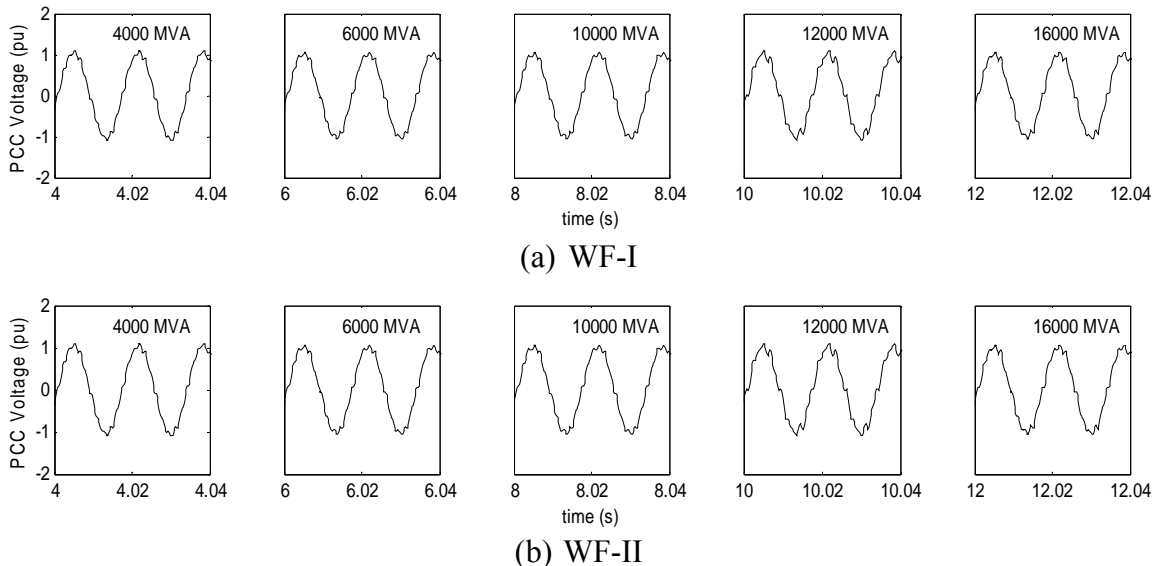
Figure 8.36 PCC Voltage with one park capacitor at each wind farm.

Table 8.9 PCC Voltage THD (%) with one park capacitor at each wind farm

$\vec{I}_h$	I_3^{max}		I_5^{max}		I_7^{max}		I_{11}^{max}		I_{13}^{max}		$\sum_{n=3,5,7,11,13}\left(I_n^{max}\right)$	
SCL (MVA)	WF-I	WF-II	WF-I	WF-II	WF-I	WF-II	WF-I	WF-II	WF-I	WF-II	WF-I	WF-II
4000	0.50	0.50	0.36	0.36	1.38	1.38	**6.28**	**6.28**	1.31	1.31	**6.58**	**6.58**
6000	0.44	0.44	3.23	3.23	0.87	0.87	**6.55**	**6.55**	1.34	1.34	**7.49**	**7.49**
10000	0.44	0.44	2.89	2.89	0.55	0.55	**6.69**	**6.69**	1.35	1.35	**7.44**	**7.44**
12000	0.43	0.43	2.76	2.76	**7.95**	**7.95**	**6.84**	**6.84**	1.36	1.36	**10.94**	**10.94**
16000	0.42	0.42	2.64	2.64	2.67	2.67	**7.38**	**7.38**	1.38	1.38	**8.40**	**8.40**

Figure 8.37 shows the PCC voltage at both wind farms with one park capacitor at WF-I and two park capacitors at WF-II. The voltage THD in percent at both the PCC is given in Table 8.10. With this configuration, parallel resonance at WF-I will occur around the 11th harmonic, whereas it will occur around the 7th harmonic at WF-II. Therefore, injection of the 11th harmonic current alone causes unacceptable voltage distortion at the PCC of WF-I and injection of the 7th harmonic current results in the distortion in voltage at the PCC of WF-II. It is seen that with all harmonic current injections, the THD of the PCC voltage at both wind farms increases beyond the acceptable limit of 5% [84], [130].

Figure 8.38 shows similar study results with a different combination of park capacitors. In this case three capacitors are connected across the PCC of WF-II along with one park

capacitor at the WF-I. Table 8.11 shows the THD of the PCC voltages. Injection of only the 5th and 11th harmonics may cause unacceptable voltage THD levels.

(a) WF-I

(b) WF-II
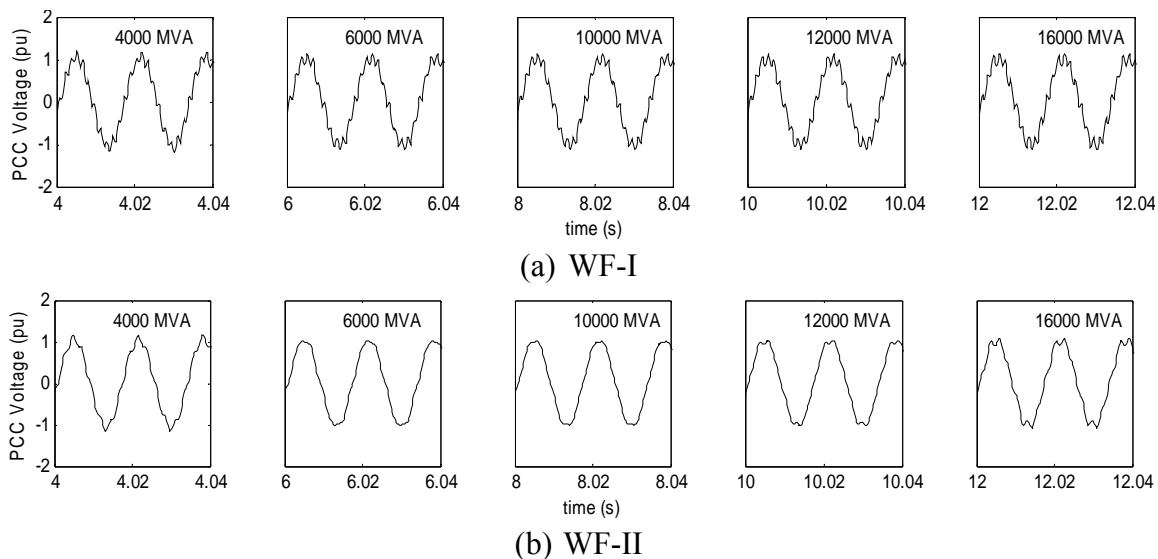
Figure 8.37 PCC voltage with one capacitor at WF-I and two capacitors at WF-II.

Table 8.10 PCC voltage THD (%) with one capacitor at WF-I and two capacitors at WF-II

$\vec{I}_h$	I_3^{max}		I_5^{max}		I_7^{max}		I_{11}^{max}		I_{13}^{max}		$\sum_{n=3,5,7,11,13}\left(I_n^{max}\right)$	
SCL (MVA)	WF-I	WF-II	WF-I	WF-II	WF-I	WF-II	WF-I	WF-II	WF-I	WF-II	WF-I	WF-II
4000	0.52	0.56	0.32	0.43	3.04	**8.90**	**12.65**	0.03	1.59	0.35	**13.11**	**8.93**
6000	1.27	0.53	4.24	**5.37**	1.44	2.47	**12.85**	0.20	1.90	0.43	**13.58**	**5.94**
10000	0.60	0.49	3.48	4.57	0.46	0.64	**13.35**	0.06	1.71	0.36	**13.90**	4.66
12000	0.61	0.48	3.25	4.27	1.23	3.47	**13.92**	0.08	1.70	0.37	**14.44**	**5.53**
16000	0.98	0.50	3.19	4.03	3.15	**8.72**	**15.24**	0.18	1.94	0.40	**15.95**	**9.63**

(a) WF-I

(b) WF-II
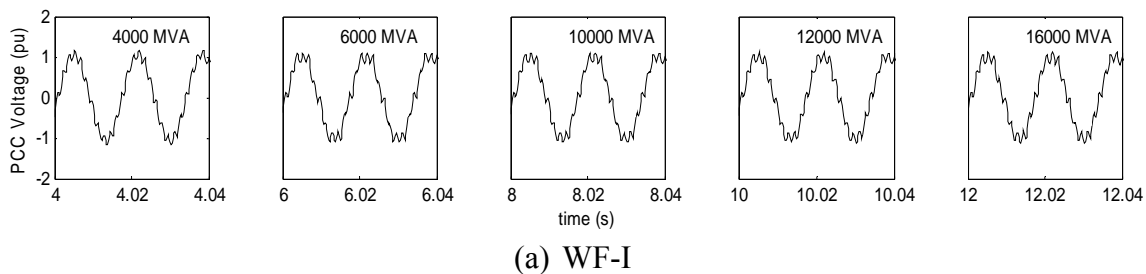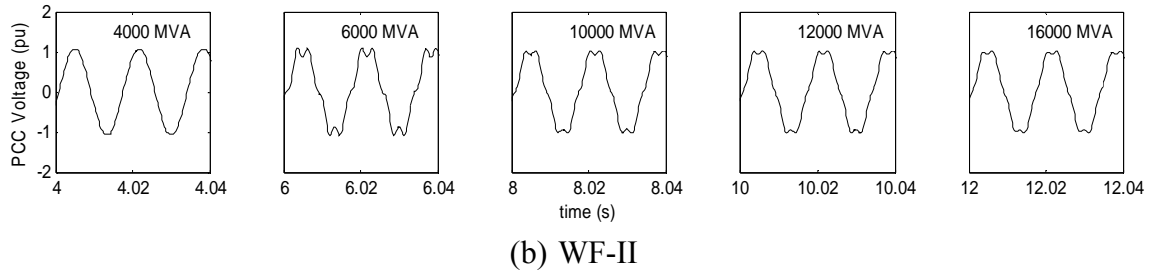
Figure 8.38 PCC voltage with one capacitor at WF-I and three capacitors at WF-II.

Table 8.11 PCC voltage THD (%) with one capacitor at WF-I and three capacitors at WF-II

$\vec{I}_h$	I_3^{max}		I_5^{max}		I_7^{max}		I_{11}^{max}		I_{13}^{max}		$\sum_{n=3,5,7,11,13}\left(I_n^{max}\right)$	
SCL (MVA)	WF-I	WF-II	WF-I	WF-II	WF-I	WF-II	WF-I	WF-II	WF-I	WF-II	WF-I	WF-II
4000	0.54	0.63	0.26	0.52	0.64	1.94	**12.55**	0.01	1.63	0.20	**12.89**	2.11
6000	0.97	0.55	**8.29**	**16.40**	1.30	2.83	**13.21**	0.07	1.84	0.22	**15.69**	**16.66**
10000	0.56	0.54	**5.63**	**11.22**	0.40	0.75	**13.51**	0.04	1.67	0.21	**14.73**	**11.26**
12000	0.57	0.53	4.90	**9.73**	0.60	1.42	**13.78**	0.07	1.71	0.22	**14.73**	**9.85**
16000	0.84	0.57	4.39	**8.62**	0.83	1.61	**15.06**	0.19	1.79	0.28	**15.78**	**8.79**

Three other combinations of park capacitors are also examined. These combinations are two capacitors at each wind farm, two capacitors at WF-I with three capacitors WF-II, and two capacitors at WF-I with five capacitors at WF-II. Figure 8.39 shows the PCC voltage of both winds farms when each wind farm employs two park capacitors at the PCC. Figure 8.40 depicts the voltage at the PCC of both wind farms corresponding to the harmonic injection when two capacitors are connected at the PCC of WF-I along with three capacitors at the PCC of WF-II. Similarly, Figure 8.41 shows the PCC voltage waveforms with two capacitors at WF-I and five capacitors at the PCC of WF-II. For each case discussed above, the calculated THD of the PCC voltages are given in Table 8.12, Table 8.13 and Table 8.14. In general it is seen that only the 5th and 7th harmonic injections from the two wind farms can create unacceptable voltage THD conditions over a substantial range of short circuit level of the Hydro One network at the Chatham SS. It is concluded that variation in the short circuit level of the Hydro One network, the combination of park capacitors, and injection of harmonic currents from the wind turbine

inverter together play a critical role in the harmonic voltage amplification in the wind farm. The excessive amplification in voltage may further cause the turbines to trip.
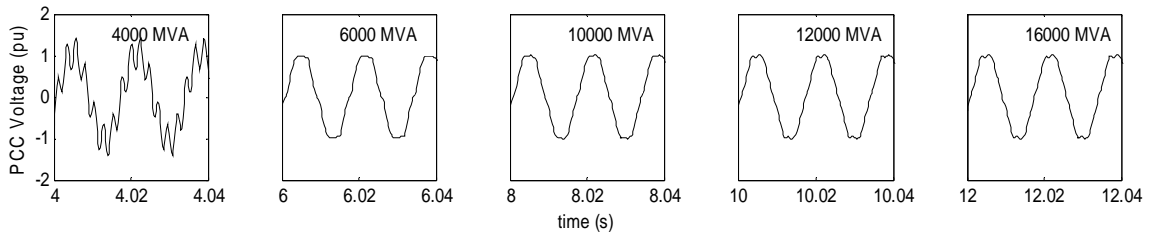
(a) WF-I
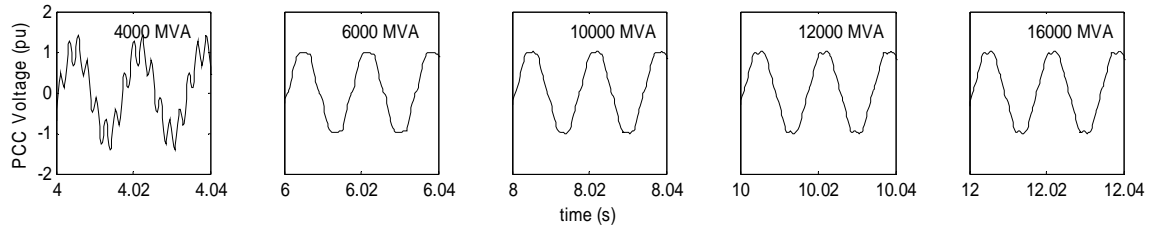
(b) WF-II

Figure 8.39 PCC voltage with two capacitors at both wind farms
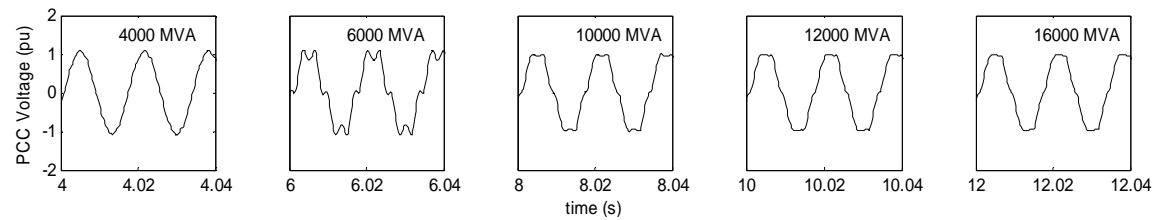
(a) WF-I
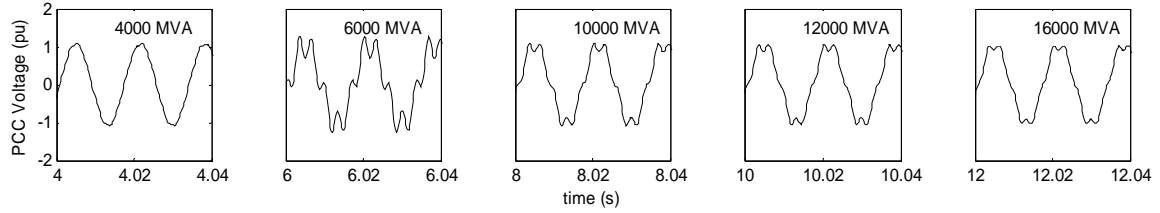
(b) WF-II

Figure 8.40 PCC voltage with two capacitors at WF-I and three capacitors at WF-II
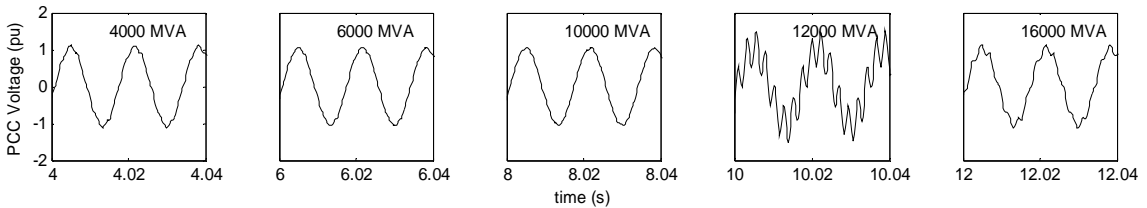
(a) WF-I
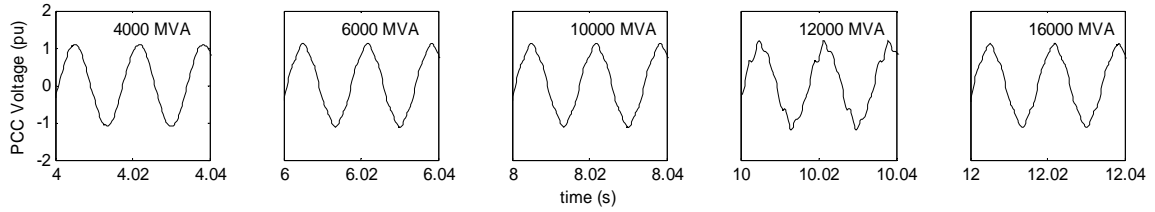
(b) WF-II

Figure 8.41 PCC voltage with two capacitors at WF-I and five capacitors at WF-II

Table 8.12 PCC voltage THD (%) with two capacitors at both wind farms.

$\vec{I}_h$	I_3^{max}		I_5^{max}		I_7^{max}		I_{11}^{max}		I_{13}^{max}		$\sum\limits_{n=3,5,7,11,13}\left(I_n^{max}\right)$	
SCL (MVA)	WF-I	WF-II	WF-I	WF-II	WF-I	WF-II	WF-I	WF-II	WF-I	WF-II	WF-I	WF-II
4000	0.58	0.58	0.38	0.38	**36.70**	**36.70**	1.48	1.48	0.45	0.45	**36.47**	**36.47**
6000	0.51	0.51	**7.21**	**7.21**	2.35	2.35	1.51	1.51	0.46	0.46	**7.71**	**7.71**
10000	0.50	0.50	**5.70**	**5.70**	0.40	0.40	1.53	1.53	0.46	0.46	**5.91**	**5.91**
12000	0.49	0.49	**5.17**	**5.17**	1.63	1.63	1.54	1.54	0.47	0.47	**5.64**	**5.64**
16000	0.48	0.48	4.75	4.75	2.83	2.83	1.57	1.57	0.47	0.47	**5.74**	**5.74**

Table 8.13 PCC voltage THD (%) with two capacitors at WF-I and three capacitors at WF-II

$\vec{I}_h$	I_3^{max}		I_5^{max}		I_7^{max}		I_{11}^{max}		I_{13}^{max}		$\sum\limits_{n=3,5,7,11,13}\left(I_n^{max}\right)$	
SCL (MVA)	WF-I	WF-II	WF-I	WF-II	WF-I	WF-II	WF-I	WF-II	WF-I	WF-II	WF-I	WF-II
4000	0.61	0.66	0.32	0.47	2.54	2.61	1.56	0.77	0.46	0.26	3.02	2.80
6000	0.96	0.59	**22.23**	**33.40**	2.97	2.78	1.85	0.79	0.97	0.30	**22.49**	**33.53**
10000	0.51	0.55	**10.93**	**16.41**	2.19	2.28	1.61	0.80	0.48	0.27	**11.28**	**16.59**
12000	0.81	0.62	**8.81**	**13.09**	2.99	2.85	1.73	0.87	0.77	0.43	**9.43**	**13.42**
16000	1.74	0.90	**7.43**	**11.00**	4.06	3.20	2.31	1.08	1.78	0.72	**8.48**	**11.49**

Table 8.14 PCC voltage THD (%) with two capacitors at WF-I and five capacitors at WF-II

$\vec{I}_h$	I_3^{max}		I_5^{max}		I_7^{max}		I_{11}^{max}		I_{13}^{max}		$\sum\limits_{n=3,5,7,11,13}\left(I_n^{max}\right)$	
SCL (MVA)	WF-I	WF-II	WF-I	WF-II	WF-I	WF-II	WF-I	WF-II	WF-I	WF-II	WF-I	WF-II
4000	0.70	0.92	0.13	0.92	4.42	0.89	1.62	0.39	0.48	0.14	4.78	1.63
6000	0.69	0.75	0.41	**5.05**	2.74	0.51	1.70	0.41	0.62	0.17	3.28	**5.14**
10000	0.56	0.74	0.11	**5.63**	1.29	0.26	1.66	0.41	0.49	0.15	2.24	**5.70**
12000	0.59	0.73	0.23	**6.01**	**47.36**	**9.48**	1.68	0.41	0.53	0.16	**47.40**	**11.25**
16000	1.18	0.70	1.07	**6.32**	**24.00**	**4.27**	1.98	0.47	1.17	0.27	**24.08**	**7.64**

8.9 CONCLUSIONS

In 2010, the tripping of several wind turbines was reported in a 101.2 MW wind farm in Ontario. The turbines tripped in the mornings following the switching of the 220 MVAR transmission network capacitor with power factor correction park capacitors installed at the wind farm. The trippings of the wind turbines caused substantial revenue loss which continued for several days. Mitigative measures were immediately taken. The over voltage trip settings on the turbines were time-delayed and the threshold voltage for trip was also increased. Further, the synchronous control unit responsible for operating the Hydro One transmission capacitor was also replaced. Due to these actions, the tripping of wind turbines stopped. However, the original reason for the turbine trip remained unknown. This project was therefore undertaken to investigate the primary reason behind the turbines tripping. This chapter presents a detailed analysis of the turbine trip events through a comprehensive study of network resonances, and makes recommendations to prevent future potential trip events in the 101.2 MW wind farm as well as in a similar wind farm of 101.2 MW that has been radially connected at the same bus.

A detailed system model in PSCAD/EMTDC software was developed for the two wind farms and the transmission network with extensive data provided by Hydro One and the wind farm owner. The variation of network impedance as a function of frequency was investigated for a wide range of system short circuit levels and different combinations of park capacitors with the transmission capacitor. The fault recorder data for the different turbine trip events was examined. Fast Fourier Transform (FFT) analysis was performed to determine the harmonic components in the voltages at the terminal of wind farm and at the 230 kV transmission bus. The harmonic impact of unsynchronized capacitor switching of three phases of the transmission capacitor was investigated. The harmonics generated by the unsynchronized capacitor switching were correlated with the resonant frequencies obtained from frequency scanning of the network impedance, as well as with the major harmonic components seen in the fault recorder data at the wind farm.

Frequency scanning studies were then performed with the two identical wind farms and the network resonant frequencies were determined for different combinations of park capacitors in both wind farms. Critical combinations of park capacitors in both wind farms were obtained for which the resonant frequencies were around the characteristic harmonic injections from wind turbine generators.

Actual harmonic injection levels were then obtained from the wind turbine generator manufacturers. These are not reported for confidentiality reasons. Maximum levels of individual characteristic harmonics were injected from the WTGs in the PSCAD/EMTDC model and voltage THDs were obtained at the wind farm terminals.

The following conclusions are made:

(a) Two resonant modes are seen in the network impedance. One is caused by the large transmission capacitor around the $4^{th} - 6^{th}$ harmonic, and the other one is caused by the park capacitor which varies from the 13th to 7th harmonic depending upon the number of park capacitors connected.

(b) Both the network resonance frequencies are strongly influenced by the system short circuit level. There are specific short circuit levels seen for which these resonance frequencies can align with the frequencies of characteristic harmonics injected by wind turbines.

(c) Unsynchronized switching of the transmission capacitor leads to the generation of the 6th harmonic currents, which together with a network resonance at the 6th harmonic can result in a high overvoltage. This harmonic amplification around the 6th harmonic is seen to be one of the main causes of wind turbine trips.

(d) Overvoltages may also be caused by harmonic amplification of frequencies around those of characteristic harmonics injected by the wind turbines at critical short circuit levels. These are typically the 11th, 7th and 5th harmonics.

(e) Overvoltages due to a combination of harmonic resonances in both iii) and iv) are seen to be the cause of wind turbine trippings.

(f) A table of potentially safe and unsafe combinations of park capacitors in both wind farms has been prepared after network resonance studies over a wide range of system short circuit levels. The unsafe combinations are those for which the

network resonant frequencies tend to align with the frequencies of injected characteristic harmonics.

(g) A conservative study is performed with maximum injection of individual harmonics from the wind turbines. This is studied to indicate potential problems. It is seen that for the critical (unsafe) combinations of park capacitors, maximum harmonic injection even of individual 7th , or 11th or their combination can result in voltage THDs in excess of that prescribed by IEEE standard 519.

(h) It is therefore recommended that the unsafe combinations of park capacitors should be avoided. However, if these combinations must be used for college support or factor correction, suitable harmonic filters may be installed, after performing network resonance studies with updated system information.

Chapter 9

CONCLUSIONS AND FUTURE WORK

9.1   GENERAL CONCLUSION

A detailed study of the potential for subsynchronous resonance in induction generator based wind farms connected to series compensated line and line commutated converter (LCC) based HVDC line is presented in this thesis. Subsequently, mitigation of subsynchronous resonance using a FACTS device - STATCOM is described. A comprehensive study of turbine trippings in an actual wind farm in Ontario due to harmonic resonance is also reported here.

A broad review of the work done and major contributions made in the thesis are discussed below. Suggestions are also included for future research in the area of subsynchronous resonance in wind farms.

9.2   MODELING OF WIND FARM COMPONENTS

In Chapter 2 a detailed model of an induction generator based wind farm connected to series compensated transmission line is developed for a study of SSR phenomenon. The overall model comprises multi-mass wind turbine, induction generator, and series compensated transmission line. The non-linear dynamic equations of each component are developed in d-q frame of reference and linearized to express the study system in a linear state space form. This model of the grid connected wind turbine generator system is reasonably validated with time domain simulations carried out with electromagnetic transient simulation software PSCAD/EMTDC.

For subsynchronous resonance studies in wind farms, eigenvalue analysis may be sufficient to predict the modal frequencies and small signal stability. However, during the large disturbances in a network, such as a terminal fault, eigenvalue analysis may not be adequate to predict the stability behavior of the induction generator based wind farm connected to series compensated line. For this purpose, an equivalent circuit analysis is

introduced. The slip dependent roots are calculated which indicate the resonant speed limits for different sizes of wind farms and levels of series compensation. This equivalent circuit analysis is utilized to calculate the resonant speed of the wind turbine generators. The stability margin of the aggregated wind turbine generator during a generator terminal fault is predicted from this analysis.

9.3 SUBSYNCHRONOUS RESONANCE ANALYSIS OF SINGLE-CAGE INDUCTION GENERATOR BASED WIND FARM

In Chapter 3 a comprehensive analysis of the subsynchronous resonance in single-cage induction generator based wind farms is presented. System eigenvalues are calculated from the linearized system for different operating scenarios: change in wind farm size, change in level of series compensation, and change in wind farm power output. From the calculated eigenvalues, the potential for subsynchronous oscillations is examined. It is found that single-cage induction generator based wind farms may experience subsynchronous resonance instability with high percent of series compensation. The critical compensation levels are found above 70%.

Participation factor analysis is performed to determine the factors affecting different critical modes in the wind farm. It is found that the electrical mode that causes the induction generator effect is associated with the voltage across the series capacitor, and currents in the stator and series compensated line. This mode is decoupled from the mechanical drive train system of the wind turbine. The electromechanical mode is found to be contributed by the generator speed and induced voltage in the rotor. The torsional mode is associated with the mechanical properties of the torsional system. A sensitivity analysis is also carried out for the various oscillatory modes with respect to changes in several electrical and mechanical parameters. This shows that the electrical mode is significantly affected by the stator and rotor resistance, whereas the mechanical parameters are found to influence the torsional mode.

Non-linear time domain simulations are carried out with PSCAD/EMTDC software over a wide range of operating conditions and the small signal model is reasonably validated.

The critical series compensation levels obtained from eigenvalue analysis are substantiated through the electromagnetic transient simulations.

Although no torsional interaction is observed, even at realistic level of series compensation (50%), a symmetrical fault at the wind farm terminals may cause significant rise in the shaft torque. This scenario was predicted by the proposed equivalent circuit analysis and reasonably validated by PSCAD/EMTDC simulations. These studies were not available previously in SSR literature.

9.4 SUBSYNCHRONOUS RESONANCE ANALYSIS OF DOUBLE-CAGE INDUCTION GENERATOR BASED WIND FARM

Most of the large induction generators used in wind farms are equipped with two rotor cages. Hence, Chapter 4 presents a comprehensive analysis of subsynchronous resonance in double-cage induction generator based wind farms connected to a series compensated line.

The SSR study is conducted through small signal analyses followed by time domain simulations using PSCAD/EMTDC. State space model of the study system is developed and eigenvalue analysis is used to predict system stability over a broad range of series compensation levels and wind farm sizes. Effect of variable power output is also investigated. It is found that double-cage induction generator based wind farms are quite susceptible to subsynchronous resonance, even at a realistic level of series compensation. For wind farms between 100 MW and 500 MW, the critical series compensation levels are obtained between 45% and 60%, which was not reported earlier in literature. Beyond the critical compensation levels, self-excitation due to induction generator effect is predicted from the eigenvalue analysis, which is then reasonably validated with the time domain simulations carried out with PSCAD/EMTDC. No torsional interaction is witnessed in this study.

Participation factor analysis is conducted for selected subsynchronous modes, and the system states contributing to these modes are determined. Sensitivity analysis is further

performed to examine how various modes are affected by variations in the electrical and mechanical parameters of the wind turbine generator system.

A thorough analysis of the impacts of fault location is carried out in this chapter. It is found that symmetrical faults at the terminal of the wind farm can cause high shaft torques in small wind farms, even with a realistic level of series compensation (50%). Although, a single occurrence of such an event may not have significant impact on the shaft, repeated occurrences may result in shaft failure due to cyclic fatigue.

9.5 SUBSYNCHRONOUS RESONANCE ANALYSIS IN IEEE SECOND BENCHMARK SYSTEM

Chapter 5 presents the subsynchronous resonance analysis in wind farms connected to non-radial series compensated lines. The mutual interactions between two wind farms connected to radial series compensated lines are also reported in detail. The IEEE Second SSR Benchmark system is modified for the studies by replacing the large synchronous generator with an equivalent aggregated wind farm.

From eigenvalue analysis it is found that there is no potential for subsynchronous resonance in wind farms which are connected to a non-radial series compensated line. This is also reasonably validated with detailed non-linear electromagnetic transient simulations carried out with PSCAD/EMTDC software. Small signal and transient simulations are also carried out for a system with the outage of the uncompensated line. Still, no potential for subsynchronous resonance is observed. During this contingency, the system configuration is comparable with the modified IEEE First Benchmark system. During such a system condition, the electrical mode oscillation sustains for a longer period without destabilizing the system, even at high level of series compensation (say 90%). This is due to the high resistance of the transmission line which increases the damping of the electrical mode.

The time domain simulation of two induction generator based wind farms connected to radial series compensated line exemplifies the mutual interaction between two similar wind farms when connected to a series compensated line. In such a scenario, no potential

for subsynchronous resonance is found. However, the elctromechanical mode of each wind farm is lightly affected by the same mode of the other wind farm. Series compensated transmission lines with low X / R ratio improves the system damping and a line resistance above its critical value successfully mitigates the instability in a wind farm following a symmetrical fault in the network.

9.6 SUBSYNCHRONOUS RESONANCE MITIGATION IN SERIES COMPENSATED WIND FARM USING STATCOM

Chapter 6 proposes a STATCOM based technique for mitigation of SSR in wind farms. Two STATCOM controllers are proposed in this chapter. In the first controller C-I, the DC voltage remains uncontrolled, whereas in the second controller C-II, the DC voltage control is incorporated. The complete system state space model is developed and reasonably validated with time domain simulations using PSCAD/EMTDC. Double-cage induction generators are used in this chapter to represent the wind turbine generator system.

The proposed STATCOM controller C-I is proposed for voltage control purpose. Since the series capacitors do not cause torsional interactions in a wind farm, no SSR damping controller is necessitated to mitigate the subsynchronous resonance oscillations caused by the induction generator effect. It is found that the STATCOM controller C-I is capable of mitigating the potential for subsynchronous resonance in wind farms at any series compensation level. This is seen from eigenvalue analysis and time domain simulations as well. However, the uncontrolled DC voltage causes large overshoot in the AC side voltage following the fault in the network.

In the STATCOM controller C-II, the modulation index and the displacement angle are independently controlled. With the modulation index control, the overshoot in the AC voltage is considerably reduced. Similarly, the DC voltage is also controlled effectively by the displacement angle. The performance of STATCOM controller C-II is found to be superior over the performance of the controller C-I. The improvement is manifested as

decreasing overshoot in voltage, reduced reactive power output of the STATCOM and faster damping.

The proposed STATCOM controller employed at the PCC also successfully mitigates the unstable electromagnetic toque oscillations caused by system electrical fault at the terminal of wind farms.

9.7 SUBSYNCHRONOUS RESONANCE STUDY OF WIND FARM CONNECTED TO LINE COMMUTATED CONVERTER (LCC) BASED HVDC LINES

Around the world, HVDC is being increasingly relied upon to integrate large amounts of wind power systems, both onshore and offshore. However, HVDC converters can potentially create subsynchronous torsional oscillations in turbine generators that are connected to the same bus as the HVDC converter.

In Chapter 7 an analysis of the potential of subsynchronous resonance in wind farms connected to the LCC HVDC line is presented. Detailed studies are also carried out with parallel series compensated AC lines and HVDC lines. The state space model of the study system is developed and system eigenvalues are calculated at different operating conditions. Participation factor and sensitivity analysis are also performed to investigate the influence of various components in the HVDC line on the SSR. Time domain simulations are carried out in electromagnetic transient simulation software PSCAD/EMTDC that validates the small signal analysis.

From small signal analysis it is found that the HVDC converter current regulator does not have any adverse interactions with wind turbine generator. The study with the AC-DC system shows that the HVDC current regulator stabilizes the electrical mode of a wind farm connected to series compensated line. This is also confirmed by the sensitivity analysis and time domain simulations. The AC line faults are simulated and no instability is found in the wind farms. The sensitivity study reported in Chapter 7 clearly shows that there is no potential for torsional interactions between the wind farm shaft system and HVDC current regulator.

After a detailed analysis, it is found that symmetrical faults in the network may excite the electromechanical mode and torsional mode but no torque increase is anticipated. When the HVDC line is blocked, the connected wind farm may suffer from potentially unstable SSR oscillations. In such a scenario the effective series compensation must be reduced to a safe limit.

9.8   WIND FARM HARMONICS RESONANCE

Chapter 8 presents a detailed analysis of the turbine trip events through a comprehensive study of network resonances and makes recommendations to prevent future potential trip events in the 101.2 MW wind farm and a similar wind farm of 101.2 MW that has been radially connected at the same bus.

The variation of network impedance as a function of frequency was investigated for a wide range of system short circuit levels and different combinations of park capacitors with the transmission capacitor. Two resonant modes are seen: one is caused by the large transmission capacitor and the other is caused by the park capacitor. Both network resonance frequencies are strongly influenced by the system short circuit level.

Frequency scanning studies were then performed with the two identical wind farms and the network resonant frequencies were determined for different combinations of park capacitors in both wind farms. A table of potentially safe and unsafe combinations of park capacitors in both wind farms has been prepared after network resonance studies over a wide range of system short circuit levels.

The harmonics generated by the unsynchronized capacitor switching were correlated with the resonant frequencies obtained from frequency scanning of the network impedance, as well as with the major harmonic components seen in the fault recorder data at the wind farm. Unsynchronized switching of transmission capacitor leads to generation of 6th harmonic currents, which together with a network resonance at the 6th harmonic can result in a high overvoltage.

A conservative study is performed with maximum injection of individual harmonics from the wind turbines. It is seen that for the critical (unsafe) combinations of park capacitors,

maximum harmonic injection even of individual 7th , or 11th or their combination can result in voltage THDs in excess of that prescribed by IEEE standard 519.It is therefore recommended that the unsafe combinations of park capacitors be avoided. However, if these combinations must be used for voltage support or power factor correction, suitable harmonic filters may be installed, after performing network resonance studies with updated system information.

9.9 CONTRIBUTIONS

The following are the major contributions of this thesis:

(a) A comprehensive model for the study of subsynchronous resonance in induction generator based wind farm has been developed. This model is adequate for small signal analysis. An equivalent circuit model is also presented for investigating system stability for symmetrical faults at generator terminals. Both models are reasonably validated by electromagnetic transient studies using PSCAD/EMTDC. Such a detailed combined model has not been reported previously in literature.

(b) The potential for the subsynchronous resonance in both single-cage and double-cage induction generator based wind farms connected to a series compensated line is examined. The single-cage and double-cage induction generators constitute a large majority of all of the commercially operating wind farms. Small signal analysis of the potential SSR is reasonably validated with electromagnetic transient simulations with PSCAD/EMTDC software. Studies are conducted for these commercially used double-cage wind turbine generators. It is shown for the first time in this thesis that induction generator based wind farms are susceptible to SSR even at realistic levels of series compensation (50%). This interaction was not known or presented in any previous literature.

(c) The study of subsynchronous resonance is also carried out with induction generator based wind farms connected to a non-radial series compensated line. Eigenvalue analysis results are reasonably validated by electromagnetic transient simulations. This study confirms that there is no potential for SSR oscillations in

the wind farms connected to non-radial series compensated lines. The mutual interaction between two wind farms connected to the series compensated line is also studied. No such SSR analysis of such wind farms was reported previously.

(d)   A STATCOM with two types of controllers is proposed to mitigate the induction generator effect SSR. Performance of the controllers has been reasonably validated with time domain simulations at different operating conditions. The proposed STATCOM control alleviates both steady state SSR and high shaft torque due to faults at generator terminals. These STATCOM controllers are proposed for the first time in literature.

(e)   A thorough analysis of SSR interaction between a rectifier controller and the wind turbine generator is presented. It is concluded that there is no potential for adverse interaction between the HVDC current controller and the wind turbine torsional system.

(f)   A comprehensive analysis of wind turbine trippings in an actual large wind farm has been performed. The causes of these tripping have been identified through network resonance analysis and recommendations made to avoid such trippings in future. Such a study with large commercially operating wind farm has not been reported anywhere before.

9.10 FUTURE WORK

The suggestions for the future research are mentioned below.

(a)   This thesis presents a comprehensive analysis of the subsynchronous resonance by considering an aggregated wind farm model. Large wind farms in the range of hundreds of MW are spread over large geographical areas. Hence, all wind turbines may not experience the same wind speed. A separate study therefore may be carried out to investigate the impact of the different wind speeds on the performance of the different wind turbine generators connected to the same series compensated lines.

(b)   A detailed subsynchronous resonance analysis should be performed with other types of wind farms connected to LCC HVDC lines and series compensated transmission lines. Particularly a DFIG based wind farm should be considered for the analysis whose controllers may have an interaction with HVDC rectifier current controller.

(c)   In this thesis, mitigation of subsynchronous resonance using only STATCOM is presented. A comprehensive study with other FACTS devices such as SVC and TCSC may also be performed to mitigate SSR in induction generator based wind farms.

Appendix-A

A.1 DERIVATION OF DOUBLE-CAGE INDUCTION GENERATOR PARAMETERS.

In literature there are two types of double cage induction generator models available. Figure A.1 (a) and (b) represent the above mentioned models which are equal among themselves. Since manufacturers' data is not readily available to the researchers, the constant parameter model of the double-cage is adopted for the various kind of studies related to the grid integration of fixed speed wind farms. In [106], a new method has been proposed to derive different parameters of a double-cage induction generator from the manufacturer provided data: nominal mechanical power, nominal power factor, maximum torque, starting torque, and current. In [107] a detailed study of equivalence between the different double cages induction motor models with six, seven, and eight parameters has been presented. Since model Figure B.1 (b) is available in PSCAD/EMTDC software, the conversion of the parameters from the model shown in Figure B.1 (a) is presented here.
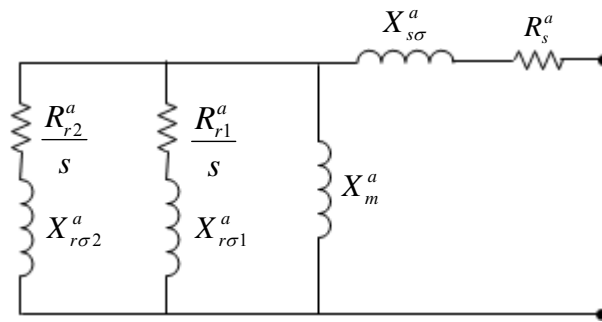
(a) Model-I
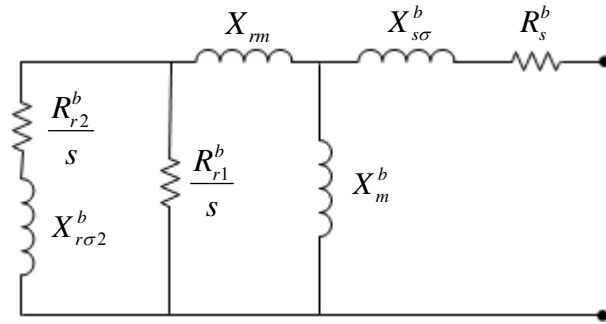
(b) Model-II

Figure A.1 Equivalent circuit of double-cage induction generator
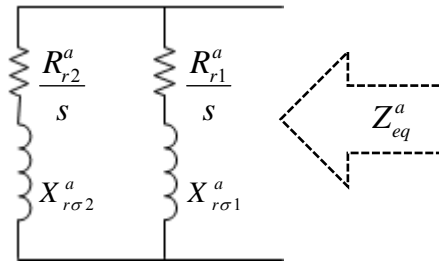
(a) Rotor circuit of Model-I
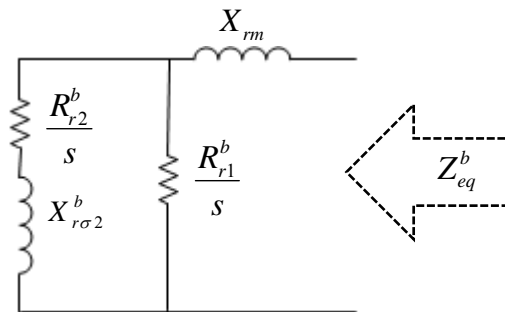
(b) Rotor circuit of Model-II

Figure A.2 Equivalent impedance of rotor circuit of a double-cage induction generator.

For the conversion of parameters, conditions adapted are $R_s^a = R_s^b$, $X_{s\sigma}^a = X_{s\sigma}^b$, $X_m^a = X_m^b$ and the slip is considered as 1: assuming the machine is at stand still. Figure A.2 (a) and (b) now only shows the rotor circuit of the both model. The equivalent input impedance of the model is shown in Figure A.2 (a).

$$Z_{eq}^a = \frac{\left(\dfrac{R_{r1}^a}{s} + jX_{r\sigma1}^a\right)\left(\dfrac{R_{r2}^a}{s} + jX_{r\sigma2}^a\right)}{\left(\dfrac{R_{r1}^a}{s} + jX_{r\sigma1}^a\right) + \left(\dfrac{R_{r2}^a}{s} + jX_{r\sigma2}^a\right)} \tag{A.1}$$

$$Z_{eq}^a = \frac{-A^a s^2 + jB^a + C^a}{jD^a s^2 + s} \tag{A.2}$$

where,

$$A^a = \frac{X_{r\sigma1}^a X_{r\sigma2}^a}{R_{r1}^a + R_{r2}^a} \tag{A.3}$$

$$B^a = \frac{X_{r\sigma1}^a R_{r2}^a + X_{r\sigma2}^a R_{r1}^a}{R_{r1}^a + R_{r2}^a} \tag{A.4}$$

$$C^a = \frac{R_{r1}^a R_{r2}^a}{R_{r1}^a + R_{r2}^a} \tag{A.5}$$

$$D^a = \frac{X_{r\sigma1}^a + X_{r\sigma2}^a}{R_{r1}^a + R_{r2}^a} \tag{A.6}$$

The equivalent input impedance of the model is shown in Figure A.2 (b)

$$Z_{eq}^b = jX_{rm} + \frac{\left(\dfrac{R_{r1}^b}{s}\right)\left(\dfrac{R_{r2}^b}{s} + jX_{r\sigma2}^b\right)}{\left(\dfrac{R_{r1}^b}{s}\right) + \left(\dfrac{R_{r2}^b}{s} + jX_{r\sigma2}^b\right)} \tag{A.7}$$

$$Z_{eq}^b = \frac{-A^b s^2 + jB^b + C^b}{jD^b s^2 + s} \tag{A.8}$$

where,

$$A^b = \frac{X_{rm} X_{r\sigma2}^b}{R_{r1}^b + R_{r2}^b} \tag{A.9}$$

$$B^a = \frac{X_{rm}\left(R_{r1}^b + R_{r2}^b\right) + X_{r\sigma2}^b R_{r1}^b}{R_{r1}^b + R_{r2}^b} \tag{A.10}$$

$$C^b = \frac{R_{r1}^b R_{r2}^b}{R_{r1}^b + R_{r2}^b} \tag{A.11}$$

$$D^b = \frac{X^b_{r\sigma 2}}{R^b_{r1} + R^b_{r2}} \tag{A.12}$$

Comparing (A.3) – (A.6) and (A.9)-(A.12)

$$X_{rm} = \frac{A^b}{D^b} \tag{A.13}$$

$$R^b_{r1} = \frac{B^a - X_{rm}}{D^a} \tag{A.14}$$

$$R^b_{r2} = \frac{C^a R^b_{r1}}{R^b_{r1} - C^a} \tag{A.15}$$

$$X^b_{r\sigma 2} = D^a \left(R^b_{r1} + R^b_{r2} \right) \tag{A.16}$$

Example:

For a 500 kW induction machine, data are given for the model I (Figure A.1 (a)) which are converted to model II (Figure A.1 (b)).

Table A.1 Calculation of Model-II parameters from Model-I parameters

Model I Figure 2.8 (a)	Model II Figure 2.8 (b)
$R^a_s = 0.00383$	$R^b_s = 0.00383$
$R^a_{r1} = 0.15052$	$R^b_{r1} = 0.0716$
$R^a_{r2} = 0.00765$	$R^b_{r2} = 0.0081$
$X^a_{s\sigma} = 0.05592$	$X^b_{s\sigma} = 0.05592$
$X^a_{r\sigma 1} = 0.05592$	$X^a_{r\sigma 1} = 0$
$X^a_{r\sigma 2} = 0.12222$	$X^b_{r\sigma 2} = 0.0898$
$X^a_m = 2.398$	$X^b_m = 2.398$
	$X_{rm} = 0.0384$
$Z^a_{eq}\,|_{s=1} = 0.0432 + 0.0703i$	$Z^b_{eq}\,|_{s=1} = 0.0432 + 0.0703i$

If the parameters for model-II are known, then through the reverse transformation model-A parameters can be calculated. However, this is not required here.

A.2 INITIALIZATION OF INDUCTION GENERATOR BASED WIND TURBINE

Small signal analysis of subsynchronous resonance phenomenon purely depends upon the accurate linearized model of the wind turbine, generator circuit, and network. Various power system dynamics simulation software applications are available for such study. Wind turbine models must be integrated into power system dynamics simulation software packages which could present a challenge. One of the problems that must be solved to make this possible is the calculation of the initial conditions of the wind turbine from load flow data in order to be able to initialize the dynamic model correctly. If the initialization is not carried out correctly, the system will start at an unsteady condition. In some cases, the system may move toward an equilibrium condition after some time, and the desired state, as obtained from the initial load flow may not be achieved. In a worst case scenario, instead of moving toward a convergence, the system may become unstable. Table A.2 shows the known variables which are obtained from the load flow study. With these variables the unknown variables are calculated which are also mentioned in Table A.2

Table A.2 List of known and unknown parameters for initialization of induction generator based wind turbine

Parameters	Single-cage Induction generator		Double-cage Induction Generator	
	Model-I	Model-II	Model-I	Model-II
Known	T_w, V_{ds}, V_{qs}	T_w, V_{ds}, V_{qs}	T_w, V_{ds}, V_{qs}	T_w, V_{ds}, V_{qs}
Unknown	$\omega_g,$ $I_{ds}, I_{qs},$ I_{dr}, I_{qr}	$\omega_g,$ $I_{ds}, I_{qs},$ E_d, E_q	$\omega_g,$ $I_{ds}, I_{qs},$ $I_{dr1}, I_{qr1},$ $I_{dr2}, I_{qr2},$	$\omega_g,$ $I_{ds}, I_{qs},$ $E_{d1}, E_{q1},$ E_{d2}, E_{q2}

Appendix-B

B.1 WIND TURBINE DATA

Table B.1 Wind turbine torsional system data [19], [93]

Parameter	Per unit value
H_t	4 s
K_{tg}	0.3 pu/ el. rad
H_g	0.5 s

Table B.2 Wind turbine torsional system data used in second wind farm in Chapter 5. [19]

Parameter	Per unit value
H_t	4 s
K_{tg}	0.2 pu/ el. rad
H_g	0.75 s

B.2 SINGLE-CAGE INDUCTION GENERATOR DATA

Table B.3 Single-cage induction generator data [19], [22], [105]

Parameters	IG-1	IG-2	IG-3	IG-4	IG-5
P	2.3 MW	2.3 MW	2 MW	1.3 MW	0.75 MW
V	690 V	690 V	690 V	690	690
f	60 Hz	60 Hz	60 Hz	60 Hz	60 Hz
R_s	0.005604	0.005604	0.00488	0.0063	0.006
$X_{s\sigma}$	0.1431	0.1098	0.09247	0.1574	0.1332
R_r	0.007246	0.0072	0.00549	0.0113	0.008
$X_{r\sigma}$	0.0514	0.1015	0.09955	0.1181	0.1332
X_m	3.2077	3.2366	3.9528	5.9043	4.3777

B.3 DOUBLE-CAGE INDUCTION GENERATOR DATA

Table B.4 Double-cage induction generator data [105], [112]

Parameters	IG-1 [112]	IG-2 [112]	IG-3 [120]
P	2.3 MW	2.3 MW	1.3 MW
V	690 V	690 V	690 V
f	60 Hz	60 Hz	60 Hz
R_s	0.00506	0.00506	0.0074
$X_{s\sigma}$	0.13176	0.12552	0.1485
R_{r1}	0.01199	0.011658	0.0129
R_{r1}	0.01923	0.018624	0.0124
$X_{r\sigma1}$	0.21172	0.28565	0.1345
$X_{r\sigma2}$	0.072175	0.078995	0.0499
X_{rm}	3.8892	4.0058	4.369
X_m	0.00506	0.00506	0.0074

Appendix-C

C.1 FIRST BENCHMARK SYSTEM
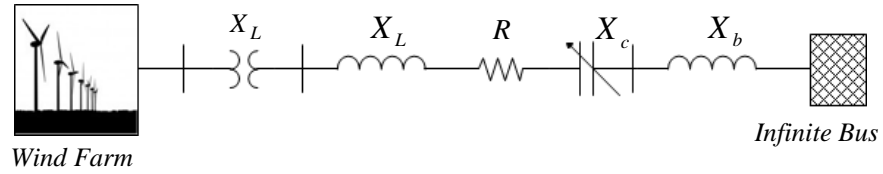
Figure C.1 First Benchmark System connected to widn farm

System Base = 892.4 MVA.

Base Voltage = 500 kV.

Table C.1 First Benchmark System parameters

X_t	0.14 pu
R	0.02 pu
X_L	0.50 pu
X_b	0.06 pu
X_c	$(10\% - 100\%)\, X_b$

C.2 SECOND BENCHMARK SYSTEM
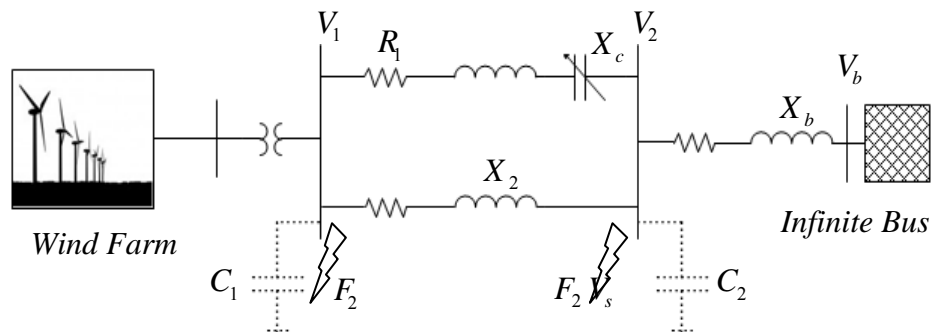
Figure C.2 Second Benchmark System-I connected to widn farm
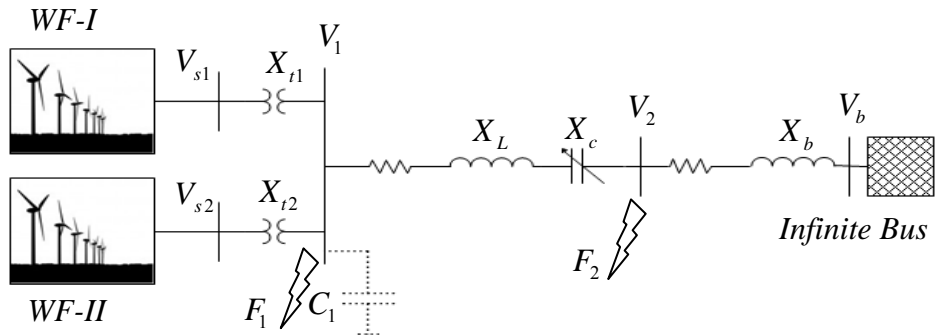
Figure C.3 Second Benchmark System-II connected to wind farm

System Base = 100 MVA.

Base Voltage = 500 kV.

Table C.2 Second Benchmark System parameters

System-I		System-II	
R_t	0.0002	R_{t1}	0.0004
X_t	0.02	X_{t1}	0.04
R_1	0.0074	R_{t2}	0.0002
X_1	0.08	X_{t2}	0.02
R_2	0.0067	R	0.0052
X_2	0.0739	X	0.054
R_b	0.0014	R_b	0.0014
X_b	0.03	X_b	0.03

C.3 STATCOM
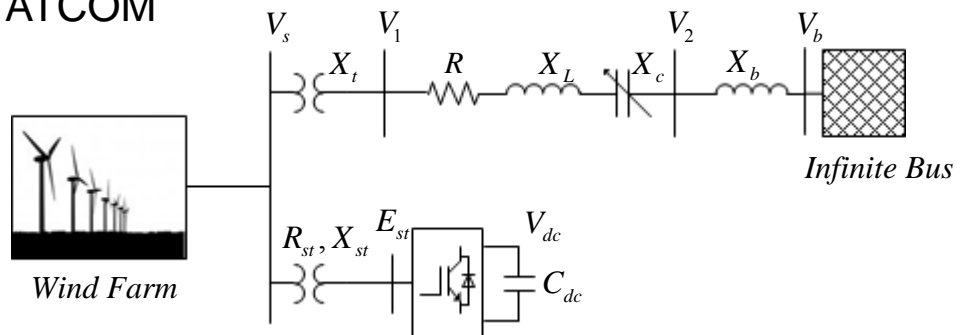
Figure C.4 Study system with STATCOM

STATCOM:

STATCOM size = 60 MVA/ 100 MW

STATCOM base = 300 MVA.

Base voltage = 25 kV.

Table C.4 STATCOM parameters

R_{st}	0.0006 pu
X_{st}	0.1 pu
C_{dc}	5000 μF

STATCOM Controller:

Table C.5 STATCOM controller parameters

Controller-I (C-I)		Controller-II (C-II)	
T_{LP}	0.0024	T_{LP}, T_{DC}	0.004, 0.004
G	0.05	G_1, G_2	1, 0.1
T_1	0.015	T_1, T_2	0.007, 0.05
T_2	0.005	T_3, T_4	0.002, 0.05
K_P	0.1	K_{P1}, T_{I1}	0.54, 0.016
T_I	0.5	K_{P2}, T_{I2}	50, 5

C.4 HVDC SYSTEM

HVDC system parameters taken from [78] and [127]
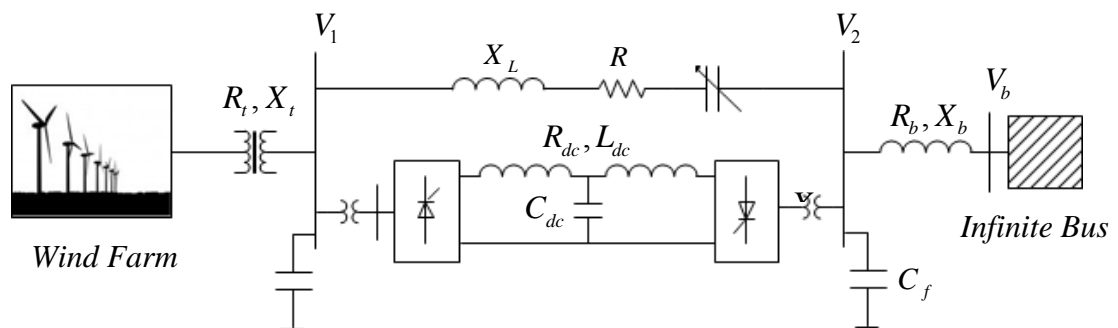
Figure C.5 Wind farm connected to AC-DC system

HVDC base = 1000 MW

Base voltage (DC) = 500 kV

Table C.6 HVDC line parameters

X_{tr}, X_{ti}	0.18 pu
X_{cf}	4 pu
C_{dc}	26 μF
R_{dc}	2.5 Ω
L_{dc}	0.5968 H

REFERENCES

[1]   Global Wind Energy Council. [Online] http://www.gwec.net/

[2]   American Wind Energy Association. [Online] http://www.awea.org /

[3]   World Energy Council. [Online] http://www.worldenergy.org/

[4]   Canada Wind Energy Association. [Online] http://www.canwea.ca/

[5]   European Wind Energy Association. [Online] http://www.ewea.org/

[6]   Indian Wind Energy Association. [Online] http://www.inwea.org/

[7]   http://www.energynautics.com/start.php

[8]   http://www.thewindpower.net/

[9]   http://www.pikeresearch.com/

[10]   http://www.pennenergy.com/index.html

[11]   World Council for Renewable Energy. [Online] http://www.wcre.de/en/index.php

[12]   Electric Reliability Council of Texas. [Online]. http://www.ercot.com/

[13]   California ISO. [Online] http://www.caiso.com/

[14]   Independent Electricity System Operator. [Online]. http://www.ieso.ca/

[15]   http://www.power-technology.com/, accessed Jul. 2012.

[16]   http://www.horizonwind.com, accessed Jul. 2012.

[17]   http://www.powerauthority.on.ca, accessed Jul. 2012.

[18]   http://www.res-group.com, accessed Jul. 2012.

[19]   T. Ackerman, *Wind power in power systems*, New York: Wiley, 2005

[20]   E. Hau, *Wind Turbines: Fundamentals, Technologies, Application, Economics*, 2nd ed., Germany: Springer, 2006.

[21]   Z. Lubosny, *Wind Turbine Operation in Electric Power Systems*, Germany: Springer, 2003.

[22]   O. Anaya-Lara, N. Jenkins, J. Ekanayake, P. Cartwright and M. Guges, *Wind Energy Generation: Modeling and Control*, USA: Wiley, 2009.

[23]   V. Akhmatov, *Induction Generators for Wind Power*, UK: Multi Science, 2007.

[24]   B. Wu, Y. Lang, N Zargari and S. Kouro, *Power Conversion and Control of Wind Energy Systems*, Canada: IEEE Press-Wiley, 2011.

[25]   I. Boldea, *Variable Speed Generators,* New York: CRC Press, 2006.

[26]   P. Pourbeik, R.J. Koessler, D.L. Dickmander and W. Wong, "Integration of Large Wind Farms into Utility Grids (Part 2 - Performance Issues)", in *Proc. 2003 IEEE PES GM*, pp. 1520-1525.

[27]   M. Henderson, D. Bertagnolli and D. Ramey, "Planning HVDC and FACTS in New England," in *Proc. 2009 IEEE/PES PSCE*. pp. 1-3.

[28]   "Ercot CREZ Transmission optimization study," [Online]. Available: www.ercot.com.http://transmission.bpa.gov/business/generation_interconnection/documents/STD-N-000001-00-01_071509.pdf

[29]   N. Bacalao, A. W. Galli, M. Hutson and R. Nadira, "Considerations on the use of HVDC for CREZ transmission," in *Proc. 2009 IEEE/PES PSCE*, pp. 1-7.

[30]   P. Bresesti, W. L. Kling, R. L. Hendriks, and R. Vailati, "HVDC Connection of Offshore Wind Farms to the Transmission System," *IEEE Trans. on Energy Conversion*, vol. 22, no. 1, pp. 37-43, Mar. 2007.

[31]   N. M. Kirby, X. Lie, M. Luckett and W. Siepmann, "HVDC transmission for large offshore wind farms," *Power Engineering Journal*, vol. 16, no. 3, pp. 135-141, Jun. 2002.

[32]   S. Bozhko, G. Asher, L. Risheng, J. Clare and Y. Liangzhong, "Large Offshore DFIG based Wind Farm with Line-Commutated HVDC Connection to the Main Grid: Engineering Studies," *IEE Trans. on Energy Conversion*, vol. 23, no. 1, pp. 119-127, Mar. 2008.

[33]   S. M. Muyeen, R. Takahashi and J. Tamura, "Operation and Control of HVDC-Connected Offshore Wind Farm," *IEEE Trans. on Sustainable Energy*, vol. 1, no. 1, pp. 30-37, Apr. 2010.

[34]   K.R. Padiyar, *Analysis of Subsynchronous Resonance in Power System*, USA: Kluwer Academic Publisher, 1999.

[35]   L. Grigsby, *Power System Stability and Control*, New York: CRC Press, 2007.

[36]   Z. Miao, L. Fan, D. Osborn and S. Yuvarajan, "Wind Farms With HVDC Delivery in Inertial Response and Primary Frequency Control," *IEEE Trans. on Energy Conversion*, vol. 25, no. 4, pp. 1171-1178, Dec. 2010.

[37]   K. Mortensen, E. V. Larsen, and R. J. Piwko, "Field Tests and Analysis of Torsional Interaction Between the Coal Creek Turbine-Generators and the CU

HVDC System," *IEEE Trans. on Power Apparatus and Systems,* vol. PAS-100, no. 1, pp. 336-344, Jan. 1981.

[38] R. J. Piwko and E. V. Larsen, "HVDC System Control for Damping of Subsynchronous Oscillations," *IEEE Trans. on Power Apparatus and Systems*, vol. PAS-101, no. 7, pp. 2203-2211, Jul. 1982.

[39] S. C. Tripathy, "Modeling and simulation of HVDC-turbine generator torsional interactions," Electric Power Components and Systems, vol. 31, no. 11, pp. 1021-1045, 2003.

[40] K.R. Padiyar and A.G. Kothari, "Analysis of the HVDC turbine generator torsional interactions," *Electric Machines and Power Systems*, vol. 16, no. 5, pp. 303-317, 1989.

[41] K.R. Padiyar, Sachchidanand, A.G. Kothari, S. Bhattacharyya and A. Srivastava, "Study of HVDC controls through efficient dynamic digital simulation of converters," *IEEE Trans. on Power Delivery*, vol. 4, no. 4, pp. 2171-2178, Oct. 1989.

[42] P. M. Anderson and R. G. Farmer, *Series Compensation of Power Systems*, California: PBLSH Publication, 1996.

[43] P. M. Anderson, B. L. Agrawal and J. E. Van Ness, *Subsynchronous Resonance in Power Systems,* New York: IEEE Publication, 1990.

[44] IEEE committee report, "First Benchmark Model for Computer Simulation of Subsynchronous Resonance," *IEEE Trans. on Power Apparatus and Systems* vol. 96, no. 5, pp. 1565- 1572, Sep. 1977.

[45] IEEE Committee Report, "Terms, Definitions and Symbols for Subsynchronous Oscillations," *IEEE Trans. on Power Apparatus and Systems,* vol. PAS-104, no. 6, pp. 1326-1334, Jun. 1985.

[46] IEEE Committee Report, "Reader's guide to subsynchronous resonance," *IEEE Trans. on Power Systems,* vol. 7, no. 1, pp. 150-157, Feb. 1992.

[47] N. Johansson, L. Angquist and H. P. Nee, "A Comparison of Different Frequency Scanning Methods for Study of Subsynchronous Resonance," *IEEE Trans. on Power Systems,* vol. 26, no. 1, pp. 356-363, Feb. 2011.

[48]   B. L. Agrawal and R. G. Farmer, "Use of Frequency Scanning Techniques for Subsynchronous Resonance Analysis," *IEEE Trans. on Power Apparatus and Systems,* vol. PAS-98, no. 2, pp. 341-349, Mar. 1979.

[49]   M. El-Marsafawy, "Use of frequency-scan techniques for subsynchronous-resonance analysis of a practical series-capacitor compensated AC network," *IEE Proc. C Generation, Transmission and Distribution*, vol. 130, no. 1, pp. 28-40, Jan.1983.

[50]   M. L. Crow, *Computational Methods for Electric Power Systems,* CRC Press: New York, 2010.

[51]   M. R. Iravani, and A. A. Edris, "Eigen analysis of series compensation schemes reducing the potential of subsynchronous resonance," *IEEE Trans. on Power Systems,* vol. 10, no. 2, pp. 876-883, May 1995.

[52]   J. W. Butler, and C. Concordia, "Analysis of Series Capacitor Application Problems," *Trans. of the American Institute of Electrical Engineers,* vol. 56, no. 8, pp. 975-988, Aug. 1937.

[53]   C. F. Wagner, "Self-Excitation of Induction Motors With Series Capacitors," *Trans. of the American Institute of Electrical Engineers,* vol. 60, no. 12, pp. 1241-1247, Dec. 1941.

[54]   J.W. Ballance, S. Goldberg, "Subsynchronous Resonance in Series Compensated Transmission Lines," *IEEE Trans. on Power Apparatus and Systems*, vol. PAS-92, no. 5, pp. 1649-1658, Sept. 1973.

[55]   B. Fox, D. Flynn, L. Bryans, N Jenkins, D. Milborrow, M. O'malley, R. Watson and O. Anaya-Lara, *Wind Power Integration: Connection and System Operation Aspects,* United Kingdom: IET Power and Energy Series, 2007.

[56]   N. Jenkins, R. Allan, P. Crossley, D Krschen and G. Strbac, *Embedded Generation,* United Kingdom: IET Power and Energy Series, 2008.

[57]   "Southern Alberta Transmission Reinforcement Needs Identification Document," [Online]. Available: http://www.aeso.ca.

[58]   D. J. N. Limebeer and R. G. Harley, "Subsynchronous resonance of single-cage induction motors," *IEE Proceedings B Electric Power Applications,* vol. 128, no. 1, pp. 33-42, Jan. 1981.

[59] D. J. N. Limebeer and R. G. Harley, "Subsynchronous resonance of deep-bar induction motors," *IEE Proc. B Electric Power Applications,* vol. 128, no. 1, pp. 43-51, Jan. 1981

[60] C. E. Bowler and E. Khan, "Wilmarth-Lakefield 345 kV Transmission Series Capacitor Study: Phase 2 SSR Evaluation Report", Xcel Energy, USA, Job-05-243, Dec. 2005.

[61] A. Tabesh and R. Iravani, "Small-signal dynamic model and analysis of a fixed-speed wind farm - a frequency response approach," *IEEE Trans. on Power Delivery*, vol. 21, no. 2 , pp. 778- 787, Apr. 2006

[62] R. K. Varma and S. Auddy, "Mitigation of subsynchronous oscillations in a series compensated wind farm with static var compensator," in *Proc. 2006 IEEE Power Engineering Society General Meeting,* pp. 1-7.

[63] R. K. Varma and S. Auddy, "Mitigation of subsynchronous resonance by SVC using PMU-acquired remote generator speed," in *Proc. 2006 IEEE Power India Conf.,* pp. 1-8.

[64] R. K. Varma, Y. Semsedini and S. Auddy, "Mitigation of subsynchronous oscillations in a series compensated wind farm with Thyristor Controlled Series Capacitor (TCSC)," in *Proc. 2007 Power Systems Conf.: Advanced Metering, Protection, Control, Communication, and Distributed Resources*, pp. 331-337.

[65] R. K. Varma, S. Auddy and Y. Semsedini, "Mitigation of Subsynchronous Resonance in a Series-Compensated Wind Farm Using FACTS Controllers," *IEEE Trans. on Power Delivery,* vol. 23, no. 3, pp. 1645-1654, Jul. 2008.

[66] M.S. El-Moursi, B. Bak-Jensen, M.H. Abdel-Rahman, "Novel STATCOM Controller for Mitigating SSR and Damping Power System Oscillations in a Series Compensated Wind Park," *IEEE Trans. on Power Electronics*, vol. 25, no. 2, pp. 429-441, Feb. 2010

[67] M.S. El-Moursi, "Mitigating subsynchronous resonance and damping power system oscillation in a series compensated wind park using a novel static synchronous series compensator control algorithm," *Wing Engineering,* vol. 15, no. 3, pp. 363-377, Apr. 2012.

[68] A. Ostadi, A. Yazdani, and R. K. Varma, "Modeling and Stability Analysis of a DFIG-Based Wind-Power Generator Interfaced With a Series-Compensated Line," *IEEE Trans. on Power Delivery,* vol. 24, no. 3, pp. 1504-1514, Jul. 2009.

[69] L. Fan, R. Kvasseri, Z. Lee Miao and C. Zhu, "Modeling of DFIG-Based Wind Farms for SSR Analysis," *IEEE Trans. on Power Delivery*, vol. 25, no. 4, pp. 2073-2082, Oct. 2010.

[70] L. Fan, C. Zhu, Z. Miao, M. Hu, "Modal Analysis of a DFIG-Based Wind Farm Interfaced With a Series Compensated Network," *IEEE Trans. on Energy Conversion*, vol. 26, no. 4, pp. 1010-1020, Dec. 2011.

[71] G. D. Irwin, A. K. Jindal, and A. L. Isaacs, "Sub-synchronous control interactions between type 3 wind turbines and series compensated AC transmission systems," in *Proc. 2011 IEEE PES GM*, pp. 1-6.

[72] L. Fan, and Z. Miao, "Mitigating SSR Using DFIG-Based Wind Generation," *IEEE Trans. on Sustainable Energy*, vol. 3, no. 3, pp. 349-358, Jul. 2012.

[73] Sub-synchronous interaction between Series-Compensated Transmission Lines and Generation. [Online]. Available: http://www.nerc.com/files/LL_45_Sub-Synchronous Interaction.pdf

[74] K. Narendra, D. Fedirchuk, R. Midence, N. Zhang, A. Mulawarman, P. Mysore and V. Sood, "New microprocessor based relay to monitor and protect power systems against sub-harmonics," in *Proc. 2011 IEEE Electrical Power and Energy Conference*, pp. 438-443.

[75] M. Bongiorno, A. Peterson and E. Agneholm, "The Impact of Wind Farms on Subsynchronous Resonance in Power Systems," Elforsk Report 11:29, Apr. 2011.

[76] K.R. Padiyar, A. G. Kothari, "Study of the HVDC-Torsional Interactions through Digital Dynamic Simulation," *Electric Machines and Power Systems,* vol. 14, no. 5, pp. 363-375, 1988.

[77] Choo Yin Chin, A. P. Agalgaonkar, K. M. Muttaqi, S. Perera, and M. Negnevitsky, "Subsynchronous torsional interaction behavior of wind turbine-generator unit connected to an HVDC system," in *Proc. 2010 36th Annual Conference on IEEE Industrial Electronics Society* , pp. 996-1002.

[78]   Y. Y. Hsu and L. Wang, "Modal control of an HVDC system for the damping of Subsynchronous oscillations," *IEE Proceedings C Generation, Transmission and Distribution*, vol. 136, no. 2, pp. 78-86, Mar. 1989.

[79]   Ruimin Zheng, M. H. J. Bollen, and Jin Zhong, "Harmonic resonances due to a grid-connected wind farm," in Proc. *2010 14th International Conference on Harmonics and Quality of Power,* pp. 1-7.

[80]   M. Bradt, B. Badrzadeh, E. Camm, D. Mueller, J. Schoene, T. Siebert, T. Smith, M. Starke, and R. Walling, "Harmonics and resonance issues in wind power plants," in Proc. *2011 IEEE PES GM*, pp. 1-8.

[81]   G. Lemieux, "Power system harmonic resonance-a documented case," *IEEE Trans. on Industry Applications*, vol. 26, no. 3, pp. 483-488, May/Jun. 1990.

[82]   W. Xu, Z. Huang, Y. Cui and H. Wang, "Harmonic resonance mode analysis," *IEEE Trans. on Power Delivery*, vol. 20, no. 2, pp. 1182- 1190, Apr. 2005.

[83]   P. C. Buddingh, "Even harmonic resonance-an unusual problem," *IEEE Trans. on Industry Applications*, vol. 39, no. 4, pp. 1181- 1186, Jul.-Aug. 2003.

[84]   Z. Huang, W. Xu, V. R. Dinavahi, "A practical harmonic resonance guideline for shunt capacitor applications," *, IEEE Trans. on Power Delivery,* vol. 18, no. 4, pp. 1382- 1387, Oct. 2003

[85]   S. Tentzerakis, N. Paraskevopoulou, S. Papathanassiou, and P. Papadopoulos, "Measurement of wind farm harmonic emissions," in Proc. *2008 IEEE Power Electronics Specialists Conf.,* pp. 1769-1775.

[86]   S. Liang, Q. Hu and Wei-Jen Lee, "A survey of harmonic emissions of a commercial operated wind farm," in Proc. *2010 IEEE* Industrial *and Commercial Power Systems Technical Conf.,* pp. 1-8.

[87]   F. Ghassemi and Kah-Leong Koo, "Equivalent Network for Wind Farm Harmonic Assessments," *IEEE Trans. on Power Delivery*, vol. 25, no. 3, pp. 1808-1815, Jul. 2010.

[88]   L. Sainz, J. J. Mesas, R. Teodorescu and P. Rodriguez, "Deterministic and Stochastic Study of Wind Farm Harmonic Currents," *IEEE Trans. on Energy Conversion,* vol. 25, no. 4, pp. 1071-1080, Dec. 2010.

[89]   "MATLAB, The language for Technical Computing," *The Mathworks Inc.* 2011.

[90]   "Application guide PSCAD/EMTDC," [Online]. Available:
         https://pscad.com/sites/default/files/documents/Application_Guide_2008.pdf

[91]   S. M. Muyeen, M. H. Ali, R. Takahashi, T. Murata, J. Tamura, Y. Tomaki, A.
         Sakahara and E. Sasano, "Comparative study on transient stability analysis of
         wind turbine generator system using different drive train models," *IET Renewable
         Power Generation, ,* vol.1, no. 2, pp. 131-141, Jun. 2007.

[92]   T. Petru and T. Thiringer, "Modeling of wind turbines for power system studies,"
         IEEE Trans. on Power Systems, vol. 17, no. 4, pp. 1132- 1139, Nov. 2002.

[93]   F. Mei, and B. Pal, "Modal Analysis of Grid-Connected Doubly Fed Induction
         Generators," *IEEE Transactions on Energy Conversion,* vol. 22, no. 3, pp. 728-
         736, Sep. 2007.

[94]   B. Pal and F. Mei, "Modelling adequacy of the doubly fed induction generator for
         small-signal stability studies in power systems," *IET Renewable Power
         Generation*, vol. 2, no. 3, pp. 181-190, Sep. 2008.

[95]   A Perdana, *Dynamic Model of Wind Turbines,* PhD dissertation, Chalmers
         University of Technology, Sweden, 2008.

[96]   D.O. Kelly and S Simmons, *Introduction to Generalized Electrical Machine
         Theory*, England: McGRAW-HILL, 1968.

[97]   P.C. Krause, O. Wasynczuk and S. D. Sudhoff, *Analysis of electric machinery
         and drive systems*, 2nd ed., United States: IEEE Press and Wiley Interscience,
         2002.

[98]   S. J. Chapman, *Electric machinery fundamentals*, 4th Edition, Toronto:
         McGRAW-HILL, 2005.

[99]   P. Kundur, *Power System Stability and Control,* New York: McGraw-Hill, 1994

[100]   J. B. Ekanayake, L. Holdsworth and N. Jenkins, "Comparison of 5th order and 3rd
         order machine models for doubly fed induction generator (DFIG) wind turbines,"
         Electric Power Systems Research, vol. 67, no. 3, pp. 207-215, 2003.

[101]   J. Zhang, A. Dyśko, J. O'Reilly, and W. E. Leithead, "Modelling and performance
         of fixed-speed induction generators in power system oscillation stability studies,"
         Electric Power Systems Research, vol. 78, no. 8, pp. 1416-1424, 2008.

[102] E. Levi, D. Rauski, "Modeling of deep-bar and double cage self-excited induction generators for wind-electricity generation studies," Electric Power Systems Research, vol. 27, no. 1, pp. 73-81, May 1993.

[103] E. Levi, "General method of magnetizing flux saturation modeling in d-q axis models of double-cage induction machines," *IEE Proc. - Electric Power Applications*, vol. 144, no. 2, pp. 101-109, Mar. 1997.

[104] J. Pedra, I. Candela and L. Sainz, "Modelling of squirrel-cage induction motors for electromagnetic transient programs," *IET Electric Power Applications,* vol. 3, no. 2, pp. 111-122, Mar. 2009.

[105] J. Pedra, F. Corcoles, L. Monjo, S. Bogarra and A. Rolan, "On Fixed-Speed WT Generator Modeling for Rotor Speed Stability Studies," *IEEE Trans. on Power Systems*, vol. 27, no. 1, pp. 397-406, Feb. 2012.

[106] J. Pedra and F. Corcoles, "Estimation of induction motor double-cage model parameters from manufacturer data," *IEEE Trans. on Energy Conversion*, vol. 19, no. 2, pp. 310- 317, Jun. 2004.

[107] A. J. Germond, and R. Podmore, "Dynamic Aggregation of Generating Unit Models," *IEEE Trans. on Power Apparatus and Systems*, vol. PAS-97, no. 4, pp. 1060-1069, Jul. 1978.

[108] S. M. Chan, R. L. Cresap, and D. H. Curtice, "Wind Turbine Cluster Model," *IEEE Trans. on Power Apparatus and Systems*, vol. PAS-103, no. 7, pp. 1692-1698, Jul. 1984.

[109] Farhad Nozari, M. Kankam, Prince David and W. William, "Aggregation of Induction Motors for Transient Stability Load Modeling," *IEEE Trans. on Power Systems,* vol. 2, no. 4, pp. 1096-1103, Nov. 1987.

[110] M. Taleb, M. Akbaba, E.A. Abdullah, "Aggregation of induction machines for power system dynamic studies," *IEEE Trans. on Power Systems,* vol. 9, no. 4, pp. 2042-2048, Nov 1994.

[111] K.W. Louie, "Aggregating Induction Motors in a Power System Based on their Standard Specifications," in *Proc. 2006 International Conf. on Power System Technology,* pp. 1-8.

[112]   S. S. Kalsi, D. D. Stephen and B Adkin, "Calculation of System-fault Currents due to Induction Motors," *IEE Proc.,* vol. 118, no. 1, pp. 201-215, 1971.

[113]   IEEE Committee Report, "Second Benchmark Model for Computer Simulation of Subsynchronous Resonance," *IEEE Trans. on Power Apparatus and Systems*, vol. PAS-104, no. 5, pp. 1057-1066, May 1985.

[114]   IEEE subsynchronous resonance working group, "Countermeasures to Subsynchronous Resonance Problems," *IEEE Trans. on Power Apparatus and Systems*, vol. PAS-99, no. 5, pp. 1810-1818, Sep. 1980.

[115]   IEEE subsynchronous resonance working group, "Series Capacitor Controls and Settings as Countermeasures to Subsynchronous Resonance," *IEEE Trans. on Power Apparatus and Systems*, vol. PAS-101, no. 6, pp. 1281-1287, Jun. 1982.

[116]   B. L. Agrawal and R. G. Farmer, "Effective damping for SSR analysis of parallel turbine-generators," *IEEE Trans. on Power Systems*, vol. 3, no. 4, pp. 1441-1448, Nov. 1988.

[117]   Y. Ichihara, T. Kotake, K. Watanabe, S. Takeda, K. Katsuki, H. Suzuki, and R. Fujiwara, "Laboratory Test and Feasibility Study of Two Countermeasures to Subsynchronous Resonance," *IEEE Trans. on Power Apparatus and Systems*, vol. PAS-102, no. 2, pp. 300-311, Feb. 1983.

[118]   L. N. Hannett and F. P. de Mello, "Mechanical countermeasures to subsynchronous torsional instability [in turbo generators]," *IEEE Trans. on Power Systems*, vol. 5, no. 4, pp. 1146-1150, Nov. 1990.

[119]   Narain G. Hingorani and Laszlo Gyugyi, *Understanding FACTS: Concepts and Technology of Flexible AC Transmission Systems*, New York: IEEE-Wiley, 1999.

[120]   K. R. Padiyar, *Facts Controllers in Power Transmission and Distribution*, New Delhi: New Age Publication, 2007.

[121]   R.M. Mathur and R.K. Varma, *Thyristor-Based FACTS Controllers for Electrical Transmission Systems,* New York: IEEE Press-Wiley, 2002.

[122]   A. E. Hammad and M. El-Sadek, "Application of a Thyristor Controlled Var Compensator for Damping Subsynchronous Oscillations in Power Systems," *IEEE Trans. on Power Apparatus and Systems*, vol. PAS-103, no. 1, pp. 198-212, Jan. 1984.

[123]   K. V. Patil, J. Senthil, J. Jiang and R. M. Mathur, "Application of STATCOM for damping torsional oscillations in series compensated AC systems," *IEEE Trans. on Energy Conversion,* vol. 13, no. 3, pp. 237-243, Sep. 1998.

[124]   C. Schauder and H. Mehta, "Vector analysis and control of advanced static VAr compensators," *IEE Proc.C Generation, Transmission and Distribution*, vol. 140, no. 4, pp. 299-306, Jul. 1993.

[125]   A. M. A Hamdan, "An investigation of the significance of singular value decomposition in power system dynamics," *International Journal of Electrical Power & Energy Systems*, vol. 21, no. 6, pp. 417-24, Aug. 1999

[126]   D. K. Lindner, J. Babenreier, and A. M. A. Hamdan, "Measures of controllability and observability and residues," *IEEE Trans. on Automatic Control,* vol. 34, no. 6, pp. 648-650, Jun. 1989.

[127]   M. Szechtman, T. Wess and C. V. Thio, "A benchmark model for HVDC system studies," in Proc. *1991 International Conference on AC and DC Power Transmission,* pp. 374-378.

[128]   X. Yang and C. Chen, "HVDC dynamic modeling for small signal analysis," *IEE Proceedings Generation, Transmission and Distribution,* vol. 151, no. 6, pp. 740-746, Nov. 2004.

[129]   Capacitor bank switching transient, Available: http://www.nepsi.com/transients.htm.

[130]   IEEE Recommended Practices and Requirements for Harmonic Control in Electrical Power Systems, IEEE Standard 519-1992, 1993.

[131]   Akshaya Moharana and Rajiv K. Varma, "Sub-synchronous resonance in single-cage self-excited-induction-generator-based wind farm connected to series-compensated lines," *IET Generation, Transmission & Distribution,* vol. 5, no. 12, pp. 1221-1232, 2011.

[132]   Akshaya Moharana and Rajiv K. Varma, "Instability in Induction Generator Based Wind Farms Connected to Series Compensated Transmission Line," in *Proc. 2011 IEEE International Conference on Energy, Automation, and Signal,* pp.1-8.

[133]   Akshaya Moharana, Rajiv K. Varma and Ravi Seethapathy, "SSR mitigation in wind farm connected to series compensated transmission line using STATCOM," in *Proc. 2012 IEEE* Power *Electronics and Machines in Wind Applications*, pp.1-8.

CURRICULUM VITAE

Name:	Akshaya Kumar Moharana
Post-secondary Education and Degrees:	Bijupatnaik University of Technology Bhubaneswar, Odisha, India 2002-2005. BE Western University London, Ontario, Canada 2009-2012. Ph.D.
Honours and Awards:	Natural Science and Engineering Research Council (NSERC) Industrial Post Graduate Scholarship 2011, 2012
Related Work Experience	Research Engineer Dept. of Science and Technology Sponsored Project. SOA University, India 2005-2008 Teaching Assistant Western University London, Ontario, Canada 2009-2012

Publications

Journals:

[1]   Rajiv K. Varma and Akshaya Moharana, "SSR in Double-cage Induction Generator Based Wind Farm Connected to Series Compensated Transmission Line," Submitted with *IEEE Transaction on Power Systems,* Apr. 2012.

[2]   Akshaya Moharana and Rajiv K. Varma, "SSR Alleviation by STATCOM in Induction Generator based Wind Farm Connected to Series Compensated Line," Submitted with *IEEE Transactions on Sustainable Energy,* Aug. 2012.

[3]   Akshaya Moharana and Rajiv K. Varma, "Subsynchronous Impact of Series Compensation on Induction Generator based Wind Farm," Submitted with *Electric Power Components and Systems,* Jul. 2012.

[4]   Akshaya Moharana and Rajiv K. Varma, "Sub-synchronous resonance in single-cage self-excited-induction-generator-based wind farm connected to series-compensated lines," *IET Generation, Transmission & Distribution,* vol. 5, no. 12, pp. 1221-1232, 2011.

[5]   P. K. Dash, P. K. Rout and A. K. Moharana, "Non-linear Control of Parallel AC Voltage Source Converter High-Voltage DC System Using a Hybrid Input-output Linearization Evolutionary Fuzzy Controller," *Electric Power Components and Systems*, vol. 38, no. 8, pp. 881-899, Jan. 2010

[6]   Akshaya Moharana and P.K.Dash, "Input-Output Linearization and Robust Sliding-Mode Controller for the VSC-HVDC Transmission Link," *IEEE Transactions on Power Delivery*, vol. 25, no. 3, pp. 1952-1961, Jul. 2010.

[7]   P.K. Dash, R.K. Mallick and A.K. Moharana, "Design of a Robust Multivariable Controller for an AC-VSC-HVDC System," *International Journal of Electrical and Power Engineering,* vol. 4, no. 3, pp. 182-192, Dec. 2010.

[8]   J. V. V. Reddy, P. K. Dash, R. Samantaray and A. K. Moharana, "Fast Tracking of Power Quality Disturbance Signals Using an Optimized Unscented Filter," *IEEE Transactions on Instrumentation and Measurement,* vol. 58, no. 12, pp. 3943-3952, Dec. 2009.

[9]   Akshaya Moharana and P.K.Dash, "H∞ controller for stability enhancement in VSC HVDC system with parallel AC lines," *International Journal of Power and Energy Conversion,* vol. 1, no. 2, pp. 215-242., 2009.

Conferences:

[1]   Akshaya Moharana, Rajiv K. Varma and Ravi Seethapathy, "Modal Analysis of Type-1 Wind Farm Connected to Series Compensated Transmission Line and LCC HVDC Transmission Line" Presented in 2012 IEEE Electric Power and Energy Conference, London.

[2]   Akshaya Moharana, Rajiv K. Varma and Ravi Seethapathy, "SSR mitigation in wind farm connected to series compensated transmission line using STATCOM," in *Proc. 2012 IEEE* Power *Electronics and Machines in Wind Applications*, pp.1-8.

[3]   Akshaya Moharana and Rajiv K. Varma, "Instability in Induction Generator Based Wind Farms Connected to Series Compensated Transmission Line," in *Proc. 2011 IEEE International Conference on Energy, Automation, and Signal*, pp.1-8.

[4]   Akshaya Moharana, J. Samarabandu and Rajiv K. Varma, "Fuzzy supervised PI controller for VSC HVDC system connected to Induction Generator based wind farm," in *Proc. 2011 IEEE Electrical Power and Energy Conference*, pp. 432-437.

[5]   Pouyan Saifi, Akshaya Moharana, Rajiv K. Varma and Ravi Seethapathy, "Influence of distributed generation interface transformer and DG configurations on Temporary Overvoltage (TOV)," in *Proc. 2010 IEEE Canadian Conference on Electrical and Computer Engineering*, pp.1-8.

[6]   Akshaya Moharana, Rajiv K. Varma and Wayne H Litzenberger, "Bibliography of HVDC transmission 2009-2010 Part 1 IEEE working group report," in *Proc. 2011 IEEE Power and Energy Society General Meeting*, pp. 1-6.

[7]   Akshaya Moharana, Rajiv K. Varma and Wayne H Litzenberger, "Bibliography of HVDC transmission 2009-2010 Part 2 IEEE working group report," in *Proc. 2011 IEEE Power and Energy Society General Meeting*, pp. 1-6.

[8]   Rajiv K. Varma, Akshaya Moharana and Wayne H Litzenberger, "Bibliography of HVDC transmission 2009 IEEE working group report," in *Proc. 2010 IEEE Power and Energy Society General Meeting*, pp. 1-6.

[9]   A. K. Moharana, B. K. Panigrahi, P. K. Dash, "VSC Based HVDC System for Passive Network with Fuzzy Controller", in *Proc. 2006 International Conference on Power Electronics, Drives and Energy Systems*, pp. 1-4.